Acoustic Wave and Bond Rupture Based Biosensor – Principle and Development

A thesis presented in partial fulfilment of the requirements for the degree of

Doctor of Philosophy

at Massey University, Palmerston North
New Zealand

by

Evan Hirst

2009

ABSTRACT

Bond rupture is an experimental methodology that is used to augment a conventional mass balance biosensor. A good point-of-care biosensor is fast, reliable, simple, cost-effective, and detects low concentrations of the target analyte. Biosensor development is a multidisciplinary field and bond rupture testing is of technical interest to many groups. The Bond rupture methodology endows a mass probe with the ability to discern bond strength. The recognition of specific bonds by mass loading is separated from erroneous non-specific binding by a probe of the force between the analyte and the transducer. Bond rupture is achieved by acoustic excitation of the point of attachment. The force is incremented gradually until rupture occurs.

The advancement of bond rupture biosensors beyond the lab requires improved understanding of the mechanisms of bond rupture by base excitation, the transducers, and the supporting hardware. Bond rupture has traditionally been used in conjunction with the Quartz Crystal Microbalance (QCM). There exists, however, a variety of sensors and transducers to which the bond rupture methodology could be applied. The time, cost and experience required for comprehensive investigation of all avenues is prohibitive.

To further the development of bond rupture characteristic experiments are designed and carried out on the QCM platform. Numerical simulations are constructed which model the current bond rupture approach. This work is limited to the simulation of bond rupture by base excitation. From the results of the experimental investigation a number of improvements to the bond rupture technique are proposed. Improvements are tested by simulation and the Surface Acoustic Wave (SAW) device is selected to advance the bond rupture craft. A prototype SAW bond rupture device is designed. The prototype device is manufactured and tested, confirming the principle of SAW bond rupture.

Future work is required to progress the SAW bond rupture methodology before possible integration with other sensor systems. Because of this work, and the evaluation of the SAW bond rupture prototype, much is learned about the advancement of SAW device bond rupture.

ACKNOWLEDGEMENTS

This work would not have been possible without the support and encouragement of my three supervisors. Although we have been frequently scattered around the country and, at times, the world, we have maintained close contact and your guidance has been invaluable. I would like to thank Yong Yuan for many helpful discussions on all manner of topics, for initiating this project and for hosting me at Industrial Research Limited (IRL). I would like to thank Peter Xu for guiding me into this PhD and all throughout, for your enthusiasm, leadership, and always prompt feedback. I would like to thank John Bronlund for his unique perspective and close guidance while I was on campus. I would like to thank Matthew van der Werff, another PhD candidate from this diverse group, without whom there would be no bond rupture hardware.

I would like to thank Massey University for the award of the Massey University Doctoral Scholarship which supported me during the first three years of this work. And thanks to IRL for keeping me gainfully employed while I finished this thesis part time. I enjoyed my time at IRL immensely and I would like to thank them for hosting me, and this project. This work was performed under the auspices of the Foundation for Research, Science and Technology of New Zealand by Industrial Research Ltd. under New Economy Research Fund C08X0408. I appreciate the invaluable help and assistance from Harry Chen without whom I would have been lost in the lab. I am grateful for the help of all the Engineering and Applied Physics Group at Industrial Research Limited, Gracefield, Lower Hutt for your technical guidance and vibrant discussions.

It is a pleasure to thank my parents, Stephen and Sandra, and sisters, Carrissa and Shaelyn, for all their support during my long university career and for their endless supply of encouraging remarks. Thank you to all my friends who keep me sane throughout this experience. I must apologise to my family and all who are close to me for all the times I have bored them with the gory details of my work. I am grateful to all who have been so patient with me over this journey. I have learned a lot and, I think, come very far since we started.

RELATED PUBLICATIONS

VAN DER WERFF, M. J., Y. J. YUAN, E.R. HIRST, J. BRONLUND, W.L. XU (2007). Quartz crystal microbalance induced bond rupture sensing for medical diagnostics. *IEEE Sensors Journal* 7(5-6): 762-769.

YUAN, Y. J., M. J. VAN DER WERFF, H. CHEN, E.R. HIRST, W.L. XU (2007). Bond rupture of biomolecular interactions by resonant Quartz crystal. *Analytical Chemistry* 79(23): 9039-9044.

HIRST, E. R., YUAN, Y. J., XU, W. L., BRONLUND, J. E. (2008) Bond rupture immunosensors - A review. *Biosensors & Bioelectronics*, 23, 1759-1768.

HIRST, E.R., XU, W.L., BRONLUND, J.E., YUAN, Y.J. (2008). Surface Acoustic Wave Delay Line for Biosensor Application, *Proceedings of the 15th Int. Conf. on Mechatronics and Machine Vision in Practice (M2VIP'09),* 40-44.

TABLE OF CONTENTS

ABSTRACT I

ACKNOWLEDGEMENTS II

RELATED PUBLICATIONS III

LIST OF FIGURES VI

NOMENCLATURE X

1. INTRODUCTION 1

1.1 AIMS AND OBJECTIVES 1

1.2 CONTRIBUTIONS TO KNOWLEDGE 2

1.3 OUTLINE 2

2. LITERATURE REVIEW 3

2.1 INTRODUCTION 3

2.2 BOND RUPTURE 3

2.3 BIOSENSORS AND DIAGNOSIS TECHNIQUES 7

2.4 BIODETECTOR 9

2.5 INTERFACE 13

2.6 TRANSDUCER 15

2.7 FLOW CELLS AND LIQUID OPERATION 30

2.8 ACOUSTIC WAVES IN LIQUID 31

2.9 LOOKING FORWARD 34

2.10 ANALYSIS OF LITERATURE 35

3. BOND RUPTURE EXPERIMENTS 38

3.1 INTRODUCTION 38

3.2 PHANTOM TARGET 38

3.3 QCM BOND RUPTURE EXPERIMENT 39

3.4 ELECTRONIC HARDWARE FOR QCM 40

3.5 MEASURED PROPERTIES 43

3.6 BOND RUPTURE SCAN FREQUENCY CHANGE 50

3.7 FREQUENCY CHANGE SHAPE 60

3.8 BOND RUPTURE SIGNAL OF INTEREST 62

3.9 CHAPTER CONCLUSION 64

4. SINGLE PARTICLE BOND RUPTURE MODEL 67

4.1 INTRODUCTION 67

4.2 EXISTING MODEL 67

4.3 POINT INTERACTION MECHANICAL MODEL 68

4.4 Particle Adhesion 71
4.5 Interactions with Liquid 79
4.6 Contact Area Mechanical Model 81
4.7 Single Bond Rupture 94
4.8 Probabilistic Model 98
4.9 Chapter Conclusion 106
5. MODELLING BOND RUPTURE DEVICES 108
5.1 Introduction 108
5.2 Idealised Bond Rupture Device 108
5.3 QCM Bond Rupture Modelling 113
5.4 Chapter Conclusion 132
6. SAW FABRICATION AND EXPERIMENTS 134
6.1 Introduction 134
6.2 Review of SAW 134
6.3 Design Optimisation of SAW Delay Line 145
6.4 SAW Designs 147
6.5 Equivalent Circuit Analysis of SAW delay-line 148
6.6 SAW microfabrication 154
6.7 SAW experiments of bond rupture 156
6.8 Limitations 162
6.9 Chapter Conclusion 163
7. CONCLUSION 164
8. REFERENCES 165

LIST OF FIGURES

Figure 2.1 Bond rupture test concept. 4
Figure 2.2 QCM rupture force spectra for streptavidin-biotin bond (1) and chemical bond (2) (Dultsev *et al.*, 2001a) 5
Figure 2.3 QCM rupture force spectra for physical bonds (Dultsev *et al.*, 2001a) 5
Figure 2.4 Sample of bond rupture data captured using a SAW device (Dultsev *et al.*, 2001a) 6
Figure 2.5 Schematic of SAW architecture as presented in the patent (Dultsev *et al.*, 2001a) 6
Figure 2.6 Functional diagram of a Biosensor 9
Figure 2.7 Intelligent Packaging (http://www.dcu.ie/~ncsr/commercial/technologies.html) 14
Figure 2.8 Sensor conversion domains 15
Figure 2.9 Couplings between electrical, mechanical and thermal fields (Ballato, 1995) 16
Figure 2.10 Piezoelectric acoustic wave devices 18
Figure 2.11 Quartz Crystal Microbalance 19
Figure 2.12 Determination of dissipation by ringing down of transducer 20
Figure 2.13 Gaussian distribution of mass sensitivity and displacement on QCM 22
Figure 2.14 Temperature sensitivity for variations of AT cut Quartz crystal (Brice, 1985) 23
Figure 2.15 Resonant frequency changing with diving power (Brice, 1985) 23
Figure 2.16 Resonant frequency changing with diving power for an AT-cut device. At low powers the variation is attributed to the variation of elastic constants with strain. At higher powers heating effects are noticeable (Brice, 1985) 24
Figure 2.17 QCM amplitude measurement (Benes *et al.*, 1995) 25
Figure 2.18 QCM modelled using the finite element method (Kurosawa et al., 2004) 25
Figure 2.19 (a) The mechanical model of an electro-acoustical system and (b) its corresponding BVD electrical equivalent (Buttry and Ward, 1992) 26
Figure 2.20 Simulated impedance spectra from the BVD equivalent circuit (Janshoff et al., 2000) 29
Figure 2.21 Acoustic Transmission Line model of a Surface Acoustic Wave Device Transducer (Bhattacharyya et al., 1995) 29
Figure 2.22 Acoustic wave decay into fluid 33
Figure 2.23 Extended Butterworth van Dyke Equivalent Circuit: (a) general model, (b) extended BVD model, and (c) BVD model (Arnau et al., 2002) 34
Figure 2.24 Schematic drawing of a 'Biochip' (Vo-Dinh et al., 2001) 35
Figure 3.1 SEM image of two micron latex spheres showing two spheres adhered to one another 38
Figure 3.2 Factory holder of QCM. Small springs attached with silver epoxy (left). Custom holder featuring Teflon cell and spring clamp. Electrical connection to the QCM electrode is achieved by 'pogo pin' (right) 40
Figure 3.3 Diagram of integrated digital approach for bond rupture testing used by van der Werff et al (2007) 42
Figure 3.4 Measured admittance and phase of QCM in air 45
Figure 3.5 Measured admittance and phase of QCM pure water 45
Figure 3.6 Measured admittance and phase of QCM in air with damping of holder 46
Figure 3.7 Measured third harmonic and third overtone plotted as a function of driving voltage. Δf is not constant during a scan 47
Figure 3.8 Frequency sweep of QCM in factory mount in air used to determine the quality factor 48
Figure 3.9 Frequency sweep of QCM showing reduced quality 48
Figure 3.10 Frequency sweep of QCM showing the effect of clamping 49
Figure 3.11 Frequency sweep of QCM showing restored quality 49
Figure 3.12 Electrode surface temperature of QCM driven at frequencies near resonance at different voltages 50
Figure 3.13 QCM image showing particles ruptured from centre 51
Figure 3.14 Microscope image of physically bound beads showing grouping. 51
Figure 3.15 Frequency change caused by bond rupture experiment of two micron particles attached by physical bonding (top) and ligand-receptor bonds (bottom) 52

Figure 3.16 Frequency change caused by bond rupture experiment of six micron particles attached by physical bonding (top) and ligand-receptor bonds (bottom) 52
Figure 3.17 Frequency change caused by bond rupture experiment of two micron particles attached by ligand-receptor bonds at various concentrations 53
Figure 3.18 Frequency axis has been offset to align the plateau before bond ruptre and normalised to remove the effect of increased mass. 53
Figure 3.19 Rate of frequency change caused by bond rupture experiment of two micron particles attached by ligand-receptor bonds at various concentrations of target particles in the prepared solution. The lines are found by differentiating high order polynomials fitted to Figure 3.17 54
Figure 3.20 Two experiments conducted on the same QCM preparation, early drift in the second scan is indicative of weaker bonds forming with the already used sensor. 55
Figure 3.21 Two micron receptor-ligand bond rupture experiment repeated on different QCM shows large variation in frequency change (top) and the location of peaks in the rate of frequency change (bottom) 56
Figure 3.22 Four micron receptor-ligand bond rupture experiment repeated on different QCM shows large variation in frequency change (top) and the location of peaks in the rate of frequency change (bottom) 56
Figure 3.23 Two micron receptor-ligand bond rupture experiment repeated at different scan rates. Normalised frequency change (top) and voltage plotted against time (bottom) 57
Figure 3.24 Two micron receptor-ligand bond rupture experiment repeated at different scan rates. Normalised frequency change plotted against voltage. 57
Figure 3.25 One micron receptor-ligand bond rupture experiment in ambient nitrogen atmosphere and aqueous environment. 58
Figure 3.26 One micron receptor-ligand bond rupture experiment repeated in ambient nitrogen atmosphere and aqueous environment. Rupture occurs at lower voltage in ambient air. Aqueous results averaged by 25-point moving mean. 58
Figure 3.27 Fifty times magnified image of QCM surface showing distribution of particles 59
Figure 3.28 Bond rupture scans of mixed beads at two different scan rates. The frequency change is plotted against voltage (top) and time (bottom) 59
Figure 3.29 Normalised frequency change results for constant voltage scan 60
Figure 3.30 Normalised frequency change results for constant voltage scan showing exponential nature of bond rupture. 61
Figure 3.31 Result of the Matlab normplot function of the numerical derivative of bond rupture frequency change results 61
Figure 3.32 Result of the Matlab normplot function of the numerical derivative of bond rupture frequency change results 62
Figure 3.33 Frequency change data confirms bond rupture has occurred 63
Figure 3.34 Comparing the STFT of first and final bond rupture scans 64
Figure 3.35 STFT showing overtone moving at the top of the plot. 64
Figure 4.1 Three dimensional forces acting on a two degree of freedom joint. Moving substrate (a), and moving fluid (b) 69
Figure 4.2 Three dimensional path of the system shows only very small angular deviations 70
Figure 4.3 Simulated force 70
Figure 4.4 The geometry of particle adhesion (Johnson et al., 1971) 71
Figure 4.5 Adhesion Map (Johnson and Greenwood, 1997) 72
Figure 4.6 Pull-off moment as a function of pull-off force and contact radius (Ziskind et al., 1997) 75
Figure 4.7 External force - displacement relation of a particle on a surface (Peri and Cetinkaya, 2005) .. 75
Figure 4.8 Rocking motion of a particle subject to base excitation (Peri and Cetinkaya, 2005) 76
Figure 4.9 SEM image of two polystyrene latex spheres bound by physical adhesion 78
Figure 4.10 Bond loading by use of laminar flow chamber. Arrested spherical particle in contact with the wall experiences a force. (Merkel, 2001). 81
Figure 4.11 a) Sphere adhesion geometry showing b) Theta, angular degree of freedom, c) gamma, shear along the axis of displacement, d) delta, vertical degree of freedom 84
Figure 4.12 Force balance on particle in horizontal (a) and vertical (b) directions 85
Figure 4.13 Forces that cause moments on the particle 86
Figure 4.14 Angular displacement vs. time shows that the particle will have rolled off its binding site ... 89
Figure 4.15 Plot of maximum angular displacement vs. substrate oscillation amplitude 89

Figure 4.16 Plot of maximum angular displacement vs. substrate oscillation frequency 90
Figure 4.17 Plot of maximum angular displacement vs. the initial length parameter of the elastic constant function.....91
Figure 4.18 Plot of maximum angular displacement vs. the contact radius.....91
Figure 4.19 Maximum angular displacement determined for multiple substrate amplitudes.....92
Figure 4.20 Maximum vertical displacement determined for multiple substrate amplitudes.....92
Figure 4.21 Maximum shear displacement determined for multiple substrate amplitudes.....93
Figure 4.22 The rupture of single bonds with ultrasensitive force probes. (Evans, 2001) 94
Figure 4.23 Kramers' theory, simple model of reaction kinetics (Hanggi et al., 1990).....96
Figure 4.24 Force histograms of streptavidin-biotin interactions 96
Figure 4.25 Rupture force depends on loading rate (Yuan et al., 2000).....97
Figure 4.26 Conceptual Landscape of streptavidin-biotin interactions (Yuan et al., 2000).....98
Figure 4.27 Bond geometry showing the approximation of bond length change in response to an angular displacementThe contribution of the angular shift in the equation 4.67 is approximated by $x\theta$. This is the arc-length of the line and because for small angles, $\sin\theta \approx \theta$, this is a good approximation of the additive length of the bond.....100
Figure 4.28 Randomly distributed bonds.....101
Figure 4.29 Product of bond extension and bond spring constant for several cycles. 101
Figure 4.30 Curve Fit Demonstration with averaging 103
Figure 4.31 Linear curve fit of the fitted decay parameter plotted vs. the natural logarithm of the maximum substrate displacement 104
Figure 4.32 Natural logarithm of the decay parameter plotted against the natural logarithm of the kBond parameter.....104
Figure 4.33 Decay parameter plotted vs. the number of bonds 105
Figure 4.34 Decay parameter plotted vs. the particle radius 105
Figure 4.35 Angular displacement vs. time in ambient air 106
Figure 5.1 Normalised number of survived bonds on an idealised sensor with constant oscillation amplitude.....109
Figure 5.2 Bond rupture events plotted against time 110
Figure 5.3 The sum of the probability of survival of all particles adhered to the device approximates the number of particles attached 111
Figure 5.4 Bond rupture histogram of idealised bond rupture device 111
Figure 5.5 The derivative of the sum of survival probabilities is analogous to the bond rupture histogram and useful for assessing the most likely rupture point.....112
Figure 5.6 The location and magnitude of the peak in the force distribution is proportional to the logarithm of the total scan time 112
Figure 5.7 a) Microscope image of QCM surface, b)determination of particle density by image analysis 113
Figure 5.8 Amplitude distribution as a function of radius 114
Figure 5.9 Post bond rupture QCM image showing concentration of rupture in centre of transducer ...115
Figure 5.10 Assuming bond breakage occurs at a defined probability then the mass change can be determined 115
Figure 5.11 Mass change can be translated to frequency change 116
Figure 5.12 Survival time plotted as a function of radial location of the particle 117
Figure 5.13 Many individual survival probabilities as a function of time 117
Figure 5.14 From an approximated number of particles the frequency change is compared to experimental data. 118
Figure 5.15 Smooth decay is symptomatic of the distributed rupture events 119
Figure 5.16 The rupture time as a function or radius indicates the origin of the distribution 119
Figure 5.17 Simulated rupture signal is concentrated at the start of the scan 120
Figure 5.18 The form of the simulated frequency change is similar to the experiment results.....120
Figure 5.19 Oscillation amplitude-decay relation for three particle sizes 121
Figure 5.20 Probability of rupture of particles does not clearly indicate that different radii are present 122
Figure 5.21 Rate of change of particle survival of all particles combined and the constituent types 123
Figure 5.22 Simulated frequency change of multiple bond experiments.....123
Figure 5.23 Stepwise amplitude function 124

Figure 5.24 During stepwise operation stronger signal results at after the amplitude step 125
Figure 5.25. Stepwise results showing the contribution of individual species 125
Figure 5.26 The real new mass added to the transducer plotted as a function of radius and the observed mass which is effected by the sensitivity of the QCM 126
Figure 5.27 Normalised bond rupture frequency change simulations of regular and modified QCM 128
Figure 5.28 Derivative of particle survival probability on strip electrode device 129
Figure 5.29 Rupture time as a function of location for each species of particle on strip electrode device 129
Figure 5.30 Particles distributed on SAW sensitive area 130
Figure 5.31 Surface acoustic wave amplitude 131
Figure 5.32 Bond rupture time as a function of distance from the transducer 131
Figure 5.33 Simulated bond rupture noise signal for amplitude for SAW device 132
Figure 6.1 Bond rupture of physical bonds captured using a SAW device The vertical axis of measures bond rupture noise in arbitrary units and the driving amplitude is measured in volts (Dultsev et al., 2001) 135
Figure 6.2 SAW delay line applied to biosensor 135
Figure 6.3 Difference between Love mode and SH-APM 136
Figure 6.4 Love Mass loading sensitivity vs. SiO_2 thickness (Du et al., 1996) 137
Figure 6.5 SAW Amplitude-Frequency effect compared to QCM 138
Figure 6.6 SAW delay-line geometry showing pitch (wavelength, $\boldsymbol{\lambda}$), IDT Length ($\boldsymbol{l}$), delay length and aperture 140
Figure 6.7 SEM image of a cross section of an aluminium finger electrode after loading with 3W for 2000 minutes, hillocks grow outward more than 1µm (Pekarcikova et al., 2005) 140
Figure 6.8 Interdigital transducer (a) split finger electrode(b) three electrode 142
Figure 6.9 Single Phase Unidirectional Transducer(Nakamura et al., 2001) 143
Figure 6.10 Encapsulated SAW biosensor (Lange et al., 2006) 144
Figure 6.11 Plot of constraints on N and f_0 variables showing the feasible region of SAW design for this sensor 146
Figure 6.12 Alternative SAW design with asymetric electrodes 147
Figure 6.13 (a) Mason equivalent circuit of IDT. (b) Circuit representation of delay-line 148
Figure 6.14 Representation of time domain signal construction and the resulting impulse response 148
Figure 6.15 Simulated resistance of fabricated device 150
Figure 6.16 Simulated Impedance of fabricated device 150
Figure 6.17 Combined IDT equivalent circuit 151
Figure 6.18 product of the frequency response of two IDTs plus effect of delay path 153
Figure 6.19 Matlab report providing dimensions of IDT 153
Figure 6.20 Microfabrication of SAW device 155
Figure 6.21 Fabricated SAW devices on 36YXLiTaO_3 before dicing 156
Figure 6.22 Fabricated SAW in mount 156
Figure 6.23 Primary scan with Pi filter (a) and without (b) 157
Figure 6.24 Five micron beads in liquid applied to a gold surface in suspension (a) and after liquid evaporation (b) 158
Figure 6.25 Time series images of SAW bond rupture scan captured using digital microscope 158
Figure 6.26 SAW delay line with surface prepared for immobilisation requires micro-fluidics integration 159
Figure 6.27 SAW surface during dry bond rupture scan 160
Figure 6.28 Entire sensor delay line showing before and after experiment. Several particles have grouped after rupture and drying. 161
Figure 6.29 Detail view. The product image is indicative of the features and particles that do not move, and the difference image shows particles that have been ruptured during the experiment. 161

NOMENCLATURE

A	Area
A	Acoustic Amplitude
B_a	Acoustic Susceptance
c_{ij}	Shear stiffness coeficients
C	Capacitance
C_0	Parallel capacitance of BVD equivalent circuit
C_m	Motional capacitance of BVD equivalent circuit
C_Q	Sensitivity of QCM to mass change
C_S	Sensitivity of SAW device to changes in mass
D	Dissipation, the reciprocal of Quality
d_{ij}	Piezoelectric coefficients
e	Piezoelectric Constant
E	Energy
E	Young's Modulus
$\boldsymbol{f}$	Body forces on a fluid
f	Frequency
f_0	Centre frequency if SAW device
g	Piezoelectric voltage coefficient
G	Shear Modulus (Modulus of Rigidity)
G_a	Radiation Conductance
h	Layer thickness
h_l	Guide layer thickness
h_q	Quartz thickness
h_s	Substrate thickness
$h(t)$	Time transfer function
$H(\omega)$	Frequency transfer function
I	Current
IL	Insertion Loss
k	Electromechanical coupling factor
l	Length of IDT
L	Inductance
L_m	Motional inductance of BVD equivalent circuit
m	Mass

N	Number of finger pairs in IDT transducer
N_f	Frequency Noise
p	Pressure
$p(t)$	Probability as a function of time
Q	Quality Factor
QCM	Quartz Crystal Microbalance
r	Radius or radial distance
R	Resistance
R_m	Motional resistance of BVD equivalent circuit
S	Sensitivity
SAW	Surface Acoustic Wave
t	Time
TCD	Temperature Coefficient of Delay
TCF	Temperature Coefficient of Frequency
u	Displacement
v	Poissons Ratio
v	Velocity
$\boldsymbol{v}$	Flow velocity
v_s	Shear Velocity
v_s	Phase velocity of substrate
v_{SAW}	Surface Acoustic Wave velocity
V	Voltage
V_d	Driving voltage
w	IDT finger Width
W_A	Work of Adhesion (J)
Z	Impedance
α	Thermal expansion coefficient
α	Angular Acceleration
ε	Dielectric Constant
θ	Angular displacement
λ	SAW wavelength
μ	Dynamic Viscosity
ρ	Density
τ	Time constant for exponential decay

τ		SAW delay time
υ		Kinematic Viscosity (μ/ρ)
ω		Angular frequency
	ω_0	Centre frequency if SAW device, angular frequency

1. INTRODUCTION

In the fields of medicine, drug discovery and environmental monitoring those on the front line cannot get the results fast enough. In the event of pandemic disease, where one particular strain of disease threatens the lifestyle and wellbeing of entire nations, it will be increasingly important to have fast effective means of point of care detection.

This work describes a robust and fast technique capable of bypassing traditional lab diagnostic processes such as radio or fluorescent labelling. The bond rupture methodology is simple, easy to operate, low cost and can be combined with a number of established technologies. A Quartz Crystal Microbalance (QCM) induces and detects the rupture of highly specific intermolecular bonds. The QCM is a well-established microbalance platform. In this work, what is learned from bond rupture on a QCM device is related to new or improved transducers.

The rupture of many bonds simultaneously provides unique means of studying the binding and rupture kinetics of multiple bond systems. The experiment hardware developed provides a means of studying the effect of forced bond rupture.

This project is a collaborative effort by researchers and technicians from many disciplines across the School of Engineering and Technology, Massey University and Industrial Research Limited. This author was tasked to assist in the development of QCM electronic hardware and conduct QCM bond rupture experiments with the goal of understanding the force experienced by the bound particles. Through models and comparison to experimental results, we can hypothesise and verify our understanding of the bond rupture mechanism, the factors that impact bond rupture and the nature of the signals detected. The ultimate ambition is to overcome the weaknesses evident in the bond rupture system.

1.1 Aims and Objectives

The aim of this thesis is "To establish the principle or foundation of Surface Acoustic Wave (SAW) / Bond Rupture based biosensor" and "to develop a proof-of-the-concept sensor for medical diagnosis".

Four core objectives mark important milestones on the way to achieving these goals: Hardware development and characterizing QCM bond rupture experiments; Single particle simulation of bond rupture by base excitation; Whole transducer simulation of existing and improving devices; Design and development of a SAW/Bond-rupture based sensor.

1.2 Contributions to knowledge

This thesis presents several contributions to knowledge. The first is a model for studying the rupture of single particles from a surface by base excitation. The model is constructed in such a way that it can be applied to a number of different particles of interest. The second contribution is a model of the behaviour of bond rupture transducers during a bond rupture scan. This model permits the simulation of existing transducers and the testing of proposed improvements and new transducers. The final contribution is a roadmap for the advancement of bond rupture transducers based on the results of the aforementioned models.

1.3 Outline

This thesis outlines the process for creating an improved bond rupture transducer. Bond rupture detection is desired before the project can advance further this requires additional hardware. Although the author has worked towards this goal, these efforts are not documented in this work. Direct involvement in the hardware design and methodology is advantageous when evaluating experiment results. Following completion of a comprehensive literature search (Chapter 2) and hardware development, the way is clear to experiment on QCM bond rupture.

Chapter three presents some of the experiments conducted to detect the rupture of streptavidin-biotin and physical bonds and characterise the signals generated by bond rupture on the QCM device. Experiments assist in the formulation and verification of hypotheses on the principle of bond rupture. The experiments investigate factors documented to effect bond rupture. These include, but are not limited to, temperature, viscosity, force ramp-rate, particle size, and test duration.

The methodology, equipment and transducers have inherent weaknesses. Chapter 4 presents the evolution of a force model into a single particle model of bond rupture by base excitation. Chapter 5 applies this model to the existing device, matching the experiments presented in Chapter 3. Changes to the methodology and transducer are tested in simulation and a new way forward is found. Chapter 6 presents the design and development of a prototype Surface Acoustic Wave device for bond rupture. Suitable models approximate the device behaviour. Where time and available resources do not permit the manufacture of an ideal device, an achievable sensor is realised. Chapter 7 concludes the thesis, with a discussion of the results and contributions presented within.

2. LITERATURE REVIEW

2.1 Introduction

This chapter reviews the field of bond rupture and the wider field of biosensors. First, an overview of the bond rupture technique demonstrates the state of the art. A brief overview of the biosensor theory leads into a discussion of the core areas of interest in bond rupture: the biodetector, interface and transducer. A discussion of the complexities presented by liquid operation follows. This review concludes with a discussion of some alternative biosensor technologies and the conclusions drawn from this literature analysis. In this review, the techniques currently employed in bond rupture receive greater emphasis. The remaining chapters introduce literature as new applications arise.

2.2 Bond Rupture

The formation of non-specific bonds plagues most biosensor applications and, most notably, acoustic wave sensors that measure an attached mass. Non-specific bonds cause the attachment of non-target molecules which are virtually indistinguishable from the attachment of target molecules. The erroneous mass influences the measurand in the same way. Bond rupture is a means to detect the attached mass and distinguish between attachments of different affinity without costly and time-consuming labelling procedures. This technique has great potential for fast and accurate detection of disease and contamination at the point of care.

The underlying principle of bond rupture diagnostics is to distinguish between the target and erroneous signals by rupturing adhered particles and separating the interactions by bond strength. Figure 2.1 outlines this method, showing the transducer surface is coated with receptors to which the target binds. The targets bind specifically and other molecules bind non-specifically (a). The surface oscillates at increasing amplitude until bond rupture occurs. Incrementing the amplitude of the oscillations increases the force experienced by the particles. Particles of lower affinity rupture from the surface first thus removing the erroneous mass (b), the specifically bound mass of interest ruptures at higher force (c).

Figure 2.1 (d) and (e) show some idealised resonant frequency and noise results respectively. The curves differentiate the effects of specific and non-specific interactions. The height of the bond rupture noise peaks (Figure 2.1 (e)) quantitatively indicates of the number of bound ligands.

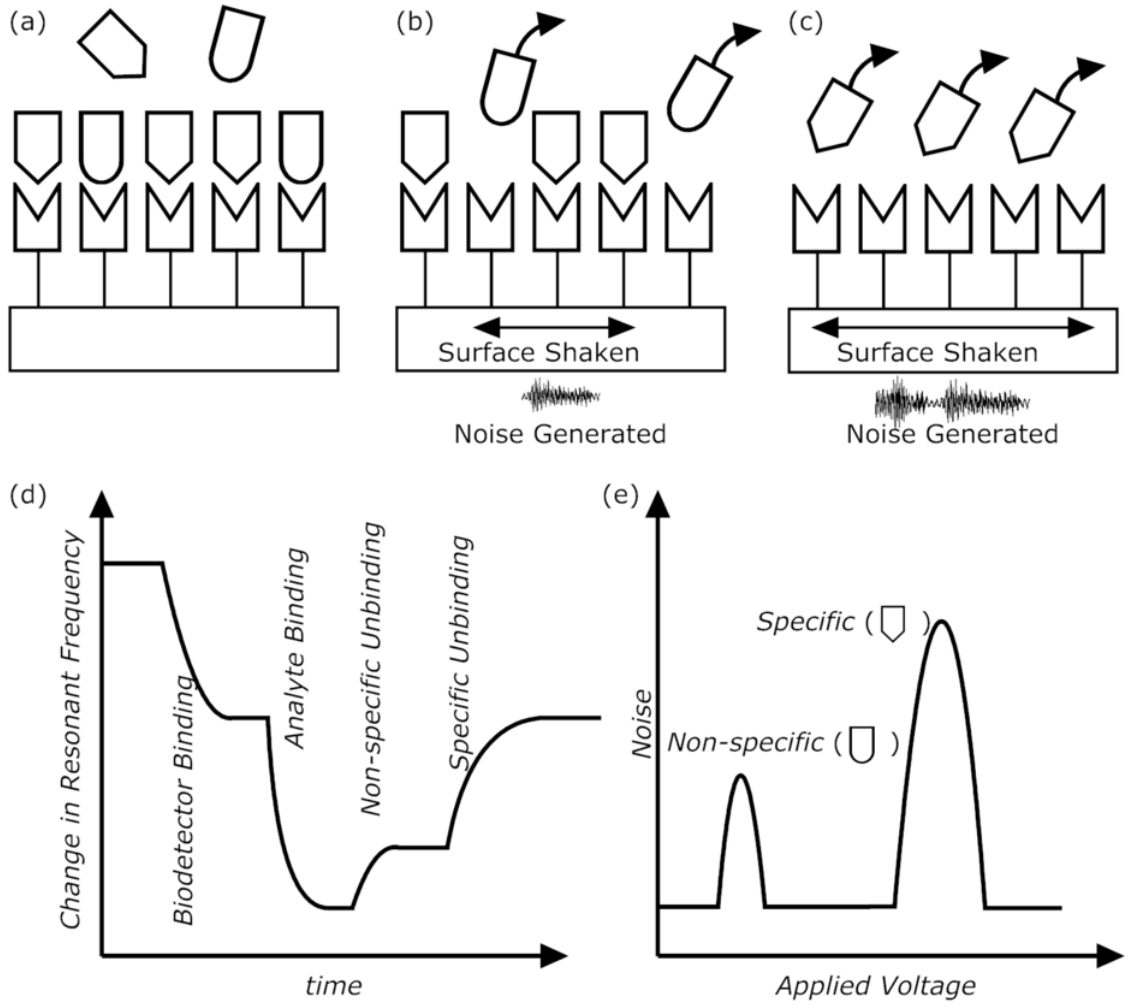

Figure 2.1 Bond rupture test concept.

Atomic Force Microscopy is a popular means of investigating the properties of single bonds and surfaces. The bonds are stretched using a piezoelectric substrate and a microscopic cantilever. The displacement of the cantilever is measured. The shear flow technique is also employed in the study of bonds, particles adhered to a substrate are removed by liquid shear and the force is controlled by the fluid speed. These technologies are discussed in greater detail in Chapter 4.

To date there have been a number of reported successful bond rupture tests with varied results. Yuan et al. (2007) simultaneously measured the frequency change and noise signals from the rupture of microspheres bound to the QCM surface by streptavidin- biotin bonds. Dultsev (2000) reported successful bond rupture tests and successful noise capture with microspheres. In addition, the authors performed tests with biological targets (Cooper et al., 2001, Dultsev et al., 2001). Edvardsson et al. (2005) attempted bond rupture using a modified QCM-D instrument but failed to rupture the bonds. The QCM-D is a commercial surface science device commonly used for biosensing applications, e.g. (Hook et al., 1999)

Dultsev (2001) reported bond rupture using 5µm diameter streptavidin-biotin latex spheres covering 1% of the QCM surface area. Figure 2.2 shows the rupture force spectra for streptavidin-biotin (1) and covalent amide-linkage, bonds (2). The results shown in Figure 2.2 are in units of A (the amplitude of the oscillations measured in volts) and S (signal strength measured in arbitrary units). A microsphere coated in streptavidin is bound to the biotin-coated surface of the sensor. The streptavidin-biotin phantom approximates antibody-ligand bonds. This is a common first step in the development of biosensors due to the robust nature of the bond and low cost of materials. Dultsev et al. estimate that each sphere experiences approximately 9µN of force at rupture. This compares to 160pN required for a single bond indicating that about 60000 bonds are broken simultaneously. The authors estimate this is half the number of bonds that initially exist between the bead and the surface.

Figure 2.3 shows the rupture force spectra for physical bonds of latex spheres placed directly on the surface and dried with nitrogen. The amplitude required to rupture these bonds is much lower than that required to rupture streptavidin-biotin bonds.

Figure 2.4 from the same patent shows the results of a single Surface Acoustic Wave (SAW) bond rupture experiment. There seems to be some irregularity in the results, most notably the results show multiple peaks. The authors attribute this to different size groups of particles

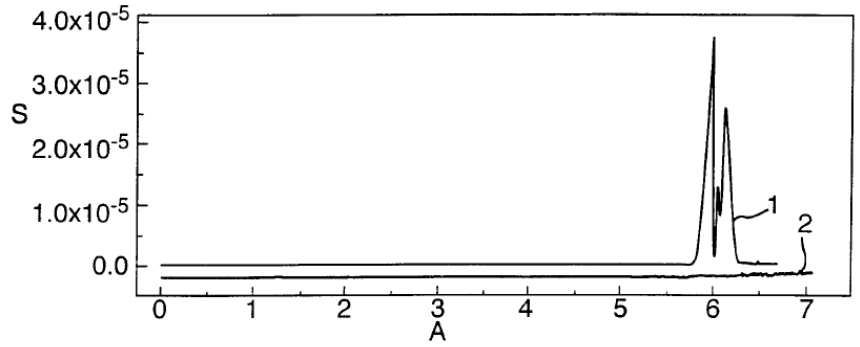

Figure 2.2 QCM rupture force spectra for streptavidin-biotin bond (1) and chemical bond (2) (Dultsev *et al.*, 2001a)

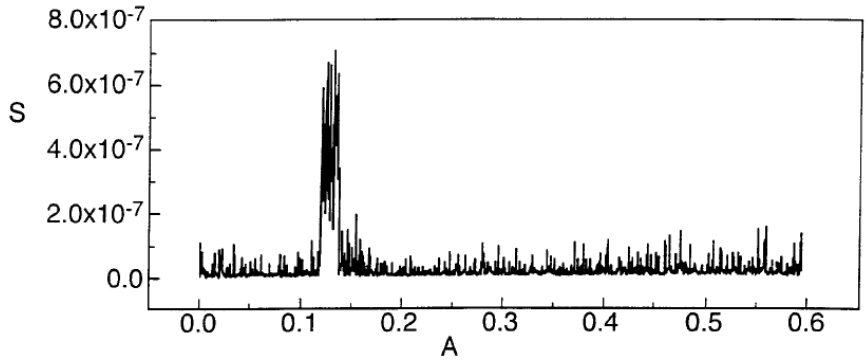

Figure 2.3 QCM rupture force spectra for physical bonds (Dultsev *et al.*, 2001a)

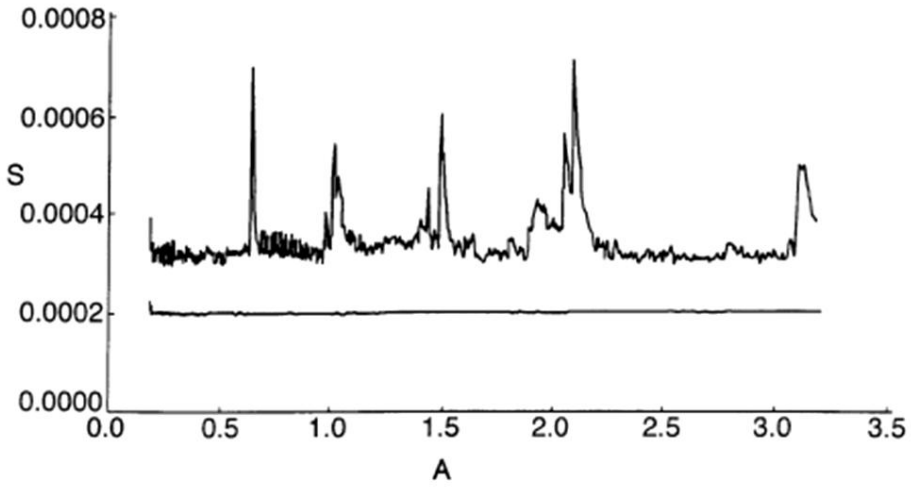

Figure 2.4 Sample of bond rupture data captured using a SAW device (Dultsev *et al.*, 2001a)

binding together and rupturing at different forces. The technique used in the patent is not well described and could potentially be refined, vastly improving the experimental results and detection capabilities.

The QCM properties are completely determined by its materials and dimensions. By comparison, the SAW offers a greater number of options for refinement and optimisation. This includes, but is not limited to changing the materials and frequency characteristics of the electrodes and substrate, as well as changing the geometry of the guiding layer. A number of different substrates support SAW generation and SAW has potential for integration with signal conditioning and other electronics. Figure 2.5 demonstrates how two receiving electrodes could be configured with the electrodes orientated at different directions. Orientated this way the electrodes may respond strongly to signals travelling in that direction, and weakly to the driving signal. The two electrodes could also measure different frequencies. To this author's knowledge this is the only mention of SAW bond rupture for diagnosis in the public domain. A few non-diagnostic applications such as SAW bond rupture for cleaning utilise similar principals to SAW bond rupture (Cular et al., 2008).

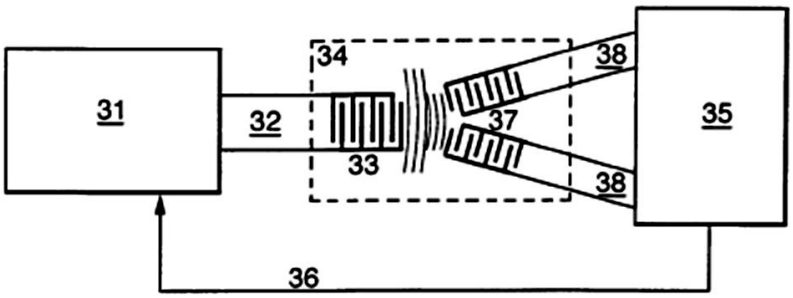

Figure 2.5 Schematic of SAW architecture as presented in the patent (Dultsev *et al.*, 2001a)

The QCM and SAW bond rupture applications utilise a single body to generate bond rupture and detect the results. Yuan et al. (2005) suggest a two transducer alternative. An acoustic signal is generated and propagates some distance through a fluid media. A sensing system such as Surface Plasmon Resonance (SPR) detects changes in surface mass. Some recent publications investigate impedance measurements in conjunction with increased oscillation amplitudes (Heitmann and Wegener, 2007) and the effects of increased vibration amplitudes on binding kinetics are discussed by Mecea (1994, 2006).

2.3 Biosensors and Diagnosis Techniques

There are a vast array of sensors, biosensors and diagnosis techniques. To cover them all here is not possible. Many of the existing techniques however share commonality with the bond rupture techniques. This section discusses these techniques as they relate to the bond rupture application.

The analytical applications of QCM are well established and the publications and commercial products that utilise QCM as an immunosensor are many (Cooper and Singleton, 2007, Godber et al., 2005, Huang and Cooper, 2006, Janshoff and Steinem, 2001, Kurosawa et al., 2003). In addition to the ever-popular QCM, other well established sensing platforms that are used as biosensors. Some examples are Surface Plasmon Resonance (SPR)(Hoa et al., 2007, Oh et al., 2004), potentiometric, capacitive (Berggren et al., 2001), biosensors and more (D'Orazio, 2003, Gizeli et al., 2003, Jin-Woo et al., 1997, Luppa et al., 2001, Nakamura and Karube, 2003, Sokoll and Chan, 1999).

Sensors are an important part of the modern world. Huijsing (1992) noted sensors enhance people's senses in the same way that computers enhance their intelligence and motors enhance their mechanical power. A biosensor is defined by McNaught and Wilkinson (1997) as a device that uses specific biochemical reactions mediated by isolated enzymes, immunosystems, tissues, organelles or whole cells to detect chemical compounds usually by electrical, thermal or optical signals. The hand held point of care glucose test developed by Clark in 1962 is widely considered the most successful biosensor to date, it exemplifies many of the critical characteristics of biosensors as outlined by Collings and Caruso (1997) and repeated below:

- High degree of selectivity of bio-detector: With the use of enzymes, whole cells or other recognition agents, high selectivity can be achieved so that the recognition event is triggered only by the target analyte.

- Maintain selectivity in the presence of other specimen: Most specific recognition elements will also recognise other things non-specifically. As commercial biosensors are required to operate in complex media containing any number of other pathogen, chemicals or drugs it is important that the selectivity of the sensor is not compromised.
- Miniaturisation: This is important for a point of care or implanted device for ease of use. Smaller devices use less consumable materials.
- Low Cost: The cost of manufacture needs to be reasonable.
- Device intelligence: A smart sensor requires sufficient built in intelligence so that it can be used by people low skill level.
- Automated with high turnaround: Much less than one hour turnaround between tests is widely considered the benchmark required to oust existing and widespread technologies.
- Reversible affinity: The analyte-receptor interaction should be reversible so that the sensor can be easily reused. Immunological devices are often considered one shot and are not used in on-line monitoring applications because of this.
- High surface mass sensitivity: This is a requirement of biosensors that rely on mass change as a means of detection. Detecting the rupture event does not explicitly require mass sensitivity.
- Operation in aqueous environment: This includes diluted samples in low viscosity liquids and possibly operation in complex biological serums.
- Low imprecision: A viable biosensor should match or better the precision of the currently used technologies.
- Small lot-lot variations: The biosensor needs to perform consistently.
- High analytical sensitivity: A biosensor has to be sensitive to very low concentrations, which means quantitative detection of very few or very small particles.
- Long calibration stability
- Low interference: With reference to drugs or other pathological sample components, closely linked to specificity.
- Superiority and Versatility: Replacing traditional technologies requires superiority and versatility of the new methodology.

Collings and Caruso (1997) define three main parts of a biosensor: the detector (Interface), the transducer, and the output system. When considering intelligent and integrated sensors – so called smart sensors, integrated electronics and signal processing become an integral part

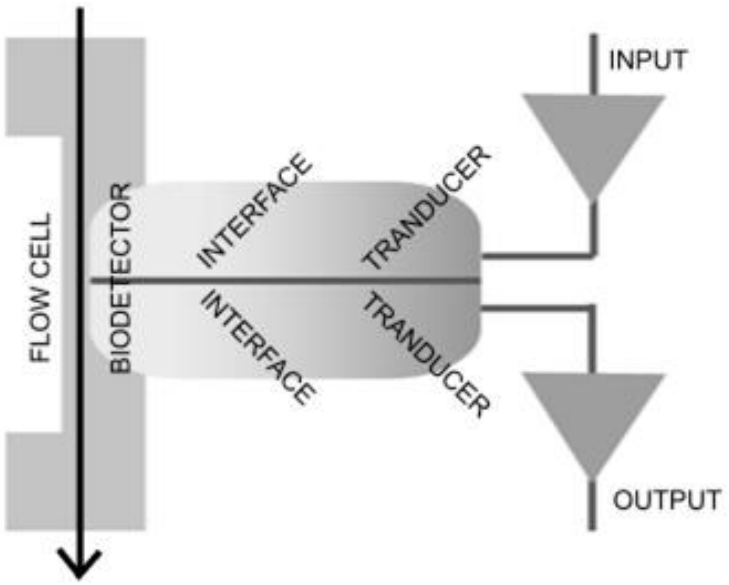

Figure 2.6 Functional diagram of a Biosensor

of the sensor itself. The sensor input and output become instructions and information respectively. Additionally microscopic flow cells are a critical part of flow based biosensor. As alluded to in the above discussion of bond rupture it is important to consider that any required input transducer need not be the same as the output transducer. Figure 2.6 presents a revised functional diagram of a biosensor.

The following sections relate directly to elements of Figure 2.6. The biodetector elements of the biosensor are discussed first.

2.4 Biodetector

The biodetector is critical to biosensor development and is the first step in connecting the presence or absence on an analyte to a meaningful output. Each new application requires the development or discovery of a new bio-derived interaction. The problem of finding, isolating, reproducing and immobilising the biosensing element is by no means trivial. This problem is common to many biosensors and is beyond the scope of this work. This section outlines important considerations that relate specifically to bond rupture.

The underlying principle of the biodetector is to utilise enzyme-ligand interactions and antibody-antigen interactions. Immunoassays have utilised antibodies for decades and they are indispensable in most routine diagnostic tests. The antibody identification process starts within an animal, making antibody generation difficult for molecules that kill the host or molecules that are inherently less immunogenic. Antibody identification is restricted to in vivo parameters; the identification of antibodies that can recognise targets outside physiological conditions is not feasible. Frozen stocks of antibody producing cells need to be stored at

multiple sites to avoid accidental loss or death of cell lines. Antibodies have a limited shelf life and undergo irreversible denaturation when heated.

Catalytic receptors are typified by enzymes and other irreversible or affinitive interactions. Enzyme Linked Assays such as the glucose test developed by Clark in 1962 use enzymes immobilised at the electrode to recognise analytes and convert them to electrically active by-products. This method is suitable for low molecular weight analytes which are more likely to give electroactive by products (Schultz et al., 2004).

Affinity receptors are typically one shot, requiring that the bond be broken after detection. Affinity receptors are less reversible than catalytic receptors due to larger bond strength. The implication that these interactions are irreversible is clearly disputable in light of bond rupture techniques, the affinity of the receptor may suffer because of repeated breakage. Antibodies, anticalins, molecular imprinting techniques, and aptamers are among this group.

As already stated, bond rupture utilises the clear distinction between specific and non-specific bonds. Specific bonds are the result of many weak local interactions summing into an overall stable bonds. Only when two molecules each possess topologically and chemically complimentary surfaces will the weak and localised interactions sum to an overall strong bond. The binding energy of a specific interaction is of the order of ten times the amount of thermal energy at room temperature. Thus, when the energy is ten times greater than normal thermal energy bond breakage is likely to occur (Merkel, 2001).

Biodetector affinity affects the rate of binding and overall strength of the bond. This has implications for test duration and the required force to rupture the particles. Bond rupture requires a highly selective biodetector that maintains its selectivity in the presence of other specimen. High affinity allows the bond to be distinguished from its non-specific counterparts in a bond rupture test. However if the affinity is too high, the bond may not rupture.

The force of induced bond dissociation falls in the range from 2-200pN. For comparison, the photons emitted by a 1mW laser pointer exert a force of 3.3pN on the pointer due to the conservation of momentum (Merkel, 2001). However with a particle of appreciable size such as a micro-bead, many thousands of such bonds will form.

2.4.1 Antibodies and Aptamers

Antibodies have been around for as long as life itself and in recent times have become indispensable in routine diagnostic tests. There are many reviews and articles published about antibodies (Dall'Acqua and Carter, 1998) and aptamers, e.g. (Bunka and Stockley, 2006). Aptamers, a relatively new and emerging technology offer a number of advantages over

traditional antibodies (Tombelli, Minunni, Luzi and Mascini, 2005). The sections which follow detail some key aspects of the receptors important to bond rupture.

The antibody identification process starts within an animal making antibody generation difficult for toxins that are not tolerated by animals or molecules that are inherently less immunogenic. Antibody identification is restricted to in vivo parameters, as such the identification of antibodies which can recognise targets outside physiological conditions is not feasible. The identification process is labour intensive and expensive. Heterophilic antibodies, human antibodies that recognise antibodies of non-human origin, may link to antibodies of non-human origin resulting in false positives. Aptamers range in mass from 6 to 40 Daltons (Da) and can bond directly with the natural form of a protein, eliminating the need for linkers. Aptamer selection is an automated process, (Systematic Evolution of Ligands by Exponential Enrichment, SELEX) (Bunka and Stockley, 2006), in contrast to the labour intensive and potentially costly antibody separation process. Aptamers with desirable properties are obtained by manipulation of the in vitro selection conditions, for example aptamers that bind to the target in a non-physiological buffer at non-physiological temperatures. The kinetic properties of aptamers can be manipulated. Batch-to-batch variation requires that immunoassays be re-optimised each batch. By contrast aptamers are highly reproducible due to reduction by chemical synthesis. The rate of association and dissociation, affinity, and affinity to close molecules can be selected based on the intended application.

Once identified, frozen stocks of antibody producing cells need to be stored at multiple sites to avoid accidental loss or death of cell lines. Antibodies have a limited shelf life compared to aptamers, which are stable to long term storage. Aptamers are transported and stored at ambient temperature. Antibodies undergo irreversible denaturation when heated; denaturation of aptamers, however, is reversible within minutes.

2.4.2 Immobilisation

Immobilisation strategies have been reviewed (Wink et al., 1997). Receptors coat the sensitive area of the bond rupture device, namely the QCM electrode. Gold is often favoured for the sensor surface because the direct attachment of recognition elements onto gold surfaces is well developed. Gold is chemically inert and used widely in piezoelectric, optical, and electrochemical sensors (Karyakin, Presnova, Rubtsova and Egorov, 2000). Gold is used extensively – though not exclusively – in non-bond rupture QCM sensor applications. Silver and platinum are also used.

Barrie and Rapp (2001) showed the sensitivity of an immunosensor depends on the immobilisation method used. Maintaining the specificity of the receptor after immobilisation is

important for the measurement of analytes in all immunosensor systems. Immobilisation can cause some losses in the binding activity of some receptors (Wang et al., 2005). This loss in function is associated with the random orientation of asymmetric molecules on the surface (Karyakin et al., 2000). In the best case the immobilisation should preserve the native structure of the biomolecules, leaving the active sites accessible and exceptionally stable (Merkel, 2001). In general, directly adsorbed or screen printed enzymes and proteins lose sensitivity (Scouten et al., 1995). Whether the distribution of receptors was random or uniform affects only the rate of binding, not the reverse reaction kinetics (Huang, Chen, Chesla *et al.*, 2004).

Lack of stability is a problem for bioreceptors, but immobilisation improves stability towards physical and chemical stress most of the time (Zoller and Smith, 1983). Out of 50 tested, 60% improved, 24% remained constant and 24% got worse.

In addition to the effect on the receptor-ligand bond characteristics, the immobilisation method directly influences the nature of the applied force during the bond rupture test. The addition of intermediate layers with imperfect physical properties, significant thickness, or inconsistent coverage changes the absolute motion of the sensor surface and the bound particle. Ideal monolayers are perfectly aligned and closely packed, almost crystal like. The reality is that due to gold imperfections and the layer itself there are pin holes at a concentration of 1% of the area (Porter et al., 1987).

Sulphur-gold covalent bonds utilised in immobilisation methods rupture at 1.4nN under a 10nN/s voltage ramp (Grandbois et al., 1999). This compares to 160pN required for a single biotin-streptavidin bond indicating that the latter will rupture first. Estimates indicate that approximately 10µN of force is exerted on each sphere at rupture. Many bonds exist in parallel and the force generated is sufficient to rupture them.

Where the transducer and operating circuit permits, the sensitive area is grounded to prevent electrical coupling to solution and degradation of attached receptors

2.4.3 Regeneration of Binding Sites

In an idealised bond rupture device the bond rupture test itself removes all receptors and regenerates the binding sites. Typical regeneration of the binding sites of antibodies requires stringent procedures to restore the receptors for another test. Damage to the antibody caused by unbinding leads to diminished life of the immobilised antibodies and insidious drift problems due to reduced affinity of, or destroyed, binding sites.

The effect of repeated bond breakage on receptor affinity is not well characterised and to date there have been no reports of any quantitative studies into the effects bond rupture has on the receptor. Other regeneration methods exist, and if a suitable surrogate is available

bound particles can be flushed away with a highly concentrated solution of related antigen with weak affinity. Regeneration using acid or alkaline solutions or ionic strength shock is potentially harmful to the binding receptor but is used in some cases.

2.5 Interface

The recognition that occurs at the point of the biodetector is transferred through the interface to the transducer. Bond rupture deals principally with the addition and removal of mass at the transducer interface. There are many different ways to detect the change in mass. Principally inertial and mechanical properties of the interface change. Further there may be measurable change to the optical, thermal, electrical, magnetic or chemical properties of the interface.

Acoustic sensors, as is discussed in the next section, probe the acoustic and inertial properties of the interface. Combining bond rupture methodology with optical sensors such as Surface Plasmon Resonance (SPR) can shift the interface from mechanical to optical domain. SPR is where binding to a metal surface causes an optical change due to the change in the refractive index at a metal-substrate interface. BIAcore (www.biacore.com) is an example of a commercial product utilising SPR phenomena and is used in key areas such as antibody characterization, proteomics, lead characterization, immunogenicity, biotherapeutic development and production. The success of the instrument is credited to the full integration of chemistry, fluidics, optical detection, and data processing. The BIAcore system is considered the industry standard and is widely used in academic and research laboratories for binding studies (Schultz et al., 2004).

Optical methods can offer more sensitivity than other methods. Fluorescence is the most commonly used optical technique. A fluorescent molecule is excited by illumination at one wavelength and emits light at a longer wavelength. Fluorescence intrinsically magnifies the signal. Additionally the emitted fluorescent wavelength is different to the incident illumination thus eliminating the effect of the interrogating signal making small signal levels easier to detect. Most single molecule research employs fluorescence due to its sensitivity.

Chemiluminescence and bioluminescence are processes where chemical or biological energy is emitted in the form of light. Jellyfish and fireflies glow because of bioluminescent bacteria.

A substance may absorb light at a specific wavelength, where the amount of absorption is proportional to the amount of the substance present. Absorbance can be used to monitor the presence of a marker or the change in absorbance can be monitored upon binding. Scattering

is similar to absorbance but the amount of light reflected is used. In true scattering methods, the scattering is dependent on particle size.

It is possible to assay for the binding of multiple materials simultaneously using optical array techniques. The types of arrays available include planar waveguide arrays, CMOS arrays, fibre optic bundles, SPR arrays and interferometry arrays. These can provide a more complete picture of the components in a complex mixture enabling subtle changes in the composition to be monitored (Schultz et al., 2004). The fields of genomics, integrated optics, micro fluidics, and bioinformatics are driving the development of optical arrays. Commercially the field is dominated by DNA arrays with fluorescent detection dominating as the detection method.

Electro-Based sensors are intrinsically interfacial. The biological recognition or physical change that follows from a recognition event directly changes the electrical properties of the containing material. The binding of analytes to an electrode leads to an alteration of the field properties in the interfacial region and a corresponding field effect can be measured (Kimura and Kuriyama, 1990). The key advantages are the simplicity of the assay and the ease and accuracy with which voltages and currents can be measured. The labelling of analytes with electroactive tags permits the detection of analytes in designs that are analogous to common fluorescence techniques.

Increased sensitivity can be achieved from nanoparticle-based sensors due to the unique physical properties inherent to dimensionally confined materials and in part from the small number of molecules needed to alter the properties of these nanoparticles (Schultz et al., 2004).

There are inexpensive sensors being developed primarily for the food industry that can be incorporated directly into the packaging alerting the consumer to product expiration. One such example is for perishable foods packaged in a CO_2 atmosphere where the sensor changes

Figure 2.7 Intelligent Packaging (http://www.dcu.ie/~ncsr/commercial/technologies.html)

colour to indicate a breech in the packaging. Such sensors are in contrast to expensive apparatus used in diagnosis

2.6 Transducer

Transducers and sensors deliver information from the optical, mechanical, thermal, electrical, magnetic and chemical domains into the electrical domain as demonstrated by Figure 2.8.

2.6.1 Piezoelectricity

The acoustic waves devices considered in this thesis utilise piezoelectricity as a transduction mechanism between the electrical and mechanical domains. Piezoelectricity is the electric polarisation produced by mechanical strain in crystals belonging to certain classes. The polarisation is proportional to the strain and changes sign with it. If the crystal is macroscopically aligned, the deformation of the crystal moves the charge of the lattice resulting in a net difference in charge. The interaction is reversible by the converse piezoelectric effect. Figure 2.9 summarises the interaction between electrical, mechanical and thermal energies.

Pyroelectricity is the phenomenon whereby a change in temperature produces an electrical charge to accumulate at the ends of the polar axes. Ten of the 20 piezoelectric crystal classes exhibit pyroelectricity. Crystals in the polar classes possess electric dipole moments along their polar axes. Lithium Niobate, for example, is a pyroelectric crystal and quartz is not.

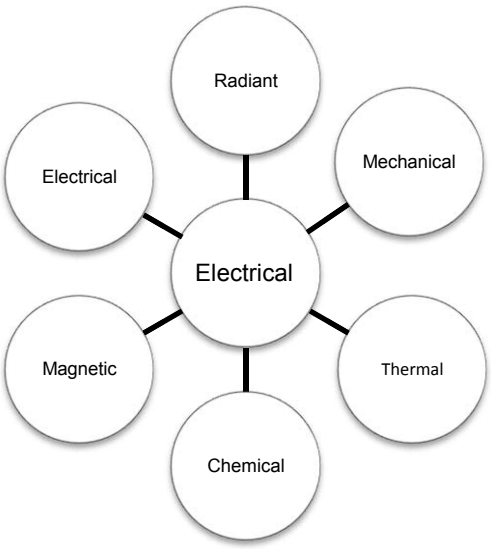

Figure 2.8 Sensor conversion domains

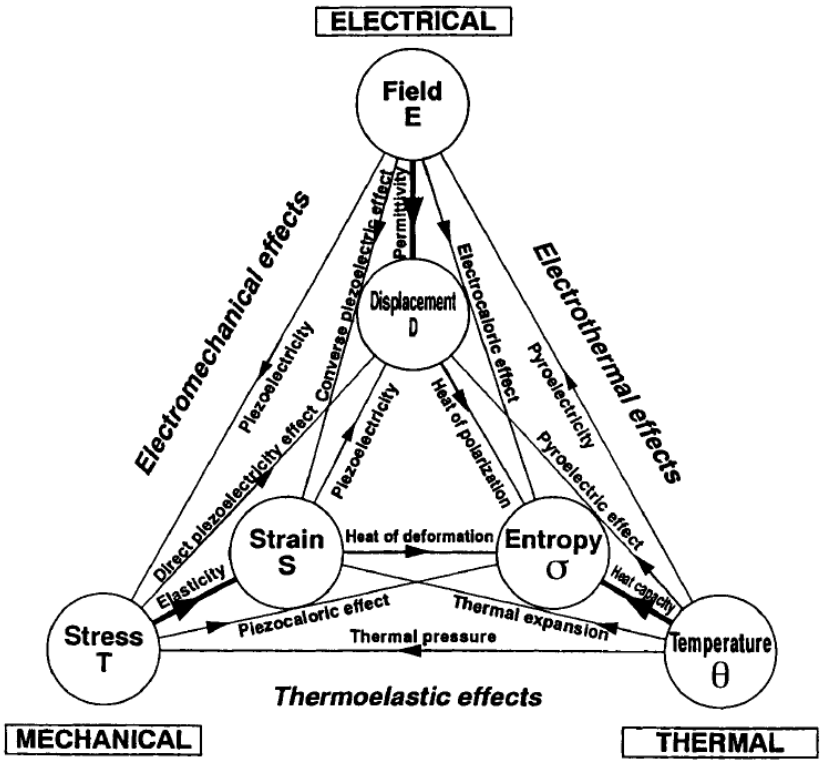

Figure 2.9 Couplings between electrical, mechanical and thermal fields (Ballato, 1995)

Ferroelectrics are a special class of piezoelectric materials that exhibit a spontaneous polarisation that can be reoriented under a realistic electric field ($10^6\ Vm^{-1}$) (Tressler et al., 1998). The term is derived by analogy with ferromagnetism, however where ferromagnetism is a property of the atoms themselves, ferroelectricity is a property of the placement of atoms in the unit structure of the crystal. The presence of a ferroelectric state only occurs in crystals of a pyroelectric class, though not all pyroelectric crystals are ferroelectric. Ferroelectric oxides with perovskite, tungsten bronze, pyrochlore, and bismuth titanate layer structures all have high dielectric constants and high electromechanical coupling coefficients (Tressler et al., 1998). Slight variations in the polarity of ferroelectric substrates can cause large variation in the device characteristics.

Ferroelectricity only exists below a critical temperature called the Curie point. In cooling through the Curie point, the crystal atoms shift slightly changing the crystal symmetry. During cooling it is a matter of chance which direction the reversible dipoles will assume. Polling is the process of cooling a crystal in the presence of an electric field to bias the pole to a particular direction. Large values of piezoelectric coupling are typical of ferroelectric materials.

With regard to ferroelectricity the dielectric constant is a quantity used to measure the displacement produced in response to an applied electric field. Near to the Curie point, the

dielectric constant assumes very large values. This behaviour, which led to the discovery of ferroelectricity, is called the 'dielectric anomaly'.

The development of the ultrasonic transducer allowed for easy measurement of viscosity and elasticity in fluids and solids, resulting in huge advances in materials research. Ultrasonic time-domain reflectometers send an ultrasonic pulse through a material and measure reflections from discontinuities and can find flaws inside cast metal and stone objects, improving structural safety.

Quartz is one of the relative few piezoelectrics to occur naturally. It is widely used because, unlike many of the naturally occurring piezoelectrics, it is completely oxidised and insoluble in water. Quartz maintains piezoelectricity at temperatures up to 579°C.

Whole crystals are cut into wafers for device applications. The angle at which the crystal is cut on is important in determining the behaviour of the crystal. Owing to its popularity for timing circuitry, much is known about quartz crystal cuts. The mode of oscillation depends on the crystal cut with respect to the principal optic axis, the major axis of growth of the crystal, usually termed the Z-axis. Most crystal cuts respond to electric fields with displacements along three axes. The resulting oscillations in response to an alternating electric potential are elliptical, featuring components of displacement in three planes. It has been widely demonstrated that by selecting appropriate cuts of crystal it is possible to restrict oscillations to a particular plane. Restricting displacement to pure shear is useful in liquid applications. Other characteristics such as temperature stability are chosen by selecting an appropriate crystal cut.

Sensitivity is the open circuit voltage that a crystal generates due to an applied stress; sensitivity is given by the equation

$$S = g \cdot t \tag{2.1}$$

where g is the relevant piezoelectric voltage tensor and t is the thickness (Tressler et al., 1998). g is related to the piezoelectric coefficient, d through the dielectric constant K by

$$g = \frac{d}{K\varepsilon_0} \tag{2.2}$$

The permittivity, ε, is a determining factor in the impedance of the device. The impedance is important when matching a device to the driving electronics. Effective permittivity is used to evaluate various parameters in devices.

$$\varepsilon_0 = \frac{1}{c^2\mu_0} \approx 8.541878176 \times 10^{-12} \tag{2.3}$$

where μ_0 is the effective permittivity of a vacuum. The relative permittivity $\varepsilon_{r,}$ of a material is the ratio of the permittivity relative to ε_0. The dielectric constant is thus $\varepsilon_r\varepsilon_0$

The Electromechanical coupling coefficient, k, defined as:

$$k^2 = \frac{\text{stored mechanical energy}}{\text{input electrical energy}} \tag{2.4}$$

$$k^2 = \frac{\text{stored electrical energy}}{\text{input mechanical energy}} \tag{2.5}$$

The electromechanical coupling factor is usually small for quartz, around 5%. Hashimoto (2000) gives the following formula for determining the coupling coefficient of the substrate:

$$K_{sf}^2 \approx -\frac{S_{sf}^2 - S_{sm}^2}{S_{sf}^2} = \frac{V_{sf}^2 - V_{sm}^2}{V_{sm}^2} \tag{2.6}$$

for the free surface, and

$$K_{sm}^2 \approx \frac{S_{sm}^2 - S_{sf}^2}{S_{sm}^2} = \frac{V_{sf}^2 - V_{sm}^2}{V_{sf}^2} \tag{2.7}$$

for the metallised surface, S_{sf} is the slowness of the free surface and is equal to V_{sf}^{-1}, S_{fm} is the slowness of the metallised surface and is equal to V_{fm}^{-1}.

2.6.2 Acoustic Wave Devices

The piezoelectric effect is utilised in acoustic wave devices, a broad category of transducers. Figure 2.10 shows a sub-set of the acoustic wave family.

In 1959, Sauerbrey pioneered the use of piezoelectric transducers as biosensors (Sauerbrey, 1959). Sauerbrey worked toward the weighing of thin films adhered to the electrode surface of a QCM. The QCM (Janshoff et al., 2000, Mecea, 2005) and other acoustic wave devices (Chang et al., 2006, Drafts, 2001, Grate and Frye, 1996) have been the subject of a number of good review papers. Shons et al. extended Sauerbrey's work to the sensing of antibodies in 1972. Figure 2.11 shows the QCM is a one-port device. Any small signal of interest generated at the electrode, such as the noise of bond rupture, is superimposed on top of the incident signal. When the signal of interest is in the same frequency range as the

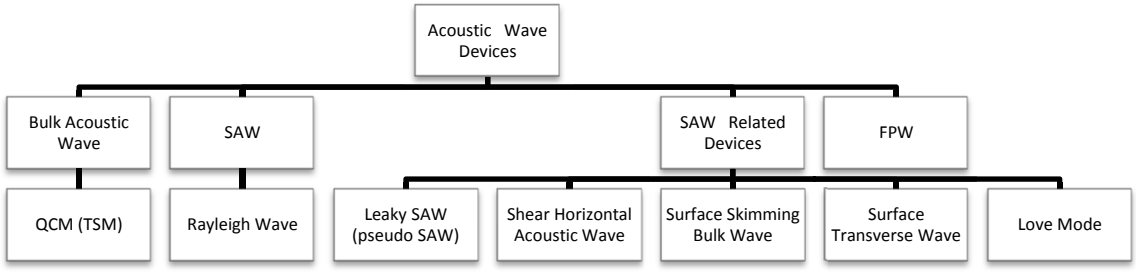

Figure 2.10 Piezoelectric acoustic wave devices

excitation voltage it is impossible to separate the two.

Bond rupture occurs as long as there is sufficient force added to the system. The primary focus of this work is the investigation of bond rupture which results from base excitation, some mechanical shaking of the surface to which the target is bound. Two acoustic wave devices are considered in this work. The first is the Quartz Crystal Microbalance (QCM), a bulk wave device commonly used in electronic oscillators and timing circuits. The second is the Surface Acoustic Wave (SAW) device, where the energy of the wave is confined to the surface in some way. The QCM is reviewed in depth in this section, the SAW device is discussed in Chapter 6.

2.6.3 Resonance

Resonance occurs when a system oscillates with increased amplitude at one or more specific frequencies. The lowest of these frequencies is the natural frequency or fundamental frequency. Examples of resonance include the acoustic resonance of musical instruments, resonance in electrical circuits and piezoelectric oscillators. In classic mechanics a harmonic oscillator is a system which, when displaced from equilibrium, experiences a restoring force proportional to the displacement. In piezoelectric crystals, Hooke's Law describes this force:

$$F = -kx$$
$$m\frac{\partial^2 x}{\partial t^2} = -kx \tag{2.8}$$

where k is a positive constant and x is the displacement.

By analogy, the mechanical element of piezoelectric oscillators is compared to traditional simple harmonic oscillators or damped oscillators. Piezoelectric oscillators differ because the displacement of the crystal also couples to the electrical energy of the system.

There are two resonant frequencies near the characteristic frequencies of the QCM, the

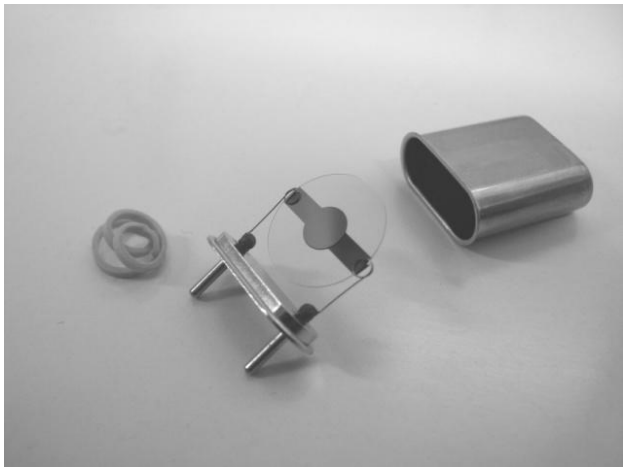

Figure 2.11 Quartz Crystal Microbalance

parallel and series resonances. The series resonance is of greatest interest in this work. Further there are harmonics of the fundamental resonances. The QCM supports only odd harmonics as these have antinodes at both surfaces.

2.6.4 QCM Quality Factor

The quality factor, or merit, is an indication of the quality of the QCM resonance. Changes in viscosity, thickness, elasticity and density of any attached film affect the quality factor. Q is the reciprocal of the damping, D.

The damping is a measure of the softness of an adhered film. Damping occurs when a soft viscoelastic film is not exactly following the oscillations of the crystal. Damping is determined from

$$D = \frac{E_{lost}}{2\pi E} \tag{2.9}$$

where E_{lost} is the energy dissipated during one oscillation and E is the total energy in the resonant oscillator. Once the QCM crystal is no longer driven, the amplitude of oscillations decay exponentially with a time constant τ. From τ, Q can be calculated as shown in Equation (2.10) and Figure 2.12:

$$Q = \frac{1}{D} = \pi f \tau \tag{2.10}$$

The quality factor also represents the 3dB bandwidth when QCM power is plotted against frequency. Where the centre frequency is f_c, we find two frequencies corresponding to a 3dB reduction, f_1 and f_2, then

$$Q = \frac{f_c}{f_1 - f_2} \tag{2.11}$$

The Q of a QCM is expected to be around 85000 in air and 2500 in water.

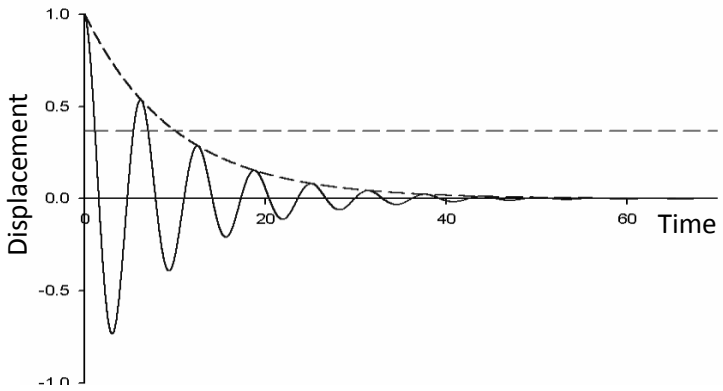

Figure 2.12 Determination of dissipation by ringing down of transducer

2.6.1 QCM Operation

Using the QCM in an oscillator is an effective technique. The QCM is the frequency determining element in an oscillator circuit and a counter is used to measure the frequency of the device. Very stable circuitry is required. Whereas oscillator circuits can be modified to permit ramping of the QCM and can provide information of the damping of the QCM it remains difficult to maintain operation in the presence of damping liquid. A further complication of oscillator circuits is that the sensing electrode must be grounded to preserve the surface chemistry.

The resonant frequency can be determined by sweeping through a range of frequencies near resonance and measuring any one of a number of quantities. Some commonly measured properties include the current through the transducer, best measured by a current-voltage converter; the voltage measured across the transducer; the power dissipated by the transducer, or the reflected power; the input impedance of the device; or the phase of the device.

Determination of the relevant maxima or minima in the returned signal yields the resonant frequency of the QCM. The resonant frequency of a QCM is sensitive to temperature, attached mass, changes in film thickness or density, elasticity, and viscosity in liquid environments. Monitoring the resonant frequency in a controlled test can used to determine the change in many quantities because the QCM resonant frequency is sensitive to its environment.

An increase in surface mass changes the resonant frequency according to the Sauerbrey equation (Sauerbrey, 1959):

$$\Delta f = \frac{C_Q f^2 \Delta m}{A} \tag{2.12}$$

where Δm is the increment of mass, A is the area of the crystal, f is the resonant frequency, and C_{Q} is the sensitivity constant. $C_Q = -\ 2.26 \times 10^{-6}\ cm^2\ s\ g^{-1}$ (Barnes, Dsilva, Jones and Lewis, 1992). C_Q depends on both the rate of propagation of the elastic transverse wave and the density of the crystal.

Sauerbrey's equation only holds if the added mass is small compared to the weight of the crystal; rigid; couples perfectly to the crystal surface; and is evenly distributed over the active area of the crystal. If the film in question is soft, then energy is dissipated through frictional losses and the frequency shift will be less that predicted by Sauerbrey's equation.

The thickness of the film, d, can be calculated from the mass, m, and film density, ρ.

$$d = \frac{\Delta m}{\rho} \tag{2.13}$$

Table 2-1 Sensor sensitivities (Wenzel and White, 1990)

Sensor	Theoretical Sensitivity S_m	Experimental Devices		
		Description	Operating Frequency (MHz)	Calculated S_m value ($\mathrm{cm^2/g}$)
Bulk	$-\frac{2}{\rho\lambda}$	AT-cut quartz resonator	6	-14
Surface	$-\frac{K(\sigma)}{\rho\lambda}$	ST-cut SAW delay line	31	-42
			112	-151
Flexural Plate	$-\frac{l}{2\rho d}$	Flexural-wave delay line	47	-450
			26	-951

Table 2-1 (Wenzel and White, 1990) compares the mass sensitivities of bulk acoustic wave sensors to those of SAW and Flexural Plate Mode devices.

If the attached mass is not evenly distributed then the relationship between frequency change and mass becomes a function of location. Displacement and frequency sensitivity exhibit Gaussian distributions across the area of the QCM. The mass sensitivity and amplitude extends slightly beyond the electrode edges. The mass loading dependence is found by applying a point load to the surface of a 6mm diameter QCM (Mecea, 2005).

QCM biosensors and timing crystals are predominantly manufactured from AT-cut quartz because the resonant frequency is stable at temperatures near the operating condition. Figure 2.14 shows the result of slight deviations from the AT cut in one of the angles of the cutting plane. By manipulation of the angle of other axes it is possible to re-locate the flat region of the temperature response for different operating conditions.

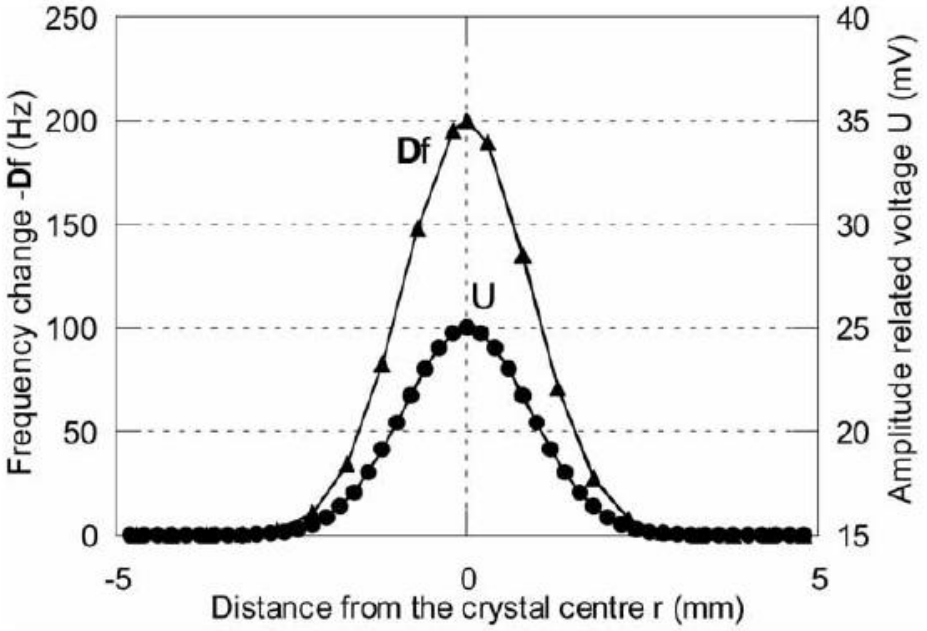

Figure 2.13 Gaussian distribution of mass sensitivity and displacement on QCM

The temperature of the QCM is an indicator of the power being dissipated in the transducer. This is the amplitude temperature effect. The operating temperature of the device and the amplitude of the driving signal are so closely coupled that the frequency change due to them are considered together. The increased power in the QCM changes the resonant frequency in a complex manner.

The temperature increases when the input power is increased, especially when operated in air. Figure 2.15 shows the resonant frequency changing because of changes to the input power. The two lines, dashed and solid, represent increasing power and decreasing power respectively.

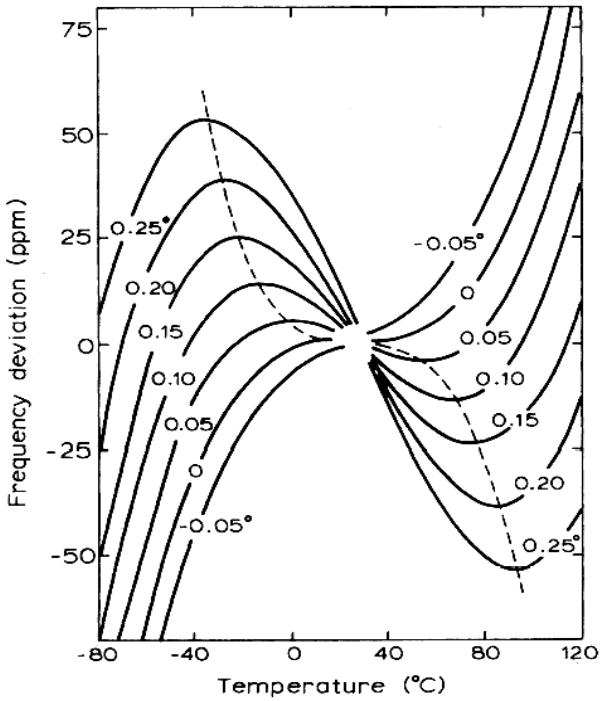

Figure 2.14 Temperature sensitivity for variations of AT cut Quartz crystal (Brice, 1985)

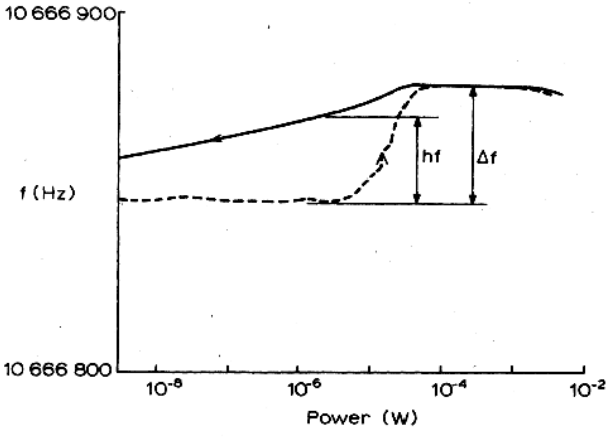

Figure 2.15 Resonant frequency changing with diving power (Brice, 1985)

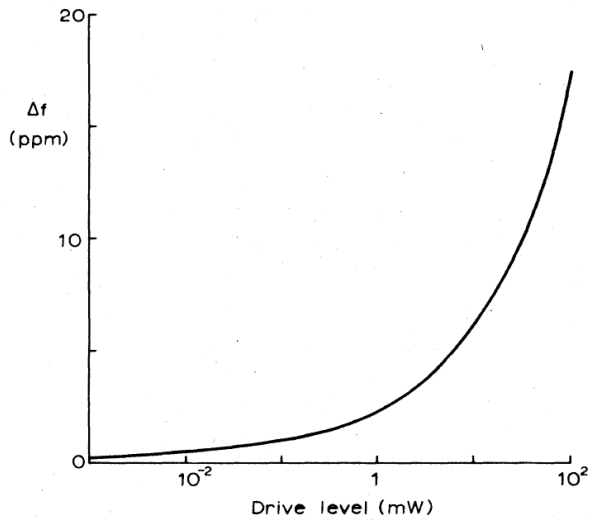

Figure 2.16 Resonant frequency changing with diving power for an AT-cut device. At low powers the variation is attributed to the variation of elastic constants with strain. At higher powers heating effects are noticeable (Brice, 1985)

In applications such as filters, the characteristics of the device are expected to remain constant over a wide range of temperatures. For consumer applications this range is between -20 °C and 60 °C. The temperature dependence of device frequency is called the temperature coefficient of frequency (TCF) which is defined by Hashimoto (2000)

$$TCF = f^{-1}\frac{\partial f}{\partial T} \tag{2.14}$$

Variation near room temperature is important – and variations near the operating temperature of the device. The TCF is often parabolic or cubic. When this happens

$$\alpha^n = \frac{1}{f_r n!}\frac{\partial^n f}{\partial T^n} \tag{2.15}$$

are called the nth order temperature coefficients of frequency. TCF is determined theoretically from

$$TCF = TCV_p - \alpha \tag{2.16}$$

where α is the thermal expansion coefficient and TCV_p is the temperature coefficient of the phase velocity. AT and BT cut quartz are favoured over the X and Y cuts because they have virtually zero temperature coefficient near 25°C. Both the AT and BT crystal cuts exhibit shear waves.

2.6.2 QCM Amplitude

The amplitude of the QCM displacement is given by (Borovsky, Mason and Krim, 2000)

$$A = CQV_d \tag{2.17}$$

where $C = 1.4 \times 10^{-12}$ is a constant determined experimentally by Borovsky et al., Q is the QCM Merit Factor and V_d is the driving voltage.

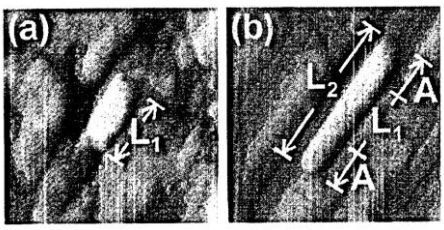

Figure 2.17 QCM amplitude measurement (Benes *et al.*, 1995)

The amplitude, A, as calculated from (2.17) is half the peak to peak displacement and equivalent to the maximal radius an oscillation path at the centre of the electrode. This linear relationship was verified for $V_d \leq 1V$ (Borovsky et al. 2000).

Dultsev (2000) used a power approximation to determine the amplitude

$$A = \sqrt{\frac{(QP)}{2\pi^3 f^3 M}} \tag{2.18}$$

where *P* is the electrical power consumed by the QCM, and *M* is the effective mass of the QCM, considering that the amplitude is greater at the electrode centre.

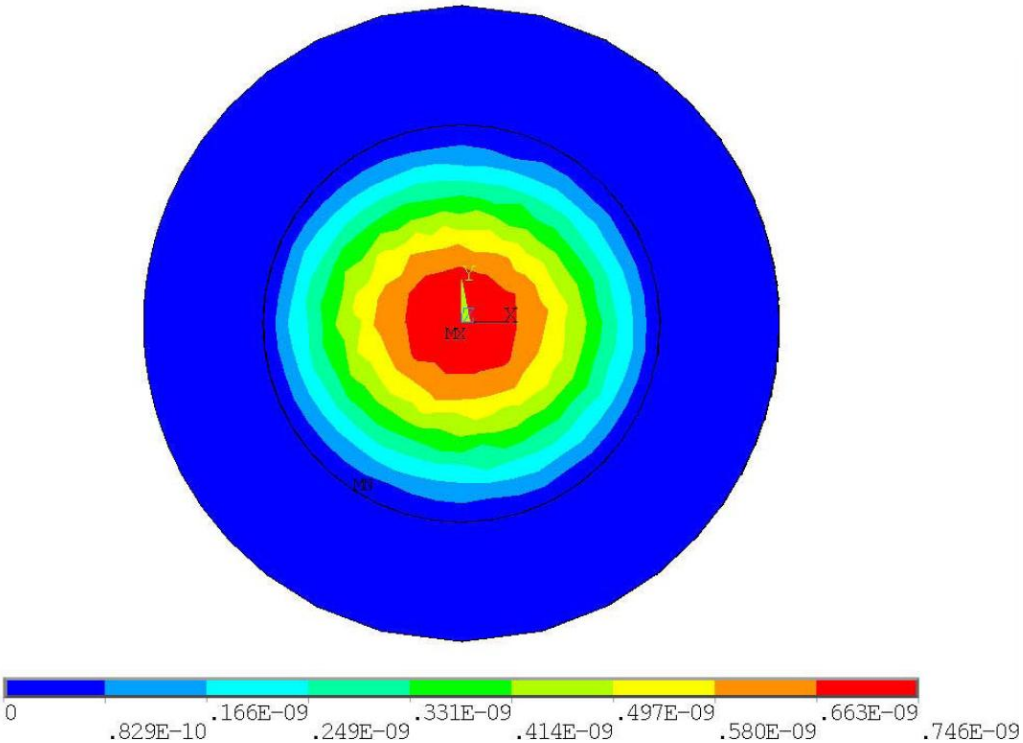

Figure 2.18 QCM modelled using the finite element method (Kurosawa et al., 2004)

The QCM amplitude distribution is approximately normal with the maximum displacement located in the centre of the electrode, approximately twice the mean displacement. Figure 2.18 shows the QCM amplitude distribution as modelled by Kurosawa et al. (2004) using the finite element method. Benes, Groschl, Burger and Schmid, (1995) showed similar results by experiment. The amplitude of QCM oscillations at a distance, r from the electrode sensor is given by

$$A(r) = A_{max} e^{-\left(\frac{r}{c}\right)^2} \tag{2.19}$$

where r is the distance from the electrode center and c is a Gaussian distribution coefficient determining the width of the curve (Edvardsson et al., 2005).

Decreasing the substrate thickness increases the resonant frequency of the QCM. Alternatively the QCM is driven at a harmonic of the fundamental frequency. Benes et al. show that the electrode displacement is increasingly confined to the electrode centre as the order of harmonic is increased.

2.6.3 QCM Equivalent Circuit

It is instructive to model the QCM using an electrical equivalent circuit that models the transducer. The device behaviour is analysed using the equivalent circuit. Perturbations such as added mass are approximated by changing the appropriate analogue in the model. The Butterworth Van Dyke (BVD) electrical model approximates QCM behaviour near resonance using known and accepted electrical techniques. The BVD circuit approximates the fundamental frequency and not higher harmonics. Figure 2.19 shows the mechanical model of an electro-acoustical system and its corresponding electrical equivalent.

The differential equations of the mechanical and electrical systems have with obvious functional symmetry.

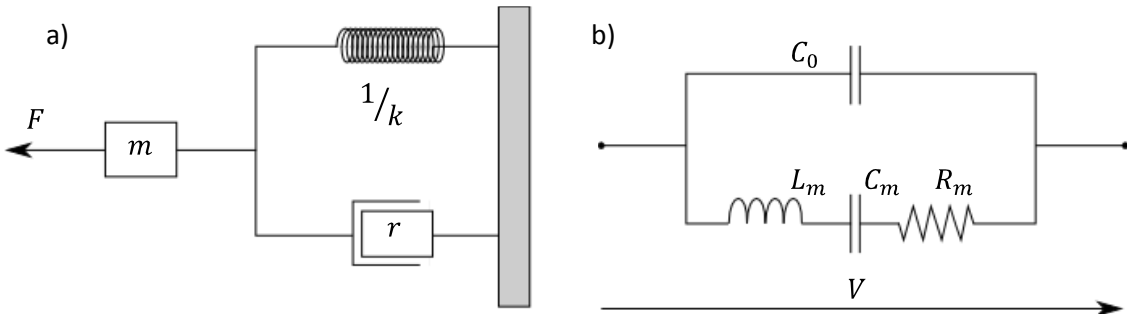

Figure 2.19 (a) The mechanical model of an electro-acoustical system and (b) its corresponding BVD electrical equivalent (Buttry and Ward, 1992)

$$F = m\frac{d^2x}{dt^2} + r\frac{dx}{dt} + \mathrm{k}x \tag{2.20}$$

$$V = L_{\mathrm{m}}\frac{d^2q}{dt^2} + R_m\frac{dq}{dt} + \frac{q}{C_{\mathrm{m}}} \tag{2.21}$$

where x is displacement, F is a force, m is a mass, r is a mechanical resistance, k is Hooke's constant for the spring, V is the voltage applied across the circuit and q is charge. The BVD equivalent circuit consists of two arms. The motional arm has three series components: a resistor representing power dissipation, R_m; a series capacitor representing the stored energy in the oscillation and related to the elasticity of the materials, C_m; and an inductor representing the inertial mass component of the resonator, L_m.

The parasitic capacitance, C_0, is not represented in (2.21) and shunts the motional arm representing the sum of the static capacitances of the crystal's electrodes, holder, and connector capacitance. In the QCM100 system, C_0 is about 20pF. Placing the electronics directly on the crystal holder, eliminating any cable capacitance, keeps C_0 small. Typical values of these parameters for 1" diameter, 5MHz crystal used in the QCM100 system are $C_m = 33\mathrm{fF}$, $L_m = 30\mathrm{mH}$, and $R_m = 10\Omega$ (for a dry crystal), $R_m = 400\Omega$ for a crystal with one face in water, or $R_m = 3500\Omega$ for a crystal with one face in 88% glycerol.

The motional inductance, L_m, of the QCM increases when mass is added to the crystal electrode. The frequency shift of the series resonance is a sensitive indicator of the added mass and films of less than $1\ \mathrm{ng.\,cm^{-2}}$ can be easily resolved by the QCM. The motional resistance, R_m, can also provide important information about a process since soft films and viscous liquids will increase motional losses and so increase the value of R_m.

Equations 2.22 to 2.29 show how the equivalent parameters are calculated (Janshoff et al., 2000)

$$C_0 = \frac{\varepsilon_{22}A}{h_q} \tag{2.22}$$

$$C_m = \frac{8Ae_{26}^2}{\pi^2 h_q \bar{c}_{66}} \tag{2.23}$$

$$L_m = \frac{h_q^3\rho_q}{8Ae_{26}^2} \tag{2.24}$$

$$R_m = \frac{h_q\eta_q\pi^2}{8Ae_{26}^2} \tag{2.25}$$

$$f_s = \frac{1}{2\pi}\sqrt{\frac{1}{L_mC_m}}\left(1 + \frac{C_0R_m^2}{2L_m}\right) \tag{2.26}$$

$$f_p = \frac{1}{2\pi}\sqrt{\frac{1}{L_m C_m}}\left(1 + \frac{C_m}{2C_0} - \frac{C_0 R_m^2}{2L_m}\right) \tag{2.27}$$

$$f_{Zmin} = \frac{1}{2\pi}\sqrt{\frac{1}{L_m C_m}}\left(1 - \frac{C_0 R_m^2}{2L_m}\right) \tag{2.28}$$

$$f_{Zmax} = \frac{1}{2\pi}\sqrt{\frac{1}{L_m C_m}}\left(1 + \frac{C_m}{2C_0} + \frac{C_0 R_m^2}{2L_m}\right) \tag{2.29}$$

where A is the electrode area, h_q is the thickness of the quartz, $\mathcal{E}_{22}$ is the dielectric constant of the quartz, e_{26} is the cutting angle dependant piezoelectric constant.

Further parameters of the QCM can be determined from the equivalent circuit. The electromechanical coupling constant is

$$k = \sqrt{\frac{C_m}{C_0}} \tag{2.30}$$

The unloaded quality factor is

$$Q_0 = L_{\omega_0}/R_m \tag{2.31}$$

which can be compared to the loaded Q factor,

$$Q_c = \frac{f_0}{BW} \tag{2.32}$$

In most cases $Q_0 \gg Q_c$. Figure 2.19 shows the effects of variation of parameters and the resulting simulation (Janshoff et al., 2000).

Figure 2.20 demonstrates that the phase crosses zero twice. The first of these crossings is the series resonance. The second crossing corresponds to the parallel resonance. The series resonance coincides with the minima in impedance, and the parallel resonance with the maxima in impedance. Bond rupture operates the QCM in series resonance because this is where the greatest displacement of the QCM is located.

An alternative to the BVD equivalent circuit is the Mason equivalent circuit. The Mason equivalent circuit is one-dimensional because the 2D and 3D effects such as diffraction, beam spreading, bond line, and parasitic vibration modes are ignored.

The particle velocity of an acoustic wave

$$u = \left(\frac{i}{\omega\rho}\right)\frac{\partial T}{\partial X} \tag{2.33}$$

is exactly analogous to Ohm's law governing transmission of electrical energy. The behaviour of electrical transmission lined predicts the behaviour of acoustic transmission lines.

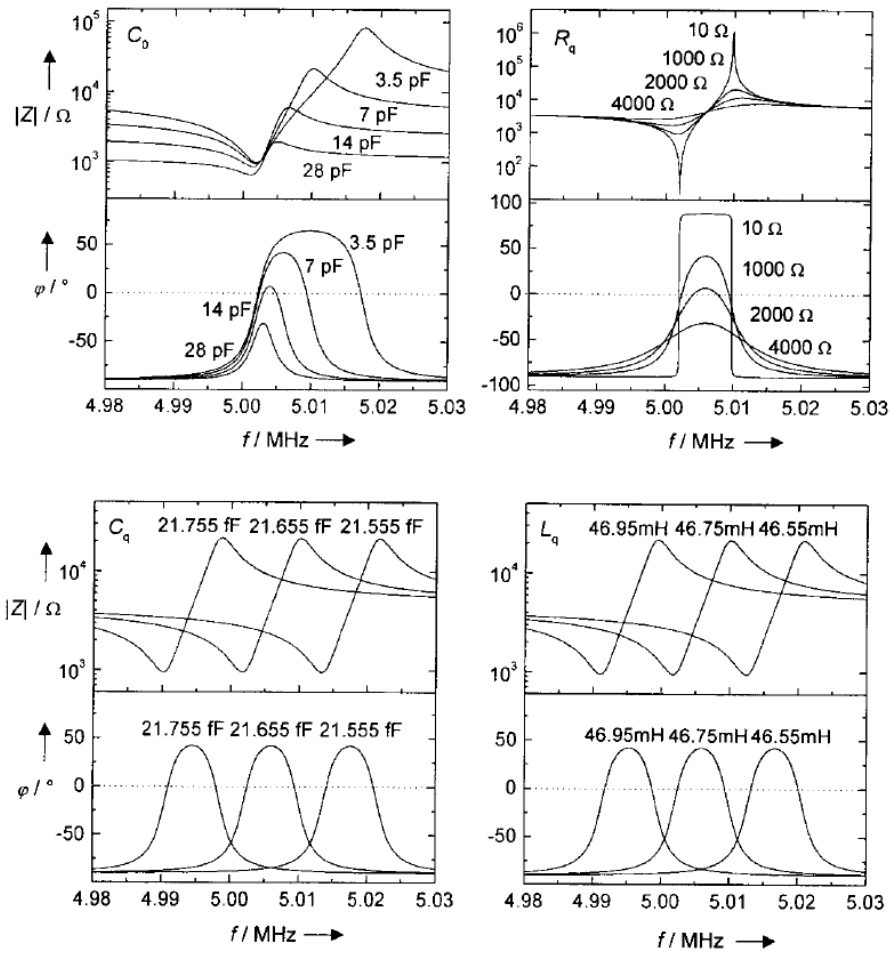

Figure 2.20 Simulated impedance spectra from the BVD equivalent circuit (Janshoff et al., 2000)

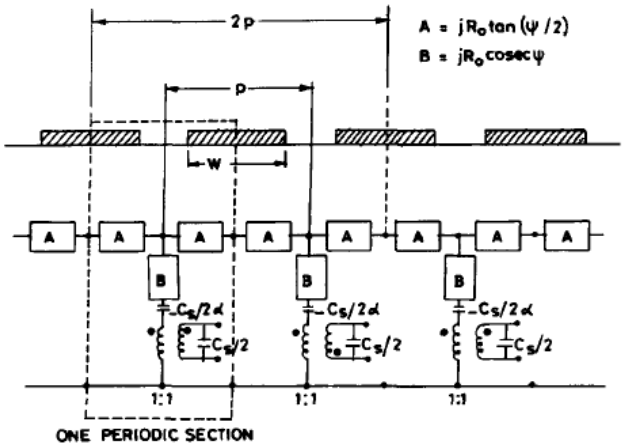

Figure 2.21 Acoustic Transmission Line model of a Surface Acoustic Wave Device Transducer (Bhattacharyya et al., 1995)

SPICE is a widely used general circuit analyser and, when endowed with the ability to handle negative capacitance and inductance, it can be used to simulate Mason equivalent circuits for SAW devices (Bhattacharyya et al., 1995).

The KLM equivalent circuit is intended to overcome the difficulties of relating changes to the electrical components of the Mason Equivalent circuit to changes to structural features. The KLM equivalent circuit was developed by Krimholtz, Leedom and Matthaei (1970).

2.7 Flow Cells and Liquid Operation

For efficient and predictable operation, it is desirable to encapsulate sensor systems into flow cells. This is such a critical part of biosensor development that it is considered in equal standing to the transducer, interface or biodetector. Clamping caused by flow cells and the attachment of wires to electrodes can cause stress in the substrate impairing performance. The electrodes and any seals are connected at an area of null displacement wherever possible. This is the case for QCM devices make electrical contact outside the centre of the QCM where the motion is confined.

In acoustic wave applications electrodes are usually connected using wires which limit the extent to which the flow cell volumes can be reduced, hardly smaller than 50µL (Lange, Bender, Voigt *et al.*, 2003). Wires can also cause air bubbles in the flow. Some transducers are probed wirelessly by capacitive coupling (Lange *et al.*, 2003), allowing transducers to be handled easily. Capacitive coupling is effective in SAW devices because at high frequencies capacitors have low impedance. Wireless probing of QCM has been achieved (Ogi et al., 2006a, Ogi et al., 2006b, Thompson et al., 2003). In this mode of operation, the electrodes of the QCM are lighter than is otherwise possible in wired QCM and the antenna are positioned on one side of the QCM. Some SAW devices offer the ability to connect electrodes on the opposite side to the sensing surface so that the connecting wires do not interfere with the flow cell.

Flow cell encapsulation affects the shear rate of the fluid at the surface as well as binding kinetics. Liquid operation of QCM causes extra damping and renders Sauerbrey's equation for frequency change invalid. When a rigid film is replaced by Newtonian bulk liquid the QCM resonant frequency shift is best approximated by Kanazawa and Gordon (1985):

$$\Delta f = f_0^{3/2} \left(\frac{\mu_L \rho_L}{\pi G_Q \rho_Q} \right)^{1/2} \tag{2.34}$$

where f_0 is the crystal frequency, μ_L is the liquid viscosity, ρ_L is the liquid density, G_Q is the elastic modulus of the quartz, and ρ_Q is the density of the quartz. Kanazawa's model is based on coupling of the shear wave in quartz to a damped shear wave in liquid. The total response of a rigid film immersed in liquid is the sum of film surface mass and the viscous contribution of the liquid (Voinova, Jonson and Kasemo, 2002).

Voinova et al. show by theoretical analysis that for non-rigid deposits the viscous loss of over layers causes the deviation from Sauerbrey behaviour (Voinova, Jonson and Kasemo, 1997). The prediction is for the special case of pure viscous layers. The result is a reduction in the measured surface mass of the film:

$$M_S = m(1-\alpha) \tag{2.35}$$

where α is the viscous correction factor, which depends on the mechanical properties of the over-layer materials and viscous solution, the viscosity, η, the density, ρ, and m, the true mass of the film.

2.8 Acoustic Waves in Liquid

Moving liquid has five defining parameters: three velocity components $\boldsymbol{v}$, pressure p, and density ρ_l. The complete system of five equations are Euler's equations of motion. For viscous incompressible liquid the Navier-Stokes equation is

$$\rho\left(\frac{\partial \boldsymbol{v}}{\partial t} + \boldsymbol{v}\cdot\nabla\boldsymbol{v}\right) = -\nabla p + \nabla\mathbb{T} + \boldsymbol{f} \tag{2.36}$$

where $\mathbb{T}$ is the deviatoric stress tensor and $\boldsymbol{f}$ is the body forces acting on the fluid. The terms on the left or equation (2.36) are concerned with the acceleration and those on the right are concerned with the body forces. The weight of the liquid may be excluded by setting the acoustic device on top of the liquid with only its lower surface in contact. In this case, the $\boldsymbol{f}$ term is neglected. The Del operator (∇) is the differential operator. In a 3D Cartesian system Del is

$$\nabla = i\frac{\partial}{\partial x} + j\frac{\partial}{\partial y} + k\frac{\partial}{\partial z} \tag{2.37}$$

where $\{i, j, k\}$ is the standard $\boldsymbol{R^3}$ basis.

The stress on the right hand side of (2.36) remains. In an incompressible Newtonian liquid, $\mathbb{T}$ is given by

$$\mathbb{T} = \mu\nabla^2\boldsymbol{v} = \mu\Delta\boldsymbol{v} \tag{2.38}$$

The ∇^2 term is the laplacian according to the following

$$\Delta = \frac{\partial^2}{\partial x^2} + \frac{\partial^2}{\partial y^2} + \frac{\partial^2}{\partial z^2} = \nabla\cdot\nabla = \nabla^2 \tag{2.39}$$

If constant temperature is considered the fluid density remains constant and conservation of mass is effectively conservation of volume as described below

$$\frac{\partial\rho}{\partial t} + \nabla\cdot(\rho\boldsymbol{v}) = 0 \tag{2.40}$$

$\nabla \cdot \boldsymbol{v} = 0$, if $\frac{\partial \rho}{\partial t} = 0$

The equations require the boundary conditions as follows. No slip at the fluid-solid interface ensures that the fluid velocities $\boldsymbol{v}$ and the surface velovities are equal. Thus if the surface is exhibiting pure shear motion in the x direction the boundary velocities are

$$v_x|_{z=0} = \frac{du_x}{dt}$$
$$v_y|_{z=0} = \frac{du_y}{dt} = 0 \quad (2.41)$$
$$v_z|_{z=0} = \frac{du_z}{dt} = 0$$

For an infinite surface, the motion of the liquid will depend on the distance from the surface and time. In the case of one dimensional motion on the x axis (2.41), where the fluid is incompressible Newtonian (2.38), temperature is constant and mass is conserved (2.40) and the weight of the fluid is not on the surface then (2.36) is reduced to (2.42).

$$\frac{\partial \boldsymbol{v}}{\partial t} = -\frac{1}{\rho}\nabla p + \frac{\mu}{\rho}\nabla^2 \boldsymbol{v} = -\frac{1}{\rho} grad(p) + \frac{\mu}{\rho}\Delta \boldsymbol{v} \quad (2.42)$$

When pressure is constant ($\partial p/\partial t = 0$) and velocity is always directed along the x-axis ($v_x = \boldsymbol{v}$) then

$$\frac{\partial v}{\partial t} = \frac{\mu}{\rho}\Delta v = \frac{\mu}{\rho}\nabla^2 v = \frac{\mu}{\rho}\frac{\partial^2 v}{\partial z^2} \quad (2.43)$$

and for very small elements of liquid

$$v(z,t) = v_0 \cdot e^{-z/\delta} \cdot e^{i\left(\frac{z}{\delta} - \omega t\right)} \quad (2.44)$$

where $v_0 = -i\omega \cdot u_0$ is the velocity of the surface and δ is the depth of penetration into the liquid is determined from

$$\delta = \sqrt{\frac{\mu}{\pi f \rho}} = \sqrt{\frac{2\mu}{\omega \rho}} \quad (2.45)$$

Figure 2.22 demonstrates that the vibration amplitude, and thus the acceleration, decays exponentially from the crystal surface into the liquid. This is important on the basis that most of the sensor area is not covered by detected particles, so the particles are surrounded by moving media. As the interface viscosity increases the shear wave penetrates further into the liquid increasing the energy lost to damping. Equation (2.46) embodies this relationship.

$$A(z) = A_0 e^{-z/\delta} \quad (2.46)$$

Some of the contacted liquid trapped in the fine variations of the moving surface will exhibit solid film behaviour. Similarly, well bound particles or groups or particles will also

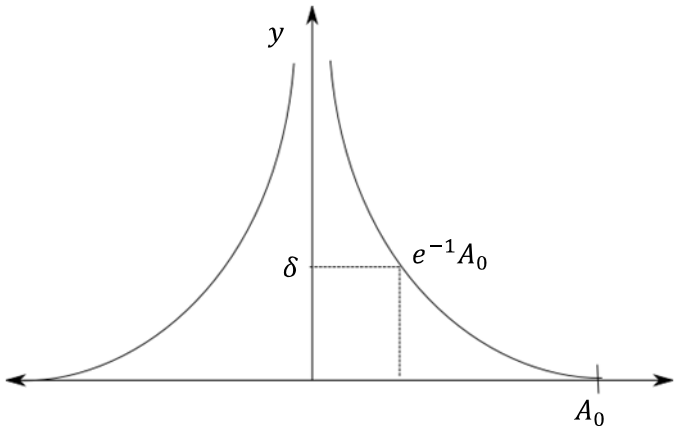

Figure 2.22 Acoustic wave decay into fluid

behave like an attached solid. However once the particles deform, wobble, stretch or exhibit any kind of phase change or hysteresis their effect on the resonant frequency must be more akin to liquid.

Barnes et al. (1992) have proposed the viscoelastic properties as a superior means of sensing to pure mass balances. Dejous et al. (1995) presented comparable methods using SH-APM devices in aqueous mixtures noting the effects of temperature and viscosity.

When the surface is oscillating with angular frequency ω, and amplitude u_0, along a linear axis x, and the velocity of the surface on the y and z axes is zero, a friction force is working on the solid surface and directed along the x axis. The friction force is proportional to the velocity and is $\pi/4$ out of phase with the surface displacement. The shear stress is related to the force F, dynamic viscosity μ , shear rate and area by the relation

$$\tau = \mu \frac{\partial u}{\partial z} = F/A \tag{2.47}$$

The friction force produces the damping and energy dissipation. The force per unit area is thus

$$\begin{aligned} \mu \frac{\partial v_x}{\partial z}\bigg|_{z=0} &= \frac{\mu}{\delta}(i-1)v_x(z,t)\bigg|_{z=0} \\ &= \omega u_0 \sqrt{\mu \rho \omega}\, e^{-i\left(\omega t - \frac{\pi}{4}\right)} \end{aligned} \tag{2.48}$$

Liquid damping, like added mass increases the motional impedance – as represented by the inductance L_2 and resistance R_2 in the modified BVD equivalent circuit shown Figure 2.23 (Arnau et al., 2002).

The increased resistance is

$$R_2 = \omega_s L_2 = \frac{n\omega_s L_1}{N\pi}\left(\frac{2\omega_2 \rho \eta}{c_{66}\rho_q}\right)^{1/2} \tag{2.49}$$

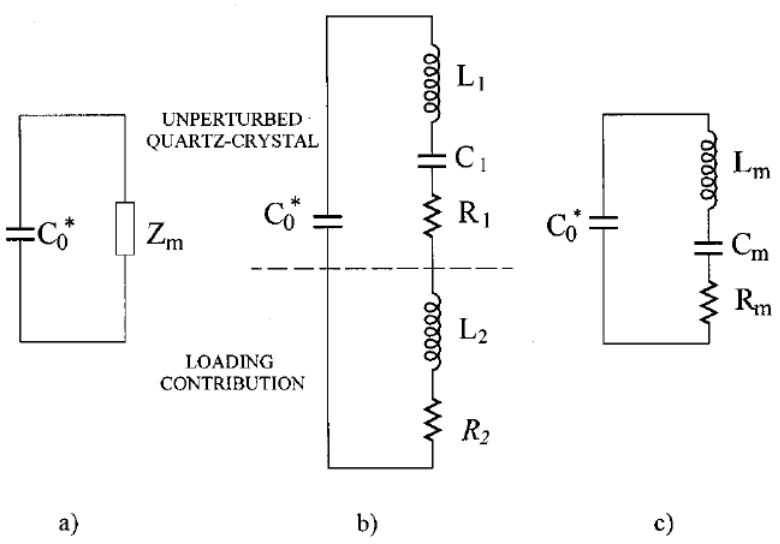

Figure 2.23 Extended Butterworth van Dyke Equivalent Circuit: (a) general model, (b) extended BVD model, and (c) BVD model (Arnau et al., 2002)

where n is the number of sides in contact with the liquid, N is the harmonic number, ω_s is the series resonant frequency, and ρ_q and c_{66} are the density and shear stiffness of the quartz. The motional elements L_2 and R_2 represent the kinetic energy and power dissipation respectively. Both are proportional to $\sqrt{\rho\eta}$. The frequency at which the motional reactance vanishes, the motional impedance becomes real. The frequency is determined by

$$f_s = \frac{1}{2\pi\sqrt{(L_1 + L_2)C_1}} \tag{2.50}$$

The change Δf_s due to liquid loading is in agreement with Kanazawa and Gordon (1985)

$$\Delta f_s \approx -\frac{L_2}{2L_1} f_s = -\frac{2nf_s^2}{N\sqrt{c_{66}\rho_q}} \left(\frac{\rho\eta}{4\pi f_s}\right)^{1/2} \tag{2.51}$$

2.9 Looking Forward

There are many contributing technologies that come together to make Lab on a Chip devices: selective (bio)chemical layers and materials; various transduction platforms; arrays and pattern recognition; planar sensors and three-dimensional MEMS devices.

The single-chip gas sensor micro system (Hagleitner et al., 2001) incorporates three different transducers which are fully integrated onto one chip with the microelectronic components. Full integration of signal amplification, conditioning and analogue to digital conversion improves the overall sensor performance. Such system integration is a long term goal of bond rupture research.

'Biochip' is a term used to describe a sensor with multiple transducer elements, usually a 2D array of reactor sites, a sample schematic shown in Figure 2.24 (Vo-Dinh et al., 2001). Such combination of multiple reactor sites would compliment bond rupture technology.

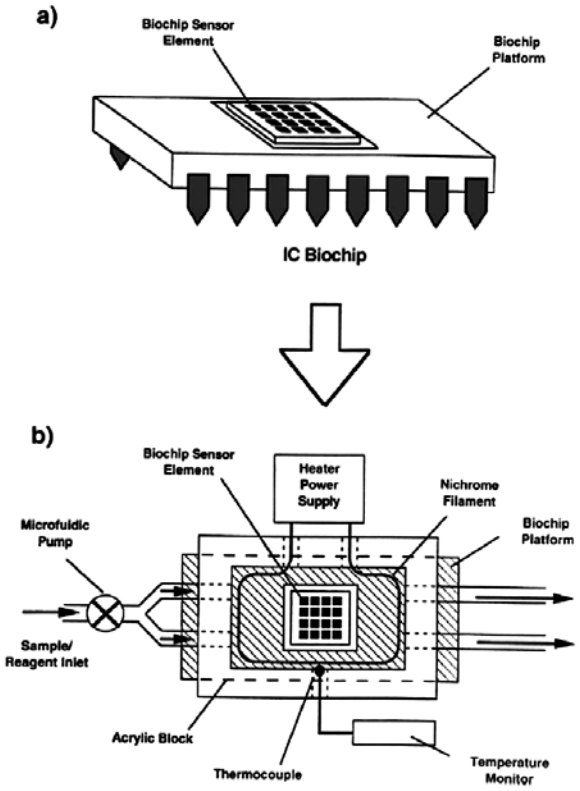

Figure 2.24 Schematic drawing of a 'Biochip' (Vo-Dinh et al., 2001)

Bond rupture biosensors could take the course of Smart Transducers. Smart Sensors are integrated sensors where the sensing element and required electronics are packaged together. In generally every sensor requires wiring and signal conditioning, which makes sensors complicated, expensive and heavy. Integrated electronics solves this problem by incorporating digital electronics into the sensor, thus permitting the use of a digital bus.

Many smart sensors could be manufactured using conventional IC manufacture techniques, or with only few additional processes, allowing for quick and easy development and manufacture. Additionally extra hardware such as ADCs would not be required in order to communicate with a controller as they can be integrated directly into the sensor.

The relevant IEEE standard (IEEE 1451) for smart sensors incorporates into every sensor a Transducer Electronic Data Sheet (TEDS). TEDS eliminates the need for human transcription of sensor configuration data eliminating calibration issues by telling the data acquisition system directly how to operate (IEEE, 2004). Progression of bond rupture to sufficient maturity for smart sensor integration is beyond the scope of this thesis.

2.10 Analysis of Literature

This literature review has covered many areas and the state of the art of bond rupture biosensors at the commencement of this research. Bond rupture is a relatively new method of diagnosis that can integrate into existing systems be they acoustic, optical or chemical. Bond rupture biosensors have the potential to deliver the state-of-the-art in clinical testing and contaminant detection technology to the point-of-care. Affirmative diagnosis of a specifically threatening disease or contamination and even quantitative determination of the concentration is achievable with a turnaround time of less than one hour.

The literature shows that few groups are pursuing the bond rupture methodology and that the success of their results is mixed. The groups use different methodologies and it is difficult to compare directly. There are a number of applications that touch on the edges of the field of bond rupture but do not utilise bond rupture as a diagnostic tool.

Real-world biosensors are required to detect low concentrations of the analyte in the presence of many interfering phenomena. Bond rupture, unlike pure mass-balance architectures could work in complex serum, e.g. blood, separating the effect of nonspecific binding. Like many biosensors, the application of the bond rupture technique depends directly on the existence or development of a suitably viable receptor.

This review has explored current progress in developing this platform and outlines some future prospects including the use of other acoustic wave devices, circuit integration and smart sensing, and microfluidic cell integration. Before progress is made in these areas there exists more pressing issues relating to the bond rupture methodology and the understanding on the bond rupture mechanisms.

There is little understanding of the mechanisms of bond rupture as a result of base excitation. Whereas much literature can be found on single bond strengths, little is known about how systems of bonds resist a force. The nature of the applied force in bond strength studies is inherently different to that experience by bonds during bond rupture. This is discussed in detail in Chapter 4.

Evidently there is some difficulty in the detection of bond rupture noise and this has been reported by multiple groups. The nature of the noise signal is unknown and it is difficult to know the amplitude and frequency of the signal. The detection limits are not easily determined. There is little consensus on the best methodology or how to best drive the transducer. When this is combined with the many available transducers that can perform, bond rupture it is clear that a versatile investigation of particle rupture is required in order to further the development of bond rupture devices.

In the chapters that follow these immediate issues are addressed. Chapter 3 contains a comprehensive investigation of QCM bond rupture using the Industrial Research Limited bond rupture hardware. The hardware is discussed and the characteristics of bond rupture are investigated. Chapter 4 develops a numerical model for single particle rupture. The result is a simplified model of single particle rupture for use in Chapter 5, which models the bond rupture device and investigates improvements. Chapter 6 is an investigation of the Surface Acoustic Wave transducer for bond rupture. During this chapter, a new bond rupture transducer is designed, fabricated and tested.

3. BOND RUPTURE EXPERIMENTS

3.1 Introduction

This chapter presents the investigation into the characteristics of the QCM during bond rupture scans. Controlled experiments explore the variation of the QCM response as the parameters of the bond rupture scans are varied. The experiments utilise a phantom receptor-ligand bond and latex particle as a surrogate for real bacteria. Protocols are presented for bond rupture experiments with phantom receptor-ligands.

For completeness and to assist in discussion of the experiment results, the bond rupture hardware is briefly reviewed and discussed. The timeframe of the development of the bond rupture hardware overlaps this research considerably. Hardware development is not the primary focus of this dissertation; however, this author's involvement in the design of the hardware both as a PhD candidate and earlier as an engineering student has been at times considerable. A number of papers were published on the hardware and a short summary is provided in the review article (Hirst, et al., 2008). The master document regarding the hardware used in this section is the thesis written on the subject by van der Werff (2008).

3.2 Phantom Target

This work uses the streptavidin-biotin receptor- ligand pair. The underlying principle of bond rupture technology requires bonding and the bond formed between streptavidin and biotin is suitably strong and stable, and does not require stringent protocols that are required for antibody-antigen use. The first publications of the groups undertaking bond rupture research (Dultsev et al., 2000, Yuan et al., 2007) use streptavidin-biotin bonds.

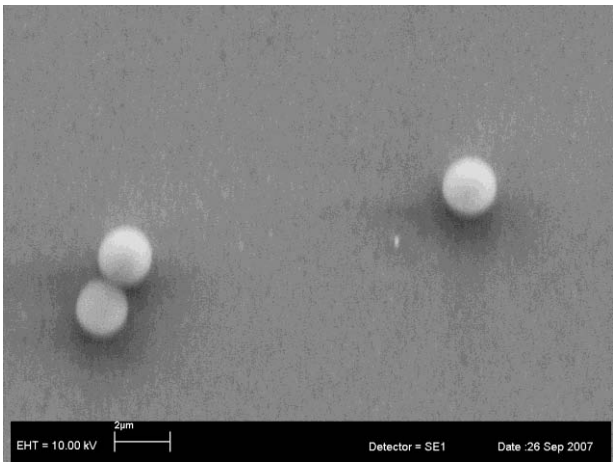

Figure 3.1 SEM image of two micron latex spheres showing two spheres adhered to one another

The particles to which the receptors are bound are latex microspheres. Latex spheres are slightly heavier than water with a specific gravity of 1.005. They do not stay suspended in solution, an important consideration when binding. The undiluted particles are suspended in a buffer solution. Their sizes are precisely determined to stringent tolerances, which serves to reduce the variability of experiment results. Figure 3.1 shows a SEM photograph of a two micron latex particle.

3.3 QCM Bond Rupture Experiment

The QCM are first prepared according to the protocol for immobilisation of streptavidin beads on biotinylated self assembled monolayer

The ingredients are:

- EDC: 1-ethyl-3-(3-dimethylaminopropyl)carbodiimide
- NHS: N-hydroxysuccinimide
- HS-$(CH_2)_{11}$-OH: 11-mercapto-1-undecanol
- HS-$(CH_2)_{15}$-COOH: 16-mercaptohexadecanoic acid
- 200X diluted for 4μm streptavidin bead solution
- 400X diluted for 2μm streptavidin bead solution
- 2000X diluted for 1μm streptavidin bead solution

The protocol for binding is:

- Cleaned with hot piranha solution (a mixture of H_2SO_4:H_2O_2 = 3:1).
- Rinsed thoroughly with Milli-Q water, then acetone, blown dry with nitrogen flow
- Immediately immersed in 1:9 mixture of 5mM HS-$(CH_2)_{15}$-COOH in ethanol and 5mM HS-$(CH_2)_{11}$-OH in ethanol for overnight.
- Rinsed with ethanol, then Milli-Q water, dried by nitrogen flow.
- Biotin incubated with 8μl drop of a 1: 4: 4: mixture of 25mM Biotin and 0.4M EDC and 0.1M NHS in H_2O for 20 minutes (2.8mM biotin).
- Rinsed with Milli-Q water.
- Exposed to 8μl drop of 1M ethanolamine-HCl for 10 minutes.
- Rinsed with Milli-Q water and dried with nitrogen flow.
- Streptavidin beads immobilised by exposing the surface in 250μl diluted bead solution (in a 10mM PBS) for 1 hrs, with vibrator induced.

Following preparation the QCM are mounted into QCM mount and placed in a Nitrogen ambient atmosphere to control humidity effects. Figure 3.2 shows the QCM in its factory holder (left) and one of the purpose built QCM mounts (right).

Figure 3.2 Factory holder of QCM. Small springs attached with silver epoxy (left). Custom holder featuring Teflon cell and spring clamp. Electrical connection to the QCM electrode is achieved by 'pogo pin' (right)

Once the experiment is prepared the software parameters are chosen and entered into the PC graphical user interface. The PC runs Prospa, a software package designed for control and processing of Nuclear Magnetic Resonance (NMR) experiments and data.

The resonant frequency of the QCM is determined and a bond rupture scan is executed. A bond rupture scan is conducted over a finite time during which the QCM resonant frequency is repeatedly tested and recorded. After each test the QCM is run for a short time at the determined resonant frequency. The voltage is increased in a step-wise manner each iteration as a linear function of time. The start and end voltage are set by the user and can practically be set in the range 0.1 to 20V. The QCM is monitored during the driving cycle over a finite bandwidth for 'bond rupture noise'.

Following the first scan, two further scans are conducted for use as a base. If the experiment is complete then the second and third scans are identical. The frequency change from the second scan is subtracted from the first to compensate for QCM nonlinearities and the voltage-frequency effect. The resulting frequency change is attributed solely to mass lost from the surface.

3.4 Electronic Hardware for QCM

The QCM bond rupture system detects the resonant frequency by sweeping the device with a variable frequency sine wave source using a digital system. The primary purpose of the hardware is to affect bond rupture and simultaneously measure the effect of mass change. The mass change is measured by the change in resonant frequency. The digital system is designed to measure the wide band noise generated by a detachment event. This impulse on the surface and the spectrum that it generated has largely evaded detection by this group.

The sensing electrode is grounded to minimise electrochemical interactions at the electrode surface. This is a requirement of the surface chemistry. This affects both the design of the QCM driving boards and the experiments that are conducted. The bond rupture application requires reasonably high power delivered to the QCM. To distinguish relative bond strengths the power must be adjustable. This requires clean input signals into high quality amplifiers.

The high dynamic range of the input voltage requires adjustable amplifiers and attenuators on the input side. These are of the highest available quality to best preserve the small signal of interest on the QCM as a result of bond rupture. The signal of interest is broadband with peaks near the fundamental frequency and its harmonics. The noise of bond rupture is sought by focusing on a frequency band that is not occupied by the driving signal or its artefacts. This signal is filtered in hardware and software.

Figure 3.3 summarises the key components of this system and the connections. The PC has control over the Digital Signal Processor (DSP). The DSP software is reloaded every experiment. The Analogue to Digital Converter (ADC) is an analogue voltage source which drives a bank of variable amplifiers. The high power input signal is connected to the QCM through filters and impedance matching. A bank of variable amplifiers controls the input of the Digital to Analogue Converter (DAC), which digitises the input signal at a high bit rate. To facilitate processing of the signal the digital receive processor filters and down-samples the data to a more manageable bit rate. The results are temporarily stored on the DSP and streamed to the PC and displayed for the user.

Voltage driving is employed by the hardware. The voltage is ramped and the current through the QCM is limited by the QCM impedance. References to driving voltage in this thesis typically refer to the voltage across the QCM some distance from resonance. Current driving is where the current input to the QCM is ramped up and the voltage over the QCM is a function of the input current and QCM load. This methodology is not used in this hardware but if implemented would simplify the impedance matching.

The voltage across the QCM is measured directly. The input power of the QCM is limited during a frequency sweep, and the impedance of the QCM is lowest at resonance. As $P = V \times I = V^2/R$, where P is constant, the voltage across the QCM must decrease with the impedance. The early versions of the QCM hardware operated in this manner. Detecting minima is more difficult and results in greater signal to noise ratio than detecting maxima. A current sensing configuration was adopted. Current sensing is achieved using a transformer as a current detector.

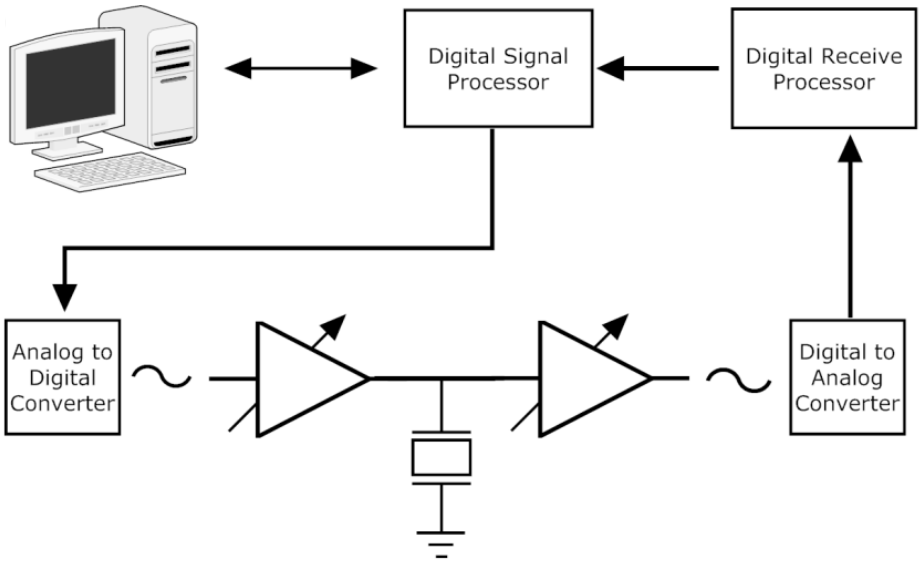

Figure 3.3 Diagram of integrated digital approach for bond rupture testing used by van der Werff et al (2007)

The second generation – FPGA based - bond rupture system utilises a current sensing transformer to convert current to voltage. The fundamental difference between the second generation hardware and that presented in Figure 3.3 is the inclusion of an FPGA in place of the Digital Receive Processor. The functions of the Digital Receive Processor are absorbed into the FPGA, which also offers much more reprogrammable functionality.

This work uses two methods of detecting resonant frequency. The first is a basic sweep of frequencies near resonance alluded to earlier. The second is a counter operation when the QCM is left unloaded for a time after driving. The QCM amplitude rings down decaying. The so called zero crossing method counts the number of zero crossings and the frequency is calculated from the timing information. There is some concern that when the QCM is not being driven it is in some way loaded by the external circuitry. The experiments presented in this chapter utilise the frequency sweep method.

The device, designed and built at Massey University, was modified to fit into the experiment procedures undertaken at Industrial Research Limited. This included the redesign of filters and impedance matching hardware. These changes make the device more user-friendly as many of the end users do not have an electronics background. Unsuccessful modifications of the system were undertaken in an effort to detect the noise of bond rupture, these are not detailed here.

Fifty Ohm transmission lines are used throughout the hardware. The QCM is not a matched 50Ω device, and the impedance is frequency dependant and changes with the surrounding media. For the purpose of driving the QCM at high amplitude, it is desirable to

match the 50Ω system to the impedance of the QCM to achieve efficient power transfer. This requires determining the impedance at the series resonance of the QCM where the admittance is greatest.

The frequencies at which the QCM operates are such that the wire length is less than one tenth the wavelength of the signal and then reflections at impedance transitions do not cause significant problems. To good approximation the product of wavelength and frequency is the speed of light, at 30 MHz gives a wavelength of 10m.

Impedance matching is carried out as a means of decoupling the QCM from the driving hardware. Transformers were selected in favour of matched LC networks because such networks are too narrow band and the objective is to develop hardware capable of operating at several frequencies. Directional couplers are not suitable as they have poor performance in cases of unbalanced impedances. In an ideal transformer, the ratio of voltages in the primary and secondary windings is equal to the ratio of the number of turns.

$$\frac{V_p}{V_s} = \frac{N_p}{N_s} = \frac{I_s}{I_p} \tag{3.1}$$

From this the following relationship is derived

$$\frac{Z_p}{Z_s} = \left(\frac{N_p}{N_s}\right)^2 \tag{3.2}$$

These relations indicate the required turn ratios to match impedance, however the equivalent circuit of the QCM, combined with the inductance of the parallel transformer changes the reactive component of the circuit impedance.

One method of QCM operation is the cancelation of the parallel capacitor by an inductor. These two elements resonate with each other at a specific frequency. Despite not cancelling the capacitance, its effect is reduced and in some cases over compensated by the reactive properties of the parallel transformer. The fastest way to achieve a coarse match is to wind a number of turns onto the toroid to act as the primary coil and to connect this to the QCM. Subsequently the secondary is wound until it presents measured impedance close to 50Ω. The variability in the QCM and between the QCM makes an ideal match impossible. Considering the impact of impedance mismatch and the length of the wires at the operating frequency of the device this is deemed adequate.

3.5 Measured Properties

In the section that follows the QCM is characterized and parameters determined to allow intelligent estimations in the chapters that follow.

Table 3-1 Impedance Measurements

Media	QCM Number	Resonance Frequency (MHz)	Admittance (mS)	Impedance (Ω)	Resistance (Ω)	Reactance X (Ω)	Series Capacitance (pF)	Series Resistance (Ω)
Air	1	9.9780	4.32	232	225	-57	273	224
	2	9.9750	4.19	239	232	-56	280	232
	3	9.9775	4.35	230	224	-52	303	225
	4	9.9873	4.09	225	239	-52	305	239
	5	9.9905	4.06	247	241	-51	306	241
	Average	9.9817	4.20	234	232	-54	293	232
Pure Water	1	9.9760	2.14	471	458	-144	118	465
	2	9.9768	2.81	438	411	-153	104	411
	3	9.9755	1.26	443	428	-113	140	430
	4	9.9843	2.22	449	428	-137	116	430
	5	9.9888	2.16	463	448	-122	132	450
	Average	9.9803	2.12	453	435	-134	122	437
Buffer	1	9.9760	2.20	460	443	-143	118	455
	2	9.9768	2.20	450	425	-155	101	419
	3	9.9755	2.26	445	425	-150	111	437
	4	9.9845	2.14	466	426	-159	96	430
	5	9.9885	2.11	469	449	-136	115	449
	Average	9.9803	2.18	458	434	-149	108	438

3.5.1 Operating Frequency and Impedance Spectra

Figure 3.4 shows the measured admittance spectra for a QCM in its factory mounting. QCM were first cleaned in hot piranha solution. Using the QCM holder and spring clamp the impedance is measured using HP 4194A Impedance Analyser. Measurement was repeated for five 10MHz QCM in air, water and buffer solution. Two phase changes are evident corresponding to the series and parallel resonance of the QCM. The series resonance of this device is found to be 9.98825MHz. The parallel resonance is 10.0120MHz. The manufacturer specification of 10MHz is centred between the series and parallel resonances.

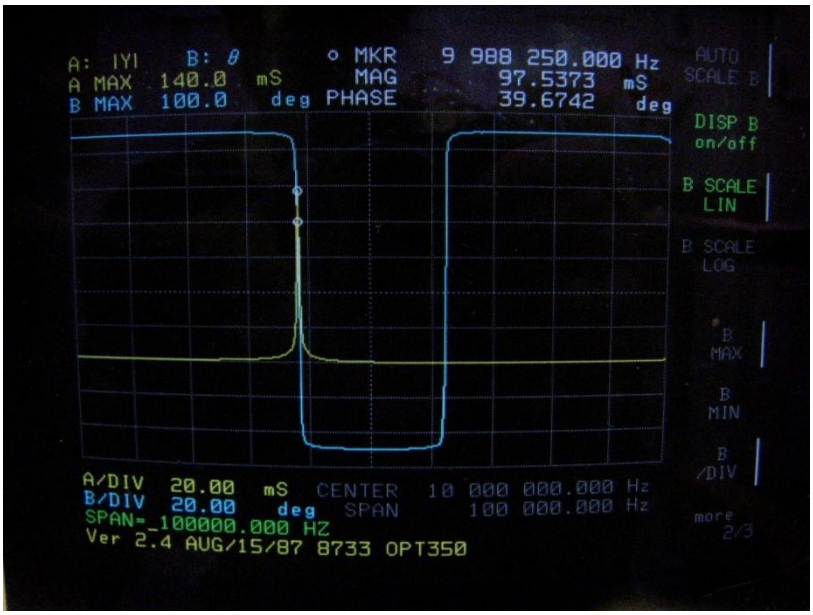

Figure 3.4 Measured admittance and phase of QCM in air

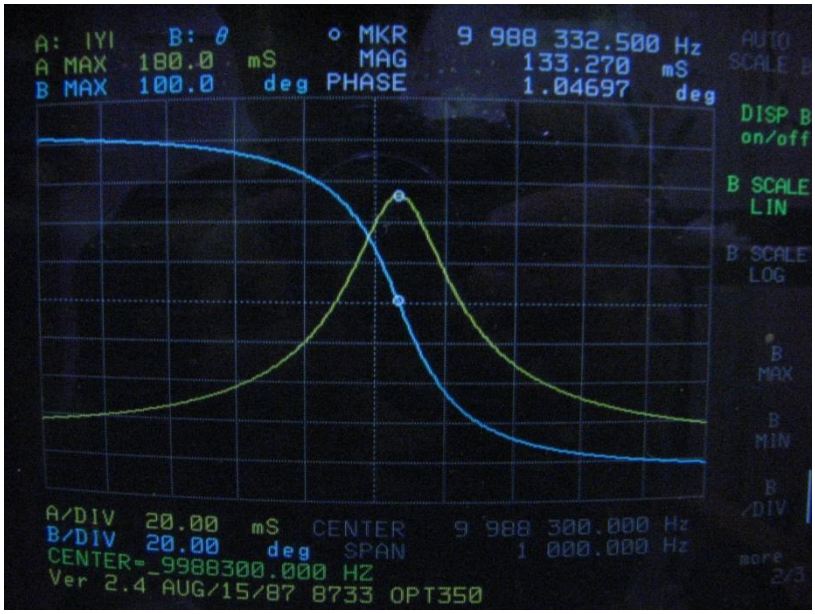

Figure 3.5 Measured admittance and phase of QCM pure water

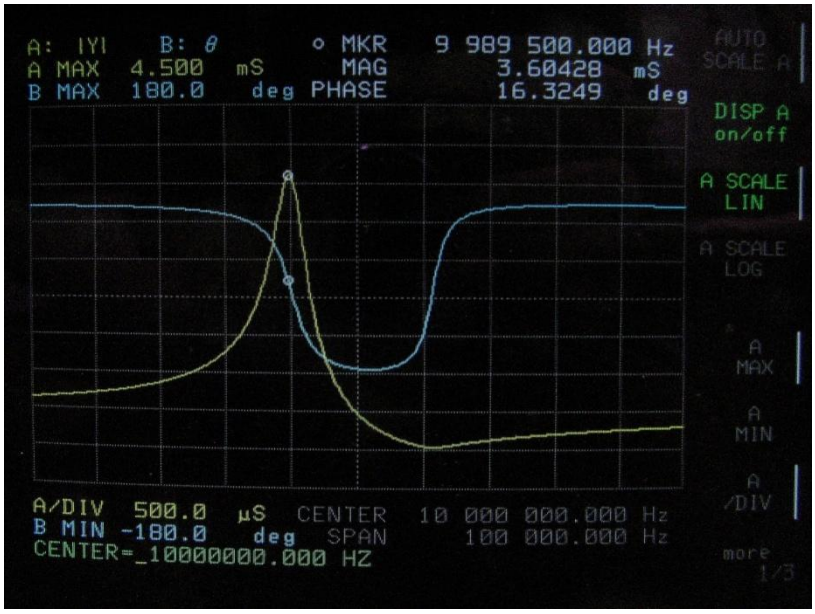

Figure 3.6 Measured admittance and phase of QCM in air with damping of holder

Figure 3.4 shows QCM measurements with the following properties: Admittance at series resonance 130.123mS at 11.55° phase. Series impedance of 7.533Ω at -1° phase angle. Third harmonic at 29.988 MHz Admittance 56.11mS at 7.94°. Impedance of 17.65Ω at -2°.

Figure 3.5 shows that once loaded with pure water on one side, the width of the admittance peak widens and the admittance increases to 133.27mS at 1°. The resistance is 7.5Ω at 0.45°. The increased width is indicative of reduced quality.

Figure 3.6 shows the admittance spectra for the QCM in the modified holder. Damping caused by the holder decreases the admittance of the QCM. Table 3-1 summarises the impedance measurements performed on several QCM.

In the discussion of the resonant frequency and its harmonics a distinction is made between the third harmonic and the third overtone. The third harmonic is the next resonance after the fundamental, it is denoted, $3f + \Delta f$. The third overtone is three times the fundamental, or $3f$. The QCM does not resonate here but this is where artefacts from the driving signal are evident. These artefacts are introduced during digital to analog conversion and amplification.

As the driving voltage is increased so does the resonant frequency and the corresponding overtone. The third harmonic increases faster indicating that the Δf parameter is voltage dependant. This is of consequence when looking for noise but has not detrimental effect on the frequency change results, the primary focus of the coming chapters.

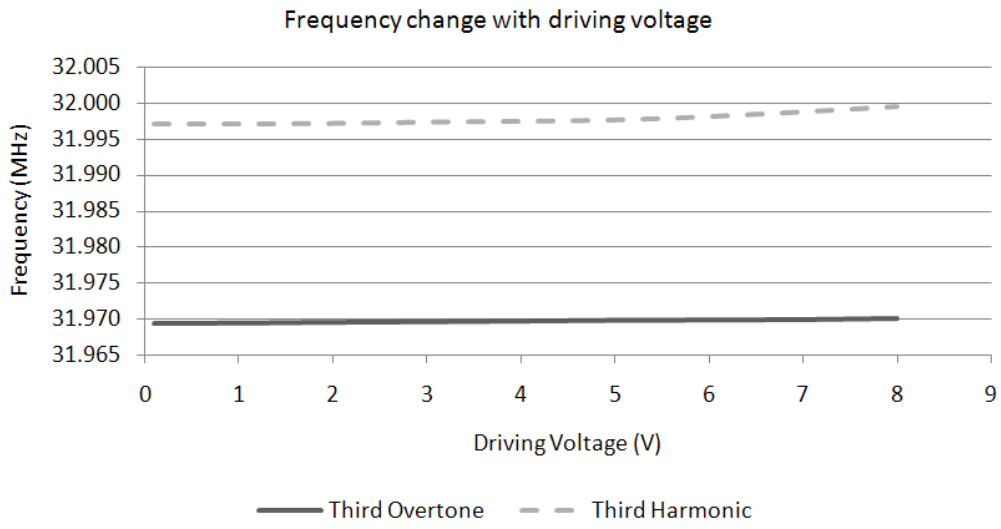

Figure 3.7 Measured third harmonic and third overtone plotted as a function of driving voltage. Δf is not constant during a scan

3.5.2 Quality Factor

The changes in admittance and impedance spectra caused by clamping and liquid operation described above are characterised by the QCM quality factor property. This is measured for the QCM factory holder. To ensure that measurements reflect the quality factor of the QCM in the bond rupture device, the bond rupture hardware was used to conduct the measurements. Figure 3.8 shows a frequency sweep conducted near resonance for a QCM in the factory holder. The centre frequency of the QCM is $f_c = 9.998427MHz$. The 3dB bandwidth is $310Hz$ measured from the spectra above. Following equation (2.32) $Q = 32{,}250$.

Figure 3.9 shows a reduction in the QCM quality when one side of the QCM is wet. The quality factor of the QCM cannot be measured in the same way as above. Figure 3.10 shows that when the modified holder is used the quality factor is similarly damped when fully clamped. The results presented in Figure 3.11 indicate that care is required to maintain contact with minimal damping. The quality factor is 35,669 for an ideally clamped QCM

3.5.1 Temperature

Measurement of QCM operating frequency by temperature measurement was achieved by Yuan et al. from Industrial Research Limited. A thermocouple attached to the QCM measures the temperature of the surface when operated at frequencies near resonance. At resonance the QCM dissipates much more power as heat.

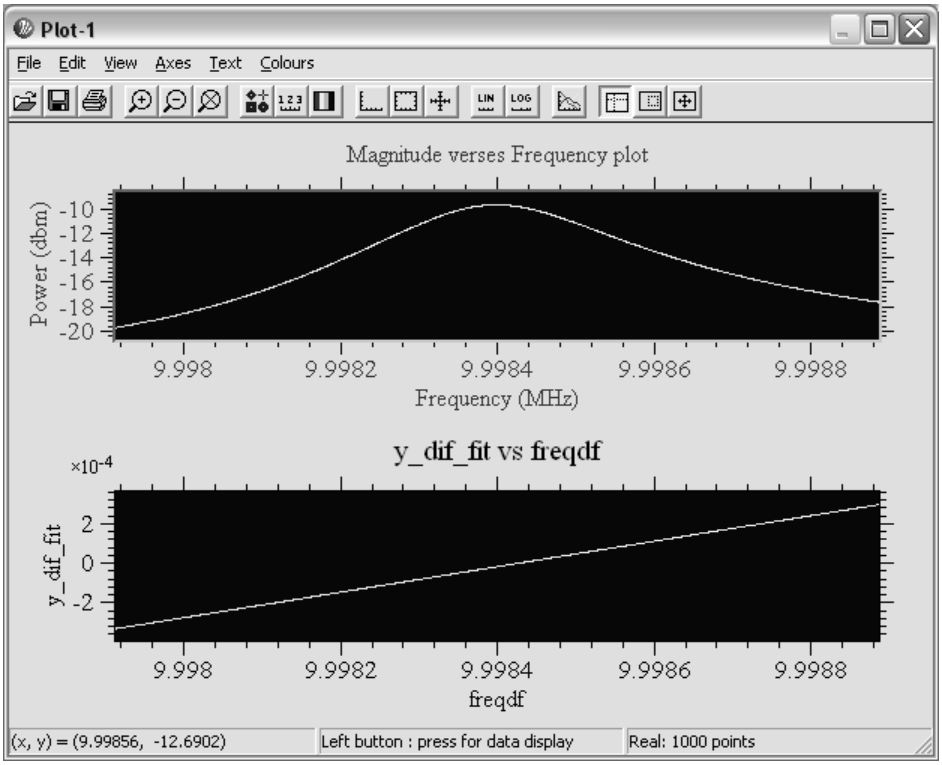

Figure 3.8 Frequency sweep of QCM in factory mount in air used to determine the quality factor

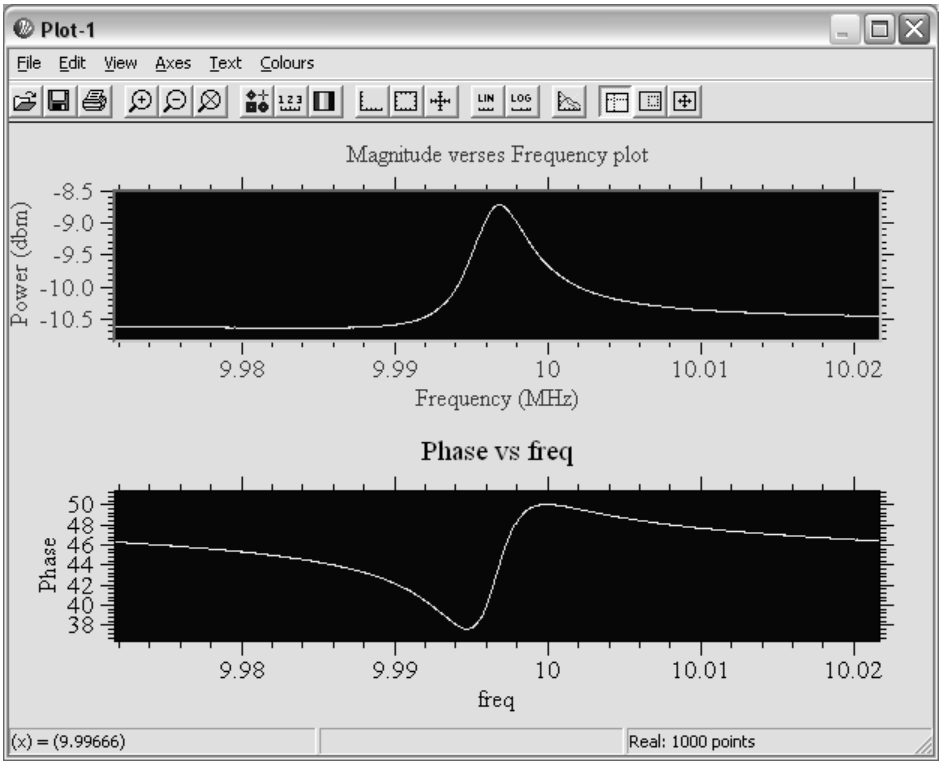

Figure 3.9 Frequency sweep of QCM showing reduced quality

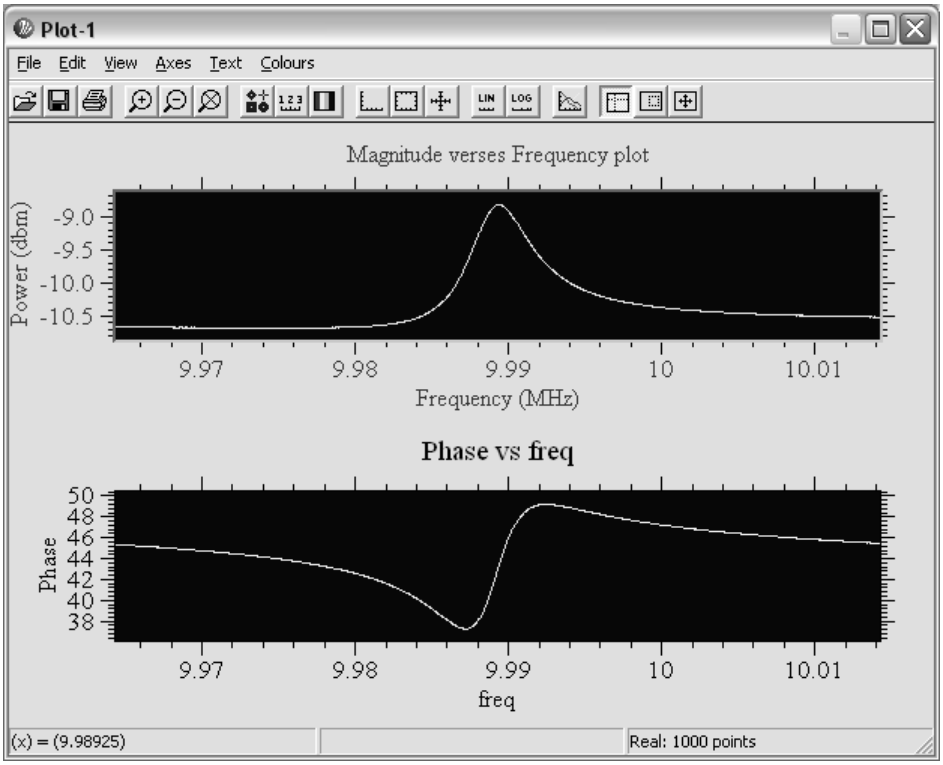

Figure 3.10 Frequency sweep of QCM showing the effect of clamping

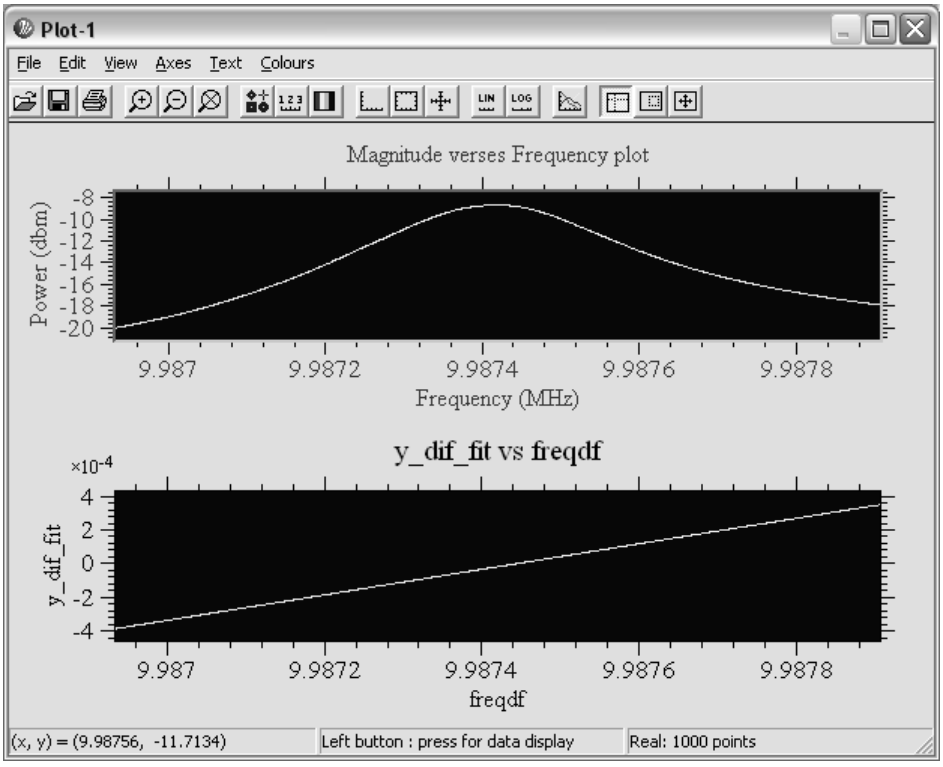

Figure 3.11 Frequency sweep of QCM showing restored quality

The temperature axis in Figure 3.12 represents the temperature above room temperature. The lab is temperature controlled at 21° C. Figure 3.12 shows that the temperature rises near resonance and that the temperature of the QCM surface at 12V has the potential to exceed 40°C. Bond rupture scans are shorter than this experiment and so the QCM will not reach these temperatures.

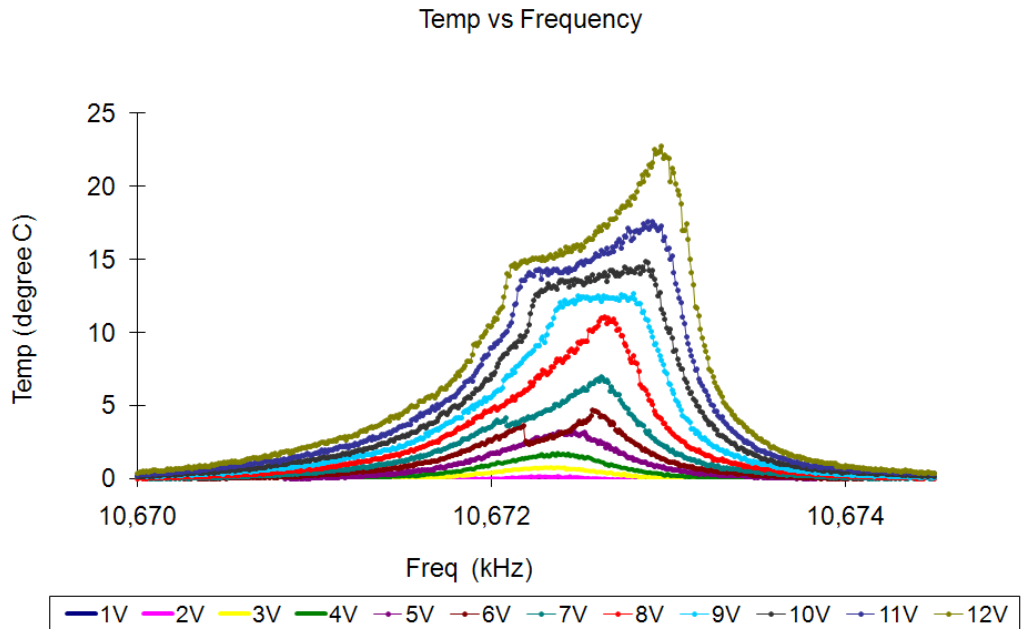

Figure 3.12 Electrode surface temperature of QCM driven at frequencies near resonance at different voltages

3.6 Bond Rupture Scan Frequency Change

Bond rupture scans in this section use frequency change observations while the QCM is subjected to increasing voltage. According to Borovsky et al. (200), the QCM amplitude increases linearly with voltage. A nonlinear relationship between voltage and amplitude is anticipated at high voltages. The effect of temperature as discussed above is one cause of nonlinearity.

A bond rupture scan, when observed in real time, proceeds with the particles near the centre rupturing first. A clear region in the middle of Figure 3.13 shows no particles.

As mentioned in the hardware description, the effects of driving voltage and temperature on resonant frequency are in some part removed from these results by subtracting consecutive scans. The QCM behaviour before binding is assumed to be the same as that of the final scan. This eliminates the requirement to characterise specimen prior to preparation. The term ‘frequency change’ refers to the change in frequency as measured between subsequent scans.

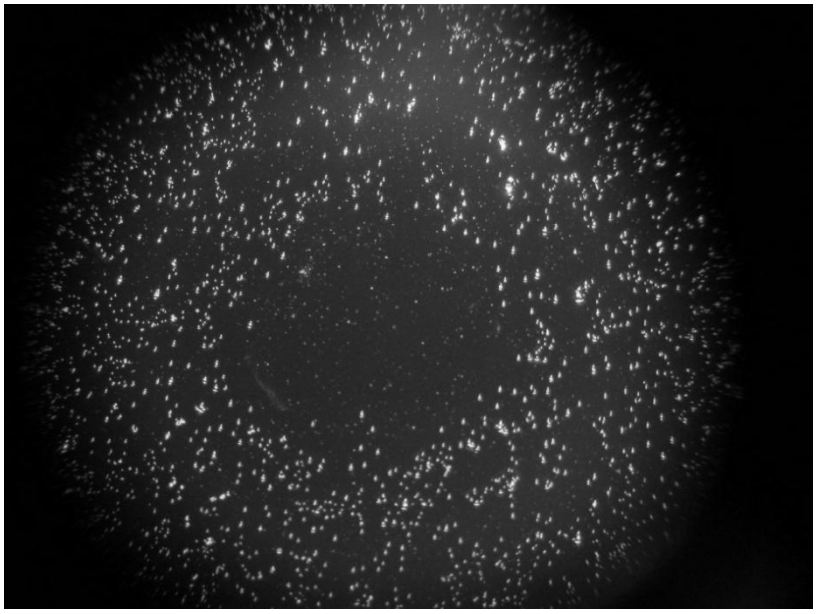

Figure 3.13 QCM image showing particles ruptured from centre

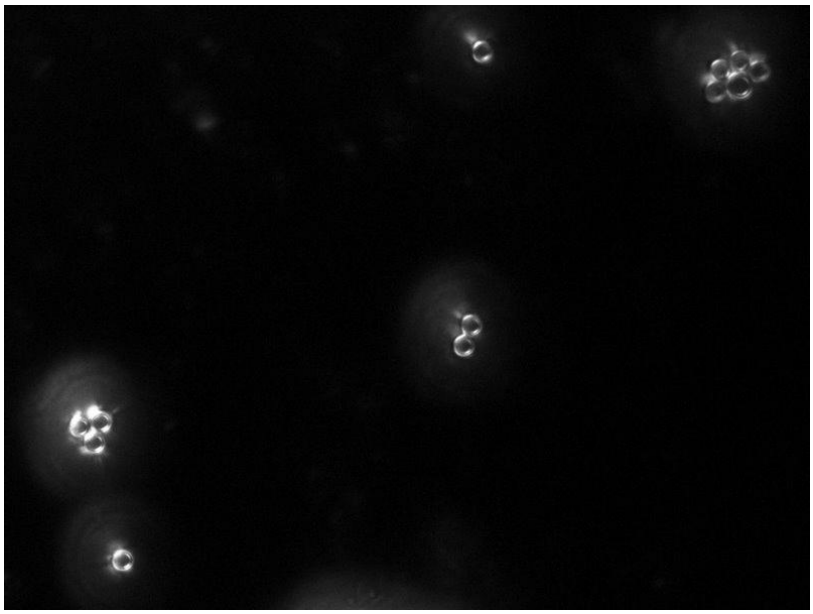

Figure 3.14 Microscope image of physically bound beads showing grouping.

Figure 3.14 shows the grouping of physically bound beads. Figure 3.15 shows results for bond rupture scans of two micron Latex beads. The rupture of physically bound particles is shown (top). This shows the frequency change occurs over a much broader voltage range than the specifically bound particle (bottom). This broadness is attributed to particle grouping and particles gathering around structural features of the substrate. The particles are never anchored and could move freely until gathering around microscopic structures on the gold surface. Physically bound preparations are not rinsed in the same manner as specifically bound particles because the forces would be sufficient to unbind the beads.

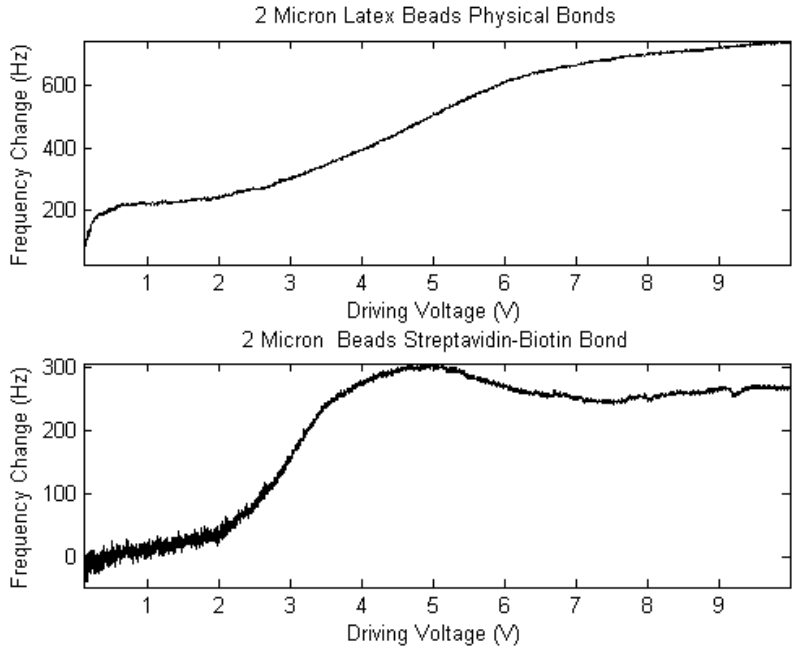

Figure 3.15 Frequency change caused by bond rupture experiment of two micron particles attached by physical bonding (top) and ligand-receptor bonds (bottom)

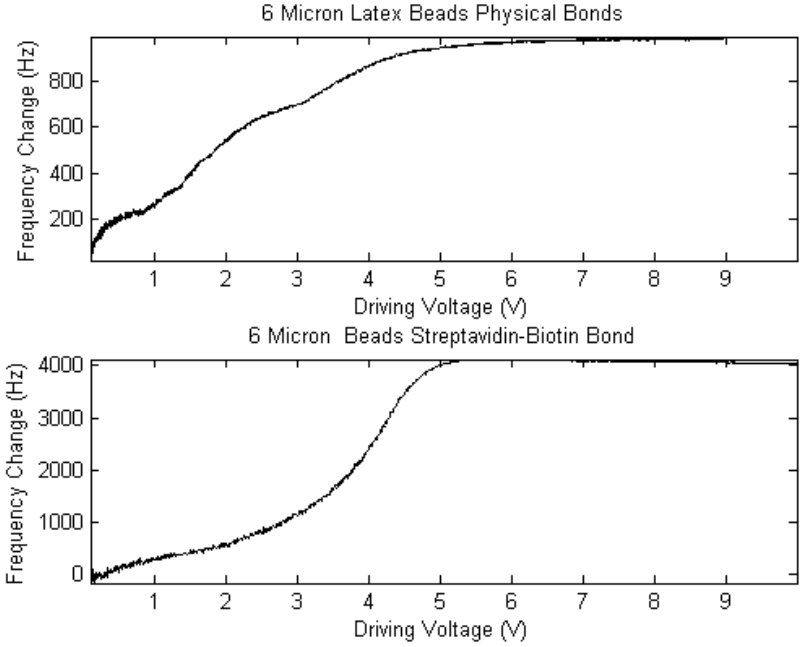

Figure 3.16 Frequency change caused by bond rupture experiment of six micron particles attached by physical bonding (top) and ligand-receptor bonds (bottom)

Figure 3.16 shows the experiment above repeated for larger particles. Again the specifically bound particles show a steeper gradient than the physically bound particles. The plots show that six micron particles rupture at higher voltages than physically bound particles.

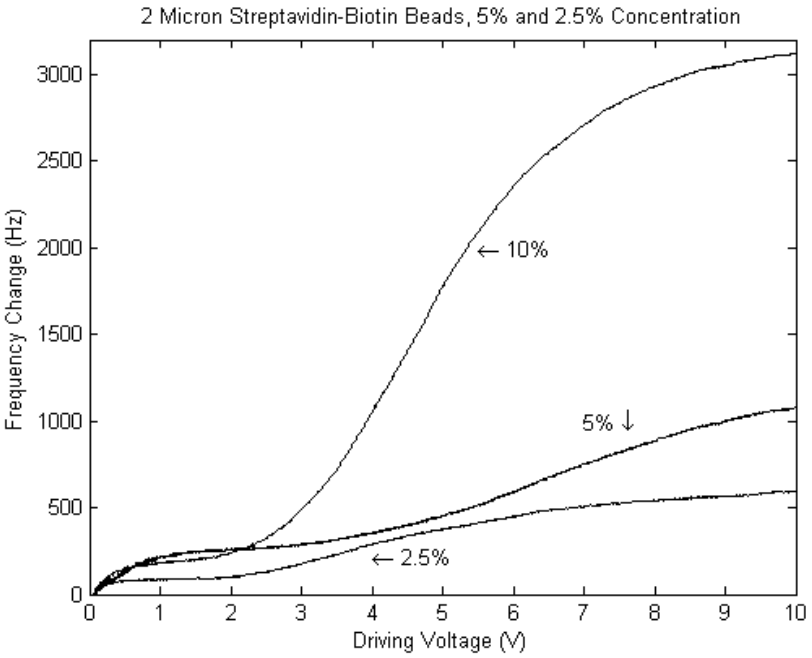

Figure 3.17 Frequency change caused by bond rupture experiment of two micron particles attached by ligand-receptor bonds at various concentrations

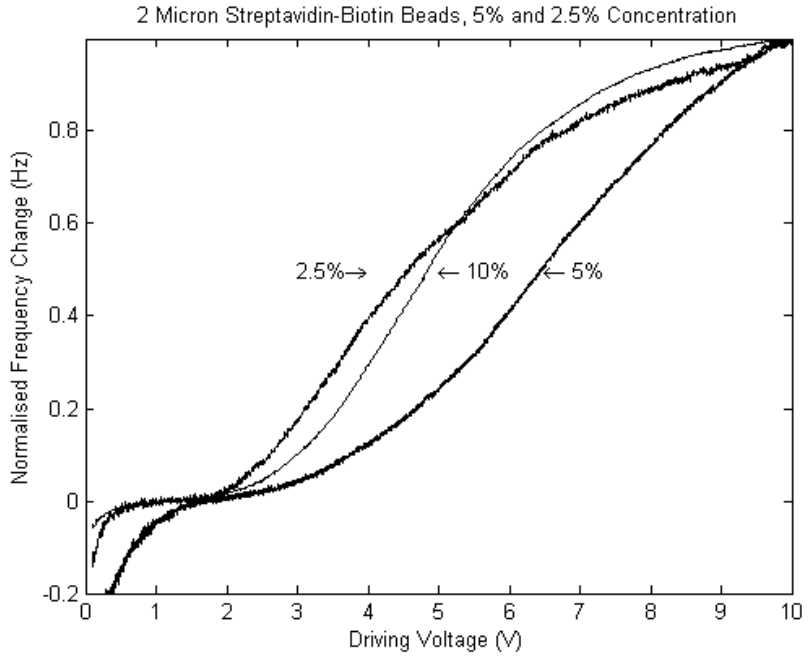

Figure 3.18 Frequency axis has been offset to align the plateau before bond ruptre and normalised to remove the effect of increased mass.

Figure 3.17 shows the effect of varying bead concentration in the preparation stage. For 2-micron beads at concentrations of 10, 5 and 2.5% it is clear that more particles results in more binding.

The results show a higher signal to noise ratio, where signal is frequency change and the noise is the frequency noise, for the 10% concentration. Figure 3.18 shows the results

presented in Figure 3.17 with an offset at the level of the first plateau and normalised by the maximum frequency change. This demonstrates the repeatability of experiments with the same particle.

A high order polynomial is fitted to the frequency change curve, removing the effects of frequency noise. The fitted line is differentiated. This gives a better result than fitting to differentiated data which is very noisy.

Figure 3.19 is interpreted in a similar way to a bond rupture histogram of single bond experiments. The peak in the derivative of the change in frequency corresponds to the location where bonds are most likely to rupture. Figure 3.19 presents a more complicated relationship because the QCM is more sensitive to changes in mass near the centre of the QCM. As the displacement, and hence the force is larger, this area also ruptures at a lower voltage. At higher voltages more particles must rupture to induce the same rate of change of frequency.

The results are useful measure in comparing frequency change curves, and it is evident that the peaks for 10 and 2.5% concentration are very similar but there are still repeatability problems.

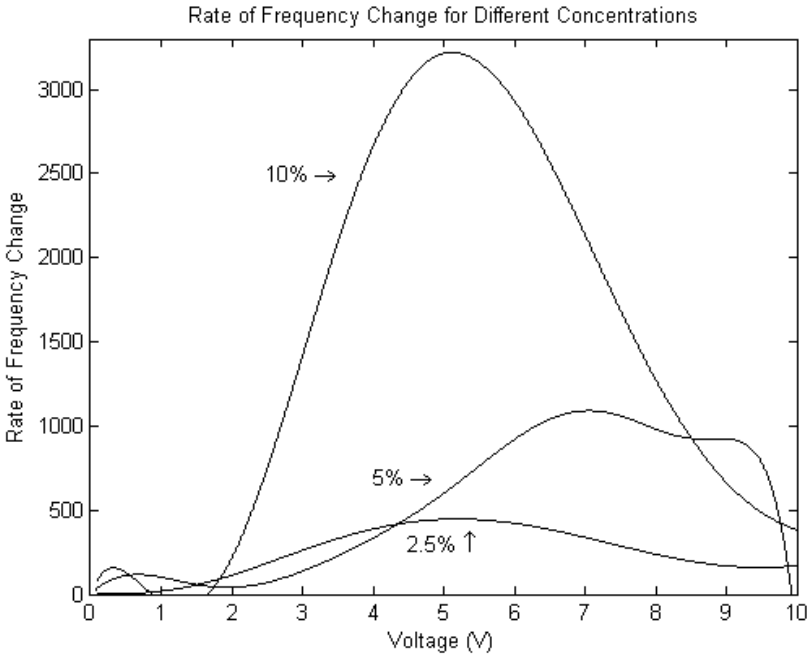

Figure 3.19 Rate of frequency change caused by bond rupture experiment of two micron particles attached by ligand-receptor bonds at various concentrations of target particles in the prepared solution. The lines are found by differentiating high order polynomials fitted to Figure 3.17

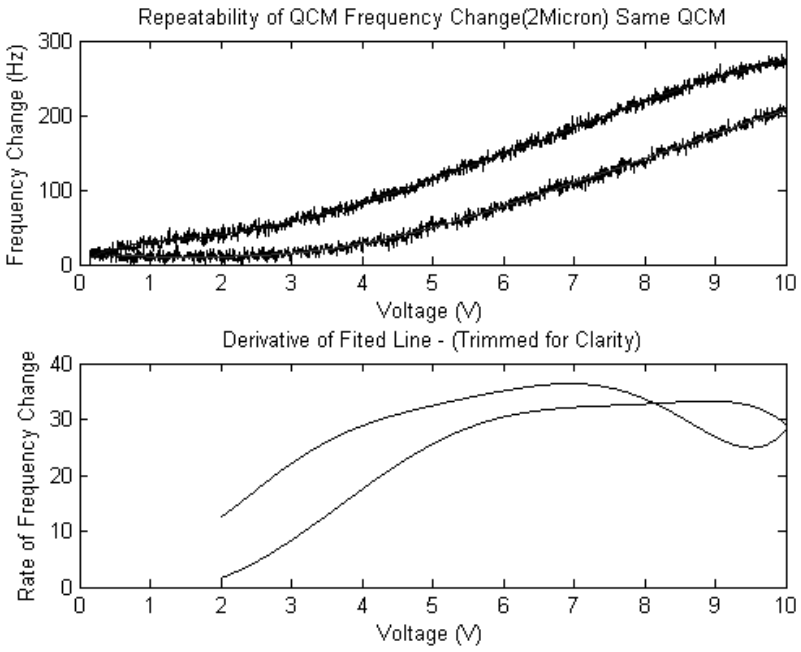

Figure 3.20 Two experiments conducted on the same QCM preparation, early drift in the second scan is indicative of weaker bonds forming with the already used sensor.

Figure 3.20 shows the effect of repeated binding of particles on a QCM that has already been used in a bond rupture experiment. The results are not evidence of receptor degradation. For each successive experiment more particles bound but the rupture occurred at a lower voltage. This indicates that the strength of binding of the particles is reduced and that more particles are binding in ways other than the target receptor-ligand interaction. Repeated use of QCM is avoided as it introduces further variation.

Figure 3.21 demonstrates the variation that is evident for the same experiment repeated on several QCM. The variation is attributed to differences between the QCM, notably the quality factor.

There is likely to be differences in the binding of the beads. This may be a function of the quality of bonds, the density of the bonds or any number of factors. The binding of particles is a random event and consistent results are difficult. Figure 3.22 shows the same experiment using 4-micron beads.

Figure 3.23 shows frequency change results for three different rates of voltage increase with time. The results indicate that it is feasible to concentrate bond rupture scans into a shorter time. This is desirable in order to concentrate bond rupture events.

The same results plotted with voltage on the x-axis indicate that the different rates share similar forces. The faster scans rupture at lower voltages than the slow scan, however the difference is negligible compared with the QCM variation described earlier.

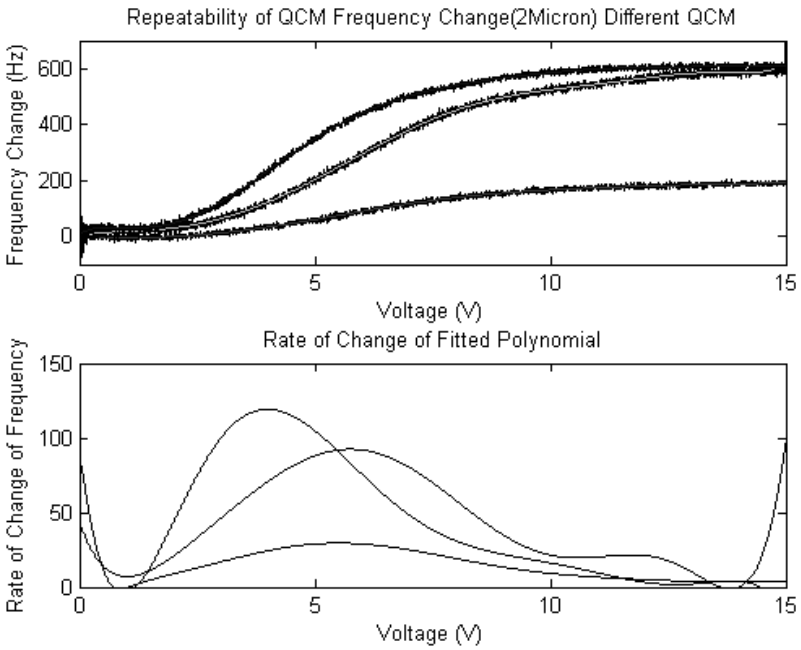

Figure 3.21 Two micron receptor-ligand bond rupture experiment repeated on different QCM shows large variation in frequency change (top) and the location of peaks in the rate of frequency change (bottom)

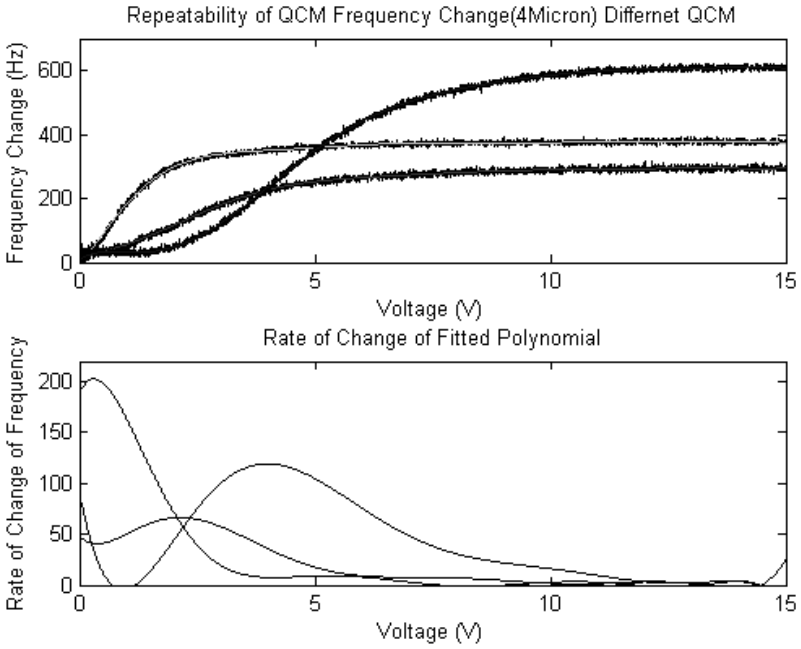

Figure 3.22 Four micron receptor-ligand bond rupture experiment repeated on different QCM shows large variation in frequency change (top) and the location of peaks in the rate of frequency change (bottom)

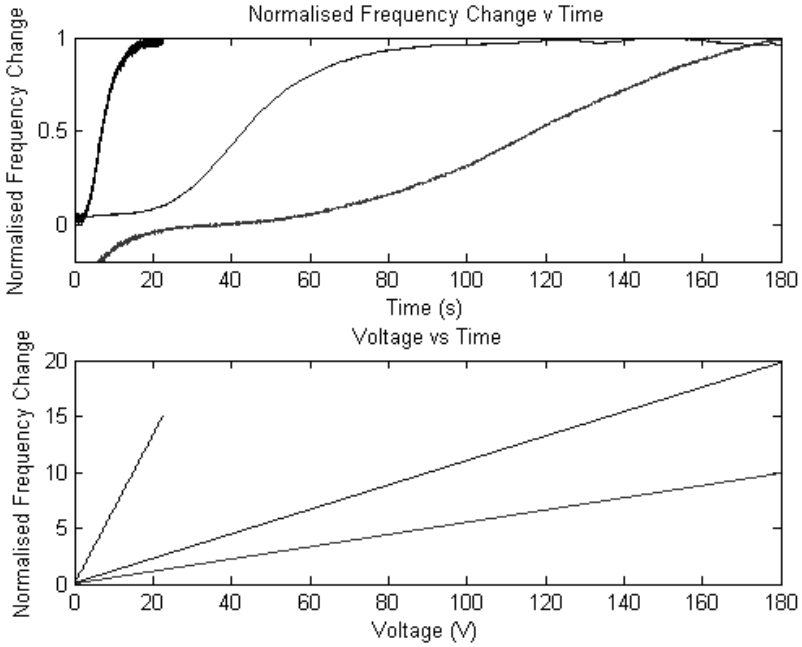

Figure 3.23 Two micron receptor-ligand bond rupture experiment repeated at different scan rates. Normalised frequency change (top) and voltage plotted against time (bottom)

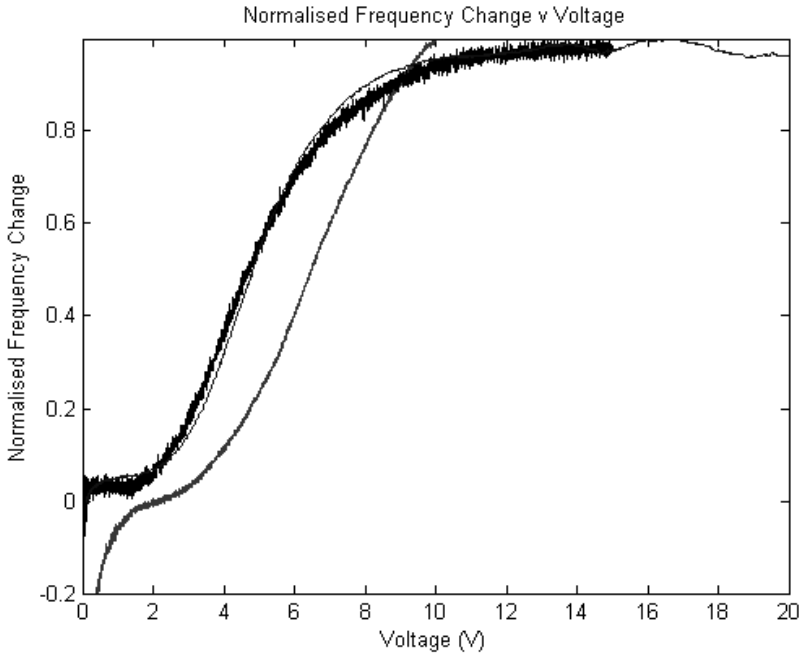

Figure 3.24 Two micron receptor-ligand bond rupture experiment repeated at different scan rates. Normalised frequency change plotted against voltage.

Figure 3.25 shows results typical of attempts to rupture particles smaller than two micron. In air it is difficult to generate force on such a small mass. The inertial forces and viscous drag is minimal. Viscous drag is increased in aqueous solution and some rupture is evident. The frequency data presented in Figure 3.25 is averaged by a moving mean window. This is necessary because the reduction in QCM quality in aqueous solution affects the accuracy of

the QCM frequency measurement. Frequency tracking is adversely affected by the reduced Q in liquid.

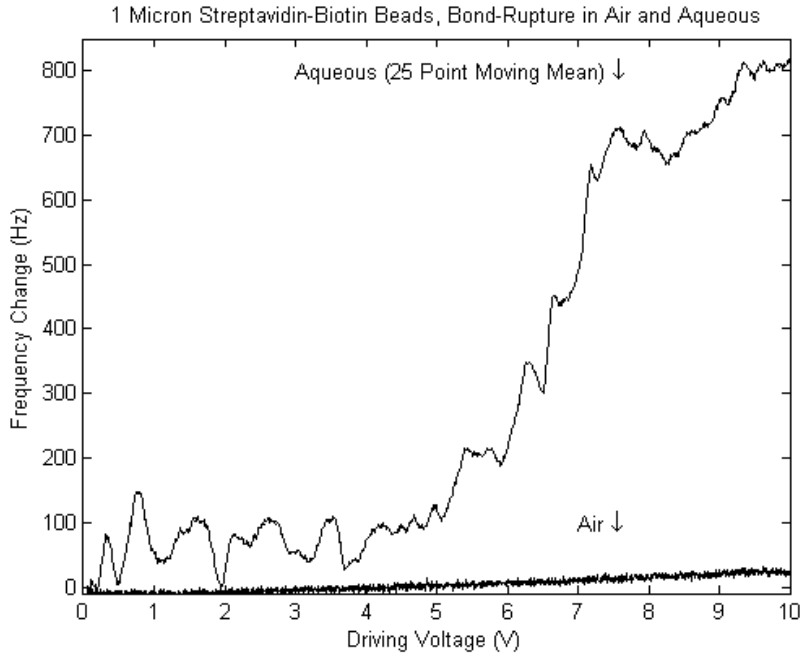

Figure 3.25 One micron receptor-ligand bond rupture experiment in ambient nitrogen atmosphere and aqueous environment.

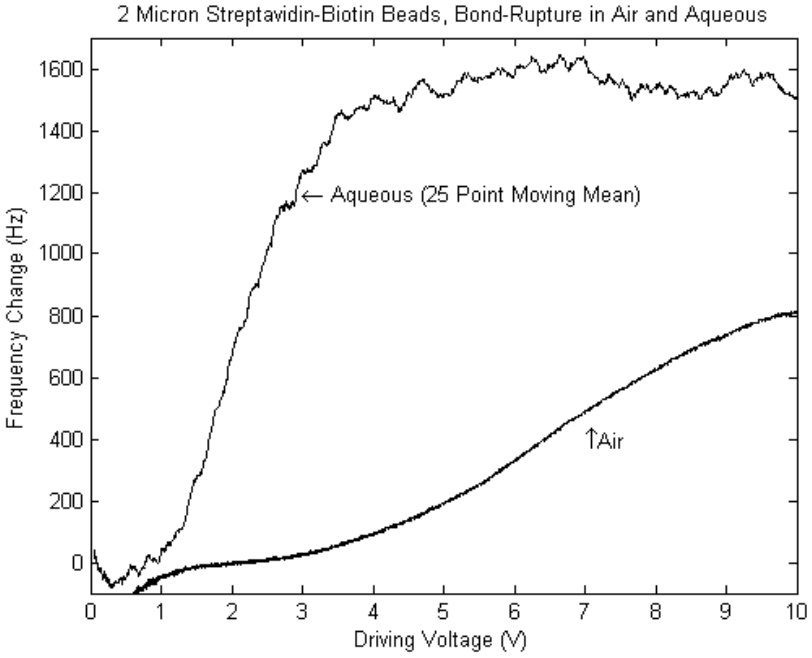

Figure 3.26 One micron receptor-ligand bond rupture experiment repeated in ambient nitrogen atmosphere and aqueous environment. Rupture occurs at lower voltage in ambient air. Aqueous results averaged by 25-point moving mean.

Figure 3.26 is evidence that if the size of the particle is increased to two micron, that the aqueous environment is exerting a greater force than in air or reducing the binding force.

To this point, all the results shown are from solutions of uniform beads. Bead strength varies slightly between beads and some are likely to be physically bound. The experiments that follow use solutions of 20x diluted 4um beads, 40x diluted 2um beads and 200x diluted 0.8um beads. Figure 3.27 shows the resulting distribution of beads on the surface.

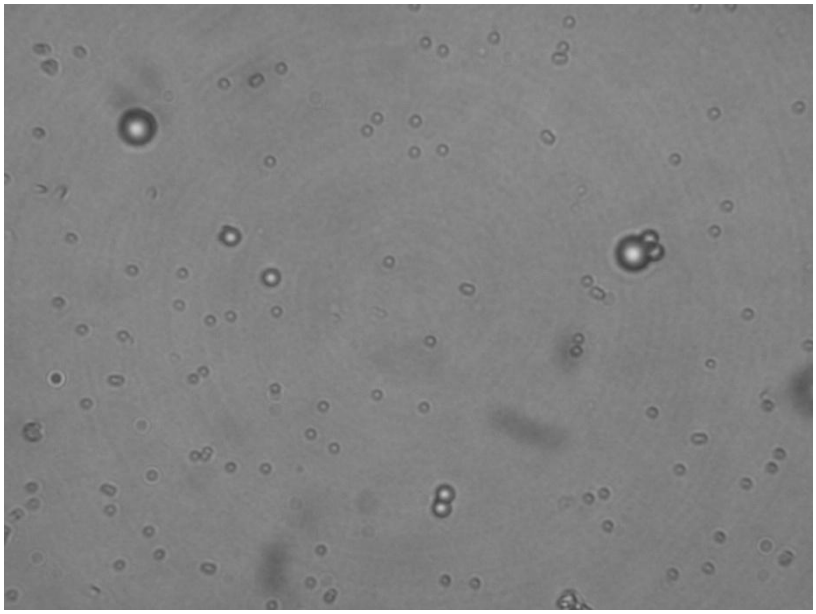

Figure 3.27 Fifty times magnified image of QCM surface showing distribution of particles

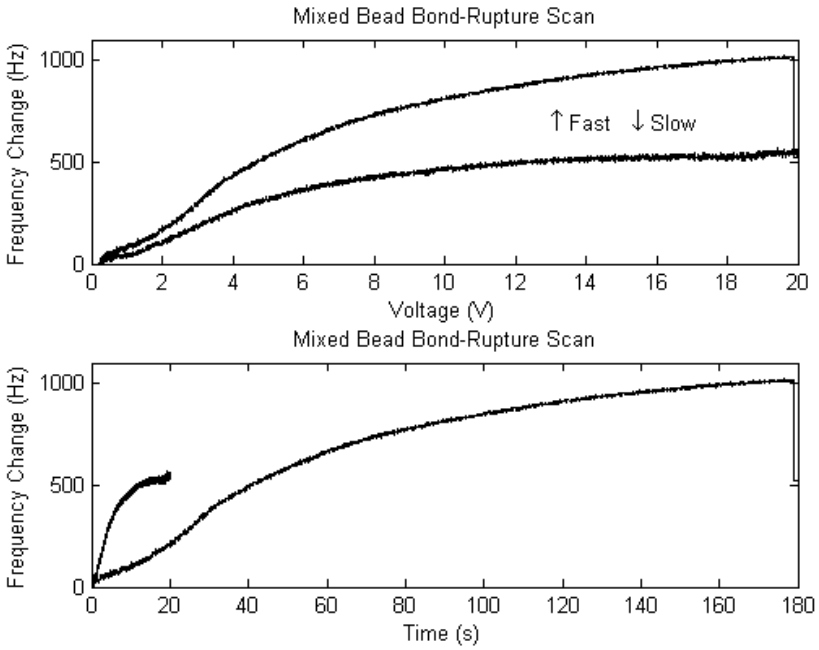

Figure 3.28 Bond rupture scans of mixed beads at two different scan rates. The frequency change is plotted against voltage (top) and time (bottom)

When the scan is repeated with a drop of water added to the device still more rupture occurs. This is consistent with the one micron particle results.

3.7 Frequency Change Shape

The bond rupture frequency change has a consistent shape distribution. The derivative of the frequency change resembles the normal distribution.

Figure 3.29 and Figure 3.30 are a constant voltage scan of 8V over 20 seconds. The frequency change curve is not slow to start as is the case for normal scan results. The transient effects at the beginning of the scan, thought to be a combination of weak bonds and 'warming up' are concentrated into the first few samples of the experiment.

The results shown in Figure 3.29 are re-presented in Figure 3.30, offset by a frequency and, normalised and then inverted. When plotted against an exponential curve the similarity to exponential decay is evident. Figure 3.31 demonstrates, using the Matlab normplot function, the frequency change results from a constant voltage experiment deviates from the form of the cumulative normal distribution.

This is markedly different to the result of the same function applied to a linear voltage bond rupture scan (Figure 3.32) which shows that the rate of frequency change during a bond rupture scan is close to normal. The differentiated data is very noisy but still appears to be a good relation to the normal distribution.

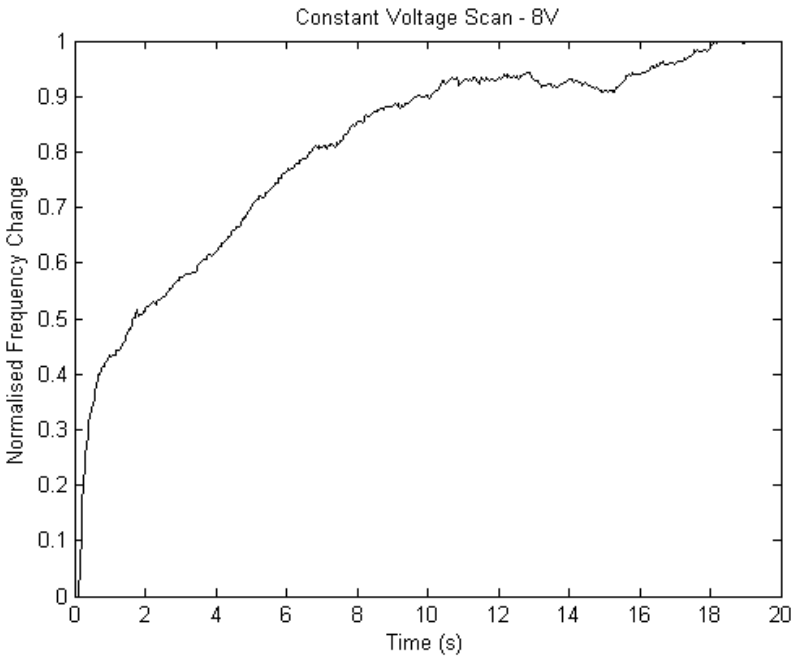

Figure 3.29 Normalised frequency change results for constant voltage scan

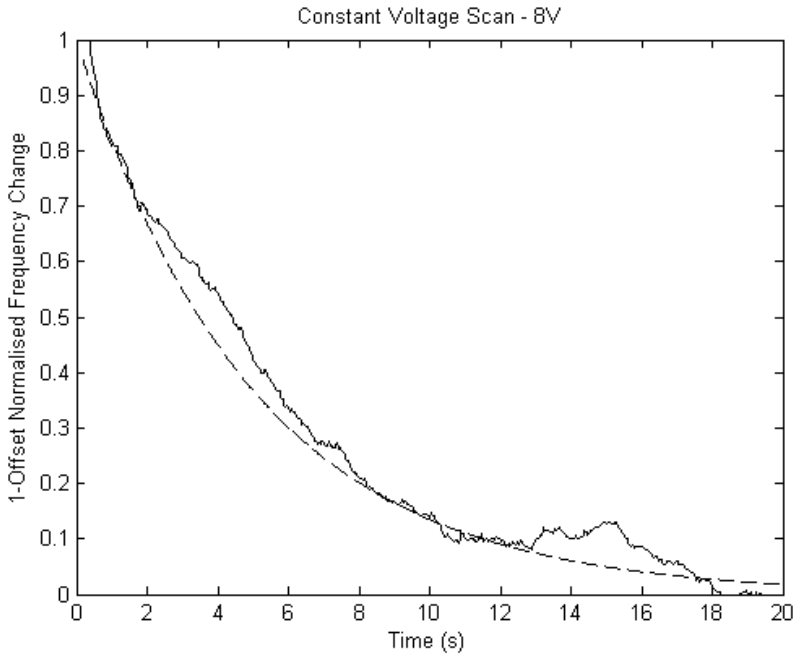

Figure 3.30 Normalised frequency change results for constant voltage scan showing exponential nature of bond rupture.

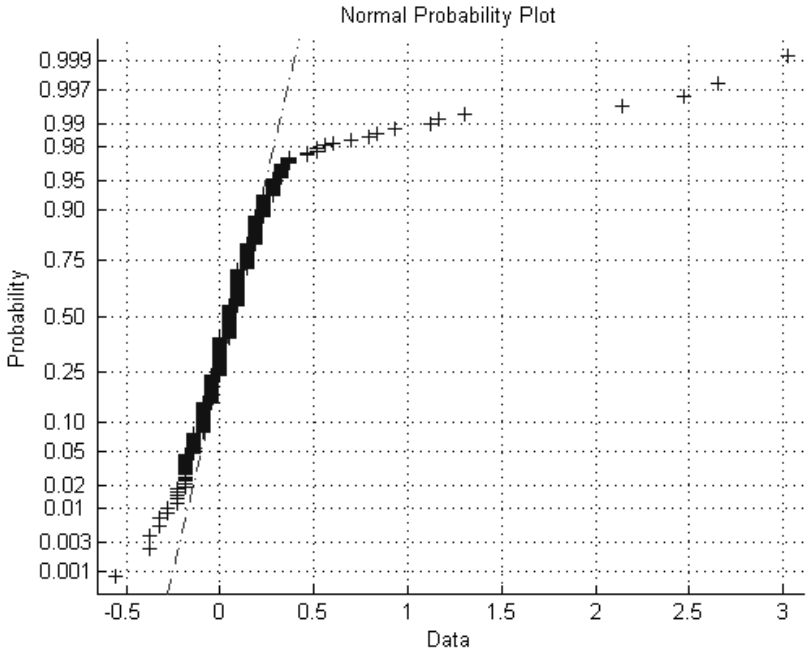

Figure 3.31 Result of the Matlab normplot function of the numerical derivative of bond rupture frequency change results

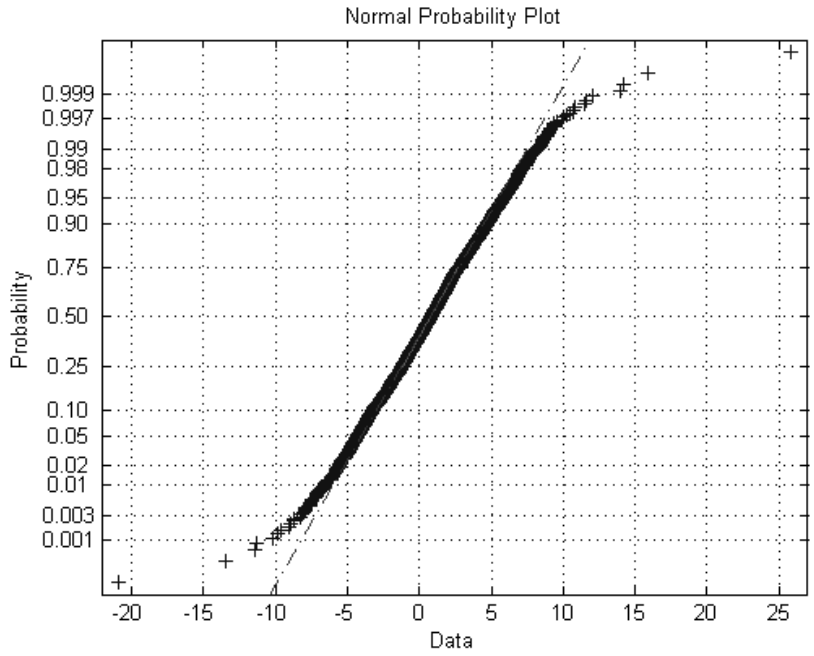

Figure 3.32 Result of the Matlab normplot function of the numerical derivative of bond rupture frequency change results

3.8 Bond Rupture Signal of Interest

Detection of the small signal of interest, as well as the frequency change, is desirable, but the hardware has not produced results. The reasons for this are twofold and not solely attributable to the hardware design. There are short falls in parts of the hardware that cannot be overcome without a significant re-design and advanced understanding of the bond rupture process. Further, there are weaknesses in the methodology; there are several settings that need to be manipulated and several tradeoffs in different areas of performance.

It is perhaps insufficient understanding of the mechanisms of bond rupture that has made the 'noise of bond rupture' to be so elusive. This gap in knowledge changed the direction of this work.

In recent years, several individuals have undertaken many experiments at different times with all versions of the bond rupture hardware and software. The results have been inconclusive and at best unrepeatable. These are not discussed here in detail.

One hypothesis is that the rupture of the particle generates an acoustic signal, perhaps a short time burst of white noise. The QCM converts this acoustic signal to an electrical signal. The number of events and the strength of the generated signal are unknown.

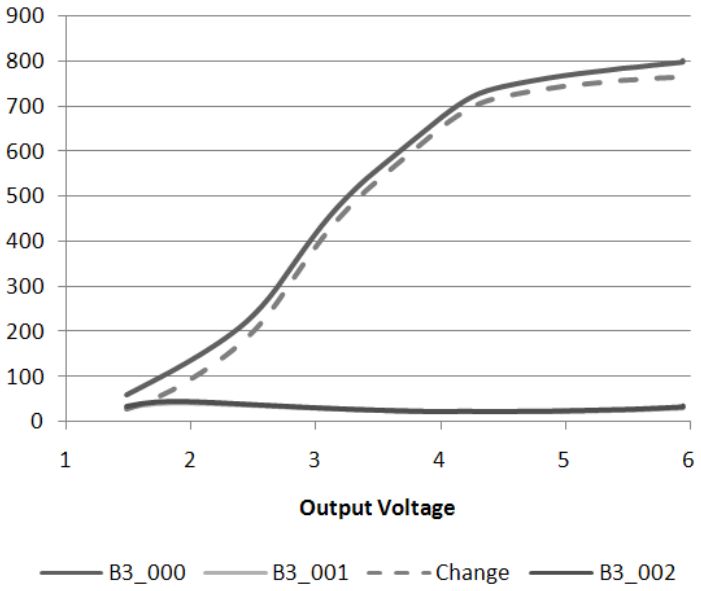

Figure 3.33 Frequency change data confirms bond rupture has occurred

The QCM filters the wide bandwidth signal and the components at the QCM resonances are not filtered. Of all the places to 'listen' for the bond rupture noise, the first harmonic unsuitable because the driving signal is located within this band.

The third harmonic, $3f + \Delta f$, is split into two components $3f$ and Δf. f shifts during the scan because of lost mass, and Δf also changes during the scan as a function of mass and voltage. The bond rupture hardware facilitates tracking of the resonant frequency but the listening frequency is fixed.

If the third harmonic is moving then the listening bandwidth must be wide enough so that the signal does not move out of band. Wide band monitoring severely restricts the scan time on the current hardware. In an attempt to isolate the noise several experiments were undertaken at very short duration. The voltage was scanned from 1 to 6V in a time of 1.3s. A 100kHz Bandwidth is monitored. The centre of the listening band is located at $3f + \Delta f/2$, half way between the third overtone and the third harmonic. These experiments were conducted using 10.7MHz QCM.

Frequency change from the experiment confirms that bond rupture has occurred. Analysis of the detected signal near the third harmonic is shown in Figure 3.34. The short time Fourier transforms show little difference between the first and final scans. The dominating signal is the third overtone, an artefact of the driving signal. The shift in the overtone caused by mass loss is evident. There is by far too much data to see the result clearly and some statistical analysis may be beneficial.

Figure 3.35 shows the short time Fourier transform near the overtone. The overtone magnitude is reduced by windowing in the plot generation and can be seen shifting at the top

First Run Final Run

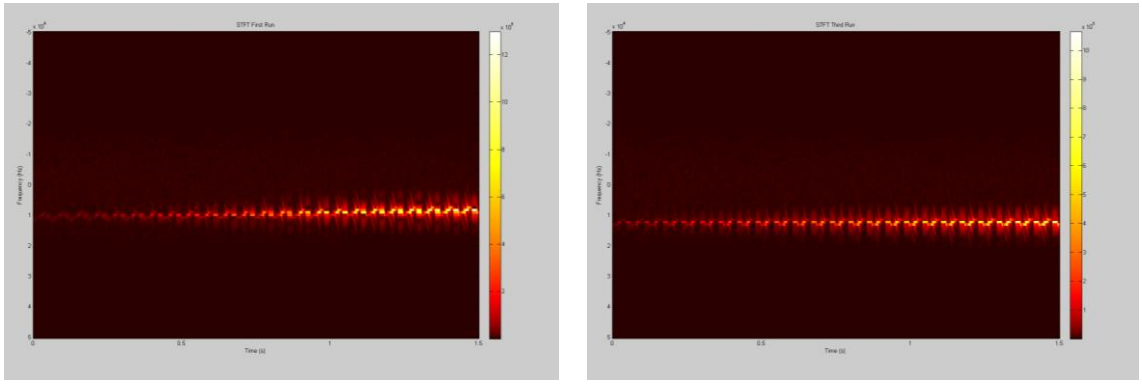

Figure 3.34 Comparing the STFT of first and final bond rupture scans

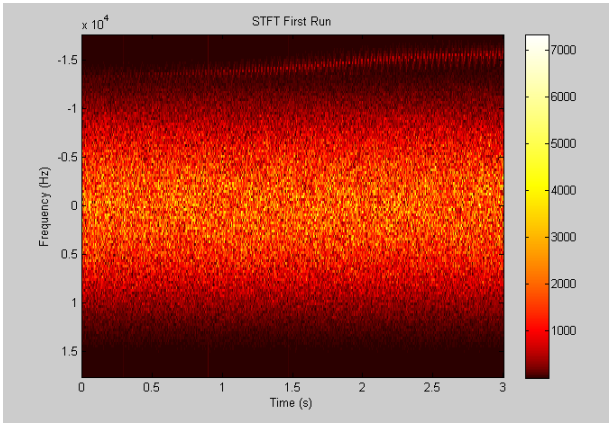

Figure 3.35 STFT showing overtone moving at the top of the plot.

of the plot. Bond rupture is confirmed but it is not evident in the wide band signal. This could be because the amplitude is too low to be detected, below the noise floor, or principally located outside this band. The signal may be buried beneath artefacts of the discontinuous driving signal. The QCM uses a single electrode effectively shorting the whole area beneath it. The noise that is sought is generated locally on the QCM, but the electrode itself is connected to a larger area.

3.9 Chapter Conclusion

Some elements of the bond rupture hardware were developed as part of this dissertation. The results presented in this chapter are evidence that the developed hardware is functional and versatile but a little limited. Importantly the current hardware provides a platform from which bond rupture could be explored.

Impedance matching in air and water is implemented using a wideband transformer match. Alternatives include active impedance matching or a circuit tuned to each QCM before the experiment. The end user of the hardware encouraged a one-size-fits-all approach and the result is an approximate impedance match.

From the bond rupture experiments, it is evident that there is some problem with the repeatability of the frequency change curves. Despite very little variation in particle size and bonding methodology there is considerable variation between experiments.

Variation between transducers and experiments means that the voltage applied does not strictly relate to amplitude. There is no clear dependable relation between voltage, power, and displacement amplitude. A voltage of one volt applied to two different QCM will generate surface oscillations of different amplitudes. If the hardware could measure input power, instead of an open loop voltage setting, then some of the uncertainty would be removed. A constant current source has been identified as a possibility to circumvent some of the variation, most notably the impedance matching. This would require a different class of input amplifier.

Surface oscillations could have different shapes. Perhaps the oscillations on some QCM tend to be elliptical and some straight. Perhaps some QCM exhibit subtle surface normal displacements and others do not. The results presented in this chapter show clear variations in QCM impedance that could affect power transfer.

The driving signal is periodically swept through frequencies near resonance creating dither in the driving signal that permeates through all harmonics. Discontinuities in the driving signal could be having an indeterminable effect on the bond rupture dynamics and noise detection.

It is demonstrated that QCM temperature at the electrode surface can reach very high temperatures. This may have the effect of increasing energy in the bonds and changing rupture kinetics. This is a drawback of the sensitive area of the transducer coinciding with the input excitation of the transducer. In most frequency change experiments we see a transient effect in the low voltages. This may result from the QCM warming and driving away surface moisture.

Further to variations between devices, the QCM amplitude and frequency sensitivities are functions of the position on the electrode. There are in effect different forces acting on every particle. This is one of the core weaknesses with the QCM technique and will be discussed further in later chapters.

Experiments were conducted to determine the effect of a number of key bond rupture experiment parameters. Despite the apparent variation in the frequency changes there is a clear and dependable form that the results take.

The force on the bonds is a function of mass, and mass is proportional to the radius cubed. The binding force is a function of the contact area, which must increase proportional to the radius squared. This leads to the assumption that as a function of particle size, the force

removing the particle increases faster than the force holding it on. The results presented in this chapter indicate that in air, a one-micron particle binds too strongly to rupture at forces the QCM is are able to exert. This is of some concern considering the relative size of biological targets such as virus can be smaller than this.

It is demonstrated that some particles that cannot be ruptured in air can be removed in water. It is not known if this is a result of increased driving force or decreased binding force in aqueous environments. If the former is true, the rupture force increases despite a reduction in Q and hence amplitude and the viscous loading are considered very important. Large particles are difficult to bond to the surface, this is possibly a result of the natural unbinding forces experienced during QCM preparation, rinsing for example, exceeding the binding forces. From the experiments described in this chapter and other work, the two-micron beads were identified as the best phantom particle as they are easily attached and ruptured.

Scan rate is an influential parameter. The rate of increase in drive level also affects the resonant frequency due to strains caused by the temperature gradient. Having identified that the normalised frequency change is largely independent of the scan time it is concluded that short scans are a valid means to concentrate bond rupture events in time and increase the chance of bond rupture noise detection.

Bond rupture experiments were conducted using a mixture of beads. There is much variation in the frequency change caused by same-sized bead rupture. This same variation appears to manifest in this experiment and the transition from small bead rupture to large is indiscernible. Experiments indicate that it is difficult to discern the difference in bond strengths.

To facilitate further improvements to devices and experiment methodology and to better interpret bond rupture results an improved understanding of bond rupture is required. This requires further understanding of the effect of shaking amplitude, frequency, direction and all aspects of the particle and the surrounding media.

This chapter also exposes a number of problems with the QCM as a platform for this technology. If a custom transducer can be developed a few key characteristics have been identified. To this end the next section reviews relevant literature for the determination of force on a particle attached to QCM. A model is developed to describe and quantify the relevant variables. This model will provide the basis for investigation of other methodologies and transducers.

4. SINGLE PARTICLE BOND RUPTURE MODEL

4.1 Introduction

In this chapter, the force experienced by the receptor-ligand bonds holding the particle to an oscillating surface is simulated and, in turn, the predicted force is used to model the rupture of bonds. The force experienced by receptor-ligand pairs is a complex function of the particle properties, location, and base excitation. As in the experiments presented in Chapter 3, the core focus of this model is the polystyrene-latex microsphere phantom target. In the coming sections, the nature of the phantom particles is discussed as relevant to the modelling of particle rupture. Where appropriate models of adhesion are reviewed and employed. Further, models are developed to address the key question of this chapter – what is the force experienced by the receptor-ligand bonds between the particle and substrate during a bond rupture experiment?

The effects of several key variables are explored, these are the particle size, bond density, and the amplitude and frequency of the base excitation. In the sections that follow models for the force on the particle are discussed. An evolution of several models is presented culminating in a final solution which represents the probability of survival of the bonds to a single particle. The results of this chapter are used in Chapter 5 to model bond rupture devices.

4.2 Existing Model

Cooper's force model (Cooper, 2003) is the only model that has been applied to the analysis of bond rupture results. The force, negating the effects of viscous drag, is

$$F = {}^{2}/_{7}\, mA(2\pi f)^2. \tag{4.1}$$

where m is the particle mass, A is the oscillation amplitude and f is the oscillation frequency. The force is derived from the relationship between force, mass and acceleration. The factor $2/7$ arises from the relationship between the acceleration of the point of attachment between the particle and substrate and the acceleration of the particle centre of mass. The centre of mass moves less than the surface. For a two micron diameter polystyrene latex bead the centre of a QCM operating at 1V in air, the force approximated by Cooper's equation is $230nN$. This force depends on the maximal amplitude of the displacement. Unless the path of the attachment point is circular then the instantaneous force will be oscillating between some maxima and minima. Borovsky et al. (2000) demonstrate that the path of a point on the QCM is linear.

A simple physical interpretation of the force on the particle in that the particle is moving and this motion must have arisen from the shaking of the substrate. The force is applied to the particle through the bonds. This is only the case if there are no other forces acting on the particle.

Inclusion of viscous forces adds additional drag that increases the force on the bond, however the same viscous effects act to reduce QCM displacement amplitude. Experiment results indicate that viscous forces makes possible the rupture of particles that otherwise could not be removed in air. It is concluded that viscous forces should be incorporated into developed models.

4.3 Point Interaction Mechanical Model

The first iteration of the force model presented in this chapter is developed using the software package Simulink. An inverted pendulum is simulated using classical mechanical methods. The particle is considered a point mass attached at the end of a mass less link. The volume is only considered when determining the cross sectional area for determination of the viscous drag. The link length is the particle radius. The link is attached to the substrate by a spring joint which holds the pendulum upright in the absence of base excitation. The link, consistent with a rigid particle, does not deform. Attachment to the surface is absolute and the attachment point follows the surface exactly. The centre of mass of the particle is free to move.

For the purpose of this model the length of the bond between the particle and substrate is much less than the radius of the bead, and sufficiently uniform and rigid that it follows the motion of the QCM surface exactly. The position of the centre of mass is defined by two angles, θ_1 and θ_2. All external forces are applied through the bead centre of mass and result in no moments about the centre of mass.

This model is an advance on the previous model as it permits the inclusion of additional forces and truly simulates the path of the particle allowing the force exerted on the particle to be determined. Principles of relative motion simplify analysis. A moving substrate and stationary fluid is replaced with a stationary substrate and moving fluid by inversion and substitution of force vectors. Figure 4.1 (a) shows the real geometry, where the substrate moves in three dimensions and the fluid remains stationary. In this configuration there is force on all three axes. These forces act through the centre of mass. For simulation of the joint it is assumed that the base of the pivot is stationary. Relative to the stationary pivot, everything else is moving.

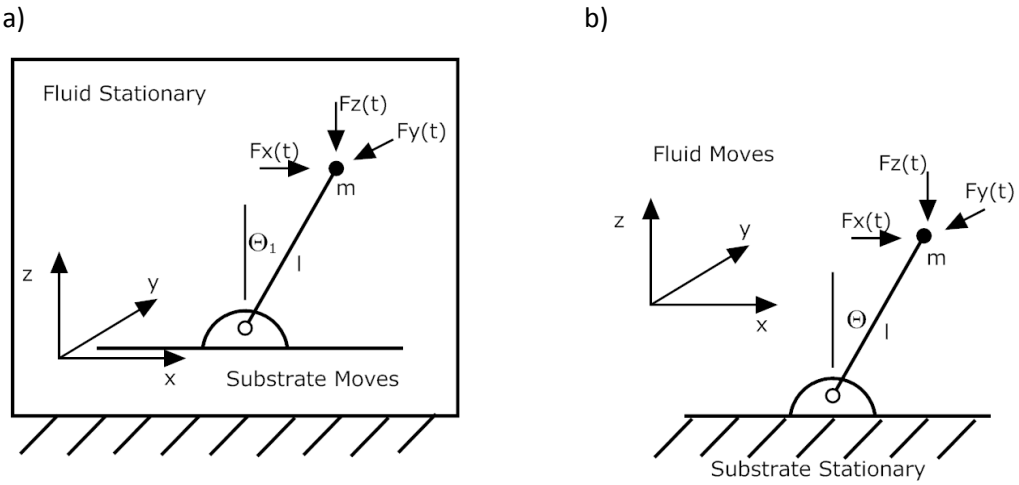

Figure 4.1 Three dimensional forces acting on a two degree of freedom joint. Moving substrate (a), and moving fluid (b)

The forces causing the moment on the joint are defined as follows.

$$F = ma \tag{4.2}$$

$$a = R\alpha = R\ddot{\theta} \tag{4.3}$$

$$\tau = FR = maR = mR^2\ddot{\theta} \tag{4.4}$$

The product of the spring constant, k, and angular displacement, θ, gives resistance from spring joint as follows

$$M(\theta) = -k\theta \tag{4.5}$$

The resistance to fluid motion is determined from the relative velocity of the mass and the fluid.

$$F_d = -\frac{1}{2}\rho v^2 A C_d \hat{v} \tag{4.6}$$

where F_d is the force of drag, ρ is the density of the fluid, v is the speed of the object relative to the fluid, A is the reference area, C_d is the drag coefficient, and $\hat{v}$ is the unit vector indicating the direction of the velocity.

The reference area A, is related to, but not exactly equal to the area of the projection of the object on a plane perpendicular to the direction of motion. Different reference areas are given for the same object in which case a drag coefficient corresponding to different areas is provided. Integration of the torques on the joint and division by the inertia gives the angular acceleration of the joint at each axis. The acceleration is twice integrated to determine the angle of each pivot.

Figure 4.2 shows the three dimensional representation of the system with very small angular movements. The vertical line in the figure joins the attachment point to the particle centre of mass. The horizontal lines show the path of the point of attachment and centre of mass. This means that the particle mass is tracking the substrate movement closely.

The product of acceleration and mass along each axis give three force vectors. The force along the axis of motion is greatest. Figure 4.3 shows the peak force of the sinusoid, estimated at $3n$N. For the same particle Cooper's equation predicts $0.83\ n$N. This difference is matched by the $2/7$ factor where Cooper's force assumes that the particle centre of mass moves less than the surface. The spring constant of the joint is difficult to determine intuitively and accounts for the discrepancy between the two models.

This model incorporates viscous interaction but treats the particle as a point mass and

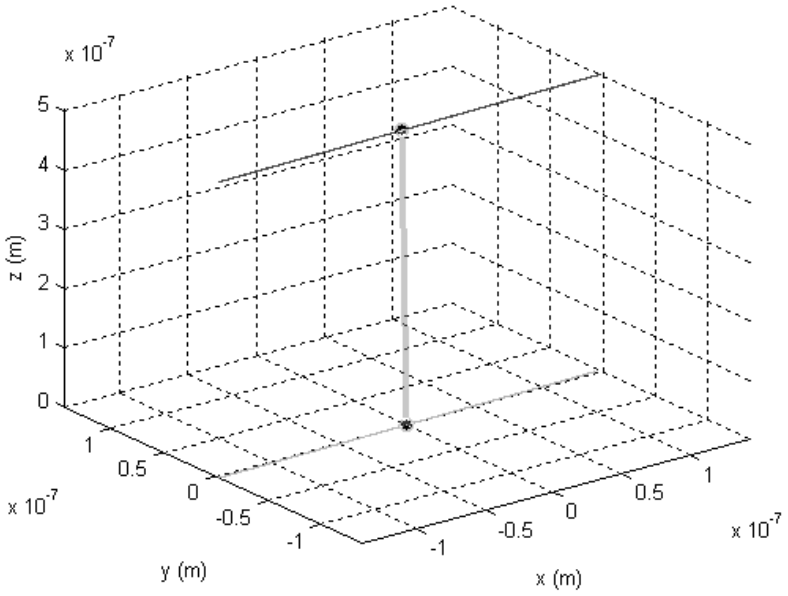

Figure 4.2 Three dimensional path of the system shows only very small angular deviations

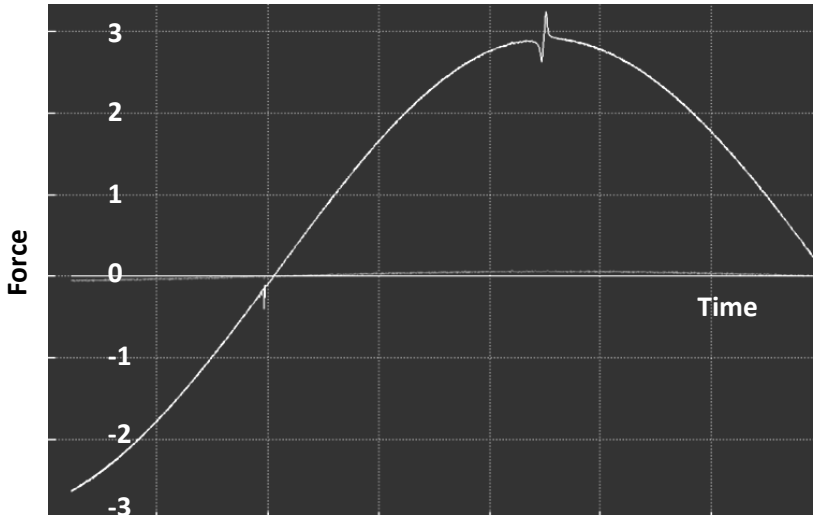

Figure 4.3 Simulated force

does not include sufficient information about the bonds for determination of the force experienced by individual bonds. This model consists of just two degrees of freedom, the angular rotations about the pivot and more are needed to completely describe the forces on each bond.

Additionally the model has no receptor-ligand bonds and there is no accounting for the forces that these bonds exert on the particle, or for the influence of other binding forces. For further development of a mechanical model, this inverted pendulum analogy is too simplistic. The following sections review literature that is relevant to the adhesive forces of particles in the absence of binding, an understanding of this is an important in addressing the weaknesses of this model.

4.4 Particle Adhesion

In this section the body of knowledge about the physical adhesion of particles is briefly reviewed and the adhesive force of physically bound latex beads is evaluated. The adhesion of elastic particles is broadly covered by a number of papers (Derjaguin et al., 1975, Johnson and Greenwood, 1997, Johnson et al., 1971, Maugis, 1992). Figure 4.4 shows the geometry of the contact of elastic spheres. Elastic deformation causes a region of intimate contact, radius a_0 , and adhesive forces that extend to radius, a_1. There is deformation in the spheres which results in a normal displacement, δ, of the centre of mass.

Since Tabor (1977), adhesion is viewed as a continuum between two theories. On one extreme is large compliant spheres represented by the Johnson Kendal Roberts (JKR) model (Johnson et al., 1971) and on the other is small stiff spheres represented by the DMT (Derjaguin et al., 1975) model. Figure 4.5 shows a map (Johnson and Greenwood, 1997) where the normalised adhesion force, $\hat{F}$, and a dimensionless scaling parameter, λ, are used to determine which model is applied.

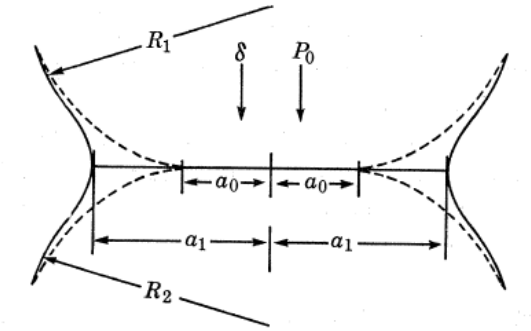

Figure 4.4 The geometry of particle adhesion (Johnson et al., 1971)

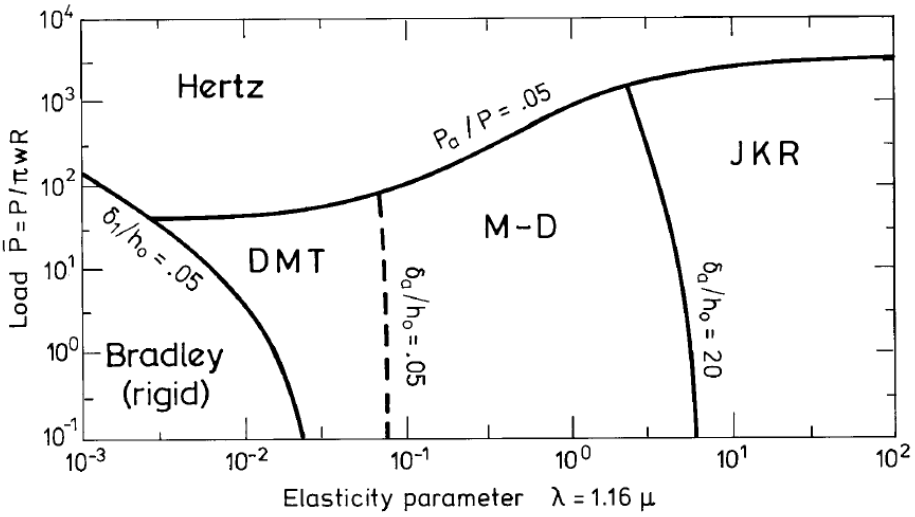

Figure 4.5 Adhesion Map (Johnson and Greenwood, 1997)

The parameters are

$$\lambda \equiv \sigma_0 \sqrt[3]{\frac{9R}{2\pi W_a E^{*2}}} = 1.16\left(\frac{RW_a^2}{E^{*2}z_0^3}\right)^{\frac{1}{3}} \tag{4.7}$$

$$\hat{F} = \frac{F_a}{\pi W_a R} \tag{4.8}$$

$$E^* = \left(\frac{(1-v_1^2)}{E_1} + \frac{(1-v_2^2)}{E_2}\right)^{-1} \tag{4.9}$$

$$R = 1/(1/R_1 + 1/R_2) \tag{4.10}$$

where E^* is the equivalent modulus, R is the reduced radius, $v_{1,2}$ are the Poisson's ratios and $E_{1,2}$ are the shear moduli. $R_{1,2}$ are the radii for the spheres, for a sphere in contact with a plane $R_2 \to \infty$ and $R \to R_2$. The equilibrium separation of the surfaces is z_0, W_a is the work of adhesion, and σ_0 is the maximum force chosen to match the Lennard-Jones potential.

For particles ranging from the latex phantom microsphere to a real bacterium the JKR theory is most applicable. When the techniques derived in later sections are applied to more compliant different target particles it may be pertinent to adjust the model to consider DMT interactions. Hertz adhesion theory is the basis for part of the JKR theory. When there is a sufficiently large compressive contact load the adhesive component may be neglected and Hertz theory is applied exclusively, however in this situation there is no compressive load on the particle. In pure hertz adhesion the work of adhesion is assumed zero. The contact radius, a, is given by the Hertz Equation

$$a = \left(\frac{3RF_L}{4E^*}\right)^{\frac{1}{3}} \tag{4.11}$$

where R is the particle radius, F_L is the external load force and E^* is the effective elastic modulus given by (4.9). The vertical displacement δ of the two bodies is

$$\delta = \frac{a^2}{R} \tag{4.12}$$

4.4.1 JKR

JKR theory holds that a strong adhesive force acts at the equilibrium distance, z_0. At distances larger than z_0 there is no such force, thus the work of adhesion is described by a delta function of area γ. JKR adhesion force consists of two components, the Hertzian component, and the adhesion component. F_H^{JKR} is the effective force introduced into (4.11) to obtain the actual contact radius. At equilibrium the apparent Hertz load is bigger than the applied load F_L

$$F_H^{JKR} = F_L + 3\pi R W_a + \sqrt{6\pi R W_a F_L + (3\pi R W_a)^2} \tag{4.13}$$

where F_L is the external load, R is the particle radius, and W_a is the work of adhesion. The contact radius is derived from the Hertz load

$$a = \left(\frac{3RF_H^{JKR}}{4E^*}\right)^{\frac{1}{3}} \tag{4.14}$$

The vertical displacement δ is related to the load by

$$\delta = \frac{F_L}{2Ea} \tag{4.15}$$

the vertical displacement of the two bodies is

$$\delta = \frac{a^2}{R} - \sqrt{\frac{2\pi W_a a}{E^*}} \tag{4.16}$$

The pressure distribution within the contact region at a distance, r, from the centre is given by

$$p(r) = \frac{2E^* a}{\pi R}\left(1 - \left(\frac{r}{a}\right)^2\right)^{\frac{1}{2}} - \sqrt{\frac{2E^* W_a}{\pi a}}\left(1 - \left(\frac{r}{a}\right)^2\right)^{-\frac{1}{2}} \tag{4.17}$$

The critical force of adhesion is the load force that only just separates the spheres, F_c is given by

$$F_c^{JKR} = \frac{3\pi R W_a}{2} \tag{4.18}$$

According to DMT theory adhesion is considered outside the contact area taking into consideration long range adhesive forces of van der Waals type. DMT-M theory is sometimes called the Hertz-plus-offset model. There are continuing developments in adhesion theory

such as Schwarz, (2003), however for the model presented in this chapter an understanding of the JKR adhesion theory is sufficient.

4.4.2 Work of Adhesion

Dupre originally defined the work of adhesion in 1869. It can be determined from

$$W_A = \gamma_1 + \gamma_2 - \gamma_{12} \tag{4.19}$$

where $\gamma_{1,2}$ are the surface energies of the two solids separately and γ_{12} is the surface energy between the two materials in contact. The surface energy is the adhesion due to London dispersion forces (γ_d) and polar forces (γ_p) such as hydrogen bonding. If there are no polar contributions as is the case in the particle-gold system, then the work of adhesion can be approximated by (Israelachvili, 1985)

$$W_A \approx 2\sqrt{\gamma_1 \gamma_2} \tag{4.20}$$

4.4.3 Moment of Adhesion

In an environment where an external force is exerted on the particle parallel to the solid surface a moment is exerted on the particle. The resistance to the moment arises from the adhesive force F_A at a distance, a. The moment of attachment is

$$M_A = F_A a \tag{4.21}$$

Ziskind et al., (1997) show the relationship between a dimensionless applied force F_a^* and dimensionless contact radius r_a^* such that $F_a^* = F_a/3\pi W_a R$ and $r_a^* = r_a/(3\pi W_a R^2/K)^{\frac{1}{3}}$. At equilibrium, using the equilibrium radius and critical force the calculated moment $F_{ae}^* r_{ae}^* = 0.5 * 1.26 = 0.63$

Suppose a hydrodynamic force applied to the particle is not great enough to detach the particle. The force is, however, sufficient to modify the contact radius. This relation is used to obtain new relations relating the moment to the force and contact radius respectively.

Figure 4.15 shows a maximum of the pull off force for certain values of force and radius. The maximum is 0.42 for JKR model. In other words the maximal force is less than the inceptive motion approach.

The maximum moment derived for the JKR is thus (Ziskind et al., 1997)

$$M_{max}^{JKR} = \frac{2}{3}(F_A^* r_{ae}^*)_{JKR} = 8.36\frac{\sigma^{\frac{4}{3}} a^{\frac{5}{3}}}{\kappa^{\frac{1}{3}}} \tag{4.22}$$

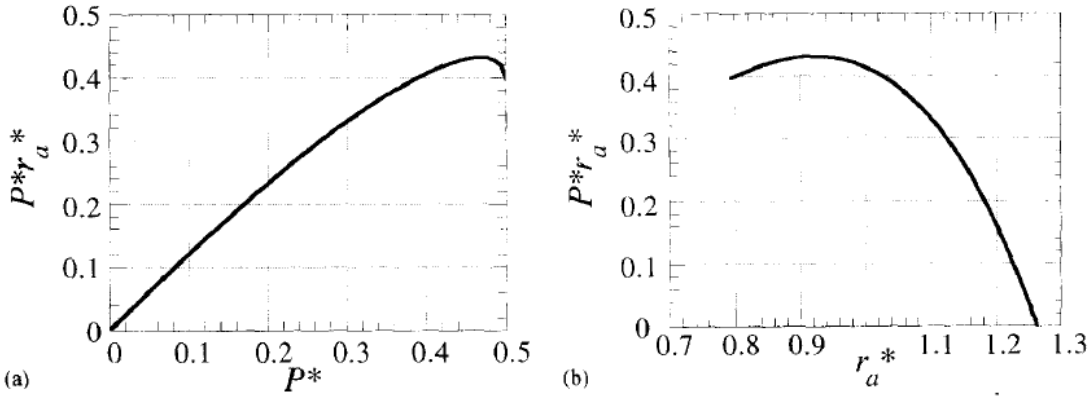

Figure 4.6 Pull-off moment as a function of pull-off force and contact radius (Ziskind et al., 1997)

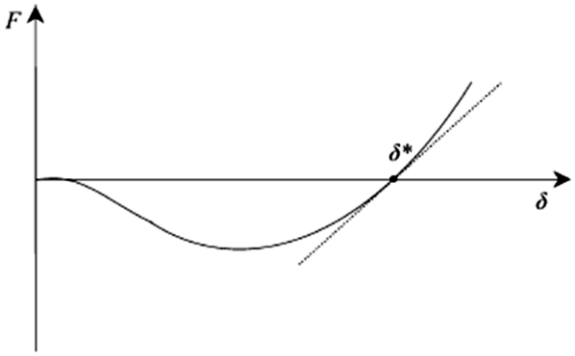

Figure 4.7 External force - displacement relation of a particle on a surface (Peri and Cetinkaya, 2005)

4.4.4 Adhesion Measurements Using Base Excitation

Peri and Cetinkaya (2005) used base excitation of spheres to measure the adhesive properties of materials. The particle response to base excitation is addressed. The particle motion is used to determine the properties of the adhesive layer. The paper does not consider bond rupture but there is a lot of valuable insight into the application of adhesion models.

The relationship between applied force and vertical displacement is considered. The stiffness expression relates nonlinearly to the applied external force as shown in Figure 4.7.

Surface shear motion induces rotational motion around the centre of the contact. The particle-substrate contact region requires a two dimensional adhesion theory. Non-uniform stress distribution in the contact area during rotational motion causes a restoring moment. Figure 4.8 illustrates the changes in the contact area.

The moment of resistance is derived from the integral of pressure and distance from the axis over the contact area

$$M = \int \int xp(x,y)dx\,dy \tag{4.23}$$

where x and y define a location within the contact area and $p(x, y)$ is the pressure at that location.

When a spherical particle experiences no external moment, the pressure distribution is cylindrically symmetrical and the moment of resistance is zero. When an external force is applied the contact area shifts and is no longer centred on the point directly below the centre of the sphere. The pressure distribution is no longer symmetrical. The pressure distribution is calculated from (4.17) and is expressed as a function of radius, r, contact radius, a, and shift in contact area, ξ. The true shifted contact area is approximated by decomposing two circles of different radii; the half circle $x < 0$ is one half of a symmetrical contact with radius $a + \xi$ and pressure distribution, $p(r, a + \xi, \delta_z)$; and the half circle $x > 0$ has a smaller contact radius $a - \xi$ and pressure distribution $p(r, a - \xi, \delta_z)$.

$$p(r, a, \delta_z) = p_H\sqrt{1 - r^2/a^2} + p_B/\sqrt{1 - r^2/a^2} \tag{4.24}$$

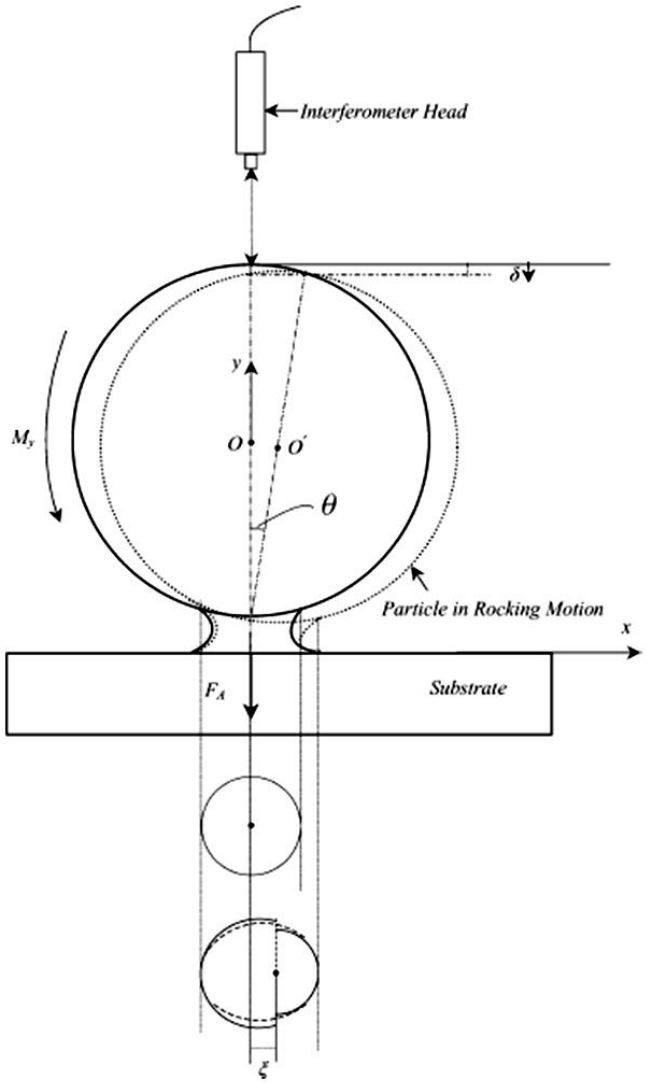

Figure 4.8 Rocking motion of a particle subject to base excitation (Peri and Cetinkaya, 2005)

The pressure corresponds to the normal displacement of the sphere and is derived from the Hertzian (p_H) and Bosinesq (p_B) pressures.

$$\delta_z = \frac{\pi a}{2E^*}(p_H + 2p_B) \tag{4.25}$$

The unsymmetrical pressure distribution comes from combination of the symmetric distributions

$$p_a(r, a, \xi) = \begin{cases} p(r, a + \xi, \delta_z), & x < 0 \\ p(r, a - \xi, \delta_z), & x > 0 \end{cases} \tag{4.26}$$

$$M = \int_{\frac{\pi}{2}}^{\frac{3\pi}{2}} \int_0^{a+\xi} xp(r, a + \xi, \delta_z) r \, dr \, d\varphi + \int_{\frac{-\pi}{2}}^{\frac{\pi}{2}} \int_0^{a-\xi} xp(r, a - \xi, \delta_z) r \, dr \, d\varphi \tag{4.27}$$

where $x = r\cos\varphi$. Integration with respect to φ gives

$$M = -2\int_0^{a+\xi} r^2 p(r, a + \xi, \delta_z) dr + 2\int_0^{a-\xi} r^2 p(r, a - \xi, \delta_z) dr \tag{4.28}$$

Evaluating the integrals, keeping δ_z constant and neglecting higer order terms of ξ/a an approximation for M_y is obtained (Peri and Cetinkaya, 2005)

$$M \cong 2\xi(-E^* a \delta_z + 3F_c \hat{a}^3) \tag{4.29}$$

$$M \cong 4F_c \hat{a}^{\frac{3}{2}} \xi \tag{4.30}$$

The moment is proportional to the pull-off force F_c and the shift of the centre of contact area. If the normal forces on the particle are within the range $-F_c < F < F_c$ then $\hat{a}^{\frac{3}{2}}$ varies between 0.5 and 1.2. Assuming $\hat{a} = 1$ the resistance moment for a particle on a flat substrate is approximately

$$M \approx 6\pi W_a r \xi \tag{4.31}$$

4.4.5 Latex Beads

In this section, the adhesive properties of the phantom particle are evaluated. The force of physical adhesion and the contact radius of the latex beads adhered to a gold surface are determined from JKR theory. The moment required to shear the bead is an analysed. For a particle at equilibrium the separation distance, z_0, is of the order of 0.3 to 0.5 nm. Table 4-1 and Table 4-2 present these properties for a range of phantom particles.

Figure 4.9 is an image of two spheres in physical contact. The contact radius of this particle is consistent with that predicted in the Table 4-2.

Table 4-1 Radius independent properties of latex microspheres

	From	Value	Unit
Equilibrium Separation, z_0	Typical value	0.4	$\times 10^{-9} m$
Work of Adhesion, W_a	(4.20)	305	$\times 10^{-3}\, J.m^{-2}$
Effective Elastic Modulus, E^*	(4.9)	1.78	$\times 10^{9}\, Pa$

Table 4-2 Theoretical Adhesion for latex microspheres of different diameter

	From	5 μm	2 μm	1 μm	unit
Dimensionless scaling parameter, λ	(4.7)	12.1	8.95	7.10	
Critical Force	(4.18)	3.60	1.44	0.720	$\times 10^{-6} N$
Contact Radius, a	(4.14)	156	84.7	53.4	$\times 10^{-9} m$
Vertical Displacement, δ	(4.16)	-3.24	-2.39	1.9	$\times 10^{-9} m$
Moment	(4.21)	0.562	0.122	0.0384	$\times 10^{-12} Nm$
Reduced Moment	(4.22)	0.374	0.0813	0.0256	

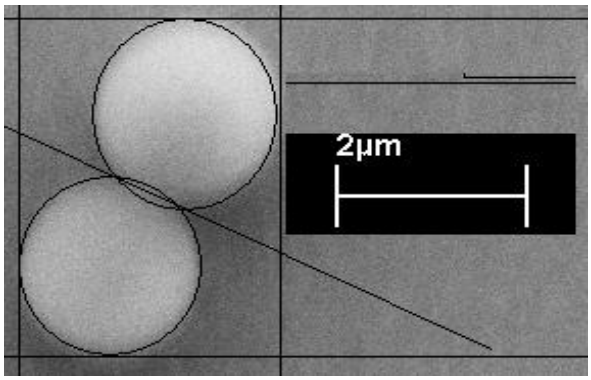

Figure 4.9 SEM image of two polystyrene latex spheres bound by physical adhesion

Grouping of particles could foreseeable alter the particle motion; the particles can group on features in the substrate giving the group greater strength. This implies that a lattice of particles is stronger in their binding than individuals, they are loosely bound to each other but each particle in a monolayer is bound to the substrate by the same strength. This the cause of the multiple spikes in the SAW bond rupture results presented in the patent (Dultsev et al., 2001). The models developed hereafter assume that the particles are bound independently and not to each other as is depicted in Figure 4.9. This is a reasonable assumption considering the concentration of binding sites and targets.

Surface cleanliness can influence the bond force. For silica microsphere adhering to a copper substrate, the pull off force increased from 120nN to 250nN after a cleaning procedure (Stegemann et al. 2007). This is particularly pertinent when the adhesion is strictly dependant

on interaction with the surface, i.e. physical bonding only. Surface asperities act to reduce the strength of this interaction. This does not have significant impact on the strength of specific bonds which is heavily dependent on the conditions of preparation, but will influence the motion of the particle and thus the forces acting on the bonds.

When considering sufficiently strict experimental protocols and the addition of monolayers or single particles to the substrate these complications are neglected. The following sections address weakness in the model. First, the interaction of acoustic waves with liquid is briefly reviewed.

4.5 Interactions with Liquid

The interaction of the ambient media with the particle is pivotal in determining the force. Cooper's model for force neglected the effects of viscous drag on the particle. When the particle and substrate are dragged through the ambient fluid, albeit over a very short distance and high speed, a force results. The interaction between the fluid and the particle however, is more complex than a simple drag opposing the velocity. When the substrate moves it captures a layer of fluid which acts as additional mass. Some of the contacted liquid is trapped in fine variations of the moving surface and will exhibit solid film behaviour. Local variations in the substrate and the adhered particles influence the fluid movement. To gauge the impact of viscous forces it is important to know the penetration of the acoustic wave into the fluid. This shows how much of the fluid moves with the particle. The difference in fluid velocity near the surface generates a torque on the particle.

4.5.1 Penetration Depth

The speed of the particle if it were to follow the surface, directly relates to the oscillation frequency of the substrate and its oscillating amplitude. The particle motion is linear and its instantaneous displacement from its centre position is sinusoidal. The vibration amplitude, and thus the acceleration, decays exponentially from the oscillating surface into the liquid. Figure 2.22 demonstrates this decay.

The amplitude at a distance, z, from the surface is given by

$$A(z) = A_0 e^{-z/\delta} \tag{4.32}$$

where A_0 is the amplitude at the surface, and δ is the penetration depth decay parameter.

$$\delta = \sqrt{\eta_l / \pi f_q \rho_l} \tag{4.33}$$

For water at room temperature δ is of the order of 5nN. The captured layer of water is thinner than the phantom particles and much of the particle is subjected to full viscous drag. The equivalent depth of penetration in air is some 200nm, more than that of water but still much less than the particle size. For a one micron particle, the acoustic wave at 20% of its height is still 36% of the amplitude of the acoustic wave at the surface. For still smaller particles, the entire ambient media around the particle will be moving with the substrate. In air, it is quite reasonable to assume that the viscous force is of no consequence. It is concluded that the viscosity and the acoustic penetration differences from liquid to gas phase that the resultant force and torque on the particle, and hence the bonds holding it to the surface, will be quite different and warrants further investigation.

The force on a particle from viscous drag in oscillating flow was studied (Stokes, 1851) and is still of scientific interest today (Vainshtein and Shapiro, 2009). The force on the particle is given by

$$F_{drag} = -6\pi\mu R U'(1+Y) - \frac{4}{3}\pi\rho_f R^3 \frac{dU'}{dt}\left(\frac{1}{2}+\frac{9}{4Y}\right) \tag{4.34}$$

where R is the particle radius, μ and ρ_f are the fluid density and viscosity respectively. U' is the instantaneous particle velocity. The parameter Y is the ratio of the particle radius to the penetration depth expressed as follows

$$Y = R\sqrt{\frac{\omega}{2v}} = \frac{R}{\delta} \tag{4.35}$$

where ω is the angular frequency of the surface oscillations and v is the kinematic viscosity of the fluid. Alternatively the attachment of an elastic particle to a smooth surface in a viscous layer flowing with shear rate, $\dot{\gamma}$. The hydrodynamic drag force is

$$F_d = 6\pi\mu\dot{\gamma}R^2 f, \qquad f = 1.7 \tag{4.36}$$

Sharma et al. (1992) assume that the hydrodynamic drag force acting on the particle can be replaced by an effective force acting at approximately $1.4R$. The moment is (Ziskind et al., 1997)

$$M_d = 1.4F_d R = 44.9\mu\dot{\gamma}R^3 \tag{4.37}$$

Table 4-3 Shear flow required to rupture physically bound polystyrene particles

	From	5 μm	2 μm	1 μm	unit
Shear rate required to generate moment	(4.37)	0.790	2.71	6.82	$\times 10^6 s^{-1}$
Shear rate required to generate reduced moment	(4.37)	0.532	1.81	4.55	$\times 10^6 s^{-1}$

Utilising the results obtained for physical adhesion and assuming the dynamic viscosity of water is $1.002 mPa.s$ the required shear rate for the set of particles from Table 4-2 is shown in Table 4-3.

4.5.2 Shear Flow on Elastic Contact

Shear flow is an analytic technique used in single bond rupture tests. The theory is relevant in the consideration of the force model for flow cell architectures where fluid flow continues during the bond rupture test. An arrested spherical particle in contact with the chamber wall experiences force, F_p and torque, T_p :

$$F_p = 32.05\mu R^2 G \tag{4.38}$$

$$T_p = 11.86\mu R^3 G \tag{4.39}$$

where μ is the fluid viscosity, R is the radius of the sphere, and G is the wall shear rate, the velocity gradient $\partial v/\partial x$ of the fluid flow at the wall. Thus the balance of force is given by (Merkel, 2001):

$$F_p = F_b \cos\Theta \tag{4.40}$$

$$F_p r + T_p = F_b l \sin\Theta \tag{4.41}$$

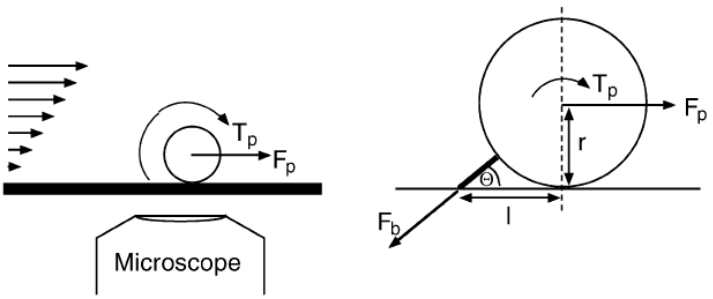

Figure 4.10 Bond loading by use of laminar flow chamber. Arrested spherical particle in contact with the wall experiences a force. (Merkel, 2001).

The force calibration is not simple because of the need to determine the distance, l. The distance, l, is measured by reversing the flow direction.

4.6 Contact Area Mechanical Model

A two dimensional adhesion combining the continuous physical adhesion with the spatially discrete receptor ligand bonds is proposed. For the integration of discrete bonds, a numerical analysis is required so that the cumulative effect of many bonds can be considered.

This method is selected in place of an alternative continuum methodology where the particle is treated as a physically bound system with artificially enhanced work of adhesion to mimic the stronger bonds. The JKR model determines the physical interaction force. If a higher work of adhesion emulates real bonds then much of the variability and versatility is lost and the actions of the bonds are unknown. It is difficult to determine the force experienced by individual bonds; one of the primary weaknesses identified in the models described earlier this chapter.

The mechanical models presented earlier in this chapter treat all bonds as being in a single place and the deformations of the particle are ignored. A more inclusive approach is sought which can consider the strength of the bonds, the forces on the bonds, force variation as a function of bond location, and importantly the forces caused by non-rotational particle movements. How systems of parallel bonds fail, especially the complex interactions between the particle and the surface are discussed later.

The elements of the previous sections are hereafter combined in a numerical model that encompasses the viscous interaction and a continuum of bonds. The force on the particle is determined from the summation of the physical interaction forces and the integration of the individual bond forces over the contact area.

Adhesion forces dominate inertial effects for small, micro – nano, length scales and low frequencies. Conversely, the inertial forces dominate at high frequencies. Low amplitude, high frequency vibration of particles influences the particle-surface adhesion properties. An inclusive and versatile model includes both these forces though in reality one may vanish in the presence of the other in certain circumstances.

Different modes of failure are possible depending on the direction and function of the applied force. Vertical forces can cause the particles to ‘pop’ off, and all bonds rupture simultaneously. This is caused by a continuous vertical force or excitation normal to the surface, such as that applied in AFM experiments. All bonds between the particle and substrate share the force. It is pertinent to consider vertical forces so that the effects of using real life QCM, which exhibit vertical movements or other transducers with normal displacement, can be considered.

Rolling failure indicates bonds failing as if the particle is peeling away. The bonds on an edge are ruptured first, and the particle rolls off from all binding sites. This is easiest to envisage in a constant flow situation where the force on the particle is constant. In this situation, the force is distributed unevenly with the peeling edge experiencing greater force.

The response of anchored objects during an earthquake has been studied. A shape parameter, defined by the height, width, length, and mass of the object, and the base excitation define the behaviour. The object can slide, roll or lift and a flat base is similar to the flat area of interaction in JKR analysis of particle adhesion. Rolling of objects are considered in applications of viscous rolling.

4.6.1 Three Degree-of-Freedom Model

In the point interaction mechanical model the attachment point between the particle and the surface was absolute and the attachment point followed the surface exactly. This model improves on that with the addition of two further degrees of freedom. The particle is rocking bouncing or sliding. It may be doing these things in any combination and the net force on any region at any time is unknown. In order to evaluate the relative effects of changes in bead size, substrate movement, chemical properties and many more influences a means to study the net effect of changes to the system is required.

The piecewise nature of the problem means that an analytical solution requires too many assumptions. The ODE solver in Matlab is used to numerically determine the motion of the particle and hence the force on the bonds.

The base excitation of the particle is one-dimensional because it acts in a single direction on the substrate plane. The x axis of the particle model is aligned with this motion. Provided the forces are, on average, distributed evenly, there will be negligible imbalance of forces around the axis parallel to the substrate displacement. Exploiting this symmetry reduces the problem to two-dimensional model. There is no displacement in the direction of the y axis and no rotation about either the y or z axes. Hence there are three degrees of freedom.

Figure 4.11 demonstrates the three degrees of freedom considered. The slip, γ, is a shear displacement of the entire sphere along the x axis, it is measured some distance from the area of interaction. The displacement along the z axis is δ, which is also measured by the relative position of points some distance from the area of interaction. Both γ and δ are bulk effects and impact all bonds. The vertical displacement is important because it permits the investigation of vertical movements that are not considered in an idealized QCM but have been shown to exist.

The particle rocks about the centre of attachment. The angle θ represents a rotation about the centre the area of attachment. Thus the location of the centre of mass is moving relative to the point of attachment. When the centre of mass is directly above the attachment point, the centre of the contact area at equilibrium and the contact area is symmetrical and circular at equilibrium. Outside of equilibrium the centre of mass shifts and the contact zone changes.

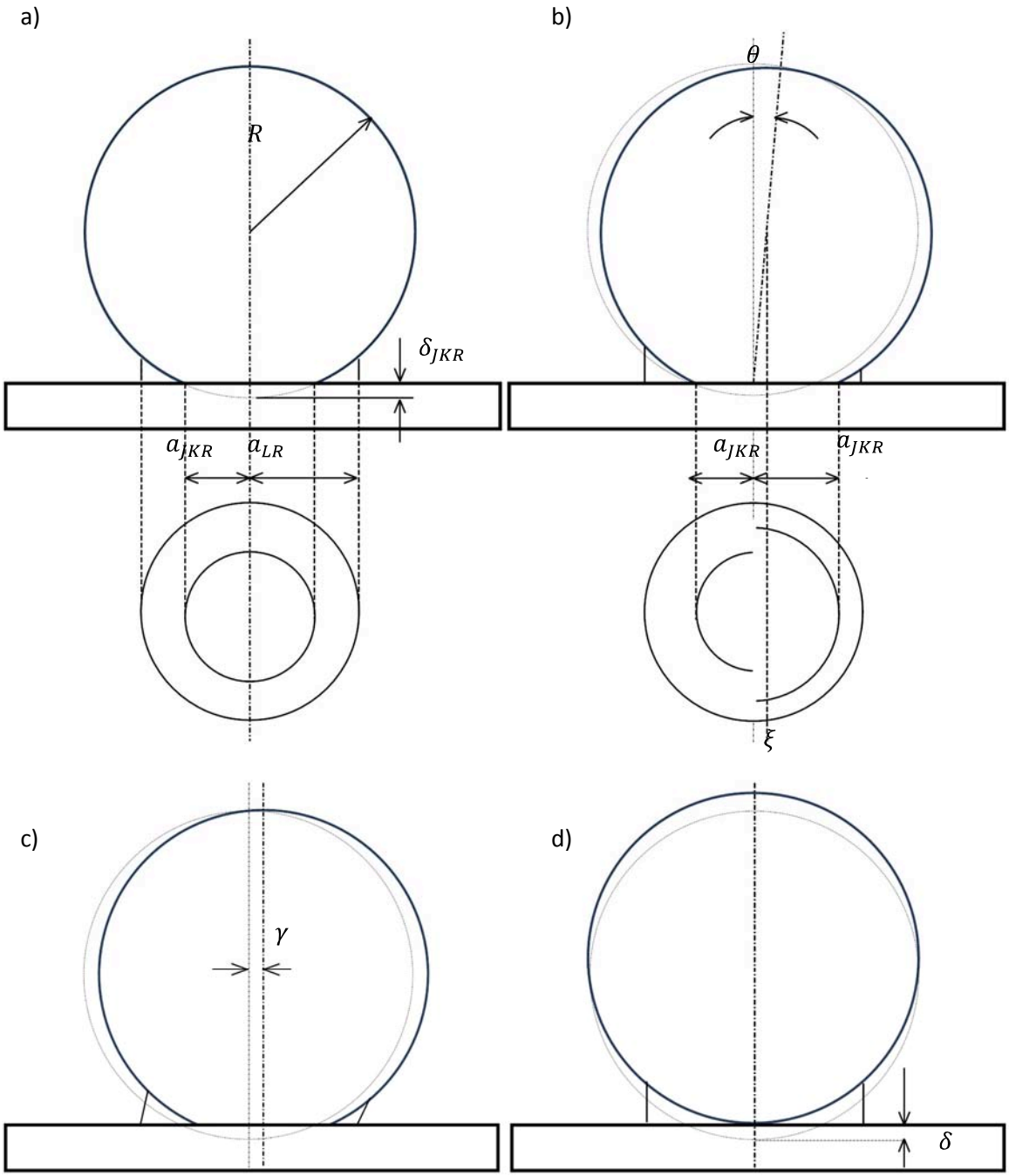

Figure 4.11 a) Sphere adhesion geometry showing b) Theta, angular degree of freedom, c) gamma, shear along the axis of displacement, d) delta, vertical degree of freedom

4.6.2 Force Balances

The same forces influence the linear degrees of freedom. Orientation of the system is unimportant as the accelerations of the surface are much greater than that of gravity. The three core forces acting on the particle are the reaction from the substrate, the reaction from the bonds, and the drag force that opposes motion through the ambient media.

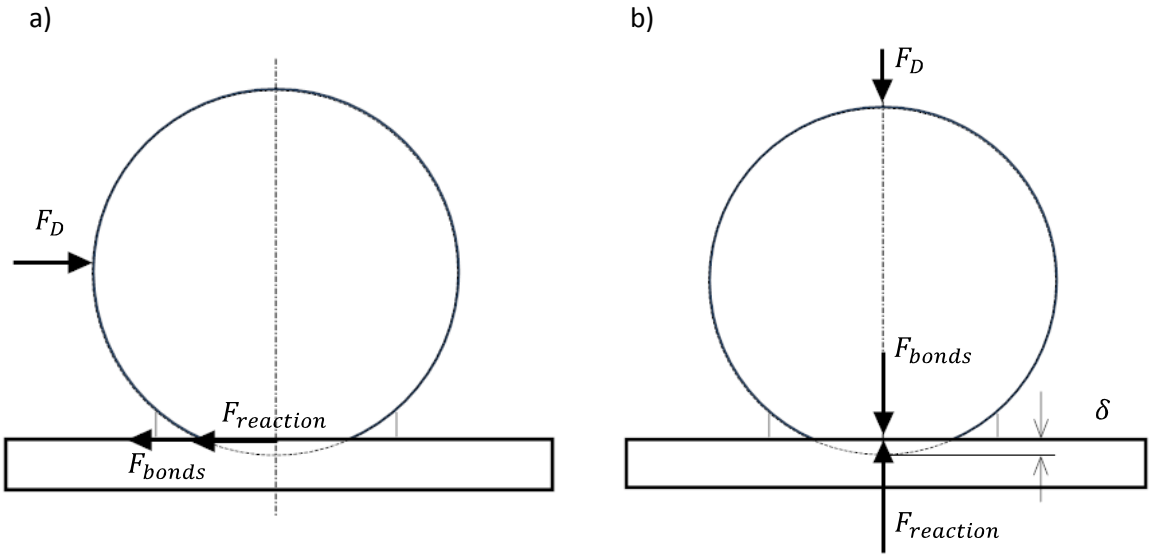

Figure 4.12 Force balance on particle in horizontal (a) and vertical (b) directions

The vertical reaction force arises from compression of the particle, substrate and everything in between. This is described by Young's modulus for a body of material, E, which can be equated to Hooke's law for a spring as follows

$$E = \frac{tensile\ stress}{tensile\ strain} = \frac{\sigma}{\varepsilon} = \frac{F/A_0}{\Delta L/L_0} = \frac{FL_0}{A_0 \Delta L} \tag{4.42}$$

$$F = \left(\frac{EA_0}{L_0}\right)\Delta L = -k_E \delta \tag{4.43}$$

where A_0 is the cross sectional area, and L_0 is the original length. A deviation from the equilibrium position of δ is opposed by a force that is linearly related to the deviation for small δ.

Likewise for the reaction force which opposes γ is derived using the shear modulus, G, where I is the initial length and A is the contact area. G is related to Young's modulus through the Poisson ratio of the material ν.

$$E = 2G(1 + \nu) \tag{4.44}$$

$$G = \frac{\tau_{xy}}{\delta_{xy}} = \frac{shear\ stress}{shear\ strain} = \frac{F/A}{\Delta x/I} = \frac{FI}{A\Delta x} \tag{4.45}$$

$$F = \left(\frac{GA}{I}\right)\Delta x \tag{4.46}$$

The drag force in both the x and z directions is related to the relative velocity of the centre of mass and the fluid. The moment from fluid friction is in phase with the moment from the substrate. Relative to the pivot point there is an inertia because the particle is moving through space .

4.6.3 Moment Balance

The moment of inertia, I, of a solid sphere about a point P on the surface of the sphere is given by the parallel axis theorem:

$$I_P = \frac{7}{5} mR^2 \tag{4.47}$$

where m is the mass of the sphere and R is the radius. So the angular acceleration $\ddot{\theta}$ can be found from the sum of torques such that

$$\ddot{\theta} = \frac{\sum \tau}{I_P} \tag{4.48}$$

Moments acting on the particle arise from an imbalance of normal forces on the substrate resulting from deformation of the sphere within the area of direct contact. Likewise, an imbalance of the force exerted by extended bonds also causes a moment. Such imbalance occurs in response to an angular shift in the centre of mass. For the physical interaction, this deviation from the centre point of the rotation through equilibrium and the resulting force is approximated for small angles using Hooke's Law. Forces arise from the fluid drag and from the inertia of the particle due to acceleration parallel to the substrate that generate moments.

A resistance moment about the pivot point is determined from the sum of pressure over an infinitesimal area ($dy\ dx$) multiplied by the distance from the x axis resulting in a moment.

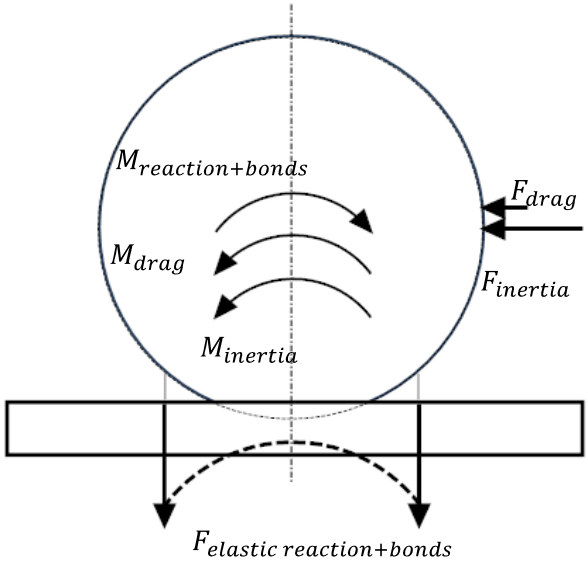

Figure 4.13 **Forces that cause moments on the particle**

$$M_{elast} = \int \int p(x,y)x\ dx\ dy \tag{4.49}$$

Expressed in radial coordinates

$$M_{elast} = \int \int xp(r,\phi)rdr\ d\phi \tag{4.50}$$

The pressure applied within the area (F/dA) is derived from the definition of Young's Modulus, E, equation (4.42)

$$\frac{F}{dA} = \frac{E}{L_0}\Delta L(r,\phi,\theta) \tag{4.51}$$

The change in length is expressed in terms of the position in the contact area (r,ϕ) and the angle of rotation of the particle (θ). The change in length at any point depends on the x position of the point, $r\cos(\phi)$, and the angle that that initial point is rotated through giving:

$$\Delta L(r,\phi,\theta) = r\ cos\ \phi\ \ sin\ \theta \approx r\theta\ cos\ \phi \tag{4.52}$$

Equation 4.52 uses the small angle approximation $\sin(\theta) = \theta$. Substituting into (4.49)

$$M_{elast} = \frac{E}{L_0}\theta \int \int r^3(cos\ \phi)^2\ dr\ d\phi \tag{4.53}$$

and solving between the limits $0 < r \leq a_{jkr}$ and $0 < \phi \leq 2\pi$ gives

$$M_{elast} = \frac{E}{L_0}\frac{\pi a_{jkr}^4}{4} \times \theta \tag{4.54}$$

The inertial force along the x axis is determined by integrating the inertial force on each volume element multiplied by the distance to the pivot point.

$$M_{inertia} = \int Fz\ dV = \int maz\ dV \tag{4.55}$$

where m is the mass of the volume, a is the acceleration and z is the normal distance of the centre of the volume to the substrate.

The particle is attached to the substrate which is moving with the defined sinusoidal motion. The particle is experiencing a time dependant acceleration that affects the entire particle equally. Each infinitesimal volume unit in the particle is moving at the same velocity. This is contrary to the angular degree of freedom. For a peak angular velocity of $\dot{\theta}$ the difference in velocity between the top and bottom of the particle is $\Delta v = 2R\dot{\theta}$. For the purpose of the simulation, it is deemed negligible and a is considered independent of volume. Thus the moment caused by the inertia of the particle along the x-axis is derived in rotational coordinates. The mass of the volume element, $m = \rho\ dV$ is the product of the material density and volume where the volume element is given by $\sin(\theta) + r$. It follows that

$$M_{inertia} = a\rho \int_{r=0}^{R}\int_{\theta=0}^{2\pi}\int_{\phi=0}^{2\pi} r^2\ sin(\theta) \times (r\ sin(\theta) + r)dr\ d\theta\ d\phi \tag{4.56}$$

$$M_{inertia} = \frac{1}{2}\rho\pi^2 aR^4 = \frac{3\pi}{2} R\ a\ m \approx 1.17\ ma\ R \tag{4.57}$$

Thus the moment associated with the inertia of the particle is approximated by the inertial force (ma) applied at a distance 1.17 times the particle radius from the pivot point.

4.6.4 ODE Formulation

In each degree of freedom the forces and torques acting on the particle result in acceleration. The model discussed above is coded using Matlab and solved with the ODE solver. Second order equations are manipulated to be solved using the Matlab first order ODE solver.

The ODE is developed as follows

$$x = [\theta \quad \dot{\theta} \quad \delta \quad \dot{\delta} \quad \gamma \quad \dot{\gamma}] \tag{4.58}$$

$$\frac{dx}{dt} = [\dot{\theta} \quad \ddot{\theta} \quad \dot{\delta} \quad \ddot{\delta} \quad \dot{\gamma} \quad \ddot{\gamma}] \tag{4.59}$$

$$\frac{dx}{dt} = [x(2) \quad \ddot{\theta} \quad x(4) \quad \ddot{\delta} \quad x(6) \quad \ddot{\gamma}] \tag{4.60}$$

At each step of the solver, based on the current state of the system, the derivatives are evaluated and the solver determines the next state of the system. Time steps are limited to a fraction of the period of the substrate oscillations.

4.6.5 Results

The parameters of the model are first set to align with the much larger particles, results and measurements conducted by Peri et al (2005). The minute vertical displacement of the particle during base excitation is measured in two experiments for normal and shear excitation.

The model variables are matched as closely as possible to the experiment conditions described. The experiment is duplicated for normal and shear displacement conditions. The shear experiment presented in Figure 4.14 shows the parameter mismatch. There is a low frequency resonance apparent in the results. To determine the best parameters for the model a number of simulations are run.

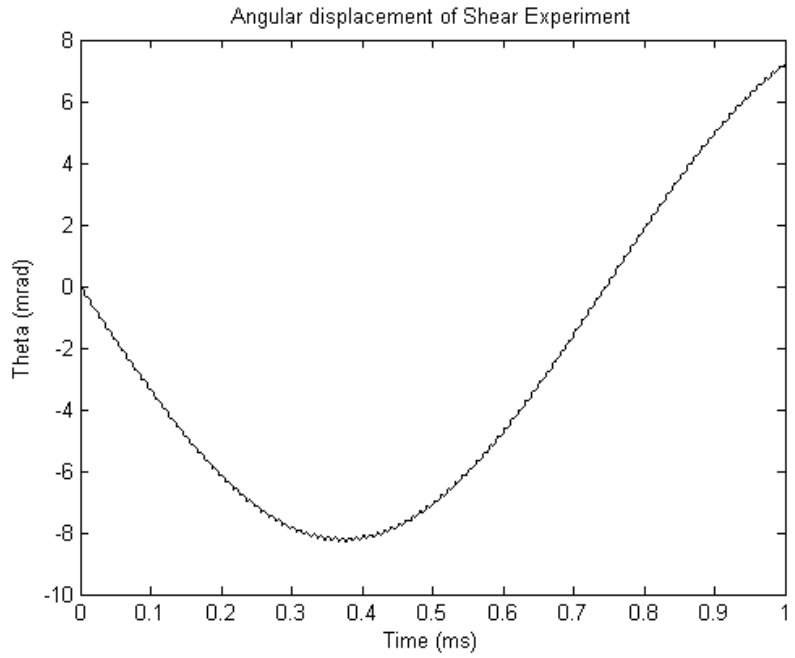

Figure 4.14 Angular displacement vs. time shows that the particle will have rolled off its binding site

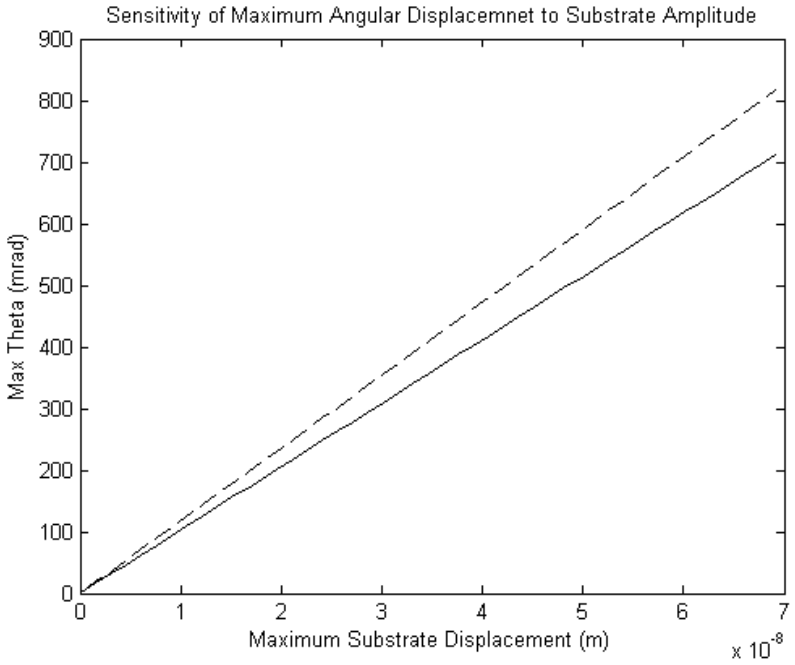

Figure 4.15 Plot of maximum angular displacement vs. substrate oscillation amplitude

The angular displacement measured by Peri et al (2005) for the bead described in this simulation was 0.16°, or 2.8 mrad. Figure 4.16 shows the maximum angular displacement of several different surface excitation amplitudes. The linear nature of the relationship is evident, though the amplitude of the oscillations is higher than anticipated. When the simulation is run, the theta, gamma and delta change periodically and have their own resonances. Peri et al (2005) determines resonance of attached particles calculated by resonances caused by the stiffness and elasticity of the pivot.

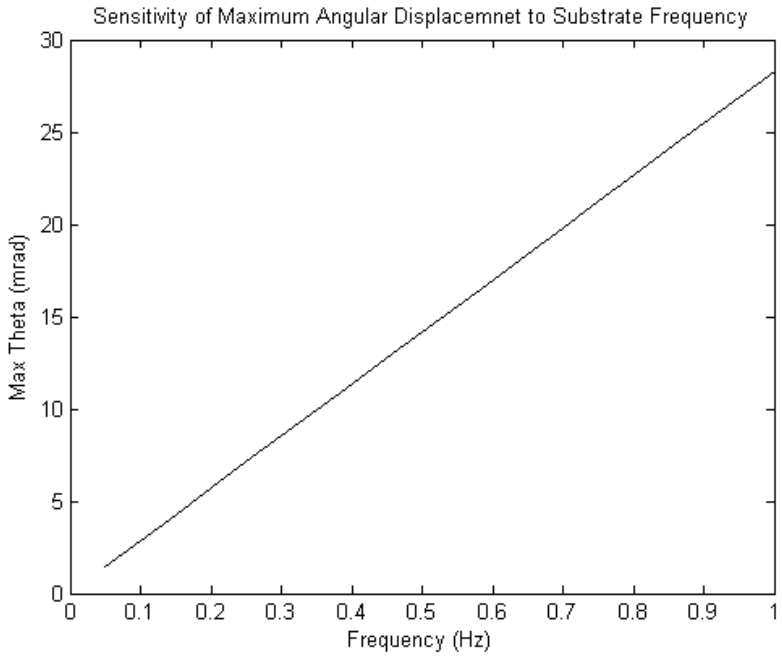

Figure 4.16 Plot of maximum angular displacement vs. substrate oscillation frequency

Figure 4.16 shows the angular displacement depends linearly on the frequency of the substrate oscillations.

In order to improve the estimates of the elastic constants, the sensitivity of the model to the estimated parameters is determined. The determining moments effecting the angular displacement depend on the elastic coefficient and the drag force. As these simulations endeavour to match experiments in air the drag force has been disabled. Two quantities affect the elasticity of the rotating degree of freedom, namely the contact radius and the estimated initial length of the plug described above (4.54).

The shear amplitude is lower than that of the QCM because a non-resonant transducer is used. Figure 4.17 demonstrates the sensitivity of the maximum displacement to the change in the L_0 parameter.

The full scale of the ratio of initial length change corresponds to the maximum interaction of the entire particle ($L_0 = 2R$). It is plausible that only some fraction of the particle volume is involved in this interaction. In Figure 4.18, $L_0 = 0.2R$. This parameter is best applied to rigid particle or particles that can be described as linearly elastic within the range of distortion experienced during base excitation.

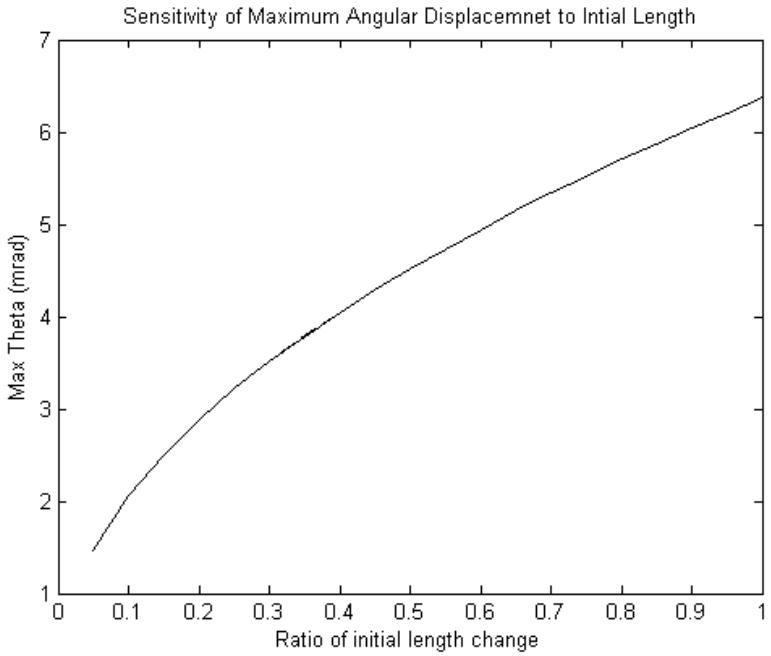

Figure 4.17 Plot of maximum angular displacement vs. the initial length parameter of the elastic constant function

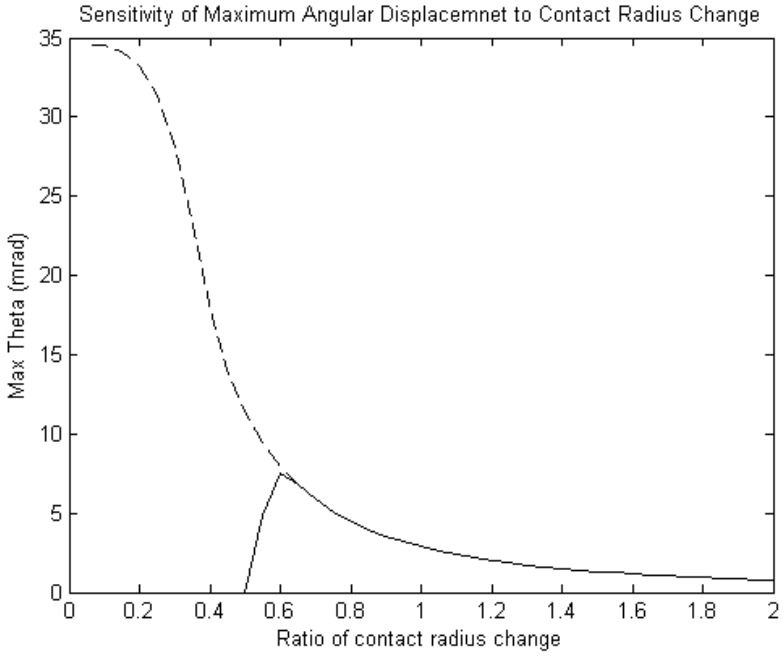

Figure 4.18 Plot of maximum angular displacement vs. the contact radius

The broken line in Figure 4.18 for contact radius less than $0.6a_{JKR}$ is indicative of the loss of symmetry in the angular displacement results. That is to say that $|\max(\theta)| \neq |\min(\theta)|$. From this result it is evident that with subtle manipulation of the simulation parameters the simulation output can be designed to closely match the published results.

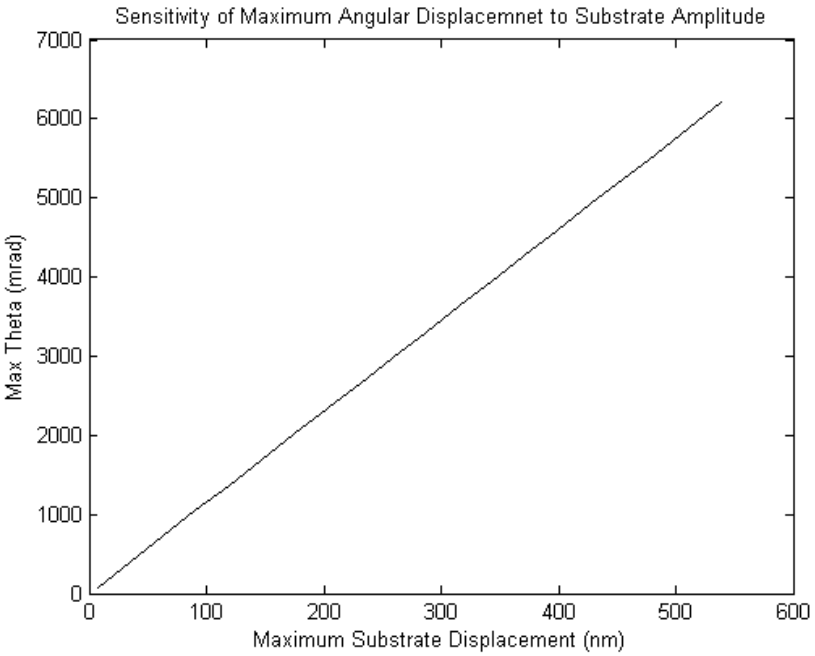

Figure 4.19 Maximum angular displacement determined for multiple substrate amplitudes.

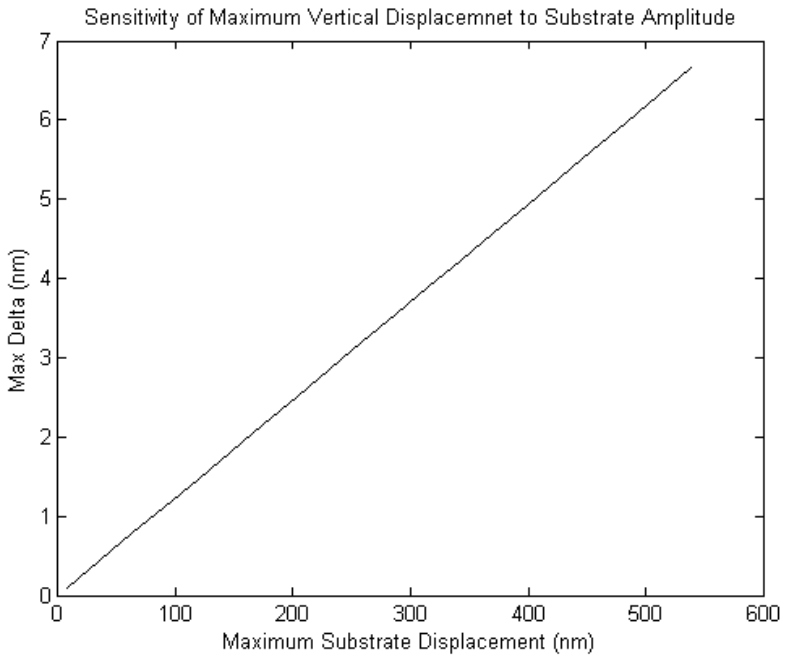

Figure 4.20 Maximum vertical displacement determined for multiple substrate amplitudes.

For subsequent simulations, the default parameters are amended to incorporate these changes. Displacement in all degrees of freedom was simulated as a function of substrate displacement amplitude and frequency for the case where only physical bonding is present. These results, presented below, are simulated beyond the point of failure. In reality, before a 1-radian angle displacement occurs the particle would have rolled off.

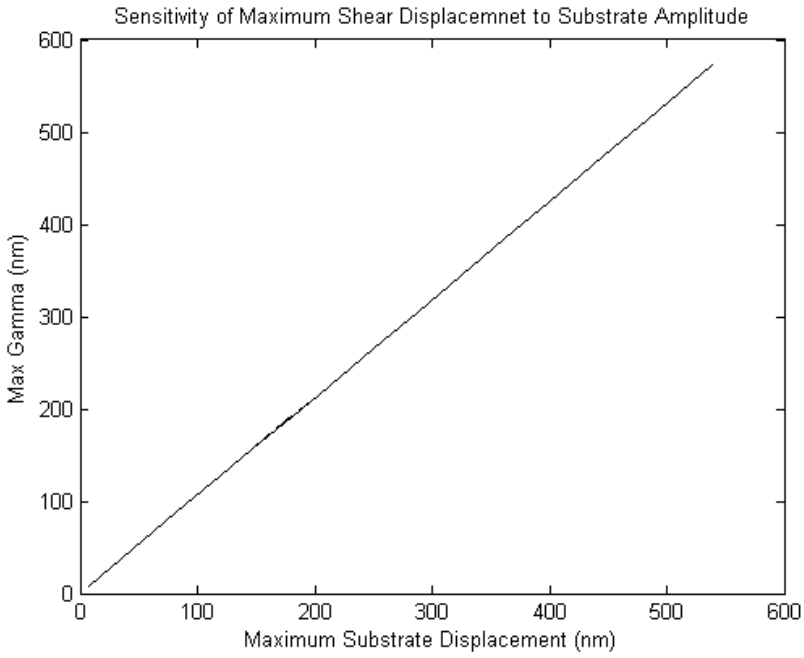

Figure 4.21 Maximum shear displacement determined for multiple substrate amplitudes.

From Figure 4.19 the amplitude at which physical bond rupture occurs by rolling failure may be estimated. Figure 3.16 indicates that the first signs of bond rupture occur at 1.5V. These first signs correspond to the particles near the centre, which, for a typical QCM used in these experiments, corresponds to amplitude near 75nm. On this plot, this corresponds to around 0.8 radian (around 45 degrees).

By similar analysis the vertical displacement of the particle (based on $A_z = 0.01A$) would be 0.9nm. This is less than δ_{JKR} predicted for this particle (1.7nm). This is not sufficient to detach the particle in this degree of freedom. The shear displacement is of the order of 75nm and the angular displacement is considerable indicating that a rolling failure is the most likely.

The γ and δ displacements are defined at some distant point beyond the particle-substrate interface. The effect of linear displacement could be reduced at the interface because of this distance. They are small in contrast the particle radius. Higher than values expected indicate that the joints are less compliant than the figures above would indicate. Further, drastic displacements are required to ensure rupture of the particle because in a physical bonding system the particle could be constantly re-binding or rolling about.

Long time simulations of bond rupture experiments require an understanding of single bond rupture, which is briefly reviewed in the coming section.

4.7 Single Bond Rupture

Specific bonds such as receptor ligand pairs are the result of many weak local interactions summing into an overall stable bonds. Only when two molecules posses topologically and chemically complimentary surfaces will it be possible that the weak and localised interactions add up to an overall strong bond with binding energy of some $10k_BT$. The bond requires 10 times the amount of energy that is available thermally to 'break' (Merkel, 2001)

Compared to covalent bonds these strong interactions are considered weak. Biomolecules are stabilised by weak interactions and the free enthalpies of typical receptor-ligand bonds are of the order of 5 to 10 kcal/mol (Merkel, 2001). AFM force spectroscopy has shown that the force required to induce bond dissociation falls in the range from 2-200pN. This can be compared to 0.1 to 20 pN required for polymer stretching. An interesting comparison of the force is that the photons emitted by a 1mW laser pointer exert a force of 3.3pN on the pointer due to conservation of momentum (Merkel, 2001).

Weak non-covalent interactions have limited lifetimes and so will dissociate under almost any level of force if pulled for modest periods. Close to equilibrium in solution, large numbers of molecules continuously bond and dissociate under zero force (Evans, 2001).

Further to the above treatment of adhesive forces between the particle and substrate, it is important to consider the strength of the receptor-ligand bonds. Bond strength is tested using an AFM, where the micro cantilever apparatus strains the bond vertically until breakage, e.g. (Janshoff and Steinem, 2001). Figure 4.22 shows typical data. A good review of the AFM

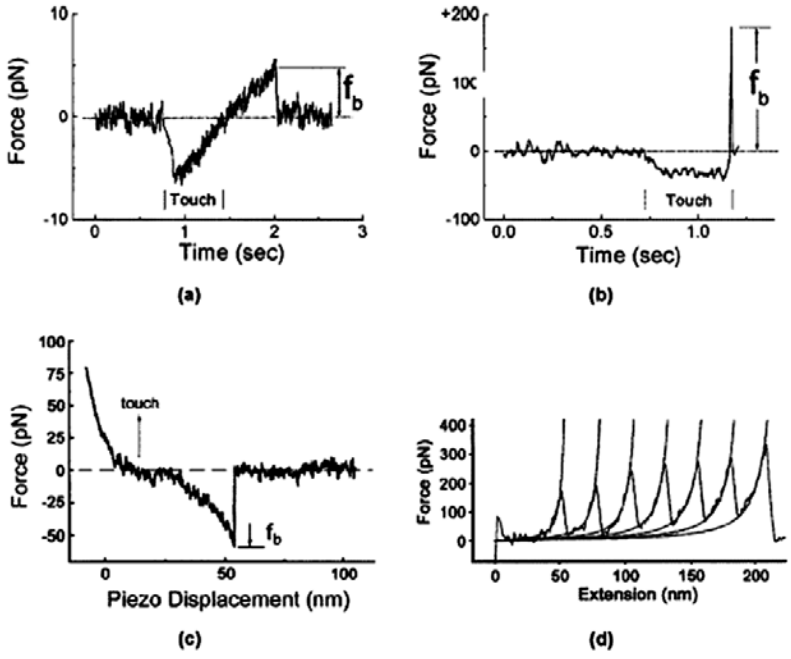

Figure 4.22 The rupture of single bonds with ultrasensitive force probes. (Evans, 2001)

apparatus is presented by (Butt et al., 2005). Other methods include parallel wall flow chamber, bead doublet in shear flow, and magnetic force breakage reviewed by Merkel (2001).

A number of authors offer mathematical descriptions of single bond rupture: (Merkel et al., 1999, Merkel, 2001, Evans et al., 1995, Evans and Ritchie, 1999, Evans and Ritchie, 1997, Evans, 2001, Evans, 1998, Raible et al., 2004), all of which address the rupture of single, or few, bonds. In force spectroscopy experiments, the effect of an applied force on the dissociation rate $k_{off}(f)$ is considered and many approximations are offered by the literature. Following Evans and Ritchie (1997) a rupture event is viewed as a thermally activated decay of a metastable state governed by reaction kinetics of the form

$$\frac{dp(t)}{dt} = -k_{off}\big(f(t)\big)p(t) \tag{4.61}$$

where $p(t)$ is the probability of bond survival up to time t and $k_{off}(f)$ is the rate of decay in the presence of a force, f. To all practical purposes the forced rupture of a bond results in infinite separation resulting in virtually no chance of bond reformation, thus the bond reformation is exponentially suppressed and therefore neglected (Raible et al., 2004). Implicit in the above assumption is that the probability of bond rupture only depends on the instantaneously acting force and not on the history. Population kinetics with rebinding follows the relation

$$\frac{dN}{dT} = -k_{off}N + k_{on}\ \cdot (1 - N) \tag{4.62}$$

where N is the number of bonds bound and k_{off} and k_{on} are the unbinding and binding rates respectively.

The effect of an applied force on the dissociation rate is considered. The thermal energy, calculated from the product of Boltzmann's constant and absolute temperature, $k_B T$, sets the scale for the interactions. As soon as an applied force exceeds this level the normal reaction kinetics of dissociation are disrupted and unbinding will occur faster than in the absence of force. If the barrier potential is close to this then the particle will be in one state, but will certainly jump out due to some thermal load in a finite time. On the other hand if the two are comparable the particle can move almost freely between states.

Figure 4.23 shows the assumed form of reaction kinetics. Confinement by a single barrier is assumed which is seldom the case. It is assumed that the application of force selects a particular path expressed as a scalar coordinate x. The energy path goes from one deep minimum over a saddle point into another deem minimum and is bound by steeply rising energy in other directions. Multiple reaction pathways are handled to some extent by Raible et al. who introduce a second meta stable bound state with different kinetics (Raible *et al.*, 2004).

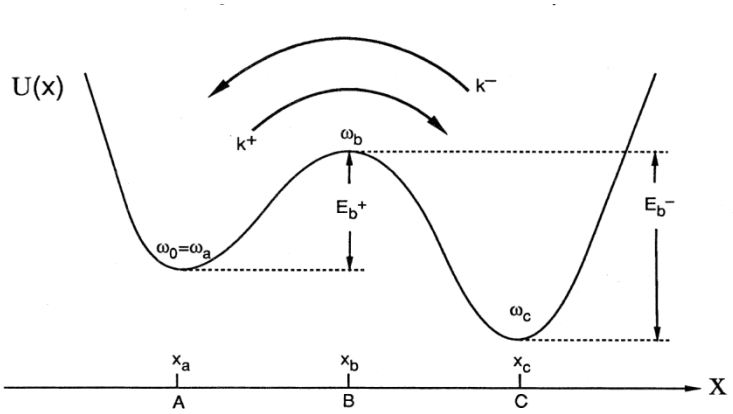

Figure 4.23 Kramers' theory, simple model of reaction kinetics (Hanggi et al., 1990)

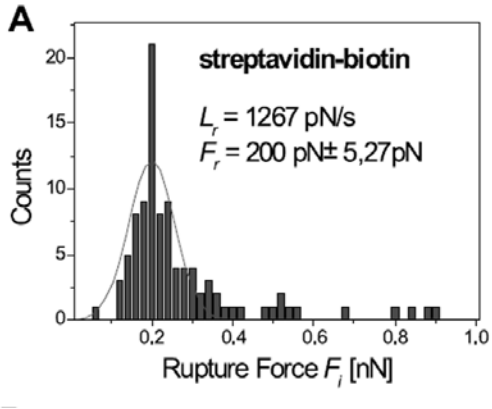

Figure 4.24 Force histograms of streptavidin-biotin interactions

Under external force, barriers in the energy landscape (E_b) are lowered and bond lifetime shortens. Bond strength, typically thought of as the force at which the bond breaks, is amended to the force at which the bond is most likely to break, i.e. the peak of the distribution of rupture forces. The distribution of forces means that the many bonds anchoring one particle may not rupture at the same time, and likewise particles on a single transducer are not liberated simultaneously. Figure 4.24 shows a typical rupture force histogram for single bond rupture experiments.

Bond strength is a dynamic property that is dependent upon the force-loading rate applied during the rupturing of the bond (Lo et al., 2001). The bond strengths scale linearly with the logarithm of the loading rate. This applies to both specific and non-specific interactions. The detachment force can range up to and even exceed the adiabatic limit defined by the intermolecular potential if the bond is broken in less time than required for diffusive relaxation (Evans, 2001). The adiabatic limit is the strength of the bond in the absence of any contributing thermal energy. In normal situations, there is some random thermal energy of the order of ~4pN.nm at biological temperatures (300°K).

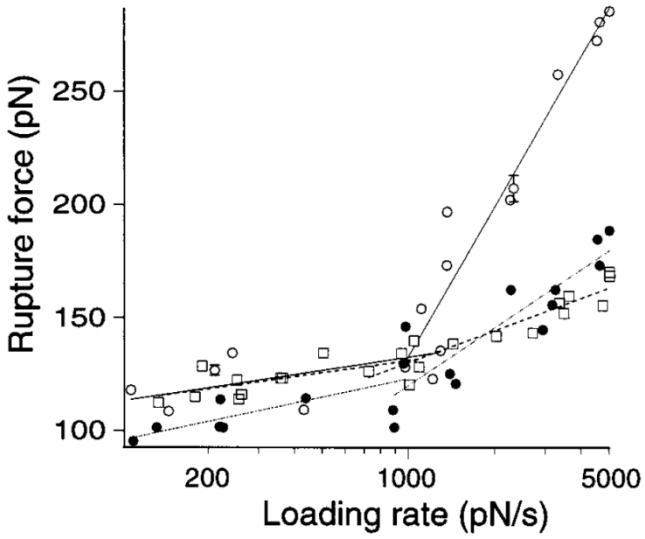

Figure 4.25 Rupture force depends on loading rate (Yuan et al., 2000)

Figure 4.25 shows that for streptavidin-biotin (O) the linear dependence of rupture force on loading rate changes schemes, indicating an energy landscape similar to that depicted in Figure 4.26.

Intra molecular thermal relaxation processes into the metastable equation are much faster than the time scale on which the applied force significantly changes (Merkel, 2001, Evans and Ritchie, 1997, Evans and Ritchie, 1999, Evans, 2001). An important consideration when comparing sets of results is the direction of the force. The main force is tangential to the surface for QCM and normal to the surface for AFM.

An applied force increases the frequency of dissociation due to changes in the thermal likelihood of reaching the top of the energy barrier, $\exp\left(-E_b(f)/k_BT\right)$ (Evans and Ritchie, 1999). For highly curved barriers, the location of the transition state remains approximately constant under force, and the barrier is lowered in proportion to a fixed distance x_β. The characteristic force, f_β, is given by the ratio of thermal energy to the fixed distance x_β, (Evans and Ritchie, 1999):

$$f_\beta = {k_BT}/{x_\beta} \tag{4.63}$$

As force rises on this scale, the analysis of dissociation past a single barrier results in the following expression for the kinetic rate

$$k_{off} = \left(\frac{1}{t_0}\right) g\left(\frac{f}{f_\beta}\right) e^{\frac{f}{f_\beta}} \tag{4.64}$$

This off rate is approximated by

$$k_{off}(f) = k_0 e^{(f/f_\beta)} \tag{4.65}$$

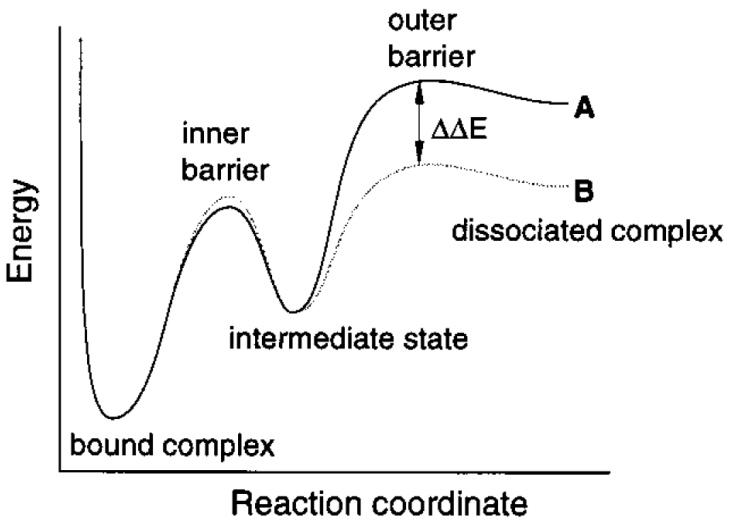

Figure 4.26 Conceptual Landscape of streptavidin-biotin interactions (Yuan et al., 2000)

where k_0 is the off rate under no external load is given by $1/t_0$, t_0 is the lifetime of a bond under no force. When pulled apart faster than $t_{off} = 1/k_{off}$ a bond resists detachment. The detachment force can range up to and even exceed the adiabatic limit defined by the intermolecular potential (Evans, 2001).

Multiple barriers have the impact of making the bond last longer at higher loading rate

$$k_{off}(f) \cong \frac{\left(\frac{1}{t_0}\right) e^{\frac{f}{f_0}}}{1 + \sum_i l_i e^{f\Delta x_\beta - \Delta E_b}} \tag{4.66}$$

which at lower forces begins with the steepest exponential dominated by the outer barrier.

The streptavidin-biotin complex has been modelled using molecular mechanics (Grubmuller et al., 1996, Heymann and Grubmuller, 2001, Stayton et al., 1999), the applied force in the model was designed to mimic an AFM experiment. The streptavidin-biotin bond has been studied extensively. From these reports, sufficient information is available to simulate the bonds. The yield force is reported to be 250pN (Merkel, 2001). The streptavidin bond features multiple barriers, the first is 1.2 Å and the second at 5 Å. (Yuan et al., 2000) and a half-life of three days under no force.

4.8 Probabilistic Model

The mechanical model discussed earlier is augmented with an interfacing layer of receptor-ligand bonds. The particle experiences a reaction force in response to bond extension. Through the simulation of particle motion, the failure rate of each bond is determined.

The phantom particle is spherical but undergoes deformation in a contact area like that approximated in the JKR model. In the absence of specific bonds, physical adhesive forces deform the particle and generate an area of interaction. This area of interaction is the area over which bonds will form. Bonds may form beyond this area as the receptor-ligand bonds act over some distance. Once specific bonds are formed, the particle is held to the substrate by a force exceeding the original physical interaction. The physical contact is maintained for displacements exceeding the equilibrium displacement.

The motion of a rocking particle extends the bonds and linking polymers. They pull against this extension like a spring resulting in a force acting to restore the particle to equilibrium. In order to explore the force generated, the extension is determined as function of the particle, bond location, and the three degrees of freedom in the model.

The simulation displacements discussed in the scope of physical binding relate to some distant point from the interaction, that is, the δ parameter measures the displacement of the centre of mass, not the displacement of the interface. In the presence of receptors ligands and the intermediate layers the distant point displacement will increasingly represent the interaction at the surface because the surface layers are more compliant than the particle and the substrate.

Only bound bonds contribute a reaction force, and so when few enough bonds survive the particle enters failure mode. The bond extension is determined as a function of the angle the particle has deviated from the centre, and the distance of the bond from the centre axis. The extension is assumed to occur along the angle determined by the vertical and horizontal shifts of the particle. This is appropriate as the extensions caused by the angular shift are small when compared to the bulk linear movements in the δ and γ degrees of freedom (Figure 4.27(b)). This approximation method is selected for computational efficiency.

The change in length is a function of the shifts in the endpoint of the bond caused by δ, γ and θ. Assuming these end shifts correspond to the far point relations in the previous paragraph then the change in bond length, ΔL, is approximated by:

$$\Delta L \approx \sqrt{\delta^2 + \gamma^2} \times \frac{sin\,\theta_3}{sin\,\theta_1} - x\theta - L_i \tag{4.67}$$

where x is the distance of the bond from the centre point along the x direction, θ_1 is the angle between the initial and shifted bond given by $\tan\theta_1 = \gamma/\delta + L_i$, and θ_3 is the angle between the original bond location and the vector difference between the bonds given by $\theta_3 = \pi/2 + \mathrm{atan}\,\delta/|\gamma|$.

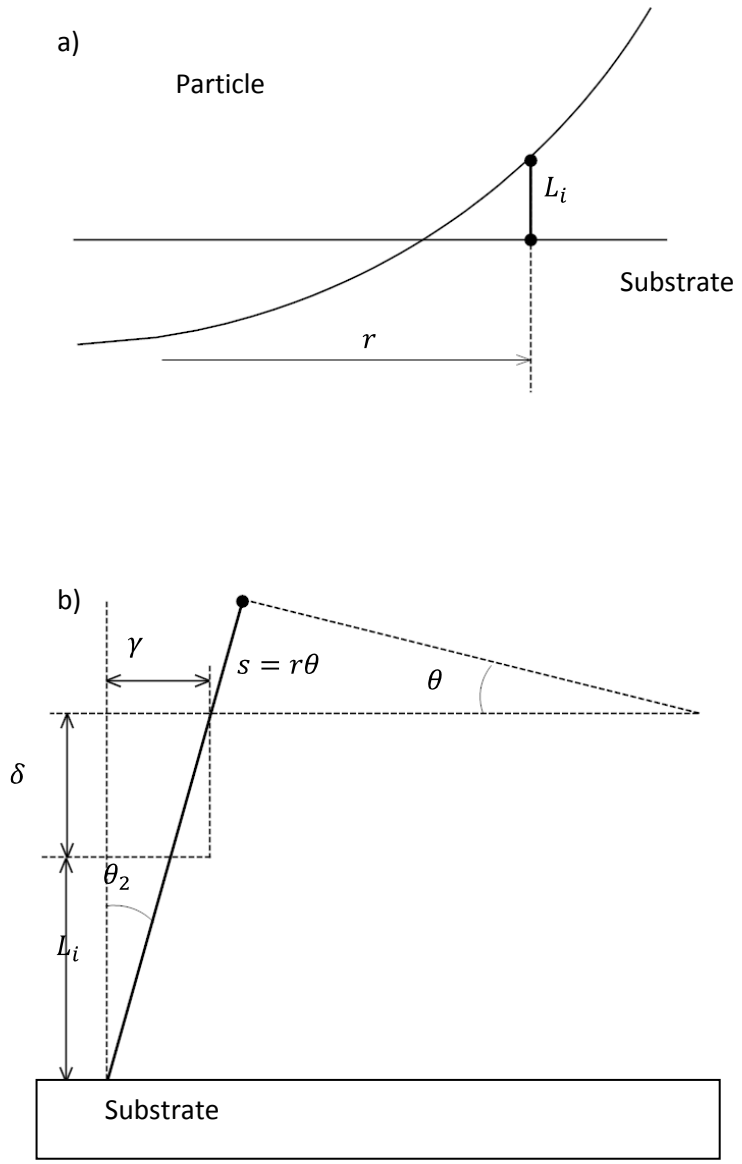

Figure 4.27 Bond geometry showing the approximation of bond length change in response to an angular displacementThe contribution of the angular shift in the equation 4.67 is approximated by $x\theta$. This is the arc-length of the line and because for small angles, $\sin\theta \approx \theta$, this is a good approximation of the additive length of the bond.

We consider a default data set representative of normal operating conditions. Figure 4.28 is an example of the uniform distribution of bonds. The parameter N defines the density of bonds in the bounding square of the interacting radius. Bonds that fall outside the contact radius are discarded.

The dynamic particle displacement is simulated over a short time. The displacement is used to determine the force on each individual bond over a long time simulation. It is

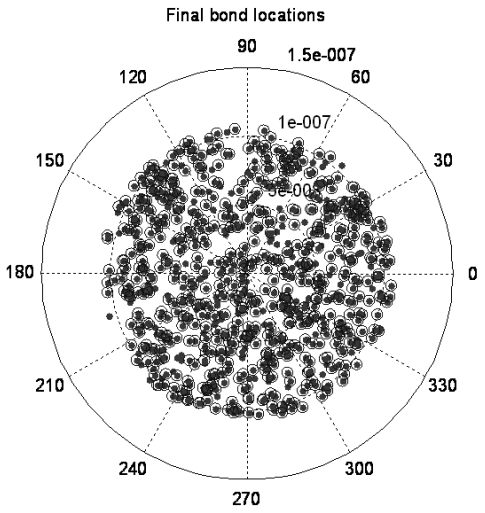

Figure 4.28 Randomly distributed bonds

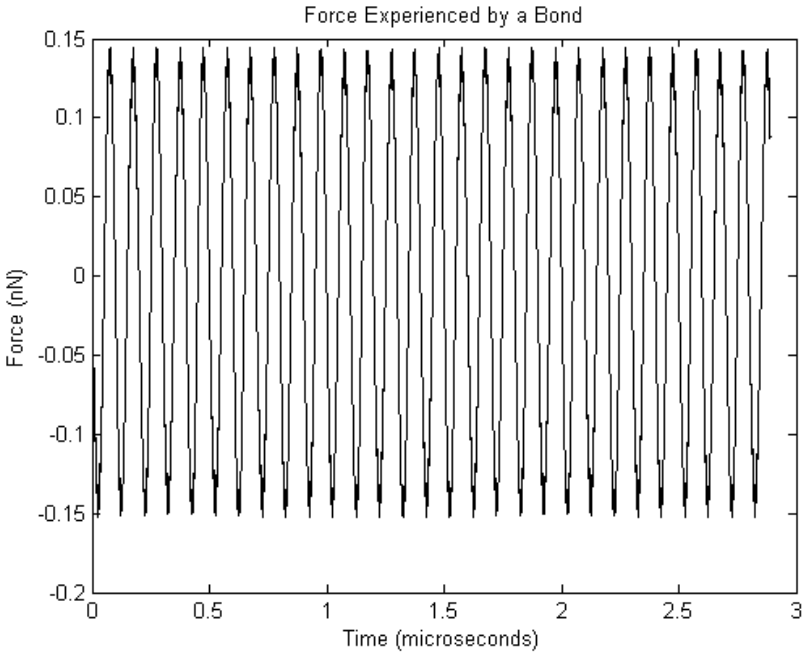

Figure 4.29 Product of bond extension and bond spring constant for several cycles.

assumed that until failure the function and magnitude of the displacements are unchanged. Displacements change as bonds break and the reaction force is reduced, however full simulation is prohibitively taxing on computer resources and time.

The force on a single bond selected at random is presented in Figure 4.29. The force is determined from the result of the multiplication of the ΔL and k_{bond} parameters. These forces subsequently clipped so that when $\Delta L < 0$ there is no force because the bonds only exert force when extended.

The predicted force is strongly dependant on the spring constant of the receptor-ligand-linkage system. The maximal force on the particle resulting from this bond is of the order of

15×10^{-9}. When compared to Cooper's force it would require 1500 such particles to reach the same magnitude. This is of the same order as the results depicted in the Mechanical/Inertial model at the beginning of the chapter. The force experienced by a single bond is larger than that determined using Cooper's equation, but the maximal force is not applied all the time. Once negative forces are removed the mean force applied to the bond is $48pN$. This is comparable to the operating range of AFM experiments.

The highest instantaneous maximum loading rate is near 1N/s. This does not reflect the real loading rate applied to the bond as the interaction will be in some way filtered by the complex mechanics of the linkage. The loading rates are not so fast as to void all the assumptions made by the single bond experiments.

It is feasible to model the physical attachment analytically, but the bonds, and modelling their lifetime is an added complication. The movement in the three degrees of freedom in the presence of receptor-ligand bonding cannot be predicted in any other way while maintaining the flexibility of this approach to experimentation.

The probability of survival of a bond (p_{sur}) is a function of force. In discrete time samples it is determined using the equation:

$$p_{sur}(t) = p_{sur}(t-1) - p_{sur}(t-1)k_{off}t_{step} \tag{4.68}$$

When integrated over the short simulation time, this gives the probability of survival of each bond. This is extended over the long time duration. The instantaneous off rate is determined as a function of the instantaneous force, this is consistent with single-bond force spectroscopy.

The output of primary interest in this investigation is the number of survived bonds. It is accepted that for constant excitation amplitude the number of survived bonds decays at an exponential rate. The curve fitting of simulated data is demonstrated in Figure 4.30.

Figure 4.30 shows the survived population of bonds after normalisation. There are three lines showing the coarse single scan, the result of averaging 30 scans and the result of the fitData function. The noise on the average scan can be removed by averaging more simulations. The computational overhead is prohibitive considering the volume of simulation required. fitData is an exponential decay starting at 1 with a parameter $decay$ that is used in subsequent models. The fit parameter is determined by a least squares fit of a constant line to the adjusted data. Before the fit the survived population is normalized by the original population size, then the natural logarithm is taken and the result is divided by the time vector. Using an exponential decay with a single parameter allows the model input to be

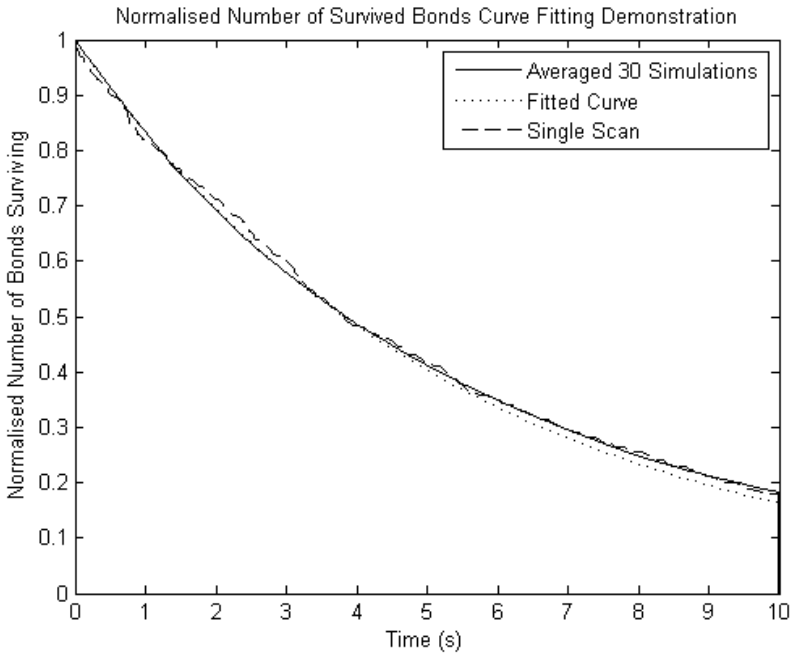

Figure 4.30 Curve Fit Demonstration with averaging

changed and the effect easily correlated. A simple generalised function is built in the next section.

Figure 4.31 shows decay is a linear function of the logarithm of the substrate displacement. This indicates that there is a strong dependence of the decay parameter on the exponent of maximum substrate displacement. The relationship between the rate of decay and oscillation is fundamental to the simulation of bond rupture devices. The relationship only holds for amplitudes much greater than zero. A relation is required where the rate tends to zero for zero displacement if exceedingly long simulations are considered. For short duration bond rupture experiments it is acceptable to use a piecewise relation where below the x intersect of the above relation the decay rate is equal to zero.

k_{bond} is the spring constant of the receptor-ligand-linker system and determines the reaction force from the bonds in all degrees of freedom. The spring constant is represented in the default function as the spring constant of the streptavidin-biotin bond. The spring constant required is the resulting force from a change in length, which depends on the entire system of linkers and receptors. It is prudent to investigate the sensitivity of the model to this parameter.

Figure 4.32 demonstrates that for large spring constants there is a linear relationship between the logarithm of kBond and the logarithm of the decay. For low k_{bond}, below $0.003Nm^{-1}$ there is significant deviation from this relationship.

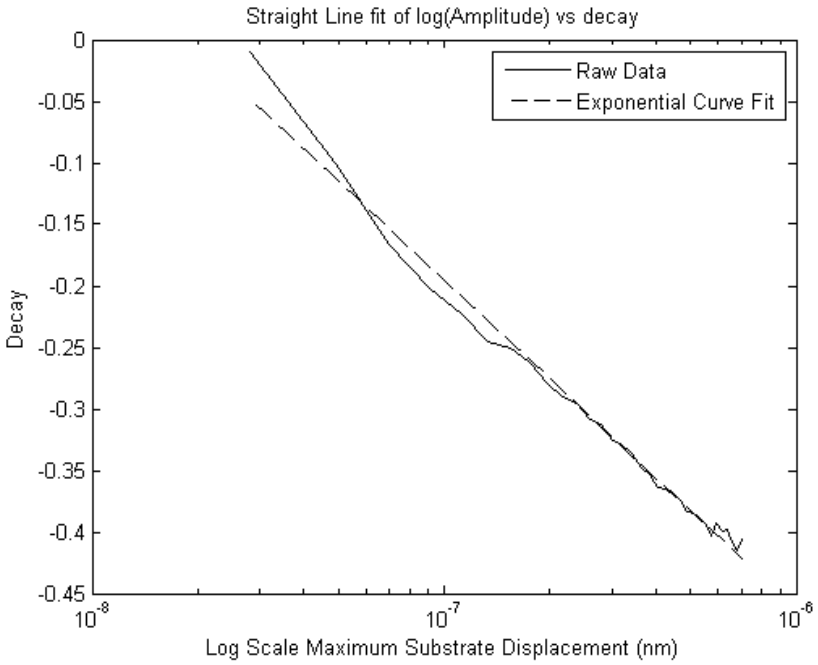

Figure 4.31 Linear curve fit of the fitted decay parameter plotted vs. the natural logarithm of the maximum substrate displacement

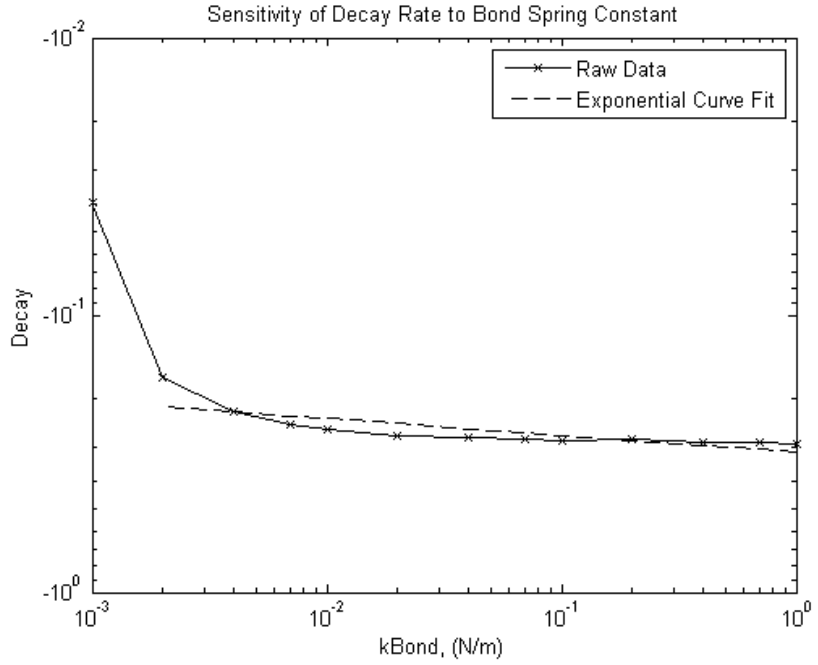

Figure 4.32 Natural logarithm of the decay parameter plotted against the natural logarithm of the kBond parameter

Figure 4.33 shows that there is not a strong dependence on the number of bonds, more bonds increases the reaction force, but the $decay$ parameter measures the decay of a function that is already normalised by the number of bonds.

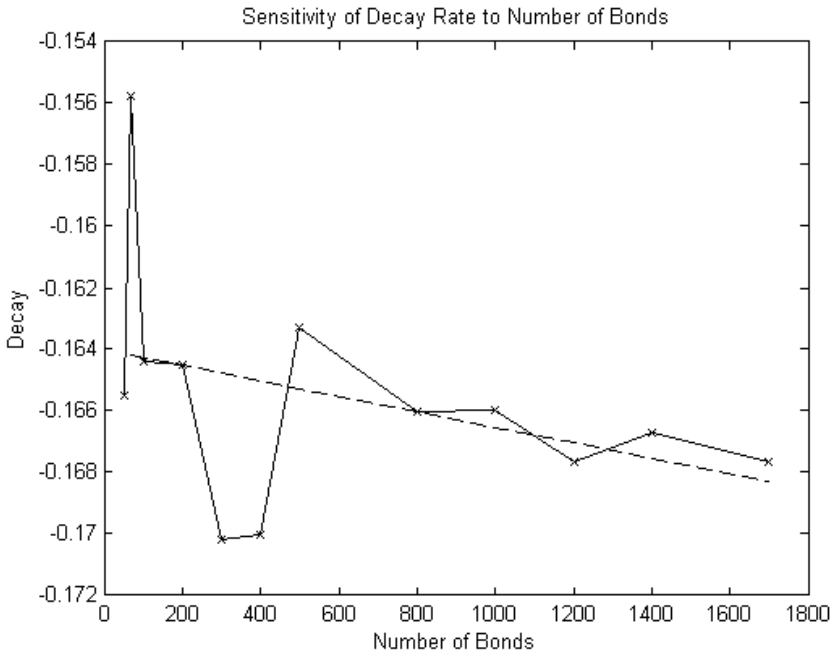

Figure 4.33 Decay parameter plotted vs. the number of bonds

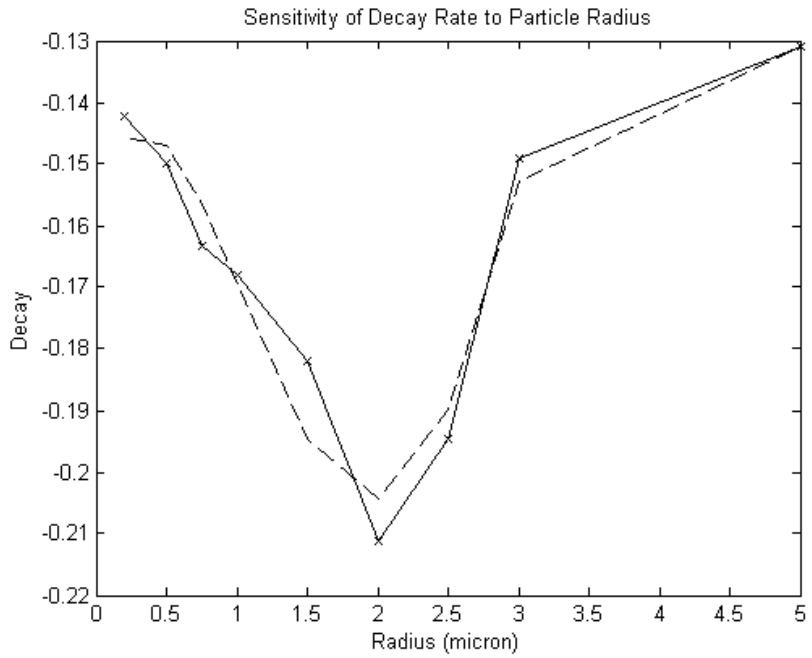

Figure 4.34 Decay parameter plotted vs. the particle radius

The response with changing radius shows that there is a minimum in the decay rate corresponding to 2 micron. The results for changing radius are determined for constant N. The effective bond density is increased for small particles and decreased for large particles. Large particles have higher mass and relatively fewer bonds compared to the mass but exhibit slower decay due to the dependence of bond-force on bond extension which is restrained by high reaction forces.

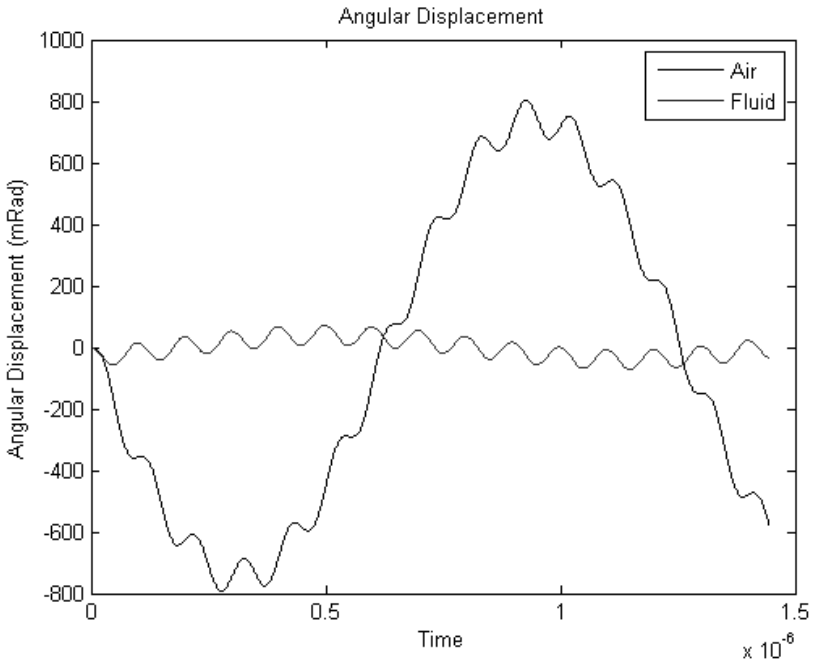

Figure 4.35 Angular displacement vs. time in ambient air

The results presented so far are a fraction of what could be produced and analysed using the model. The simulations are configured for ambient air because this is the circumstance of most bond rupture experiments undertaken by our team. Figures 4.35 and 4.36 show the change in angular displacement caused by enabling fluid drag. In liquid the angular displacement is reduced during fluid operation. The particle centre of mass follows the surface oscillations more closely because there is more damping on its motion. A greater reaction force from the bonds contributes to this along with the other forces on the particle. This is expected as experimental results suggest that particles which cannot be ruptured in air can be ruptured in fluid.

4.9 Chapter Conclusion

In the beginning of this chapter, Cooper's force was discussed and evaluated for the spherical phantom particles. This force has been compared with the total force on the particle and the bond-reaction component of the total force. The body of work on single-bond force spectroscopy was briefly reviewed. Further comparison has been drawn to the single-bond experiments conducted on AFM. In both cases we find that this model yields comparable forces and can conclude that there are several hundred, possibly thousands of bonds between the particle and substrate.

Many analogies were considered during the investigation of binding of particles and appropriate analyses. An earthquake is a natural situation where buildings are subject to base excitation. Buildings are supported by many parallel supports akin to the multiple bonds in

parallel. A pure mechanical analysis of the linkage between particle and substrate was found to be inadequate for the determination of the force applied to the bond.

As with single bonds the rupture of single particles is closely approximated by an exponential decay where the rate is approximated as a function of the instantaneous conditions of the particle. This serves to even out the high frequency effects of the substrate motion considerably shortening the computation time for further analyses.

When a bond is stretched it has an additive effect on the total reaction force. Therefore, in the presence of bonds, we expect lower displacement in all degrees of freedom for similar surface excitation amplitude.

The final solution, while still a mechanical approach offers more of a continuum treatment of the interaction area. A model is discussed where the attachment is considered across an area of interaction. The force is not constant across this area during shaking and thus the instantaneous force on each bond is used to determine the probability of failure. The determination of the probability of failure is based on the propagation of the force on the bond in a long-time experiment. For the entire particle we arrive at the outcome for this chapter – the failure rate of a particle-substrate connection as a function of the particle, its binding parameters and the displacement of the substrate.

The key variables of interest are the particle radius, substrate displacement amplitude and oscillating frequency, the number of bonds between the particle and the bond constants. Particle radius and the transducer frequency are precisely controlled and constant across the entire transducer and between experiments. In real bond rupture experiments the rest of the variables are subject to variation of known distributions. This is discussed in the next chapter.

The model developed is flexible and easily modified to explore the effects of changes to the phantom particle, transducer or chemistry going forward. Core relationships have been demonstrated between the decay parameter and the fundamental variables. These relationships will be used to simulate the behaviour of bond rupture devices in the coming chapters.

The effects of physical interactions have been maintained in this model. This is important for the consideration of non-phantom targets, and for the consideration of non-specific binding. Looking towards detection of bacteria, for example, bacteria may be more compliant than the phantom particles, and as such have different contact radius and force constants.

5. MODELLING BOND RUPTURE DEVICES

5.1 Introduction

The previous chapter explored the many variables that affect the forced rupture of a particle by base excitation. This manifested a single parameter decay constant for a single particle. In this chapter, the results are first used to model an idealised bond rupture transducer. Subsequently, QCM bond rupture is simulated. This is achieved by considering the distribution of surface forces, the function of applied oscillation amplitude and the effects of mass on the QCM to simulate bond rupture experiments. The simulations are validated by comparison to the experiments presented in Chapter 3.

The validated results are used to model and quantify the effects of a number of methodology changes and alternative transducers. An alternative bond rupture transducer and methodology is developed. The model is developed in several parts; first the constant amplitude experiment is emulated, followed by the traditional amplitude ramp.

5.2 Idealised Bond Rupture Device

The strength of adhesion of multiple bonds in parallel is a complicated situation. The previous chapter developed a single decay parameter that is a function of many variables. This chapter uses the term 'survival probability' to describe the probability that a particle is attached at a given instant in time. Following the previous chapter

$$p_{sur}(t) = e^{-decay \times t} \tag{5.1}$$

where $decay$ is a function of the maximal displacement amplitude, oscillation frequency and particle radius, to name a few. When this function is determined, the problem of parallel bonds becomes less complex as the effect on the particle can be closely approximated. Knowing the distribution of the variables that determine the decay of particles, Monte-Carlo analysis of the known distributions is undertaken.

The first step in the modelling of bond rupture devices is to consider an idealised device in which the inputs to the decay function are constant. The ideal bond rupture transducer provides uniform base excitation over a finite area. Over that area the surface excitation is perfectly uniform. Particles are bound to the substrate with a number of bonds that varies randomly within some reasonable range.

A constant amplitude scan on the idealised device results in a distribution of rupture events despite all particles being exposed to the same force because bond rupture is a

probabilistic phenomenon. Figure 5.1 shows the first metric of device performance. The normalised probability of survival is given by

$$p_{norm}(t) = \frac{\sum p_i(t)}{N} \tag{5.2}$$

where $p_i(t)$ is the survival probability of survival of the ith particle at time t and N is the total number of particles attached to the device. The average behaviour determined from sum of the individual probabilities is divided by the total number of particles. This is a useful for deriving average effects such as bulk mass change but does not provide sufficient information for simulation of bond rupture noise.

The second metric of device performance is the simulated bond rupture noise signal depicted in Figure 5.2. When individual particles are simulated the probability of survival decreases with time. For determining a rupture time, a random probability is assigned for each particle. This determines the limit of the probability of survival below which the particle ceases to be attached to the substrate. The rupture time, t_{rupt} is determined by the solution to

$$p_{sur}(t_{rupt}) - p_{thres} = 0 \tag{5.3}$$

where p_{thresh} is a randomly determined value within the range of rupture probability. p_{thres} is dependant on the number of bonds between he particle and substrate and the particle size.

The determination of the rupture time of each particle provides the temporal location of a bond rupture event. An impulse train is generated with unit impulses at each time step where

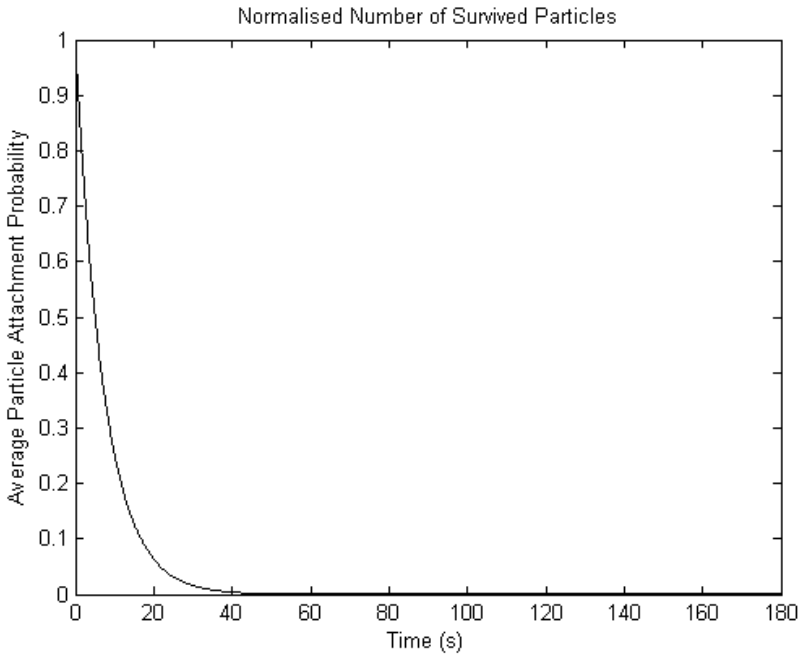

Figure 5.1 Normalised number of survived bonds on an idealised sensor with constant oscillation amplitude

a rupture is located. This impulse train is cross correlated with an arbitrary exponentially decaying signal. This signal represents the 'noise' of a single bond rupture. Although the nature of this noise is not known at this time, it is assumed to be a wide band signal which decays with time. Cross correlation builds up a simulated noise signal which is highest when many rupture events are occurring in a short time span. Figure 5.2 shows the simulated rupture noise signal for the idealised constant amplitude scan. It is evident that much of the rupture occurs early in the scan.

When the oscillation amplitude of the substrate is gradually increased from zero the shape of the normalised probability curves and bond rupture event distributions changes. The onset of bond rupture is delayed until the amplitude of the surface oscillations is sufficient. This effectively distributes the bond rupture events over a greater time. Figure 5.3 shows the results of a linear amplitude ramp on an idealised bond rupture device.

The bond rupture histogram is a more familiar treatment of the rupture force relationship. Single bond experiments utilise the histogram to demonstrate the variance of bond rupture force for identical conditions. Figure 5.4 is the histogram of the idealised bond rupture device, it is beginning to resemble that of the single rupture scans.

Figure 5.5 shows the rate of bond rupture and locates the time, and hence amplitude, at which the particle survival probability is falling fastest. This is not a quantitative determination of the position at which most rupture is occurring because the fastest rate of decay of bonds and the time at which most bonds rupture is not exactly coincident.

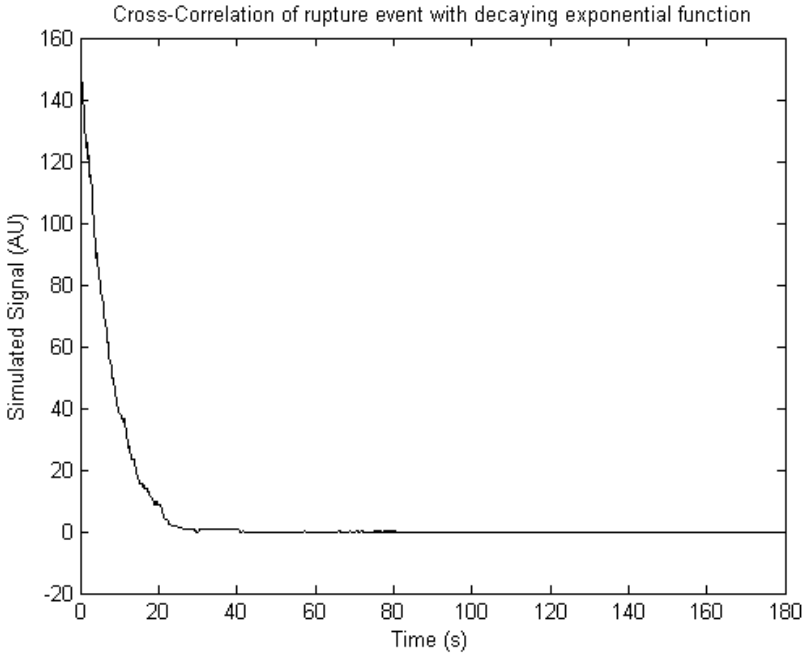

Figure 5.2 Bond rupture events plotted against time

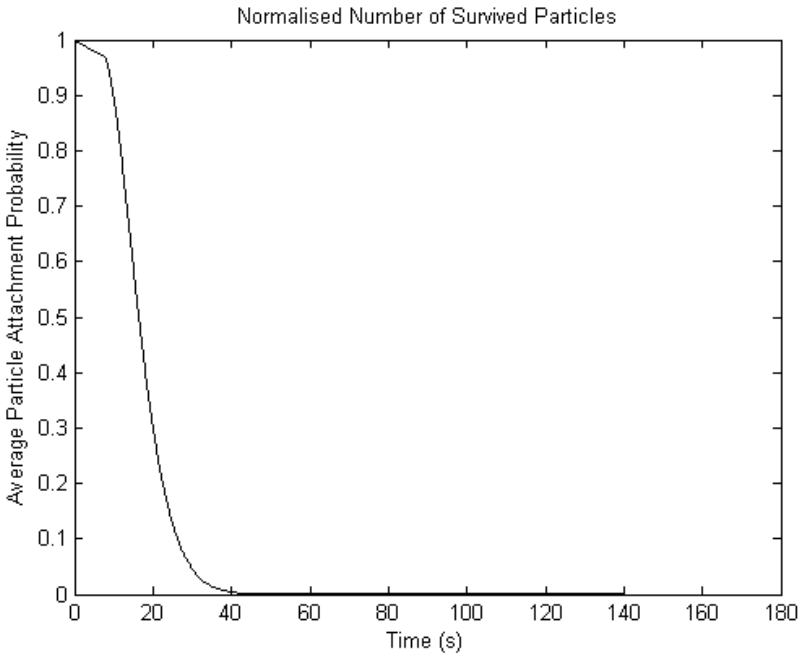

Figure 5.3 The sum of the probability of survival of all particles adhered to the device approximates the number of particles attached

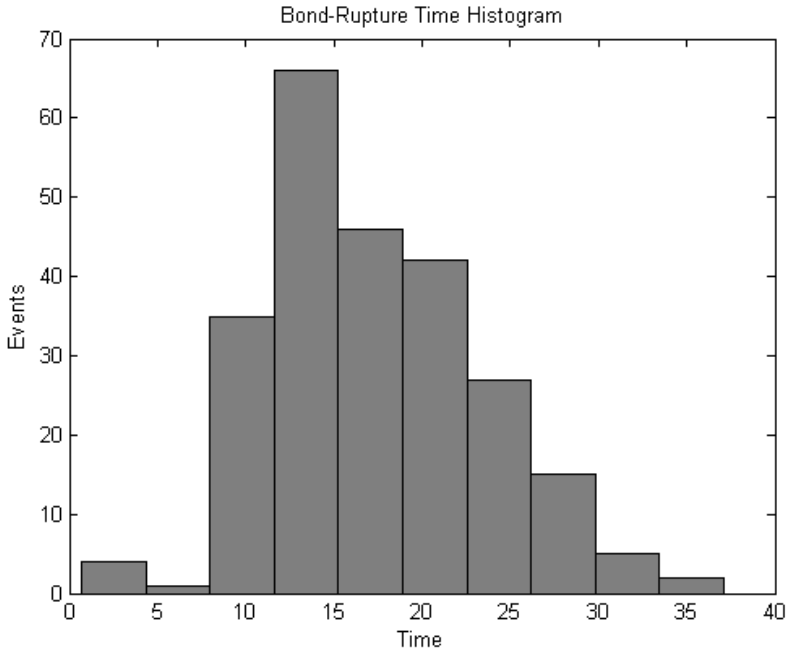

Figure 5.4 Bond rupture histogram of idealised bond rupture device

For comparison of different experiments a measure of the width of the peak is useful. The 3dB width, that is the width of the peak at half the maximum value in Figure 5.5 is 13.7s. It is desirable for clear and concise results that this time is as small as possible, thus concentrating frequency change and bond rupture noise into a short time.

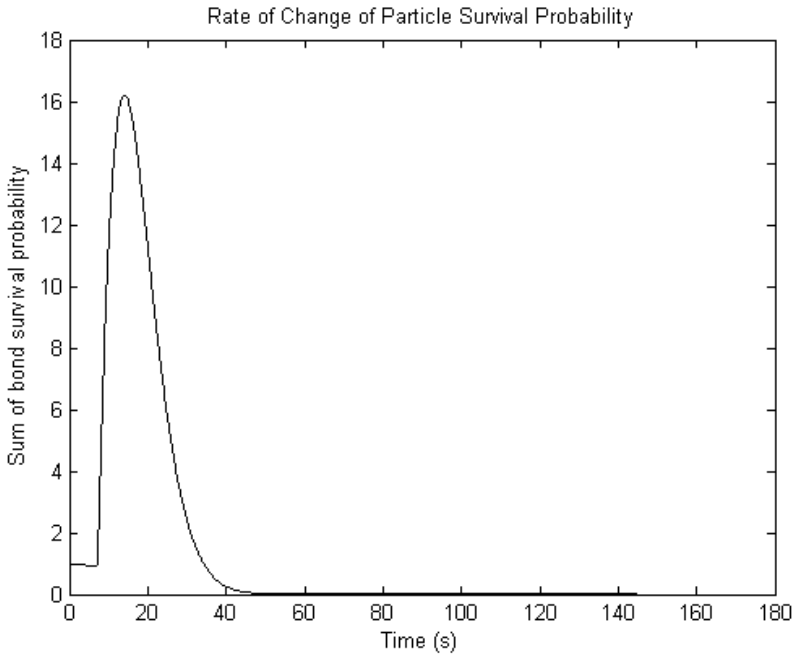

Figure 5.5 The derivative of the sum of survival probabilities is analogous to the bond rupture histogram and useful for assessing the most likely rupture point

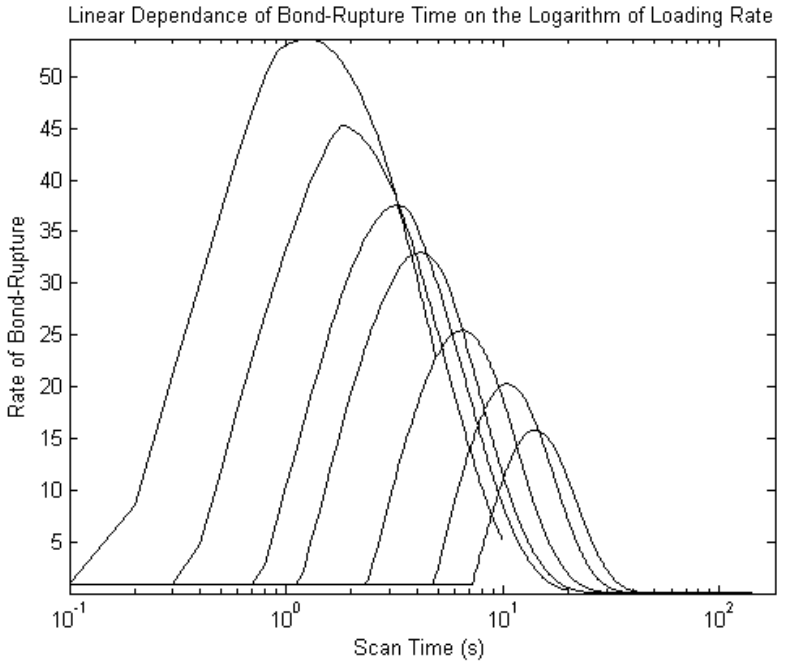

Figure 5.6 The location and magnitude of the peak in the force distribution is proportional to the logarithm of the total scan time

During an amplitude ramp scan the amplitude at a given time is the product of the loading rate and time. The location of the peak changes when the loading rate of the simulation is modified. Figure 5.6 shows the relationship. The location of the peak is a linear function of the logarithm of loading rate. This is consistent with single bond rupture literature from which part of the particle model in the previous chapter was derived. The model indicates that the loading

rate of the bonds impacts at what force the particle is most likely to detach. The 3dB width of the curves in Figure 5.6 is shortest for the fastest scan. This indicates a confinement of bond rupture events to a shorter time. However the amplitude is increasing at a higher rate and the range of forces covered in that shorter time is greater. Longer scans apply lower forces to the particle for a longer duration; this increases the likelihood that the particle will rupture at a lower force.

It is evident that even in the best possible circumstance the particle rupture events are distributed in time. In real QCM experiments there is even greater distribution of rupture events because of variation across the transducer. The simulation is amended hereafter to better reflect the QCM transducer used in bond rupture tests.

5.3 QCM Bond Rupture Modelling

Bond rupture on QCM is modelled for comparison to real experiments. For this purpose it is necessary to determine the number of particles on the surface of the QCM. It is prohibitively time consuming to perform this exercise for every QCM experiment performed in the lab. The number of phantom particles bound to the QCM is not precisely known, but is estimated from photographs of typical preparations. Figure 5.7 (a) shows a microscope photograph taken of 2µm diameter phantom particles adhered to the substrate. The image is processed to isolate only the particles (b) and the ratio of areas is calculated to determine the QCM coverage. This represents the best case binding of particles. The grouping of particles in the image suggests that some particles are bound, not to the substrate, but loosely to other particles. These are bound non-specifically by physical interactions only and are expected to rupture when subject to small excitation. It is expected that the QCM coverage of specifically bound particles will is less than 1%.

a) b)

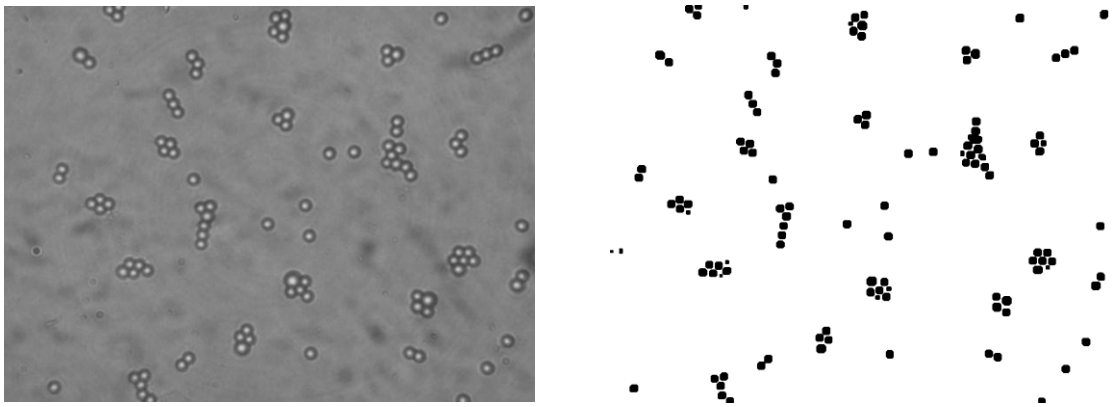

Figure 5.7 a) Microscope image of QCM surface, b)determination of particle density by image analysis

$$\frac{A_{particles}}{A_{total}} = \frac{40228}{1228800} = 3.27\% \tag{5.4}$$

Given that the electrode area $28.3mm^2$ it is estimated that $1.05mm^2$ will be covered by particles. With the particle area $3.14 \times 10^{-6}mm^2$ there would be some 330 thousand particles on the surface with 100,000 bound specifically. This is more than can be reasonably simulated numerically, and more that is necessary. This number is reduced in simulation so that an average can be determined and the results extrapolated to the entire sensor.

5.3.1 Constant Amplitude Scans

The most significant difference between the QCM and idealised device is the distribution of the average probability of survival arising from the QCM amplitude. Using a priori knowledge of the QCM distribution the particle surface displacement is determined as a function of particle location. Displacement and frequency sensitivity are both shown to exhibit Gaussian distributions as is direct result of the distribution of amplitude and hence acceleration. A Gaussian distribution is applied to the surface amplitude to account for the distribution of displacement across the QCM such that

$$A(r) = A_0 e^{-\left(\frac{r}{c}\right)^2} \tag{5.5}$$

where r is the distance from the centre of the QCM electrode to the particle and c is the Gaussian parameter of the decay function. Figure 5.7 demonstrates the form of the amplitude function. The amplitude at the centre of the surface, A_0, is determined using the Borovsky

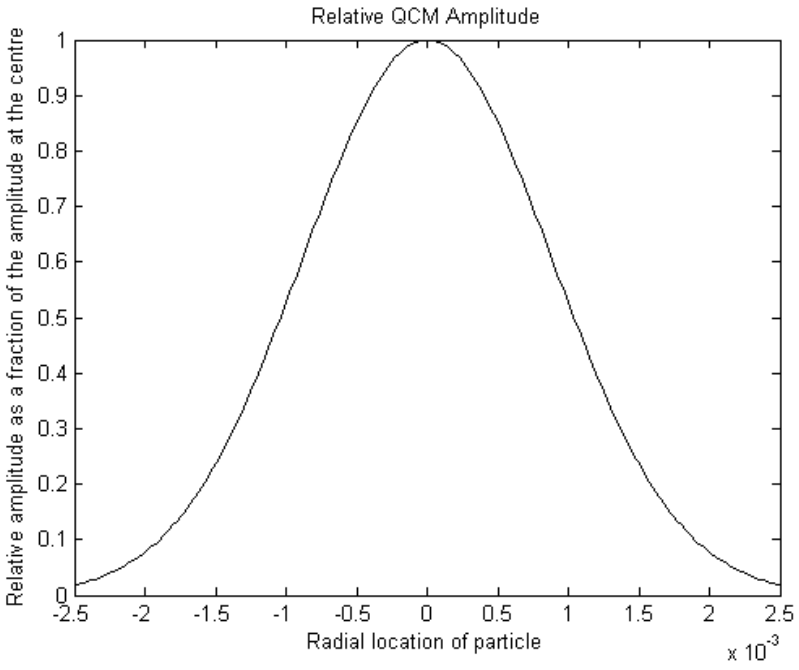

Figure 5.8 Amplitude distribution as a function of radius

equation. Using the rupture time results and the mass of the particle the mass change on the QCM surface is determined as a function of time. This is consistent with experimental results. Figure 5.9 shows only the center area of the QCM is clear of attached particles when the experiment is incomplete. The bond rupture experiment was terminated at low amplitude.

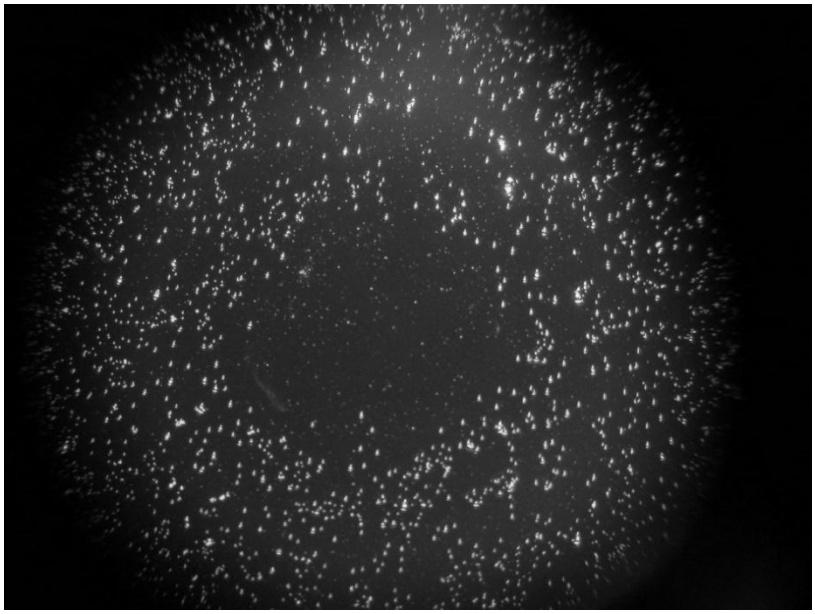

Figure 5.9 Post bond rupture QCM image showing concentration of rupture in centre of transducer

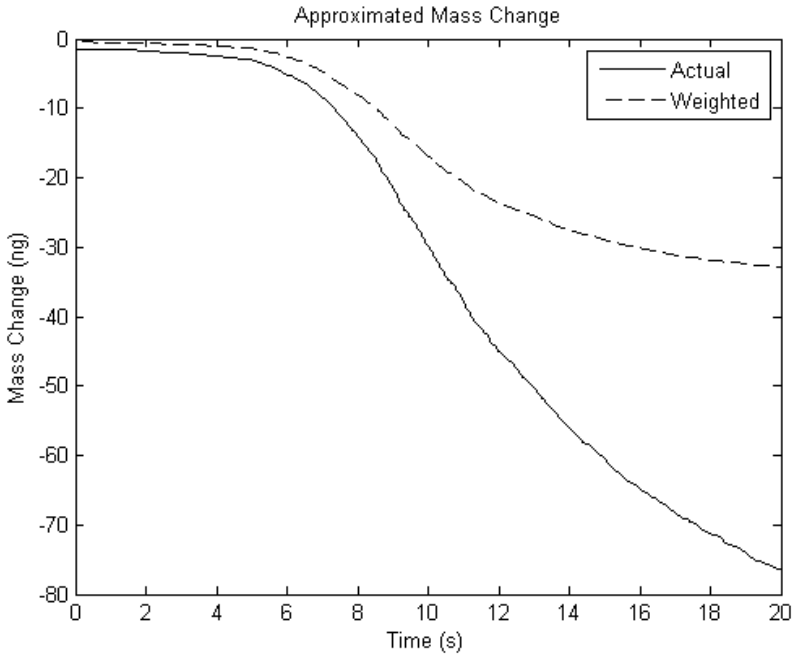

Figure 5.10 Assuming bond breakage occurs at a defined probability then the mass change can be determined

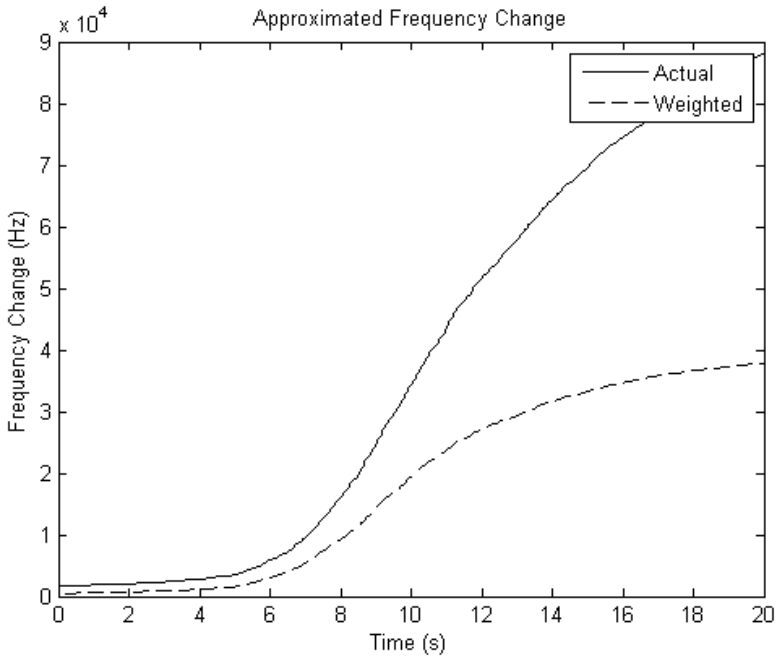

Figure 5.11 Mass change can be translated to frequency change

The real mass change is weighted according to the radial position of the particle to account for variation in the mass sensitivity across the QCM electrode. Figure 5.10 shows the actual mass change on a ramped QCM device subject to constant amplitude scan.

The weighted mass change is lower because most of the area of the QCM electrode is oscillating well below the oscillation amplitude at the center. The sensitivity to mass change falls away with radius. These results consider a distribution on the oscillation amplitude and mass sensitivity, and qualitatively agree with real bond rupture experiments.

Figure 5.11 shows the translation of the mass change to a measured frequency change using Sauerbrey's Equation. Sauerbrey's Equation is based on the adhesion of uniform thin film layers to the QCM. This is not the case in bond rupture experiments such as these where the particles are discrete and cover around 1% of the electrode surface. It is expected that the relationship is sufficiently close to allow comparison of experimental data.

The simulated rupture events can be visualised in an alternative way as demonstrated in Figure 5.12. Here the survival time of the particle is plotted against the particle radius. Many particles do not rupture in this short duration experiment.

When fewer bonds are considered, the results can be visualised effectively as individual probability functions. This shows that the probability functions are not evenly distributed and that many particles experience similar decay rates. There are fast decaying particles near the centre which have the greatest effect on the measured frequency and mass change. The

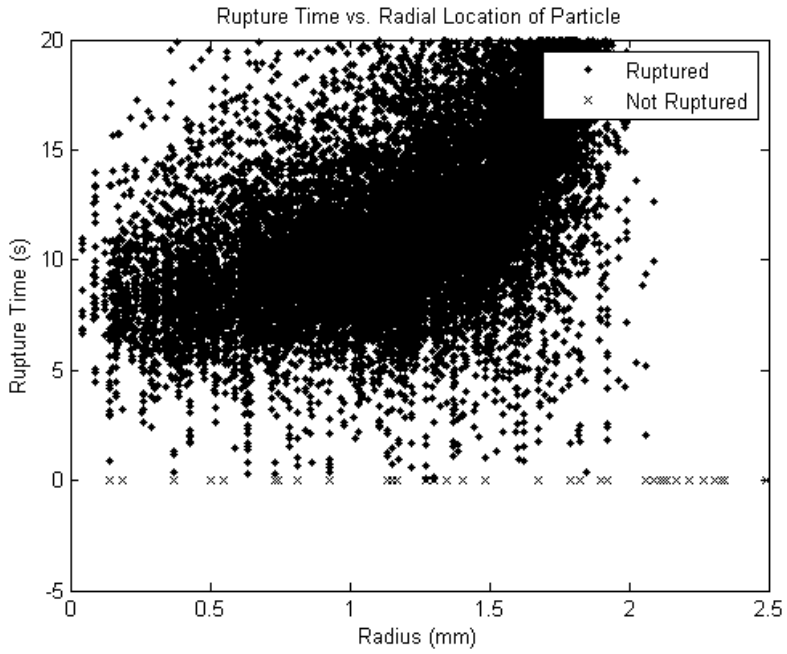

Figure 5.12 Survival time plotted as a function of radial location of the particle

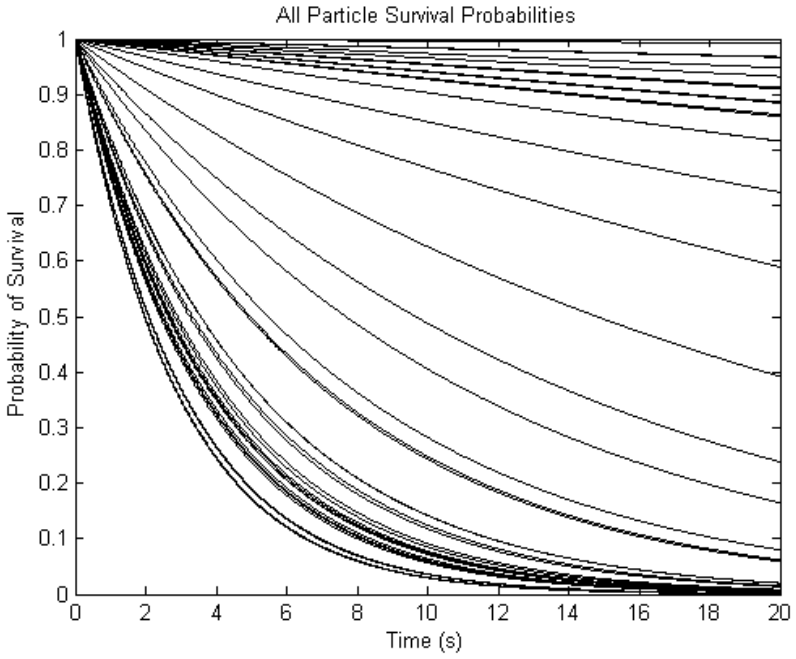

Figure 5.13 Many individual survival probabilities as a function of time

particles located farther from the centre decay very slowly and effect the measurand less. These soften the response of the experiment.

When the results from Figure 5.13 are summed for all particles, the combined probability of survival is used to estimate the number of bonds surviving at a given time. This in turn can be converted to an average change in resonant frequency. Figure 5.14 is this curve plotted alongside real data from a constant amplitude experiment. The experimental data is from an

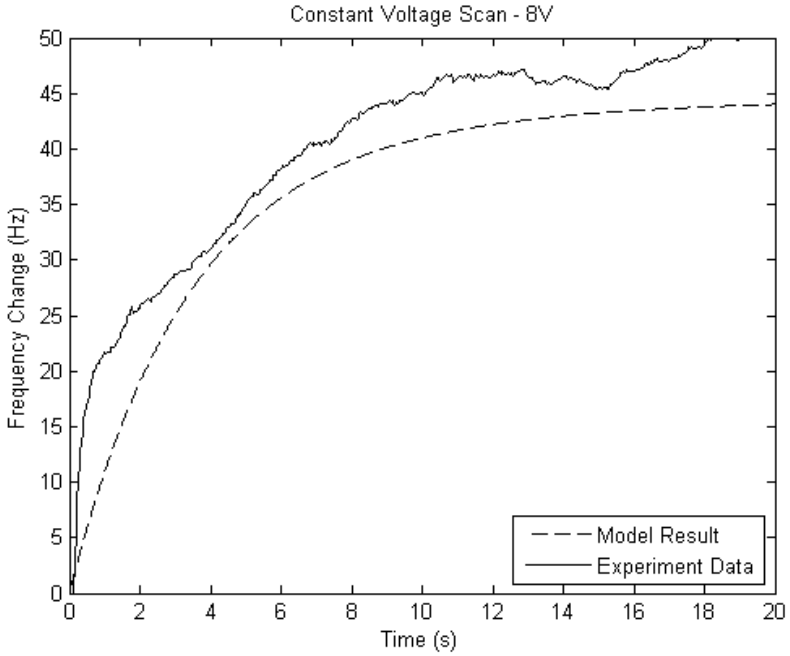

Figure 5.14 From an approximated number of particles the frequency change is compared to experimental data.

8V voltage scan and the simulation amplitude was determined from this using Borovsky's Equation.

The simulation results presented in Figure 5.14 trend toward the same asymptote as the experiment results. This is tuned by approximation of the number of bonds originally attached to the particle. This is achieved by manipulation of the coverage parameter. Density of particles is controlled by the protocols for binding the particles. This manipulation in simulation corrects for errors in the particle distribution and the mass-change to frequency-change conversion.

There is good agreement with the QCM simulation and experiment results for constant amplitude scans. Most bond rupture scans ramp the amplitude up with time and is considered in the following section.

5.3.2 Linear Amplitude Ramps

The QCM simulation is modified to include an amplitude ramp at a loading rate dictated by the operating range of the equipment and the experiment duration. Figure 5.15 shows the normalised probability of survival for a linear amplitude ramp.

It is helpful to visualise the rupture time as a function of particle radius. There is a clear spread of particles and those nearer the edge take longer to rupture. Figure 5.16 clearly demonstrates a concentration of rupture events in time. Figure 5.17 shows the cross

correlation of the rupture impulse train and an arbitrary noise signal shows that there is a clear peak in the noise, but the noise continues for the duration of the scan.

The frequency change determined from the average probability model and the probability threshold model are demonstrated in Figure 5.18 and compared to the real frequency change data. There is good agreement between the simulated and real curves. The real data is from a amplitude ramp experiment using two micron phantom particles. The frequency change during

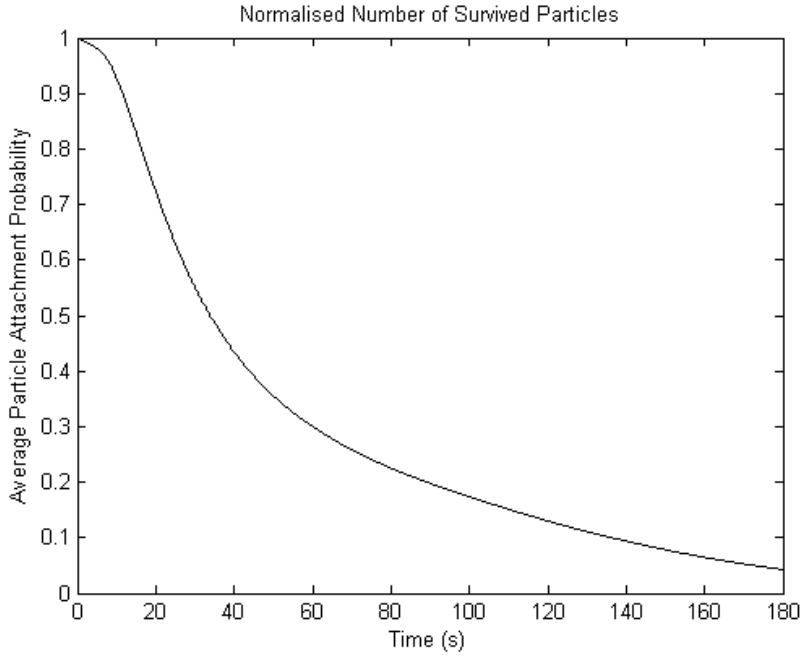

Figure 5.15 Smooth decay is symptomatic of the distributed rupture events

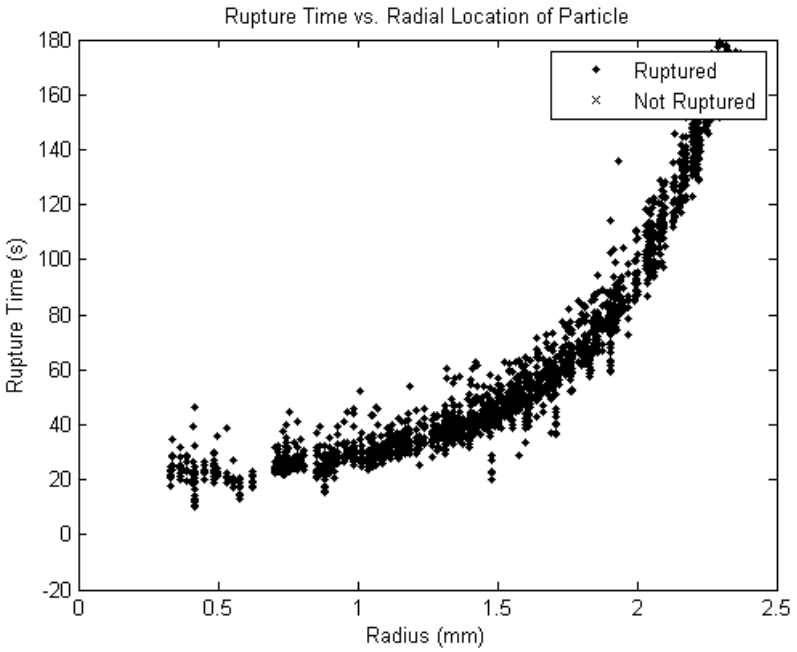

Figure 5.16 The rupture time as a function or radius indicates the origin of the distribution

the first 20s of the experiment is attributed to the rupture of weakly bound particles adhered to the substrate and the increases in temperature of the QCM driving away moisture. These effects are not explicitly included in the device simulation as the amount and strength of such bonds varies greatly and is difficult to quantify.

The threshold model result is more closely aligned with the experimental results because the threshold model considers a finite probability of survival below which the particle is certain

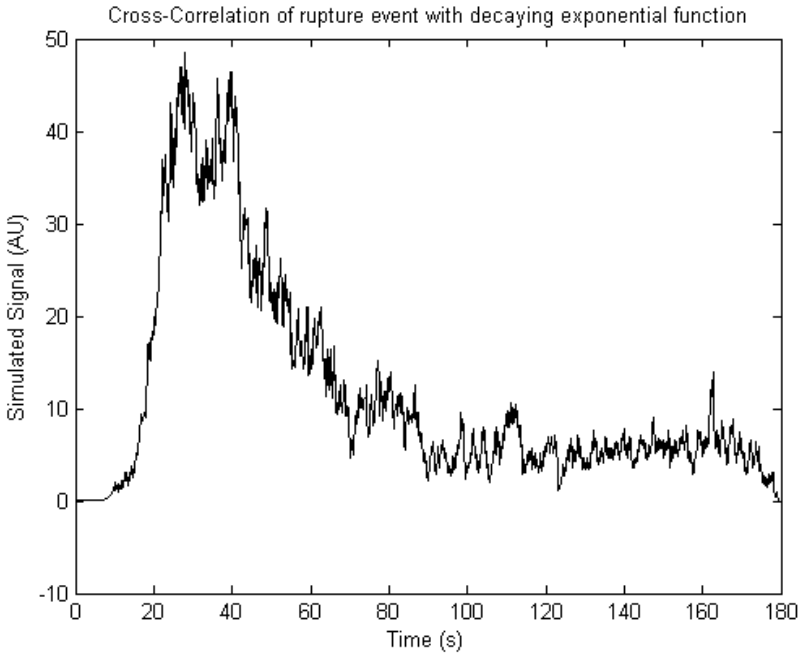

Figure 5.17 Simulated rupture signal is concentrated at the start of the scan

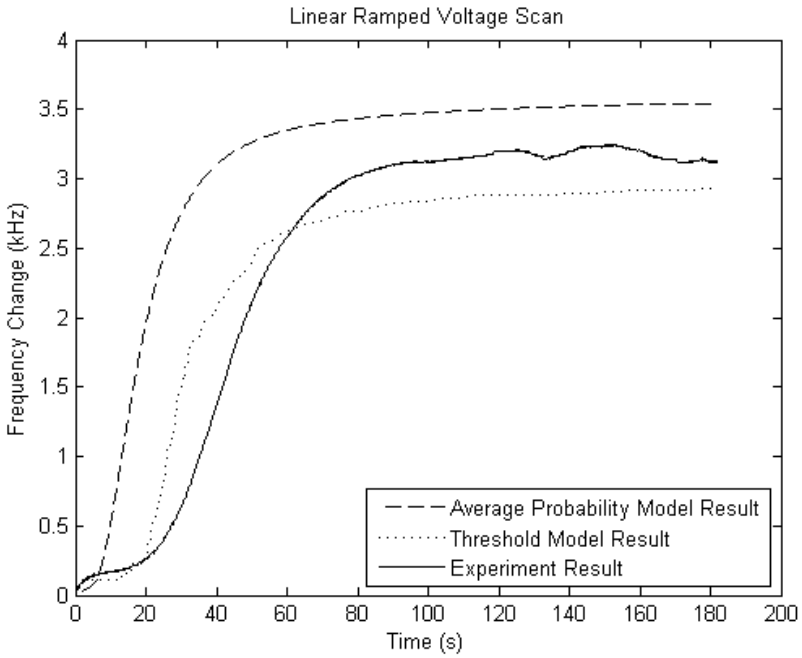

Figure 5.18 The form of the simulated frequency change is similar to the experiment results

to rupture. The average probability model arises from the sum of all probabilities so, if all the probabilities are around 0.5 this model predicts 50% particles have ruptured when in reality it means that 50% of the individual bonds between particle and substrate are likely to have ruptured and the particle itself is still attached by the remaining bonds.

The range of the randomly determined rupture thresholds can be manipulated to provide even closer aligned results however, the amplitude ramp simulation of Figure 5.18 are in close agreement and is sufficient to further investigate the bond rupture phenomena.

5.3.3 Mixed Particle Scan

An experiment is designed and undertaken that mixes three species of phantom particle that have different rupture strengths. This is achieved by using particles of three different diameter: one, two and four micron. For simulation of these in bond rupture experiments, the amplitude-decay relation was determined for each particle size using the model developed in the previous chapter. The fitted function consists of two exponential regimes, the transition between the regimes occurs at 133nm displacement amplitude. Figure 5.19 shows the simulated decay of particle survival as a function of amplitude and the fitted relationship used in this simulation.

From photographs of the surface (Figure 3.27) it is evident that the species do not exist in equal quantities. More one micron particles are adhered to the surface than other species. For the bond rupture technique to succeed each species should be distinguished during the bond

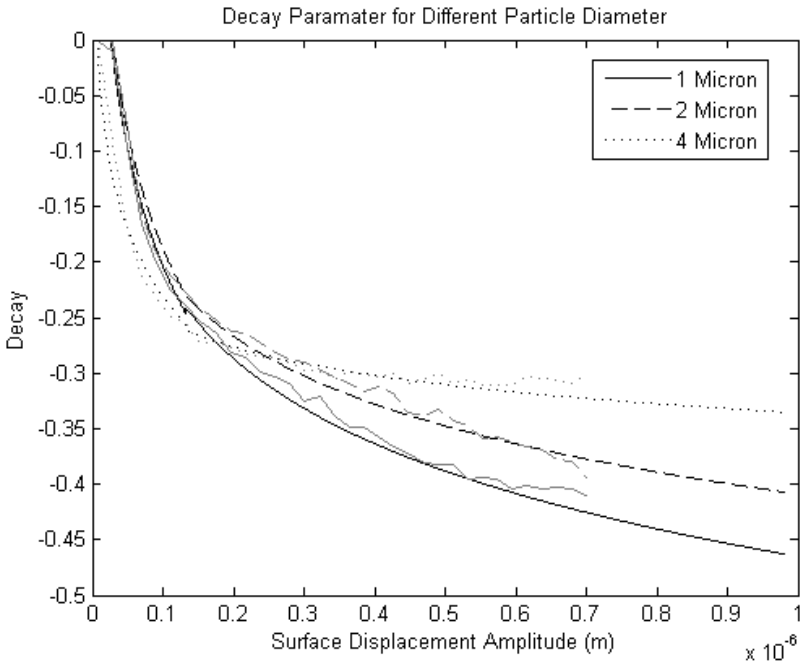

Figure 5.19 Oscillation amplitude-decay relation for three particle sizes

rupture scan and a quantitative measure of their concentration is required.

During the scan the effect of the individual particles cannot be separated. The frequency change of mixed particle scans does not look remarkably different to single particle experiments and it is difficult to visualise the different species. In simulation, however, the influence of each species of particle is plotted explicitly as demonstrated in Figure 5.20 and Figure 5.21. The thick line represents the summed effect as observed by the equipment, and the other lines represent the constituent contributions of the individual particles.

It is evident that the two micron particles have ruptured before the others and that the one and four micron particles exhibit very similar behaviour. Similar analysis of the rates shows that the particles have different rupture strengths, as indicated by the different peak locations. The combined rate of change does not give any indication that there are multiple species of particle present on the surface.

As a final comparison, Figure 5.22 shows the simulated frequency change is plotted alongside the experimental results. The one micron particles are shown to have a large effect on the frequency change, this is because they are present in the simulation in greater quantities than the others. There is good agreement between the total frequency change curve and the experimental data but there is no indication that there is more than one species present. The bond rupture events are too distributed and the contributions from each species overlap.

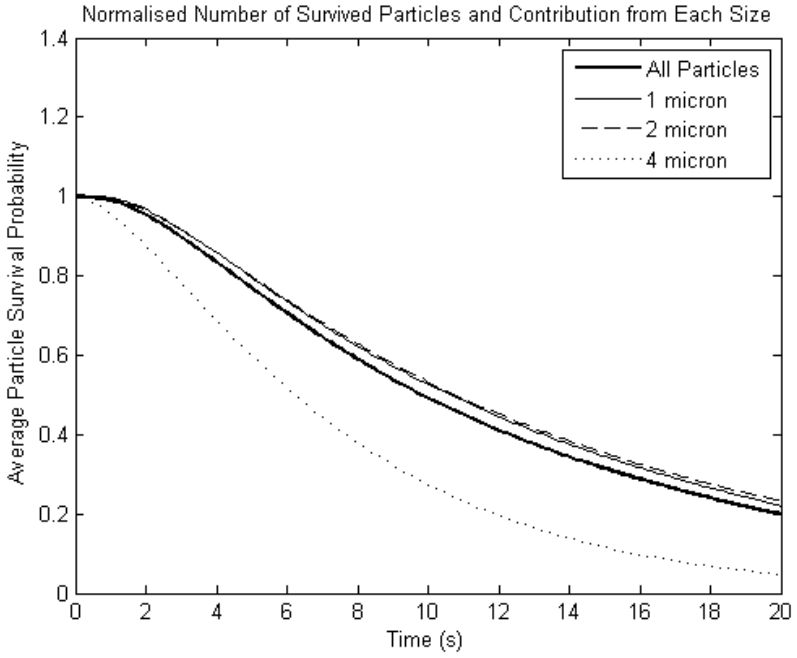

Figure 5.20 Probability of rupture of particles does not clearly indicate that different radii are present

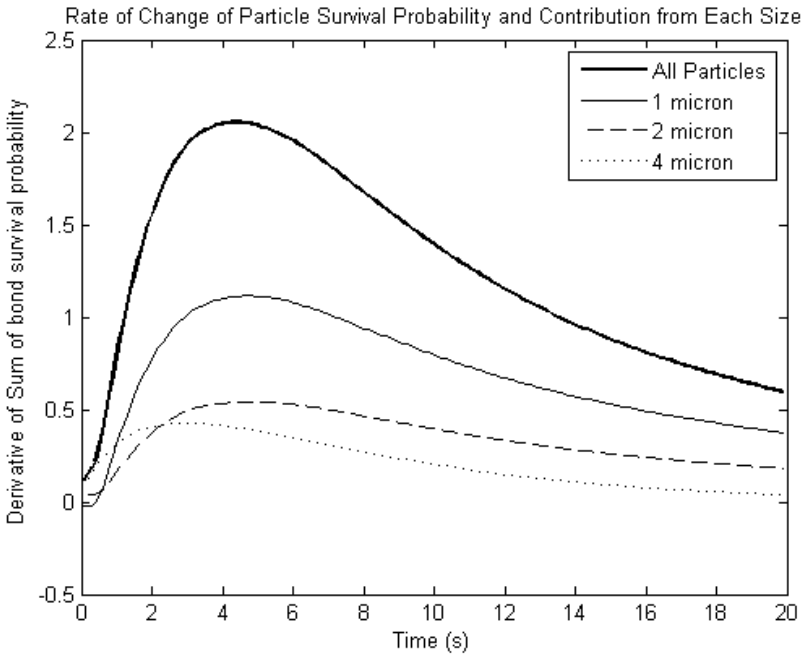

Figure 5.21 Rate of change of particle survival of all particles combined and the constituent types

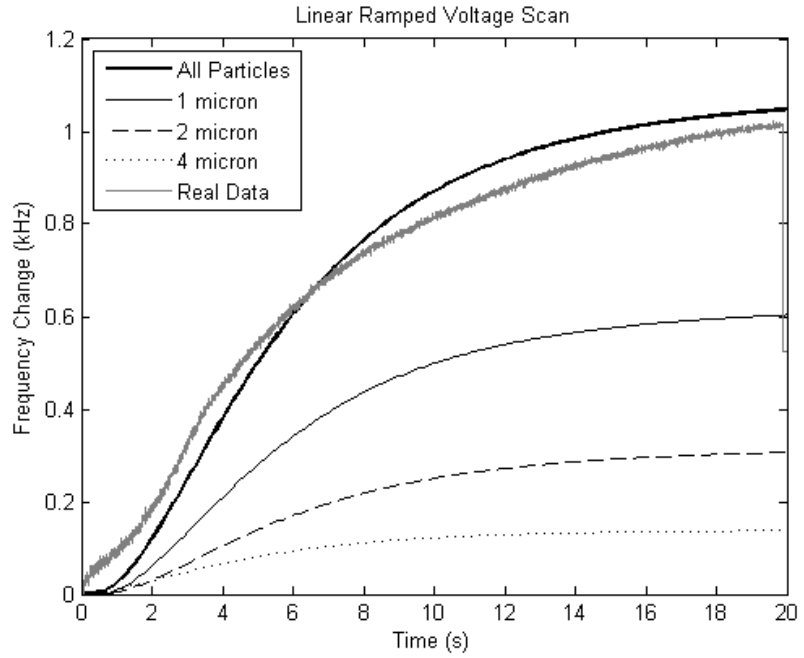

Figure 5.22 Simulated frequency change of multiple bond experiments

5.3.4 Alternative Amplitude Functions

The simulations presented so far in this chapter align very well with the experiments presented in Chapter 3. There is good agreement between the simulated and real data and the simulations have assisted in the identification of core problems in the bond rupture system and methodology as presented thus far. The model is well placed to test improvements to the transducer.

The bond rupture hardware used in the lab is designed for linear amplitude ramps. In the pursuit of a better bond rupture experiment methodology, different driving functions are considered first by simulation. The principle weakness in the QCM bond rupture experiment is identified as the wide distribution of bond rupture events for identical particles. The first hypothesis to be tested by simulation is the amplitude ramp function. It is hypothesised that coarser increments in the ramp function will yield miniature constant amplitude scans at each step, and that the rupture events will be concentrated at that step.

It is assumed that more bond rupture events concentrated into a shorter time will yield better detection of bond rupture events by noise detection methods. Better detection here means both noticeable frequency change and bond rupture noise. The conditions of the simulation are largely identical to the QCM simulation so that the results can be easily compared. Figure 5.23 shows the maximal QCM amplitude as a function of time.

The survival probability of particles attached to a QCM in these conditions shows steeper falling at the amplitude transitions. The rate of change of the probability is high at the amplitude transitions and falls shortly after. The rate of bond rupture falls to half its peak in 3.1 seconds for two-micron particles. In practice, the QCM displacement will not change in perfectly square steps due to the physical response of the QCM and the time taken to reach new equilibrium. It is anticipated that this would soften the peaks in Figure 5.24, however there appears to be considerable improvement.

There remains an element of bond rupture at each subsequent amplitude step although at

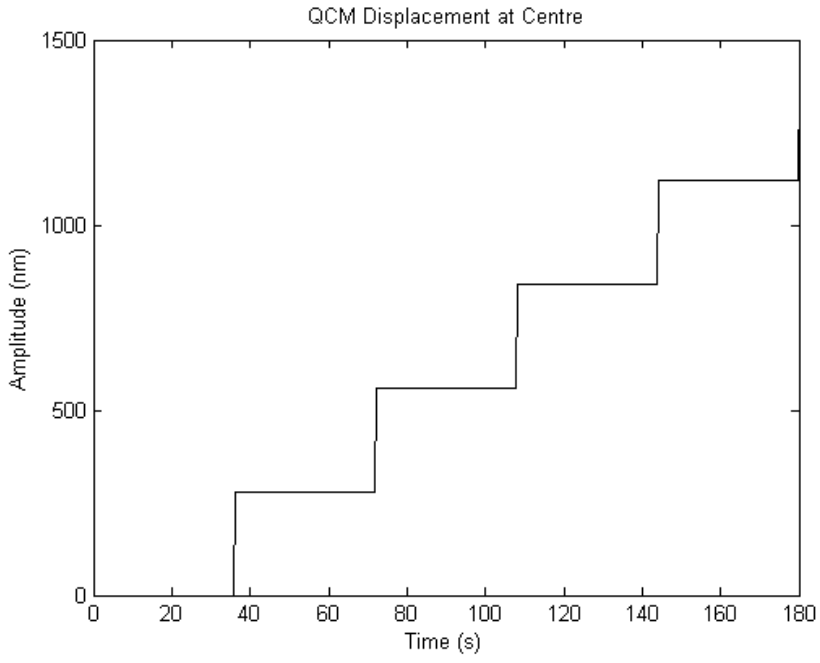

Figure 5.23 Stepwise amplitude function

lower amplitude than the first. Figure 5.25 shows the simulated results of using this methodology on the mixed particle experiment. This time the contribution of each particle species is plotted explicitly.

The revised amplitude function delays the rupture of some particles creating echoes of the main peak at every amplitude step. When the simulation contains several species of particles all exhibit similar behaviour and the revised amplitude function cannot in isolation identify the

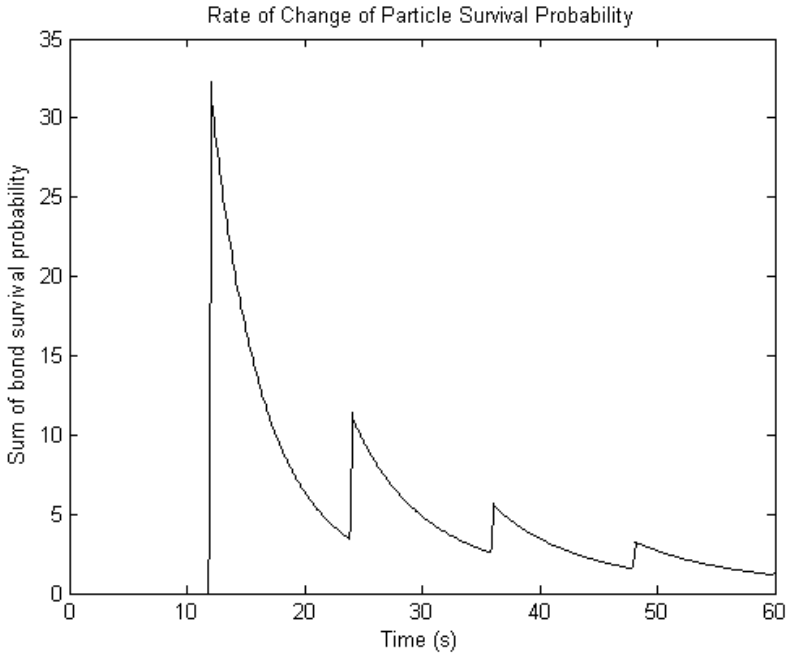

Figure 5.24 During stepwise operation stronger signal results at after the amplitude step

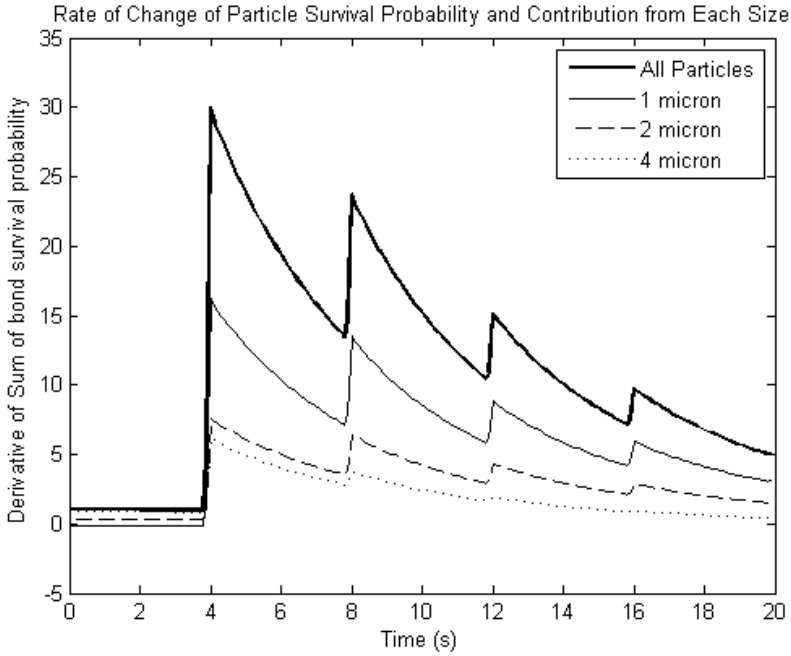

Figure 5.25. Stepwise results showing the contribution of individual species

presence of multiple species of particle. Had this revised methodology been successfully it could have been implemented using comparatively simple software changes. Changes to the bond rupture hardware are considered in the sections that follow.

5.3.5 QCM Electrode Modification

It is conceded that the use of off the shelf QCM transducers intended for thin film mass measurement do not represent the best possible bond rupture device. It is proposed that the QCM electrodes are modified to better suit the bond rupture application. The modifications are tested here by simulation.

Two possible modifications have been identified – the first to be considered below is masking of the QCM binding area, the second is the use of strip electrodes in place of the round electrodes currently used.

The basis for these modifications is the observation of decreased amplitude and mass sensitivity near the edge of the electrode. Figure 5.26 shows the rate of increase of mass on the electrode as a greater radius of the QCM electrode is considered. The area of the transducer covered by bonds is expressed as a function of normalised radius. As more of the QCM is considered, the additional area covered by particles increases linearly because the area increases with the square of the radius. The mass sensed by the QCM is less than that which is attached because the mass sensitivity of the QCM decreases with radius. The apparent mass

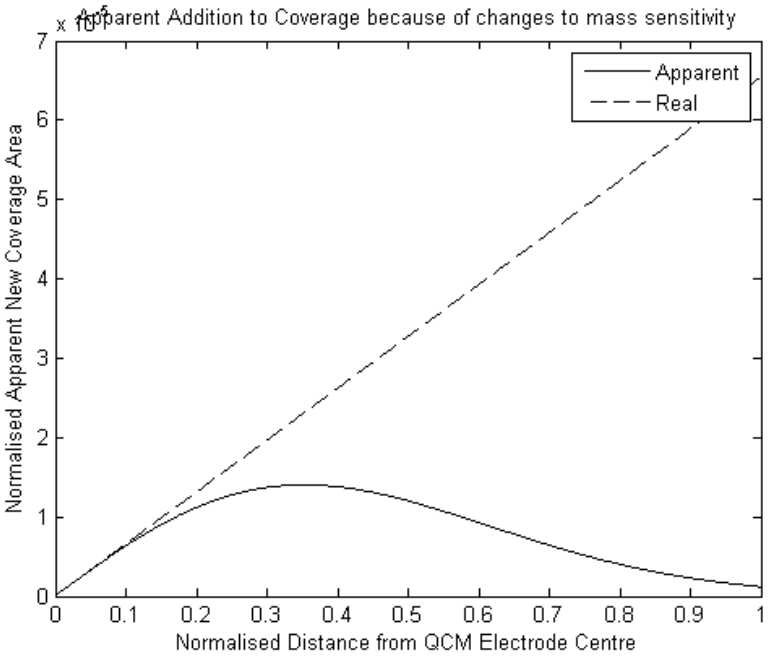

Figure 5.26 The real new mass added to the transducer plotted as a function of radius and the observed mass which is effected by the sensitivity of the QCM

sensed becomes proportionately less and severely affects the response when the rate of apparent mass increased becomes negative. This occurs when the radius is less than greater than $0.35R$ because the relationship depicted in Figure 5.26 is falling below that point.

In the simulations that follow a maximum radius is considered because consideration of a greater area is causing a softer response of the transducer. It is suggested that binding to the electrode beyond this radius could be eliminated to improve the device response. This is not a matter of reducing the electrode size, as the Gaussian falloff of amplitude will realign to the new electrode dimensions. The reduced area is best achieved in the binding stage of the experiment methodology. One or all of the layers in the binding procedure may be blocked by chemical or lithographical techniques.

It is suggested that the QCM electrode be masked with a thin layer of SU-8 epoxy or similar in order to prevent the bonding of the intermediate layers to gold. It is anticipated that this layer will reduce the QCM resonant frequency by some constant factor and will be sufficiently pliable to withstand the stress caused by bond rupture excitation in the medium term. The new structure on the electrode surface may increase physical binding on the region outside the active area.

As an alternative to the masking considered above is that the QCM electrodes have their shape changed by photolithography techniques so that the electrodes are narrow strips with an overlapping area in the centre. This removes the ballast at the top and bottom of the electrode that oscillates with low amplitude. The strips will be aligned with the axis of QCM displacement. It is anticipated that this will not significantly reduce the QCM amplitude oscillation at the edges. Strip electrodes behave similarly enough to round ones and may be better microphones for listening to the noise of bond rupture because a smaller area of piezoelectric is shorted by the electrode.

Figure 5.27 shows simulated results of bond rupture scans using the proposed modified QCM. The results of the strip electrode and masked QCM are closely aligned and have a much better rate of bond rupture and hence rate frequency change. The circular mask is marginally better performing than the strip electrode because there are fewer low amplitude areas of the QCM with binding.

The 3dB width of the rate of change of bond survival probability is used to measure the relative improvement in the devices. This width is 22 seconds for the unmodified QCM. That is

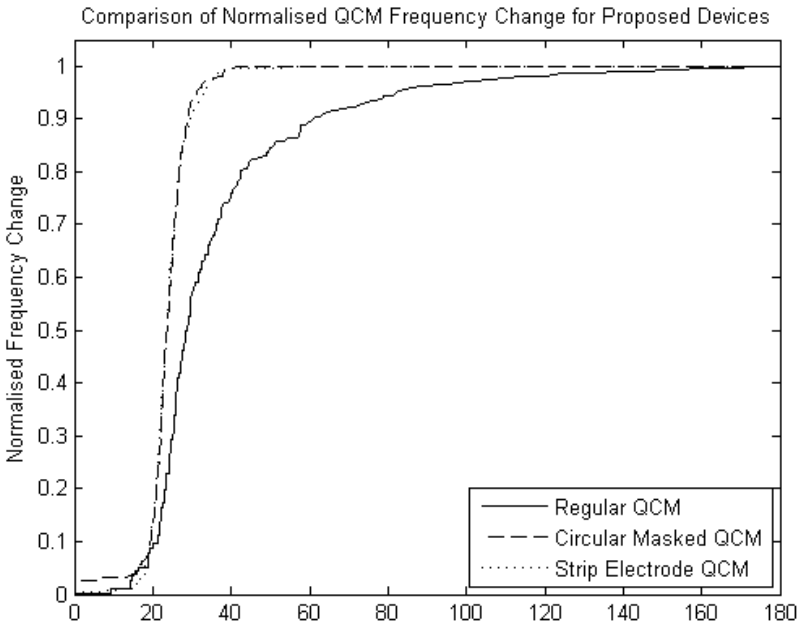

Figure 5.27 Normalised bond rupture frequency change simulations of regular and modified QCM

to say that many of the bond rupture events are concentrated into a 22 second interval. This same measure is 11.5 seconds for the modified QCM effectively halving the distribution of bond rupture events in time. It is anticipated that this would translate into better signal-noise ratio for bond rupture noise detection. Concentration of the noise signal in one interval of time is desired for homogeneous particles. It is evident that either of the proposed modifications has the potential to improve QCM bond rupture frequency change results.

On the QCM device, the bonds that do rupture have greater effect on the frequency because they are on average nearer the centre of the QCM electrode. Where amplitude is greater sensitivity of resonant frequency is more susceptible to mass changes. However, for similar density of particles and binding sites there are fewer attached particles in total and the net frequency change is lower.

The results for the multiple particle radius are experiment simulated with the electrode changes. Figure 5.28 shows that there is considerable overlap in the rate of change of probability of the revised strip electrode transducer. Figure 5.29 shows greater promise. There is a good deal of concentration of each species into a different rupture times although there is still some overlap. This may suit applications where species are separated by a large difference in rupture force.

The concentration of rupture events in time is achieved by reduction of the distribution of binding forces. However this is not easy to achieve on the QCM platform. In the section that

follows alternative transducers are considered which do not exhibit such extreme variation in surface amplitude.

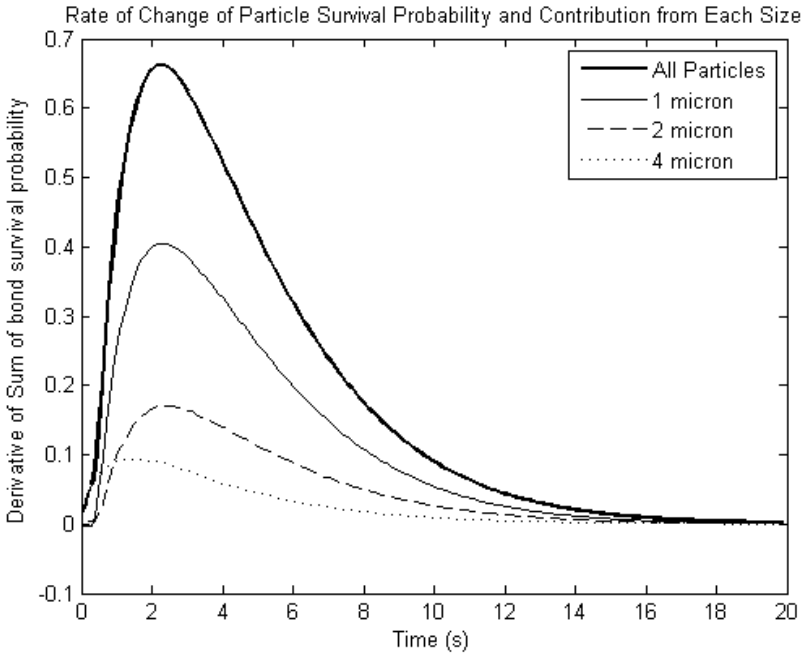

Figure 5.28 Derivative of particle survival probability on strip electrode device

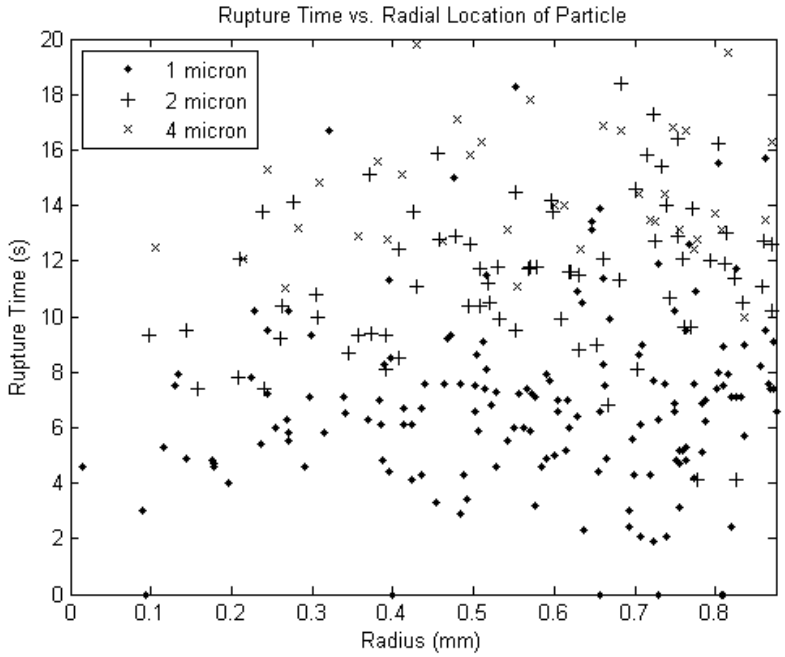

Figure 5.29 Rupture time as a function of location for each species of particle on strip electrode device

5.3.6 SAW Transducer Model

There are many acoustic wave devices that could potentially be applied to bond rupture. These include, but not limited to, Flexural Plate Wave (FPW) devices, Micro-Electro-Mechanical Systems (MEMS) devices such as cantilevers and a multitude of different SAW configurations (Grate and Frye, 1996, Chang et al., 2000, Hauptmann et al., 2003, Drafts, 2001, Janshoff et al., 2000, Du et al., 1996, Lange et al., 2003).

SAW devices operate at high frequency without thinning the substrate and making the device fragile. SAW devices operate on simple principles and can be manufactured with the required properties using simple photolithographic techniques.

In this chapter and others, several weaknesses of the QCM device are identified. The Surface Acoustic Wave device is fundamentally similar in principle in many ways to the QCM but offers some key advantages that make it a promising avenue for exploration. Most notable of the differences is that the SAW can be fabricated as a two port device. This decouples the input and output electrodes which are one-in-the-same on the QCM. The output transducer can be engineered to be sensitive to the noise of bond rupture, more so than the QCM, and perhaps totally insensitive to the input signal if that is desired.

By employing the same surface chemistry the model used for QCM above is modified for the SAW transducer. Figure 5.30 shows the distribution of particles on a square area 2.5mm in width.

For the purpose of this exercise we assume an input transducer generating a sinusoidal surface acoustic wave at the resonant frequency of the input transducer, nominally 32MHz.

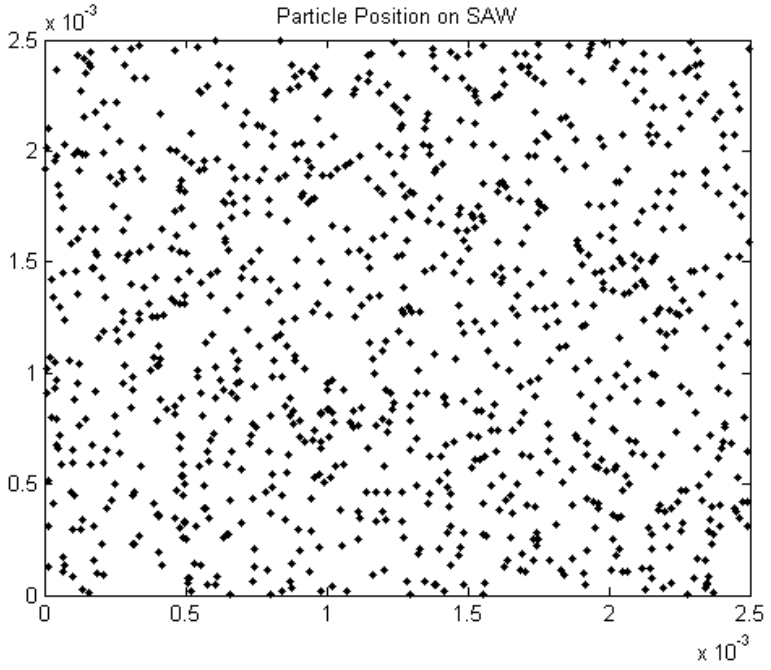

Figure 5.30 Particles distributed on SAW sensitive area

The acoustic wave propagates from left to right across the sensitive area with exponentially decaying amplitude following the function in Figure 5.31. The sensitive area of a SAW delay line is built to the desired geometry between the input and output transducers and so the amplitude is assumed constant in the other dimension assuming that the input transducer is suitably constructed.

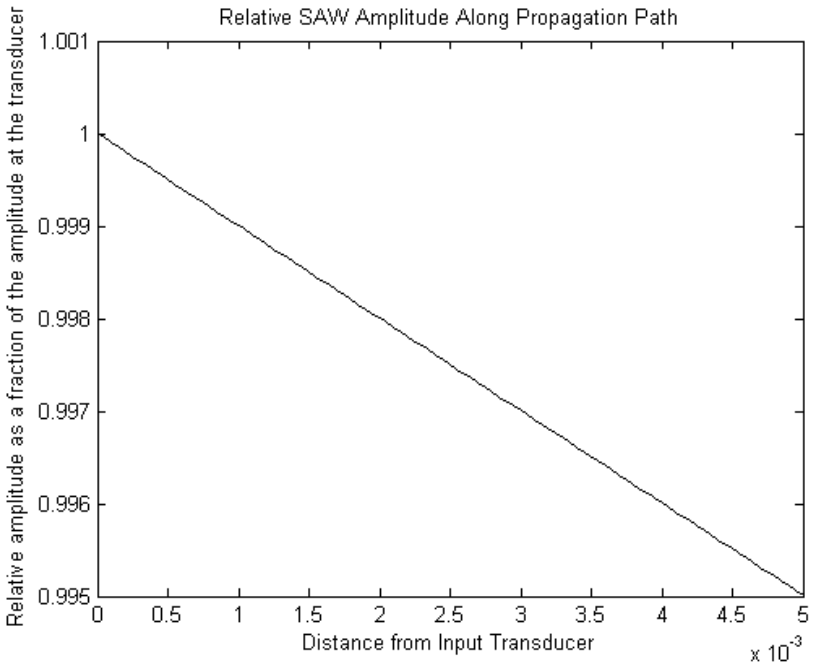

Figure 5.31 Surface acoustic wave amplitude

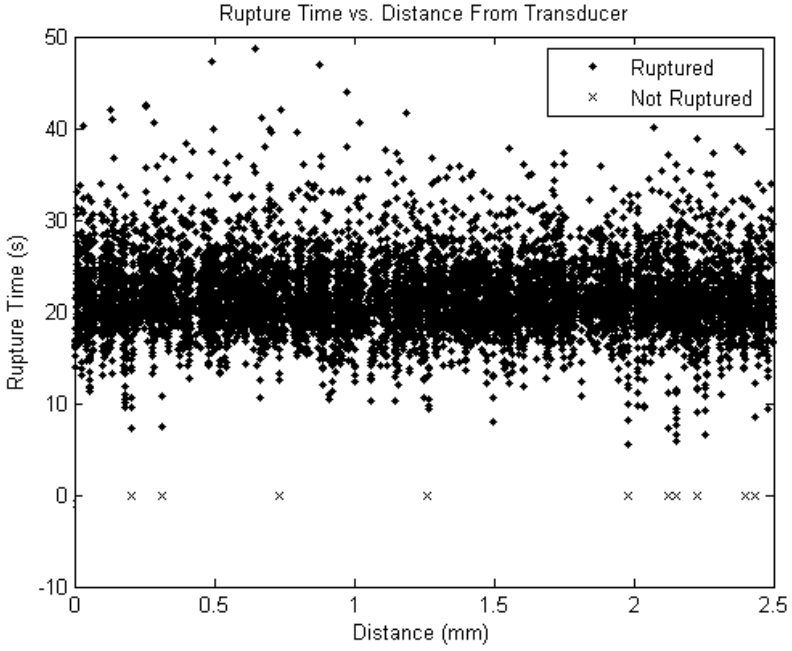

Figure 5.32 Bond rupture time as a function of distance from the transducer

The SAW amplitude function considerably reduces variation of maximal surface amplitude compared to the QCM. Assuming similar displacement amplitudes to QCM for easy

comparison the SAW device bond rupture model predicts the following relationship between rupture time and distance from the transducer.

The time taken for most bonds to rupture is to a good approximation independent of the particle position. For similar conditions the width of the rate of bond rupture curve, as described for QCM above, is 10s. This is an improvement of 10% on the modified QCM designs mentioned earlier. Figure 5.33 shows that the simulated noise is considerably concentrated within a short time interval.

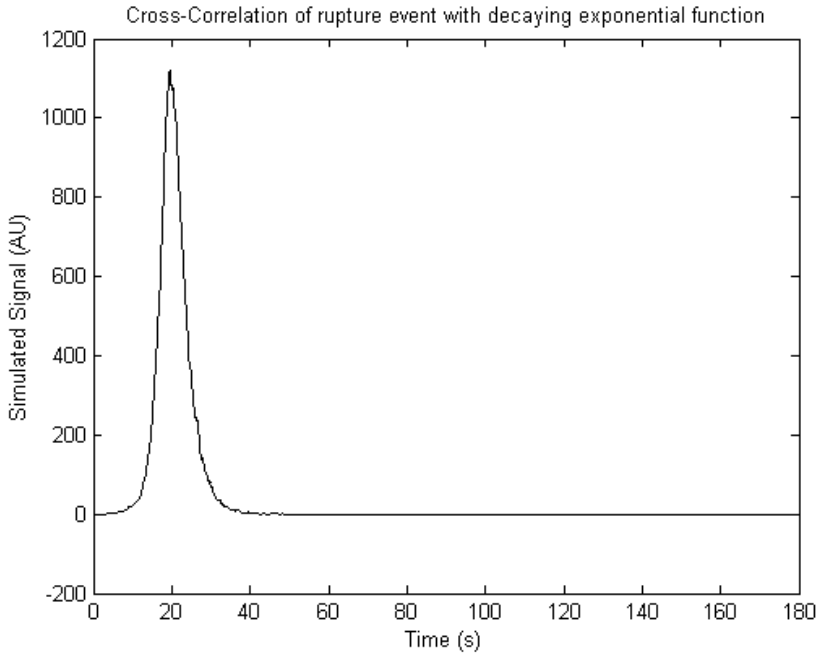

Figure 5.33 Simulated bond rupture noise signal for amplitude for SAW device

5.4 Chapter Conclusion

The simulations presented in this chapter demonstrate that in its current form the QCM bond rupture device requires further development not just in the hardware and methodology but also the transducer. Changes to the driving amplitude function offer little scope for improvement beyond a binary diagnosis because multiple species of particle cannot be adequately separated.

In the simulations presented no distribution is applied to the particle radius or the operating frequency as these are precisely controlled and uniform in the phantom experiments. This is not the case in real-world diagnostics and these parameters will be subject to some variation within and most notably between experiments. Despite these phantom tests representing the best possible case, they have been found to be unsatisfactory.

Two possible improvements to the QCM have been outlined, namely electrode masking and cropping. The effects of these improvements are of considerable interest to this group but

fall beyond the scope of this investigation. It is anticipated that in spite of the suggested improvements the rest of the bond rupture hardware will not be able to detect the bond rupture noise.

Based on superior performance and greater academic interest, the SAW transducer is identified as the next step in bond rupture scanning. Chapter 6 outlines the design and manufacture of a prototype SAW device and details the direction of further research.

6. SAW FABRICATION AND EXPERIMENTS

6.1 Introduction

Chapter 5 introduced the Surface Acoustic Wave device, the best method for the advancement of bond rupture transducers. SAW devices have been used as sensors for their sensitivity to attached mass and were recognised as a potential biosensor by Slobodni and Budreau (1972), and Wohltjen and Dessy (1979a, 1979b, 1979c). Such SAW sensors utilise the influence of attached mass on the acoustic wave velocity. This has the effect of slowing the wave and increasing wave damping.

The sections that follow review literature relevant to the design and modelling of SAW devices. Prototype SAW devices are designed and manufactured, the devices are tested, electronics hardware is modified and experiments are carried out.

6.2 Review of SAW

SAW devices are an attractive platform for bond rupture because they do not rely on thin piezoelectric films to achieve high frequency operation. SAW operate at higher frequencies than QCM without becoming fragile. In addition, SAW devices have potential for integration of bond rupture with established technologies such as Surface Plasmon Resonance (SPR), SPR was combined with SAW by Francis et al. (2006).

The principle of SAW bond rupture is the same for as QCM and briefly presented in a patent by Dultsev et al. (2001). The results, shown in Figure 6.1, are less consistent than those reported using QCM as less effort has been concentrated on the SAW platform. One of the main differences between SAW and QCM is the electrode layout. SAW is a single sided architecture and it has been suggested that two or more transducers can be incorporated into one sensor to detect the noise in different frequency bands or propagation direction.

Figure 6.2 depicts a SAW delay-line for bond rupture. The Inter Digitised Transducers (ITD) generates surface acoustic waves on a piezoelectric substrate. The acoustic energy is confined to the surface of the substrate. The input IDT emits the SAW and the acoustic wave travels from the input transducer, across the delay line area to the output transducer. The output can itself act as a filter for the signal of interest generated by particle detachment, or simply as a monitor of the signal from the input.

In some SAW sensors the entire substrate is affected by what is being measured, this is the homogeneous case such as SAW temperature sensors. Alternatively, if the sensor is affected

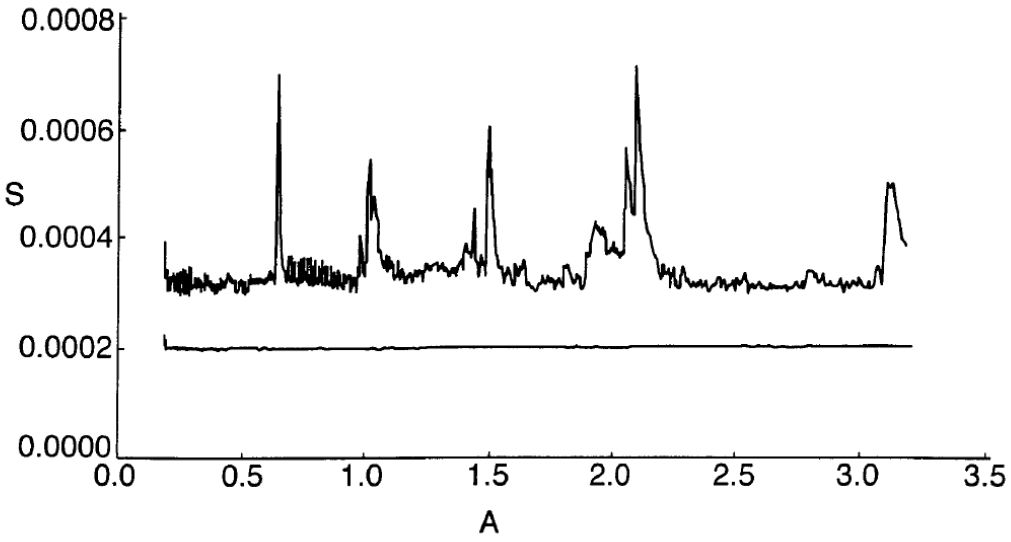

Figure 6.1 Bond rupture of physical bonds captured using a SAW device The vertical axis of measures bond rupture noise in arbitrary units and the driving amplitude is measured in volts (Dultsev et al., 2001)

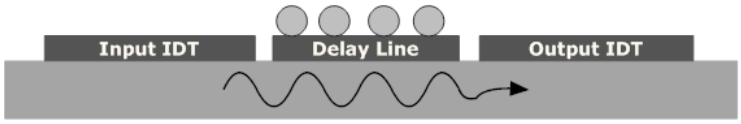

Figure 6.2 SAW delay line applied to biosensor

by changes to the overlying, this layer is termed the composite resonator case. SAW delay lines feature an area between two transducers that can be made sensitive to target particles.

IDT are made by patterning electrodes onto a piezoelectric substrate. The process by which electrodes are made is the same as photolithographic techniques used in the manufacture of silicon integrated circuits and CMOS processes. This means active signal processing could also be incorporated into the sensor device. The electrodes are usually IDT, comb structures that generate dynamic stress in the substrate when an alternating voltage is applied. Conversely, the same structure generates an electrical signal in response to a SAW wave. The key factors in SAW development is the selection of substrate and the design of the transducers. Specific frequency characteristics of the IDT structure can incorporate passive signal processing into the device itself.

6.2.1 SAW Device Architectures

There are many types of SAW device but only Love mode and Acoustic Plate Mode (APM) are considered here. These represent a subset of SH-SAW. Love Mode devices considered here are a delay line with a suitable guiding layer over top of the electrodes. The guiding layer confines the energy of the SAW and protects the electrodes. The APM device has a guiding

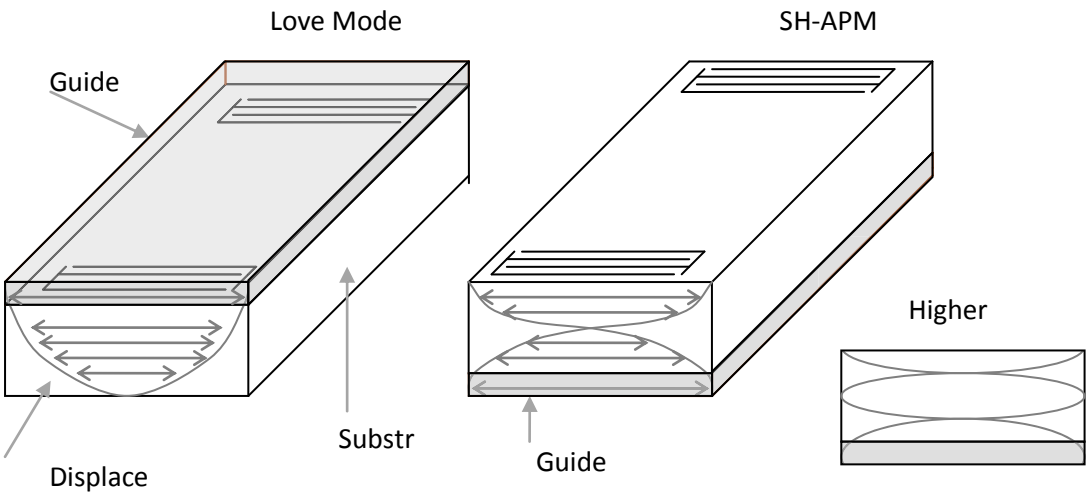

Figure 6.3 Difference between Love mode and SH-APM

layer on the opposite side to the electrode and SAW displacement occurs on both the top and bottom surface. The defining difference between Love wave and SH-APM is that Love waves require a decaying displacement with depth into the substrate whilst the SH-APM uses a resonating solution. Figure 6.3 demonstrated the difference.

In theory, both the Love Wave and the lowest order SH-APM mode correspond to a plane wave (McHale et al., 2002). Generally Love mode is regarded as distinct from Acoustic Plate Modes and is considered a cross between a SAW and a QCM.

SH-SAW can be used in liquids because shear occurs horizontally resulting in no radiation loss, this is because the particle motion is confined entirely within the plate. Compressional radiation into the liquid does not occur. The first report of the use of a SAW device for a liquid immunoassay was for the detection of human IgG by a goat antihuman IgG antibody (Roederer and Bastiaans, 1983). It was subsequently shown that the device was functioning via an acoustic plate mode rather than a SAW wave (Calabrese et al., 1987). APM substrate thickness is of the order of 0.2mm, which is the same as the QCM and so inherits a similar weakness arising from thin substrates. Higher sensitivity can be achieved when driving frequencies other that the fundamental mode is used just as is done using QCM.

A two-port SAW delay line features two IDT. The delay occurs in the propagation path between two IDTs, the first is the transmitter, the second the receiver. The delay changes when the speed of the wave or length of the delay line is changed.

The delay time between electrical input and output is determined by

$$t_d = \frac{l}{v_{SAW}} \tag{6.1}$$

where, l is the mean spacing between the two IDTs, and v_{SAW} is the SAW phase propagation speed.

In Love mode theory, multiple modes can occur with the lowest order mode containing a node in the displacement at infinite depth into the substrate and an antinode at the free surface (McHale et al., 2002). For thicker layers more than one love wave mode may be supported.

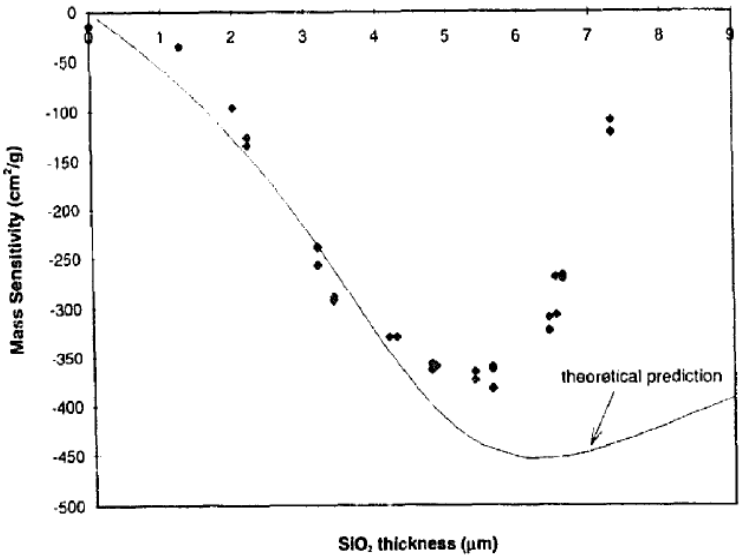

Figure 6.4 Love Mass loading sensitivity vs. SiO_2 thickness (Du et al., 1996)

6.2.2 Substrate

A number of key parameters of the SAW device are determined by the material on which the electrodes are fabricated. SAW wafers can be purchased in a variety of materials and orientations. The acoustic velocity of the substrate determined by the shear modulus and is called the shear velocity. The shear velocity of the substrate is a material property given by

$$v_s = \sqrt{G/\rho} \tag{6.2}$$

The acoustic velocity of the SAW is computed by the Viktorov approximation

$$v_{SAW} = \frac{0.436 + {}^{\lambda}/_{\lambda + 2\mu}}{0.5 + {}^{\lambda}/_{\lambda + 2\mu}} \sqrt{\frac{\mu}{\rho}} \tag{6.3}$$

The acoustic velocity is always slower than the bulk shear velocity.

The velocity the surface acoustic wave, known as the phase velocity is distinct from the velocity of the shear wave and is denoted by v_{SAW}. Surface acoustic waves are very slow, some 10^5 times slower than the speed of the light. The phase velocity is independent of the frequency and smaller than that of the slowest bulk mode, therefore on a plane surface no radiation into the substrate occurs. In anisotropic crystal structures, the velocity will depend on the orientation of the surface and direction of the wave. The velocity of the SAW changes

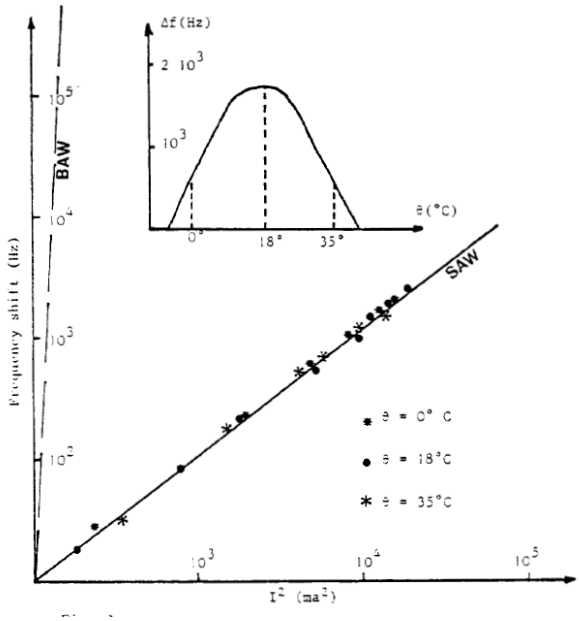

Figure 6.5 SAW Amplitude-Frequency effect compared to QCM

with the surface electrical boundary condition. The extent of the change is of the order of the coupling factor.

In SH-APM the phase speed is higher than that of the shear acoustic speed of the substrate because the energy is distributed throughout (McHale et al., 2002). Higher SAW velocities can increase device frequency without the need to improve lithography processes, conversely, lower SAW velocities are utilised in low frequency devices to keep the device size down.

The effects of temperature and amplitude are difficult to distinguish and are typically considered together (Gagnepain, 1981). The amplitude-frequency effect in SAW device has been experimentally determined to be around 200 times lower than bulk acoustic wave devices such as the QCM as demonstrated in Figure 6.5. The rate of increase in drive level also affects the IDT resonant frequency due to strains caused by the temperature gradient.

The temperature coefficient of delay (TCD) relates the change in delay time to temperature for SAW devices. The TCD is evaluated using the expression

$$TCD = \frac{1}{\tau}\frac{\partial \tau}{\partial T} \tag{6.4}$$

$$TCD = \alpha - TCV_{SAW} \tag{6.5}$$

where τ is the delay time, α is the thermal expansion coefficient for the SAW propagation direction and TCV_{SAW} is the temperature coefficient of the group velocity.

Quartz is not favoured among SAW manufacturers because of its low electromagnetic coupling coefficient. Temperature stability is traded for higher coupling and lower insertion loss. Lithium Niobate and Lithium Tantalate are ferroelectric crystals that exhibit strong

piezoelectricity. Both are commonly used as transducers; and experience very high depoling and consequent loss of efficiency at very high power and temperature levels (Ballato, 1995). Considerable information is available from commercial sources about these crystals.

Lithium Niobate ($LiNbO_3$) is a compound of niobium and lithium. It is a colourless solid material. Czochralski-grown monocrystals have unique electro-optical, piezoelectric, photoelastic and nonlinear optical properties. Lithium Niobate is the material of choice for the manufacture of surface acoustic wave devices but for some uses is replaced by Lithium Tantalate ($LiTO_3$). Lithium Tantalate has a lower stability and lower Q factor than quartz but a higher coupling coefficient. It has a high dielectric constant, sufficiently high that it can be used in liquid without a shielding layer (Lange et al., 2003). Lithium Tantalate can be can be used at higher drive levels than quartz, up to 5 Watts in a filter.

Table 6-1 shows the properties for the selected substrate on which the prototype SAW is built. This is a standard SAW wafer.

Table 6-1 Substrate Material Properties

Material and Angle	String	Coupling Factor k^2 (%)	SAW velocity v_{SAW} (m/s)	$\frac{\varepsilon_{11}^T}{\varepsilon_0}$	$\frac{\varepsilon_{33}^T}{\varepsilon_0}$
36° Yrot Xprop $LiTaO_3$	'36YXLT'	4.7	4742	38.3	46.2

6.2.3 Transducers

IDT are a comb structure of alternating finger pairs as shown in Figure 6.6. IDT are made from aluminium, gold, chromium or other metals depending on the application. In protected environments light metals such as aluminium are used to reduce the negative effects of heavy electrodes. For sensor applications, owing to exposure to ambient air or liquids, a more durable metal is required. Gold is often used for biosensors and the chemistry required to immobilise receptors is well developed.

SAW bond rupture has an additional complication not shared by other SAW biosensors. The device is required to withstand the high powers required to cause bond rupture. Pekarcikova et al. (2005) showed the effect of high power in SAW electrode structures. Metal migration, as shown in Figure 6.7, can cause shorts or discontinuities, reduction in device life and drift problems. A copper metallisation system showed only tiny damage and unchanged frequency and electrical resistance after high power loading. Damage was observed in the cross section beneath the undamaged copper covering.

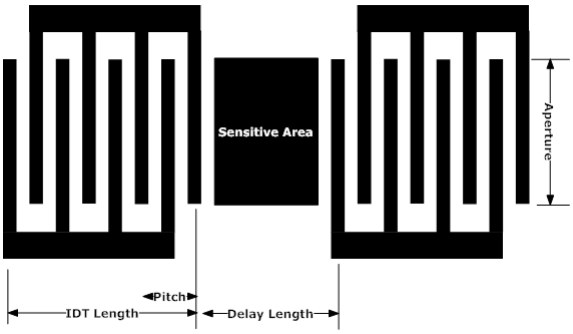

Figure 6.6 SAW delay-line geometry showing pitch (wavelength, λ), IDT Length (l), delay length and aperture

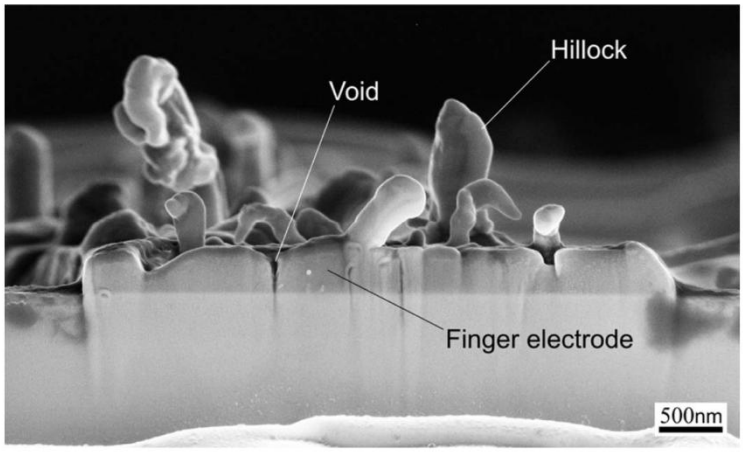

Figure 6.7 SEM image of a cross section of an aluminium finger electrode after loading with 3W for 2000 minutes, hillocks grow outward more than 1µm (Pekarcikova et al., 2005)

The amplitude of a SAW wave depends on the applied voltage signal, the piezoelectric coupling of the substrate, and the electrode structure. Rayleigh SAW amplitude of 1nm was measured using X-Ray topography (Roshchupkin et al., 2005). X-Ray topography requires Rayleigh SAW waves and as such is not well suited to SAW biosensors. Behme et al. used an AFM technique to determine the amplitude of shear SAW displacement (Behme et al., 1998). Operating the SAW device below 10dBm (Watanabe et al., 2007, Watanabe et al., 2002) use optical techniques utilising laser speckle and interference to measure the amplitude and mode shapes of SAW devices.

The amplitude of the SAW is small compared to wavelength and falls off exponentially with distance from the surface (evanescent). The penetration depth varies inversely with frequency. The particle path at the surface in every depth is elliptical and confined to the plane perpendicular to the surface and parallel to the direction of propagation. The amplitude of the Rayleigh waves was calculated to be 1.13nm for a SAW with a 34.88MHz frequency and wavelength of 100µm.

The basic assumption in determination of SAW amplitude is that the acoustic signal generated by a finger is proportional to the charge, Q on it. Then for N fingers of width w and propagation in the z direction the amplitude at z due to a source element dz' is:

$$dA(z,z',w) = k\sigma(w,z')e^{-j\left(\frac{2\pi}{\lambda}\right)(z-z')}dz' \tag{6.6}$$

where k is the coupling factor and σ is the charge per unit length. If the charge outside the region of the transducer is zero, which is normally the case, then this expression can be integrated over space to give the IDT response:

$$A(z) = jkQe^{-jkz}\frac{sin\left(\frac{\pi lN}{\lambda}\right)}{cos\left(\frac{\pi l}{2\lambda}\right)}sinc\frac{l_1}{\lambda}e^{j\left(\frac{2\pi}{\lambda}\right)(N-1)\frac{l}{2}} \tag{6.7}$$

The distance between neighbouring strips on the electrode determines the centre frequency of the transducer. The fundamental frequency is given by

$$f_0 = v_{SAW}/\lambda \tag{6.8}$$

where f_0 is the SAW operating frequency, v_{SAW} is the phase velocity of the SAW wave and λ is the SAW wavelength. There are many nearby excitable resonances Eq. (6.8) is generalised for the nth harmonic of the structure is given by

$$f_n = v_{SAW}/n\lambda \tag{6.9}$$

where n is an integer. The frequency range of SAW devices starts at around 25 MHz and ends at a few GHz. The excitability of these resonances decreases with increasing difference between f_n and f_0.

The operating frequency of a SAW delay line changes with attached mass, the viscosity of the surrounding media, and the temperature of the substrate. The reason for this dependence is the effect that these variables have on the phase velocity of the substrate. The change of frequency with attached mass is described by Sauerbrey's equation,

$$\Delta f = \frac{C_s f^2 \Delta m}{A} \tag{6.10}$$

where C_S is the sensitivity, $1.35 \times 10^{-6}\ cm^2\ s\ g^{-1}$ for quartz (Wohltjen, 1984). While $C_S < C_Q$, the sensitivity of SAW devices to mass change is higher because the operating frequency of SAW devices can far exceed that of QCM devices.

Mass changes can only be measured in this way when they affect the area of the IDT. If the effect of these variables is limited to the delay line and not the IDT then the effect on the characteristic frequency of the IDT is reduced.

The sensitivity of a love mode device is strongly linked to layer thickness. The distribution of Love-wave energy depends on the ratio of overlay thickness to wavelength, for low values considerable energy remains in the quartz (Du et al., 1996). As the ratio increases towards 0.14, the wave is increasingly confined in the guiding layer. Further increases in thickness result in further confinement of energy within the layer, but a smaller normalised amplitude.

IDT fabricated on piezoelectric materials with weak coupling coefficients require many finger pairs which the surface wave must propagate through. Each finger has a finite probability of reflecting and scattering the surface wave into the substrate resulting in energy losses.

Scattering into the substrate reduces the SAW power delivered outside the IDTs and scattering can cause spurious resonances. Embedding of IDTs into the substrate reduces scattering (de Lima et al., 2004). Embedded IDT fingers facilitate the design of focussing IDTs which rely on precise knowledge of the angular dependence of the SAW propagation velocity.

Acoustic mismatch caused by differences between the acoustic properties of the metal-free and the metal-covered regions is reduced by appropriate selection of the metal acoustic properties. The mismatch can normally be minimised by using a low-density metal for the fingers to reduce the mass loading effect. As an example IDTs on GaAs substrates with aluminium fingers exhibit lower reflection levels. Another approach is to design the geometry of the metal fingers within a SAW period in such a way as to induce destructive interference of the beams reflected at successive fingers. This requires at least two fingers and precise finger width and separation. SAW reflection and dispersion are discussed by de Lima et al. (2004).

The IDT pictured in Figure 6.6 is the simplest IDT structure. The acoustic reflection effect is particularly strong in single finger IDTs where the period of the metal grating fulfils the Bragg condition for constructive reflection of the SAW beam. Such reflections turn the IDTs into a standing wave acoustic cavity with high acoustic amplitude inside the transducers. Alternative configurations include split-electrode (Figure 6.8a) and three-electrode (Figure 6.8b). The split finger electrode requires four times smaller features than the solid finger electrode.

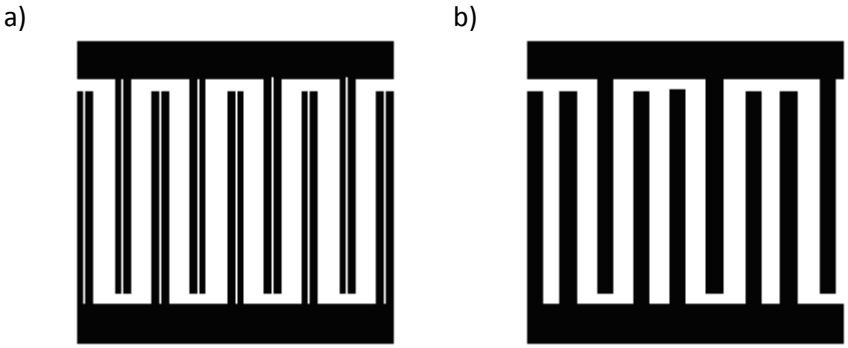

Figure 6.8 Interdigital transducer (a) split finger electrode(b) three electrode

The SAW is radiated perpendicular to the structures in both directions. An example of a unidirectional transducer (UDT) pattern is shown in Figure 6.9. Some other reported UDT: (Kodama et al., 1986, Hartmann and Abbott, 1989, Hunsinger and Hanma, 1979, Wright et al., 1995, Martin et al., 2004).

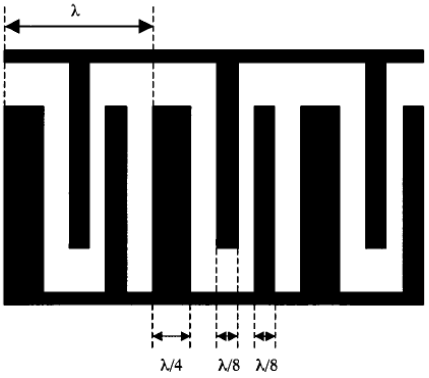

Figure 6.9 Single Phase Unidirectional Transducer(Nakamura et al., 2001)

The number of finger pairs is denoted N. For $N \to \infty$ this gives values of the product of wave number and length for zero response

$$\frac{2\pi l}{\lambda} = 2\pi\left(1 \pm \frac{1}{N}\right) \tag{6.11}$$

The bandwidth of an IDT is determined by the number of finger pairs.

$$\frac{\Delta\omega(between\ zeros)}{\omega_0} = \frac{2}{N} \tag{6.12}$$

$$\frac{\Delta\omega(3dB)}{\omega_0} = \frac{0.89}{N} \tag{6.13}$$

Wave guiding layers are employed in SAW devices to increase efficiency. Optimal layer thickness depends on the shear velocity of the material and can be determined experimentally or by calculation (Du et al., 1996) .Guiding layers must be non-conductive, well adhesive and uniform.

Guiding layers with favourable elastic properties reduce acoustic adsorption. Low shear velocity and low density are desirable. Polymer guiding layers are unfavourable because the acoustic adsorption of the layer quickly increases with thickness (Barie et al., 2004). SiO_2 is an attractive guiding layer on quartz crystal because it has lower acoustic adsorption than polymers. The thickness of applied SiO_2 guiding layers is limited by due to technical problems related to film adhesion and stresses (Du et al., 1996). However, for bond rupture SAW devices gold covered delay line is used for better binding of analytes. The phase velocity of the gold layer is 3.74 km/s for zero film thickness and decreases linearly to 3.21 km/s at a thickness of 5000Å (Smith et al., 1969). The elastic dispersive effect of the film and the electrical shorting of the interface surface reduce the phase velocity. The effect of the electrode shorting is given by

Campbell and Jones as $\Delta v/v = -0.0025$ and is small in comparison with the elastic dispersive effect.

Surface coatings can be fabricated such that they taper towards the ends to avoid acoustic reflections. This has been achieved by evaporating through a mask 0.6cm from the surface so that the taper is like a shadow of the evaporation source through the mask (Smith et al., 1969). The prototype SAW bond rupture device electrodes are not tapered at the edges.

6.2.4 SAW Devices in Liquid

To operate in liquid and avoid high damping acoustic waves must be shear horizontally polarised or have phase speed lower than the speed of sound in liquid. The high dielectric constant of the water ($\varepsilon_r \approx 80$) can cause electrical impedance mismatch and weak acoustic coupling. Substrates with low dielectric constants like quartz ($\varepsilon_r \approx 4.7$) can only be used as lamb or love wave devices after coating with an acoustically thick guiding layer Lithium Tantalate ($\varepsilon_r \approx 43$) does not require such a coating.

Flow cell integration of a SAW device such as that shown in Figure 6.10 can achieve very

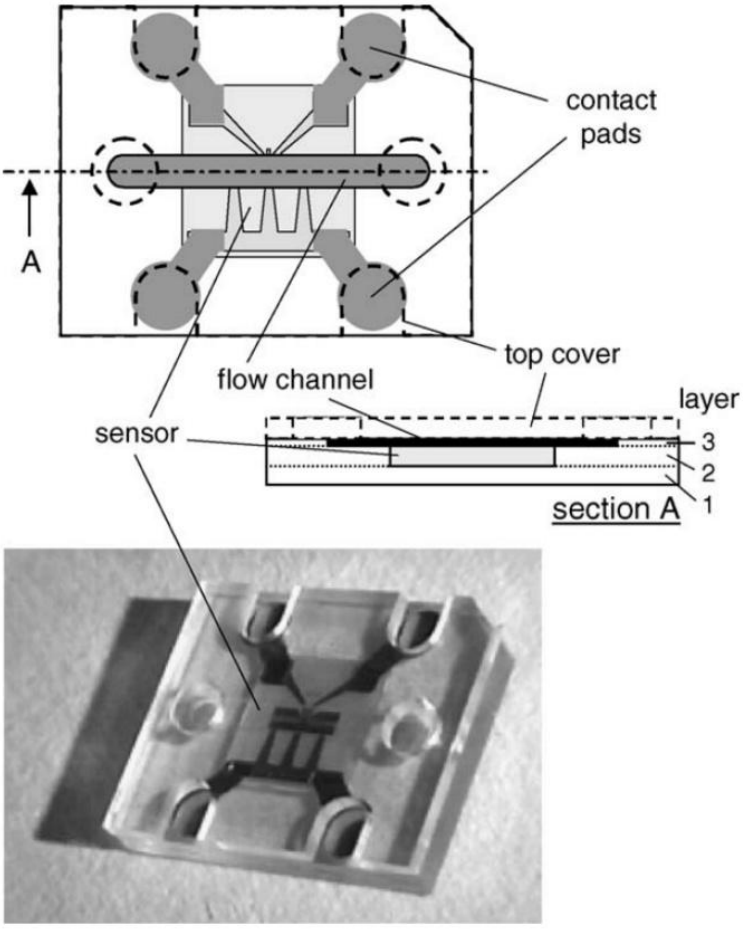

Figure 6.10 Encapsulated SAW biosensor (Lange et al., 2006)

low volumes. To alleviate the difficulty of sealing a flow cell, and to reduce flow cell volumes it is possible to manufacture the flow cell with the sensor using MEMS-like processes. To reduce pressure on the piezoelectric substrate capacitive coupling is used (Lange et al., 2006). The flat channel passes directly over the sensitive area and is less than 1µl in volume, an advantage as small volumes increase the speed of diffusion-limited bio-reactions. Bond rupture would compliment 'lab on a chip' type devices.

6.3 Design Optimisation of SAW Delay Line

In this section, the immediate capabilities of the fabrication and electronics hardware are considers and SAW devices are designed in accordance with the limitations. The dimensions of the SAW transducers are optimised for fabrication and the electrical equivalent of the SAW is considered using the Impulse Response model.

It is usual practise to optimise SAW device design for a specific impedance and frequency response. The purpose of this optimisation is to determine the dimensions of the SAW IDTs. The rudimentary parameters of SAW devices relate primarily on the operating frequency, f_0, and the number of electrode finger pairs, N. Some paramaters of the substrate are required. These parameters are unique to the particular crystal and the specific angle of the crystal cut. 36° Y-Cut X-Propagating Lithium Tantalate (36YXLiTaO$_3$) was selected for this application for its high coupling factor and shear horizontal piezoelectric displacements.

SAW devices do not operate at low frequencies, and these devices are near the boundary of feasible operation. The first constraint on the device is thus

$$f_0 \geq 25MHz \tag{6.14}$$

To integrate within existing electronic hardware without the aid of further analogue electronics, the operating frequency of the device must be within Nyquist's sampling parameters of the hardware van der Werff et al. (2007), and within the operating range of the Digital to Analogue converter.

$$f_0 \leq 50MHz \tag{6.15}$$

The capabilities of the fabrication process available are considered. The fabrication process is outlined in detail in Section 6.6. The smallest increment in dimensions of the pattern generator is 1.27µm. Once reduced by ten times during the fabrication process the finest feature resolution available is 0.127µm. After the reduction at the masking stage the smallest structure that can be etched will be around 2µm. For solid finger pairs this gives a minimum wavelength of 8µm, $f_0 \leq 590$MHz. For split finger electrodes, the minimum wavelength that

could be realised is 24µm, $f_0 \leq 190$MHZ. These bounds of the operating frequency are higher than the bounds introduced by the electronic hardware capabilities Eq. (6.15).

The dimensions of the reduced and repeated pattern are at most 6.2× 6.2mm, ultimately limiting the size of the finished device. Acoustic absorbers and bonding pads, some 1mm^2, need to be included for sensor connection. The length of the delay path and the aperture of the IDT determine the sensitive area of the sensor. To ensure that the device is usable and that the required sample sizes are practical the transducers are spaced sufficiently far apart.

The maximum allowable length of the transducer is determined by the substrate size. Two transducers, one for input and one for output, as well as the delay line must fit into this length. To this end, the length of the transducer is must not exceed 2.2mm. Expressed in terms of f_0 and N:

$$l = {}^{Nv_{SAW}}/_{f_0} \leq 2.2 \times 10^{-3} \quad N \in \mathbb{Z} \tag{6.16}$$

The capabilities of the fabrication process and hardware make the implementation of an optimal bandwidth difficult. It necessary to impose a maximum bandwidth of the sensor as the bandwidth determines the quality of the acoustic waves. Narrower bandwidth IDTs are better for this application:

$$BW = {}^{2f_0}/_{N} \leq 6 \times 10^6 \quad N \in \mathbb{Z} \tag{6.17}$$

6.3.1 Feasible Geometry

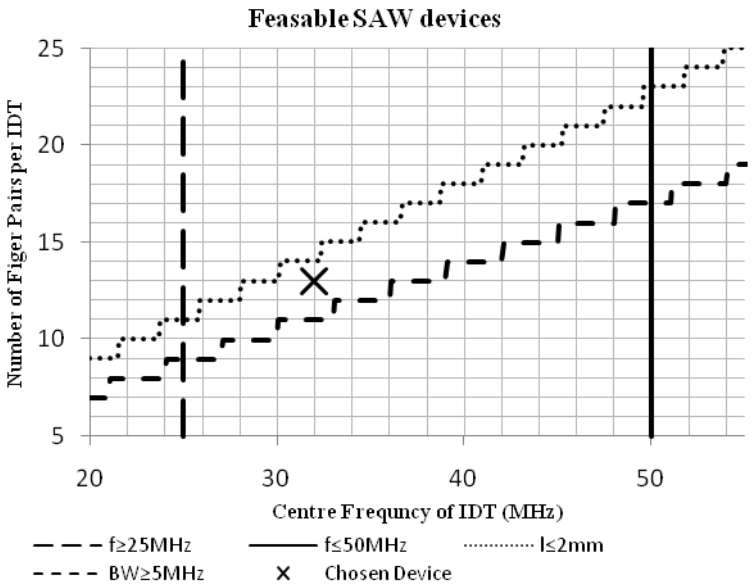

Figure 6.11 Plot of constraints on *N* and f_0 variables showing the feasible region of SAW design for this sensor

Figure 6.11 indicates the set of feasible SAW devices in the f_0-N space contained within the bounding lines. The location of the parameters of the device fabricated is indicated by the ×. Operation near 32 MHz was selected from this feasible region because it is situated near the third overtone of the QCM used in other works within the group (Yuan et al., 2007).

6.4 SAW Designs

To increase diversity of the SAW prototype devices for different devices are designed. The four devices each featured combinations of electrodes with different bandwidths and characteristic frequencies. The devices are designated 01001-01004, where the last three digits denote the design number and the preceding two denote the material and cut. The primary device of interest is 01001 and has two identical electrodes for input and output at 32MHz. The bandwidth is identical.

The second device features IDT designed to operate at the same frequency but with different bandwidths. A small number of finger pairs can be used to monitor wider band signals, whereas more finger pair can generate a narrower bandwidth, higher amplitude input signal. Figure 6.12 shows a device of this kind.

The other configurations have IDT of different input frequencies. One at 32MHz, the other 500kHz lower. This makes the output electrode less sensitive to the input excitation signal. The current version of the bond rupture hardware cannot monitor the output signal from this electrode and still drive the SAW because it requires that the input to the device is monitored for frequency determination.

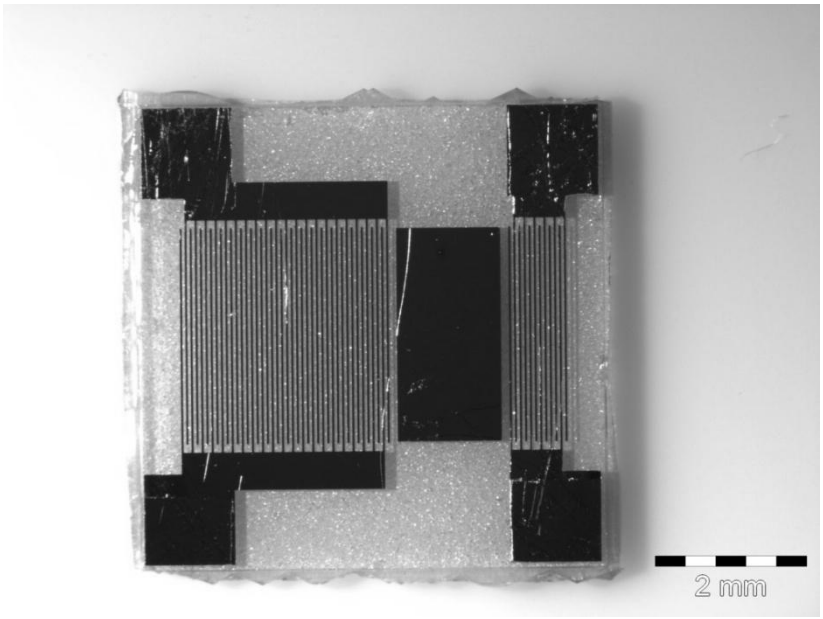

Figure 6.12 Alternative SAW design with asymetric electrodes

6.5 Equivalent Circuit Analysis of SAW delay-line

The electrical response of the device is modelled for the chosen geometry. The model is valid for un-weighted IDTs only and equal finger width and spacing. The Impulse Response method is a first order method and the effects of reflections and beam spreading are ignored. The Mason Equivalent circuit for a single IDT, Figure 6.13 (a) is composed of the radiation conductance $G_a(f)$, the acoustic susceptance $B_a(f)$, and the total capacitance C_T. In the Impulse Response method the two transducers, H_1 and H_2, are connected by a broadband time delay, H_{delay} as shown in Figure 6.13 (b). The transfer function of the system is approximated by:

$$V_1/V_2 \cong H_1(\omega) \cdot H_{delay}(\omega) \cdot H_2(\omega) \tag{6.18}$$

The impulse response, $h(t)$, and frequency response, $H(\omega)$, are a Fourier pair. The impulse response is finite as the time delay maps to substrate surface, which is of finite length. Sine waves describe the waveform shape generated by a single IDT finger pair. Other valid descriptions include impulse and square functions but sine waves result in simpler mathematics. The model performance is similar near the fundamental frequency of the transducer for the different descriptions.

The time domain function, $h(t)$, is generated by placing one-half sine wave for each set of electrodes of opposite polarity. The phase is chosen so that the zero crossings coincide with the electrode centres.

An expression for $h(t)$ for an N-pair electrode of regular periodicity

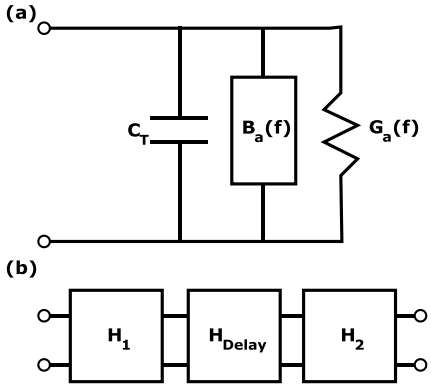

Figure 6.13 (a) Mason equivalent circuit of IDT. (b) Circuit representation of delay-line.

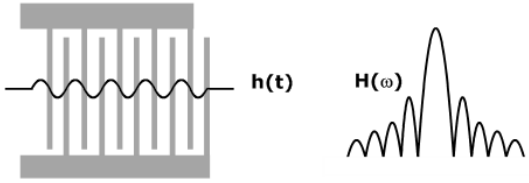

Figure 6.14 Representation of time domain signal construction and the resulting impulse response

$$h(t) = f_0^{3/2}\, 4k\sqrt{C_s}\, sin\, \omega_0\, t \quad 0 \le t \le \frac{N}{f_0} \tag{6.19}$$

$$= 0 \quad otherwise$$

where t is the impulse response time coordinate, k is the SAW coupling coefficient, and C_s is the capacitance per unit length per finger pair.

$H(\omega)$, the Fourier transform of the transducer impulse response $h(t)$ for an N-pair transducer is

$$H(\omega) \cong 2k\sqrt{C_s f_0} N \frac{\sin X}{X} e^{-\frac{j\omega N}{2f_0}} \tag{6.20}$$

where the substitution

$$X = N\pi \frac{(\omega - \omega_0)}{\omega_0} \tag{6.21}$$

is used to simplify the expression:

The input admittance is determined by the energy in the impulse response and by assuming that all the dissipated energy is radiated acoustically. Hartman (1989) shows that for a unit impulse the real part of the admittance is given by:

$$G_a(\omega) = 2|H(\omega)|^2 = 8k^2 C_s f_0 N^2 \frac{sin^2 X}{X^2} = G_0 \frac{sin^2 X}{X^2} \tag{6.22}$$

The imaginary part of the input admittance is the Hilbert transform of the real part and is given by

$$B_a(\omega) = \frac{1}{\pi} \int_{-\infty}^{\infty} \frac{G_a(\omega')}{\omega' - \omega} d\omega' = \frac{G_0(sin2X - X)}{2X^2} \tag{6.23}$$

This is the radiation susceptance and an additional term is required to account for the susceptance of the static capacitance. The total capacitance is

$$C_T = NC_s \tag{6.24}$$

where C_s is the per finger capacitance.

The first step is to determine capacitance of the finger pairs for the electrode width and spacing. The static capacitance for a finger pair is given by:

$$C_S = W_a \varepsilon(\infty) \frac{P_2^{-1}\{cos(2\pi w/p_1)\}}{P_2^{-1}\{-cos(2\pi w/p_1)\}} \tag{6.25}$$

where W_a is the aperture, w is the electrode width, $P_y(x)$ is the Legendre function, $\varepsilon(S)\varepsilon$ is the effective permittivity. Under the low frequency approximation:

$$\varepsilon(\infty) = \varepsilon_0 + \sqrt{\varepsilon_{11}^T \varepsilon_{33}^T - \varepsilon_{13}^T} \tag{6.26}$$

where ϵ^T is the permittivity measured under no stress.

The admittance for the ideal case is

$$Y = G_a(\omega) + j\omega C_T + jB_a(\omega) \tag{6.27}$$

and the impedance is given by

$$Z = {}^{1}/_{Y} = R + jX$$

$$= \frac{G_a(\omega)}{G_a(\omega)^2 + \left(\omega C_T + B_a(\omega)\right)^2} + j\frac{-\left(\omega C_T + B_a(\omega)\right)}{G_a(\omega)^2 + \left(\omega C_T + B_a(\omega)\right)^2} \tag{6.28}$$

Equation (6.28) is dependent on C_s, the per finger static capacitance of the IDT. C_s is determined by the finger overlap, or aperture. The electronic hardware used for QCM operation is a 50Ω matched system. Matching the SAW transducers to 50Ω at the characteristic frequency of the IDT optimises power transfer to the electrodes. This optimal match occurs when the IDT resistance, the real part of the impedance is matched to the impedance of the driving hardware. Figure 6.15 shows the simulated resistance of the fabricated SAW device and the impedance is shown in Figure 6.16.

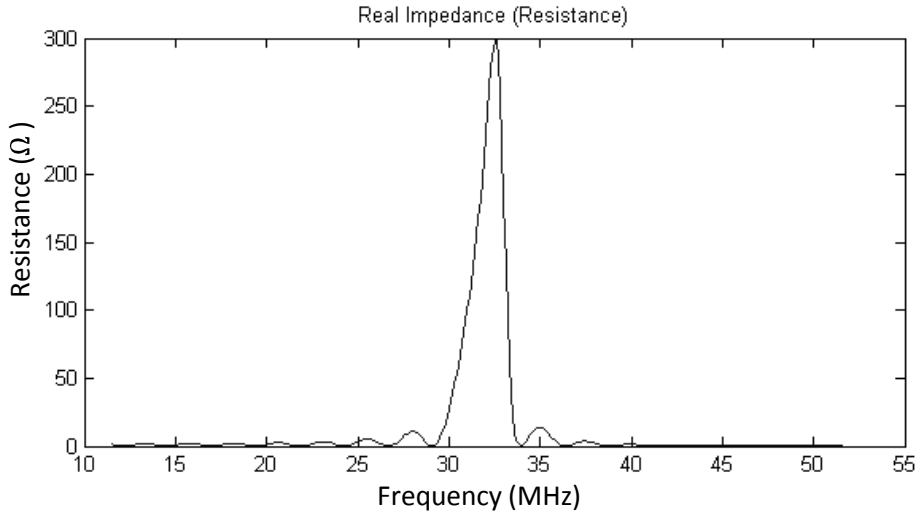

Figure 6.15 Simulated resistance of fabricated device

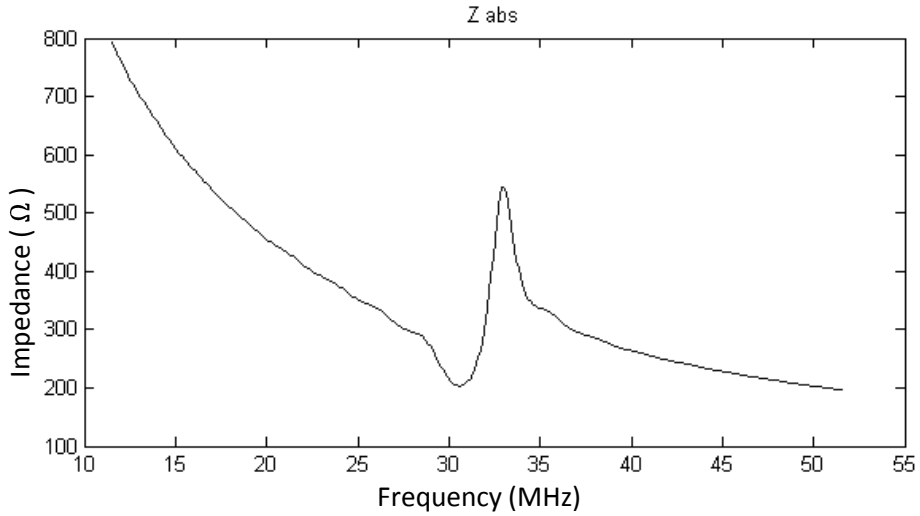

Figure 6.16 Simulated Impedance of fabricated device

The following equation gives the optimal aperture. Making C_T the subject gives the optimal total capacitance as a function of the target resistance:

$$C_T(R) = \frac{1}{R\omega} \times \frac{4k^2N}{(4k^2N)^2 + \pi^2} \tag{6.29}$$

Further the optimal aperture, A, is equal to

$$A = {C_T(R)}\Big/{NC_s'} \tag{6.30}$$

where C_s' is the capacitance per unit length of the finger pair. When equation. 4.37 is solved for the chosen finger number and operating frequency the required aperture is larger than that which can be fabricated in the available area. In this case some auxiliary matching hardware may be utilised.

The delay path causes a time delay between the input and output transducers.

$$H_{delay} = e^{\frac{-j\omega l}{v}} \tag{6.31}$$

The delay path, the sensitive area of the sensor is $l/\lambda = 21.4$ wavelengths long. For 36YX LT the propagation loss across a metallised delay line was determined experimentally (Hickernell, 2000), and found to be 0.02 dB/λ provided the ratio of film thickness to wavelength is less than 0.2 ($t/\lambda < 0.02$). As the devices designed here operate at low frequency this criteria is satisfied.

The bi-directionality and electrical mismatch contribute to the device insertion loss. At the input transducer, 3dB loss arises from the radiation of energy in two directions. At the output transducer, a further 3dB loss occurs when the transducer is perfectly matched and half the energy from the electrical potential generated from the incident acoustic wave is regenerated

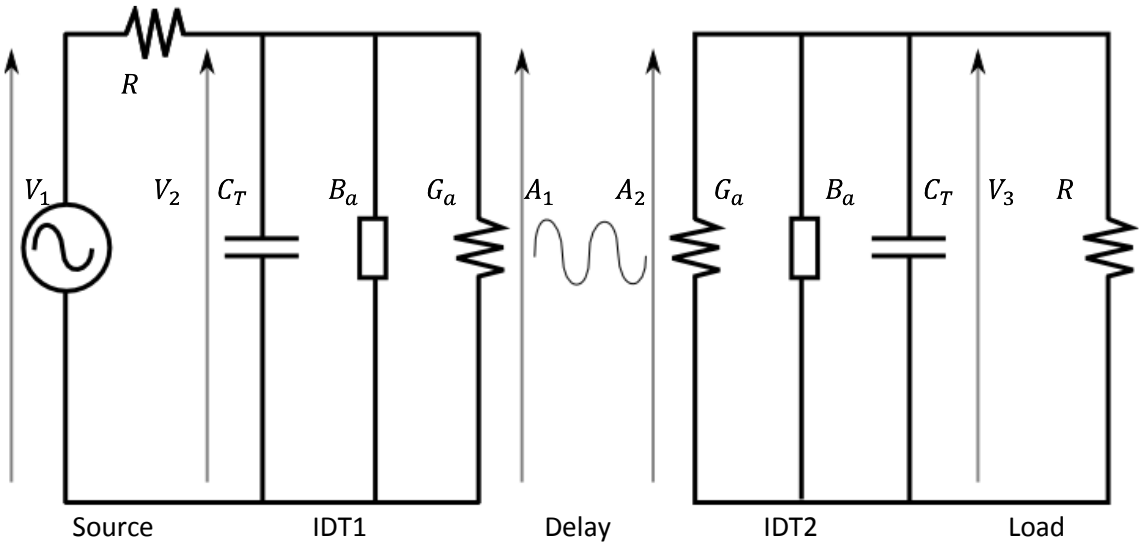

Figure 6.17 Combined IDT equivalent circuit

into acoustic waves. Further loss occurs according to the efficiency of the conversion between electrical and mechanical energy and back as embodied in the coupling coefficient.

The insertion loss can be determined using the conductance and susceptance along with the parameters of the driving circuit. This is important, in the driving hardware the device will perform differently than when connected to the measuring hardware.

The gain function of each block can be determined and the product yields the frequency dependant gain of the entire system such that

$$IL = -10\,log\left(\frac{A_1}{V_1}\times\frac{A_2}{A_1}\times\frac{V_3}{A_2}\right) \tag{6.32}$$

where $A_i$and V_i represents the acoustic wave amplitude and voltages at different stages in the transducer as shown in Figure 6.17. The transfer function of the transducer is give by

$$\begin{aligned}\frac{A_1}{V_1} &= \frac{1}{1-R\left(G_a(f)+j\omega C_T+jB_a(f)\right)}\\ &= \frac{1+RG_a(f)}{\left(1+RG_a(f)\right)^2+\left(R\left(\omega C_T+B_a(f)\right)\right)^2}\end{aligned} \tag{6.33}$$

For the manufactured SAW devices the wavelength is equal to four times the finger width, namely the pitch of the device. The delay path, where $\lambda = 132\mu m$ and the delay length $l = 2.83mm$ the delay path is $l/\lambda = 21.4$ wavelengths long. For 36XY-LT the , the material used in this work

$$\frac{t}{\lambda} = \frac{300\times10^{-9}}{132\times10^{-6}} = 0.0023 < 0.02 \tag{6.34}$$

The attenuation of the delay path is approximated by:

$$\frac{A_2}{A_1} = 10^{-0.02^{l}/_{\lambda}} \tag{6.35}$$

By reciprocity the transfer function of the receiving IDT is equal to the transfer function of the output IDT.

$$\frac{V_3}{A_2} = \frac{A_1}{V_1} \tag{6.36}$$

and the insertion loss of the entire sensor is given by Wilson et. al

$$IL = -10\,log\left(\frac{2\left(RG_a(f)\right)}{\left(1+RG_a(f)\right)^2+\left(R\left(\omega C_T+B_a(f)\right)\right)^2}\right) \tag{6.37}$$

The simulated and measured insertion loss is qualitatively similar. The insertion loss is lower than predicted because the simulated impedance matches but does not model second order effects such as reflections and the effects of external circuitry are not considered. The electromechanical coupling coefficient is difficult to determine from literature and impacts the

insertion loss calculation. The surface wave velocity affects the frequency of the device and is difficult to determine before fabrication.

A Matlab script was written that, for a chosen substrate, centre frequency, number of fingers, and aperture, determines the dimensions of the structure to be fabricated. A report generated by Matlab, an example of which is shown in Figure 6.19, provides lasting documentation of the design parameters. A coarse representation of the geometry is also generated so that the user can visualise the device. From this report the pattern for the transducer is produced manually using L-Edit, a microfabrication software package.

Realising the design requires compromise and rounding. The design values and the true fabricated results are presented in Table 6-2.

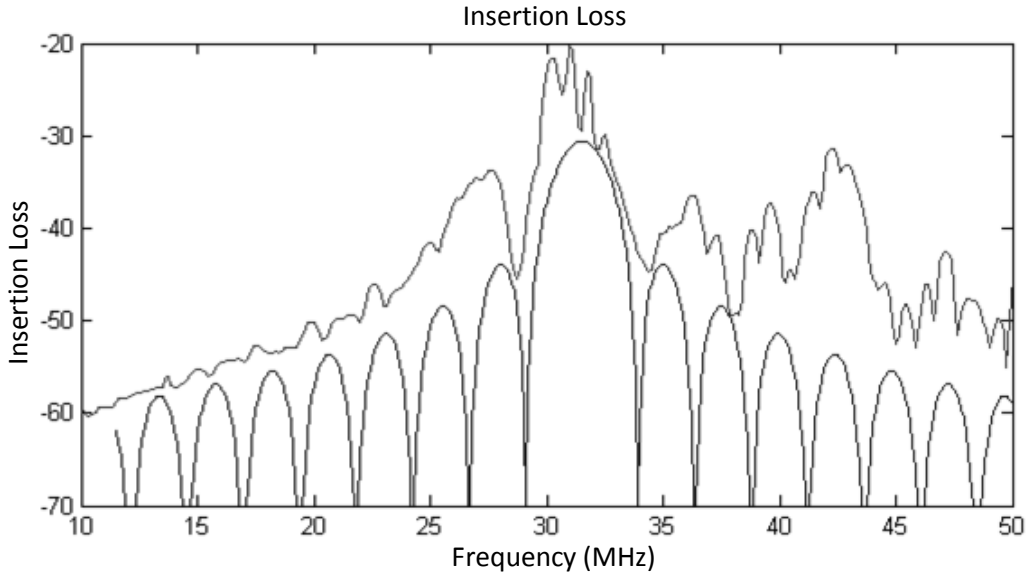

Figure 6.18 product of the frequency response of two IDTs plus effect of delay path

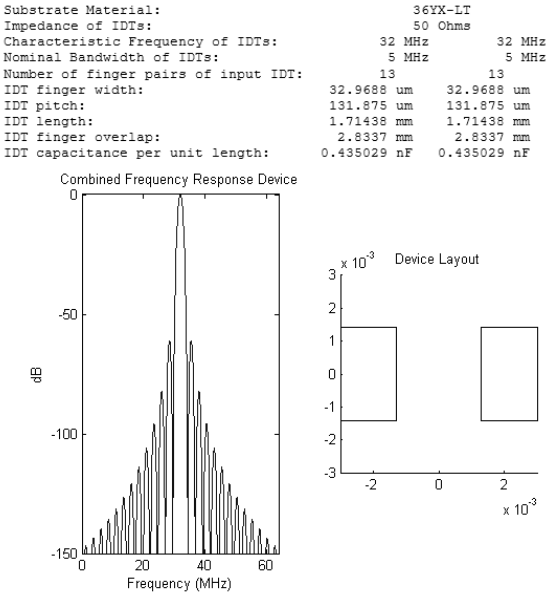

Figure 6.19 Matlab report providing dimensions of IDT

Table 6-2 Design function output and actual values used for symmetrical SAW

	Design	Manufacture
Substrate Material	36YX-LT	
Impedance of IDTs	50 Ohms	
Characteristic Frequency of IDTs	32 MHz	32 MHz
Nominal Bandwidth of IDTs	5 MHz	5 MHz
Number of finger pairs of input IDT	13	13
IDT finger width	32.9688 um	32.9688 um
IDT pitch	131.875 um	131.875 um
IDT length	1.71438 mm	1.71438 mm
IDT finger overlap	2.8337 mm	2.8337 mm
IDT capacitance per unit length	0.435029 nF	0.435029 nF

6.6 SAW microfabrication

The transducer electrode pattern is etched into a thin metal film deposited onto the substrate by electron beam evaporation. The photo-lithography process is outlined in this section.

The pattern of the SAW device is designed using the L-Edit software package. The L-Edit pattern is transferred to a reticle by the pattern generator which selectively exposes rectangular sections of the photo sensitive coating of the reticle with infra red light. Once the reticle exposure is completed the reticle is developed. This turns the exposed areas of the reticle black.

The developed reticle image is a large version of the SAW pattern. The reticle pattern is optically reduced 10× and reproduced in a grid by the step and repeat camera to generate a mask. This is a negative of the pattern produced on the gold layer. The mask is a 1:1 inverted representation of the structure that will be etched into the gold surface. This is conducted under yellow safe light.

Once exposed the mask is developed for one minute in 7:1 Shipley AZ606 developer at 22° C. The developed wafer is rinsed thoroughly and spun dry. For later identification a label is scribed onto mask. The chrome is etched from the mask by agitation in chrome etch solution for 50 seconds. The photo resist is stripped by vigorous agitation in Shipley 1112A stripper.

The finished mask can be used repeatedly to fabricate devices. Figure 6.20 outlines the electrode fabrication process from the mask stage onwards. The preparation of SAW wafers requires gold metallisation. The wafer is blown clean and further cleaned in hot piranha solution and oxygen plasma. Electron beam evaporation of 14nm of Chromium is followed by 296nm Gold.

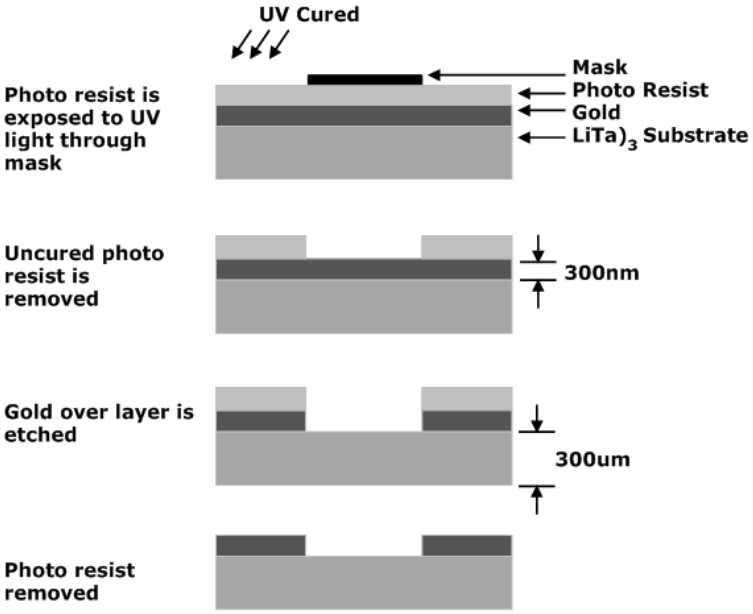

Figure 6.20 Microfabrication of SAW device

The gold wafer is primed with HDMS for 2 minutes, and flushed with pure Nitrogen. AZ 1500 20 photo resist is filtered through a clean filter and spin coated onto the substrate at 5000 RPM for one minute.

The photo resist is exposed through the mask which cures the photo resist. Wafer is soft baked at 100° C for 90 sec. The mask is exposed for 22 seconds and post baked at 100° C for 30 minutes. Uncured resist is removed from the wafer. The pattern is clearly visible in photo resist on the wafer. The metal is then etched from the wafer. Gold is etched using 340g KI : 200mL D.I. H_2O : 7g I_2 ,,diluted four times with H_2O. Immerse Wafer in etch solution for 6 sec per micron of gold, agitating occasionally. The wafer is rinsed with D.I. water and blown dry. The chromium adhesion layer and uncured photo-resist is similarly removed.

SU-8 layers provide protection for the electrodes. The SU-8 layer is applied as follows. The wafer is rinsed with acetone and prepared for coating by oxygen plasma cleaning. The forward power of plasma cleaner is reduced for SAW because of pyroelectric effects. Cleaning takes 2 minutes. Omnicoat Coating promotes adhesion of SU-8 and makes SU-8 coating easier to reverse if the need arises. Spin coating 3000RPM for 1 minute for both Omnicoat and SU-8. Soft bake on hot plate. Increase linearly from 20°C to 110°C over 2min. Bake at 110°C for further 3min. SU-8 is spin coated and soft baked. Increase linearly from 20°C to 110°C over 4min. Baked at 110°C for further 5min.

The contact pads are masked and the whole wafer is exposed to UV for 30s to cure the layer. Post bake is achieved by increasing linearly from 20°C to 110°C over 2min. Bake at 110°C for further 3min.

The patterned layer is developed in SU-8 Developer for one minute. Rinse with iso-propyl-alcohol (IPA) on spinner and further hard baked. Figure 6.21 shows the SAW wafer before dicing. Figure 6.22 shows a single completed SAW device in a mount which permits electrical connection using SMB connectors.

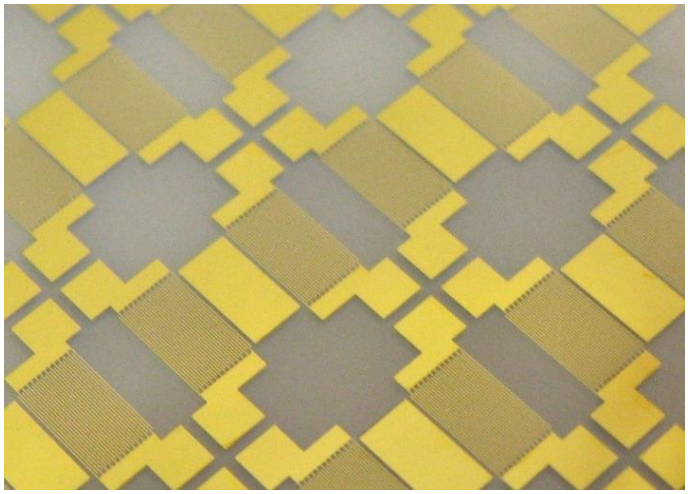

Figure 6.21 Fabricated SAW devices on 36YXLiTaO$_3$ before dicing

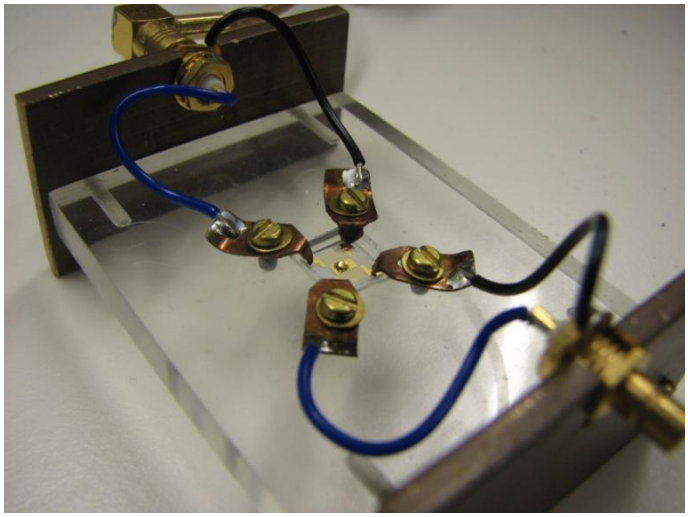

Figure 6.22 Fabricated SAW in mount

6.7 SAW experiments of bond rupture

The SAW device developed and manufactured as per the earlier sections is used to test the viability of SAW bond rupture. The device is not refined to a final solution and does not feature many of the traits earlier identified. The device is not integrated into a micro fabricated flow cell and must be used in its open configuration.

Operation of a SAW is achieved with the existing bond rupture equipment. The FPGA bond rupture system board has a pi filter before the switch on the output. The purpose of this is to suppress the harmonics of the DAC output so that they are not aliased. This is temporarily modified for SAW operation

a) b)

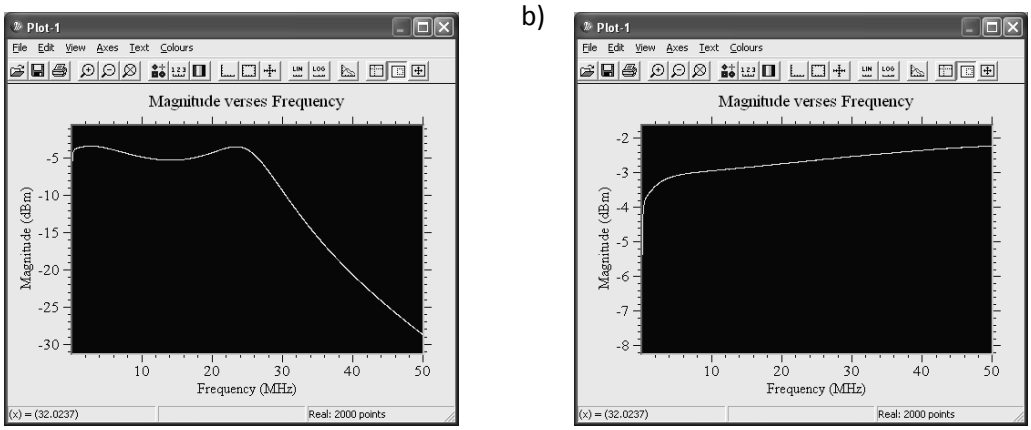

Figure 6.23 Primary scan with Pi filter (a) and without (b)

As shown in Figure 6.23 there is significant attenuation (12dB) at the SAW operating frequency of 32MHz. This manifests as a reduction in the maximum driving voltage at which the SAW can be driven. With the filter in place the hardware can drive a 50 ohm load at 8V at 32 MHz, compared to 15V achieved at the QCM operating frequency (10.7MHz). Once the filter is removed the primary scan looks very different. The hardware can drive at 32MHz up to a voltage of 24V. Some peripheral filters and impedance matching devices were built for the SAW device to change the operation of the hardware from a voltage monitoring feedback to a current monitor.

Binding the phantom particles using a liquid drop is difficult. Pictured Figure 6.24 (a) is 5µm beads on a gold surface. Some of the beads settle onto the surface and some remain suspended in the fluid and are out of focus. Beads applied in this manner are prone to grouping once the liquid evaporates as demonstrated in Figure 6.24 (b). This is overcome by experimentally determining a suitable concentration of particles and a suitable solvent. Dilution 40-50 times with ethanol is suitable for five micron beads.

Phantom particles, two micron in diameter are diluted 40 times and a drop placed in the middle of the SAW delay line. Free beads move randomly around the drop by Brownian motion. When the microscope is focused at the surface, beads resting on the surface are visible. It is evident from successive images that these bound beads are stationary. In the absence of binding chemistry the surface is hydrophilic and the droplet is flat and easily imaged through.

Figure 6.25 shows evidence of something moving. The droplet is distorted by the acoustic activity during the scan and the before and after images show different locations of particles. These images are gray scale inverses of the original dark field microscope images. The large black spots in each frame result from reflections from the illumination.

a) b)

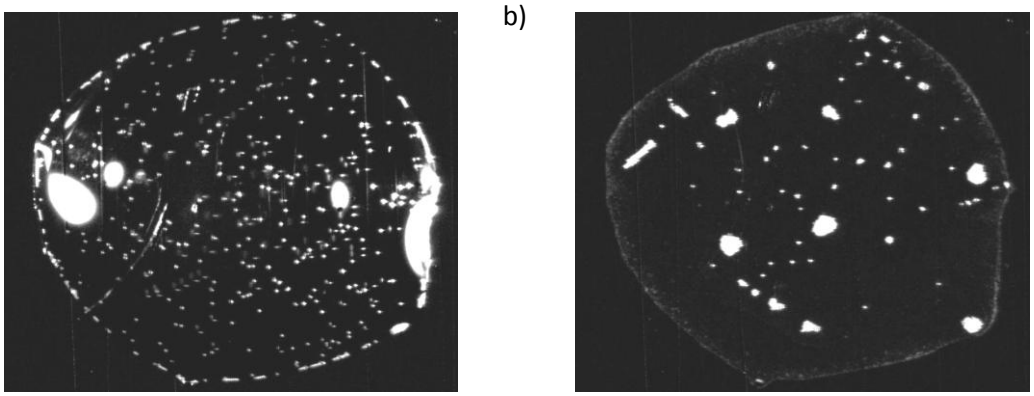

Figure 6.24 Five micron beads in liquid applied to a gold surface in suspension (a) and after liquid evaporation (b)

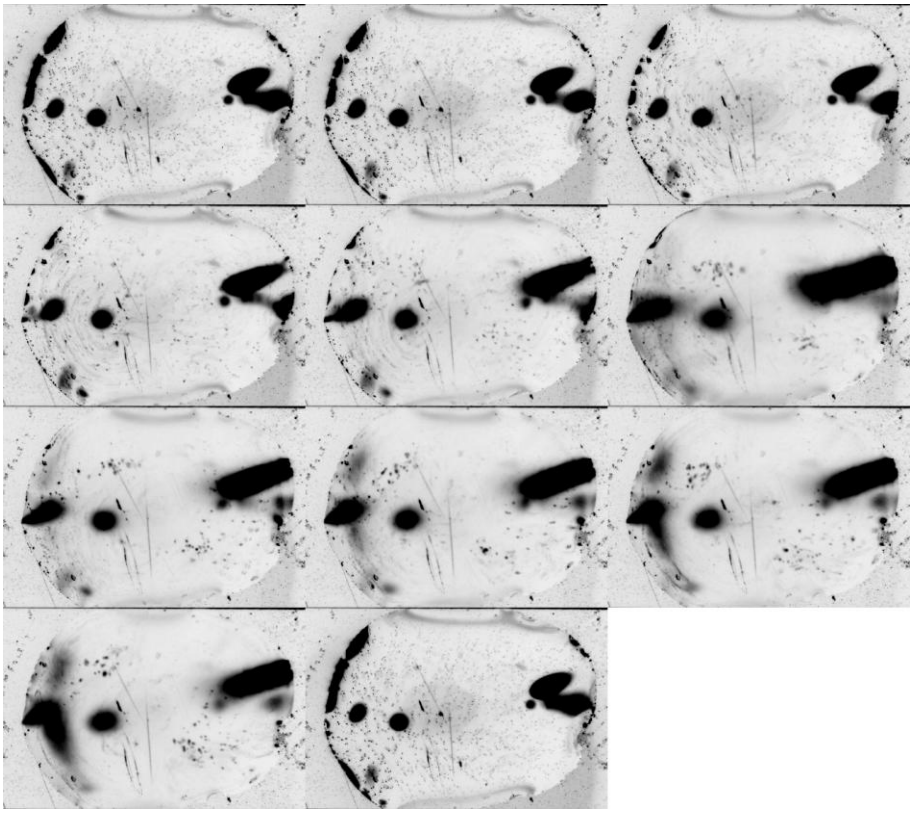

Figure 6.25 Time series images of SAW bond rupture scan captured using digital microscope

When the streptavidin-biotin phantom interaction is used the immobilisation process has made the SAW delay line hydrophobic. This causes a migration of the droplet on the surface as shown in Figure 6.26. In addition the vigorous shaking causes turbulence in the droplet. This is evidence that the SAW platform requires microfluidic integration.

To work around this problem an alternative experiment methodology is developed. The solution in the droplet is allowed to dry. Physically adhered two micron phantom particles are applied and are scanned from 1 to 24V in 20 seconds. The bond rupture device is designed to monitor the transducer frequency, however the SAW delay line frequency is largely insensitive

to attached mass. During the scan images are taken to monitor the attached particles. Several frames are presented in Figure 6.27.

It is evident that large groups of particles formed as the surface preparation dries survive the scan but single particles are removed. The particles, once ruptured do not leave the frame but trend left to right. In a microfluidic flow sensor these would be carried away.

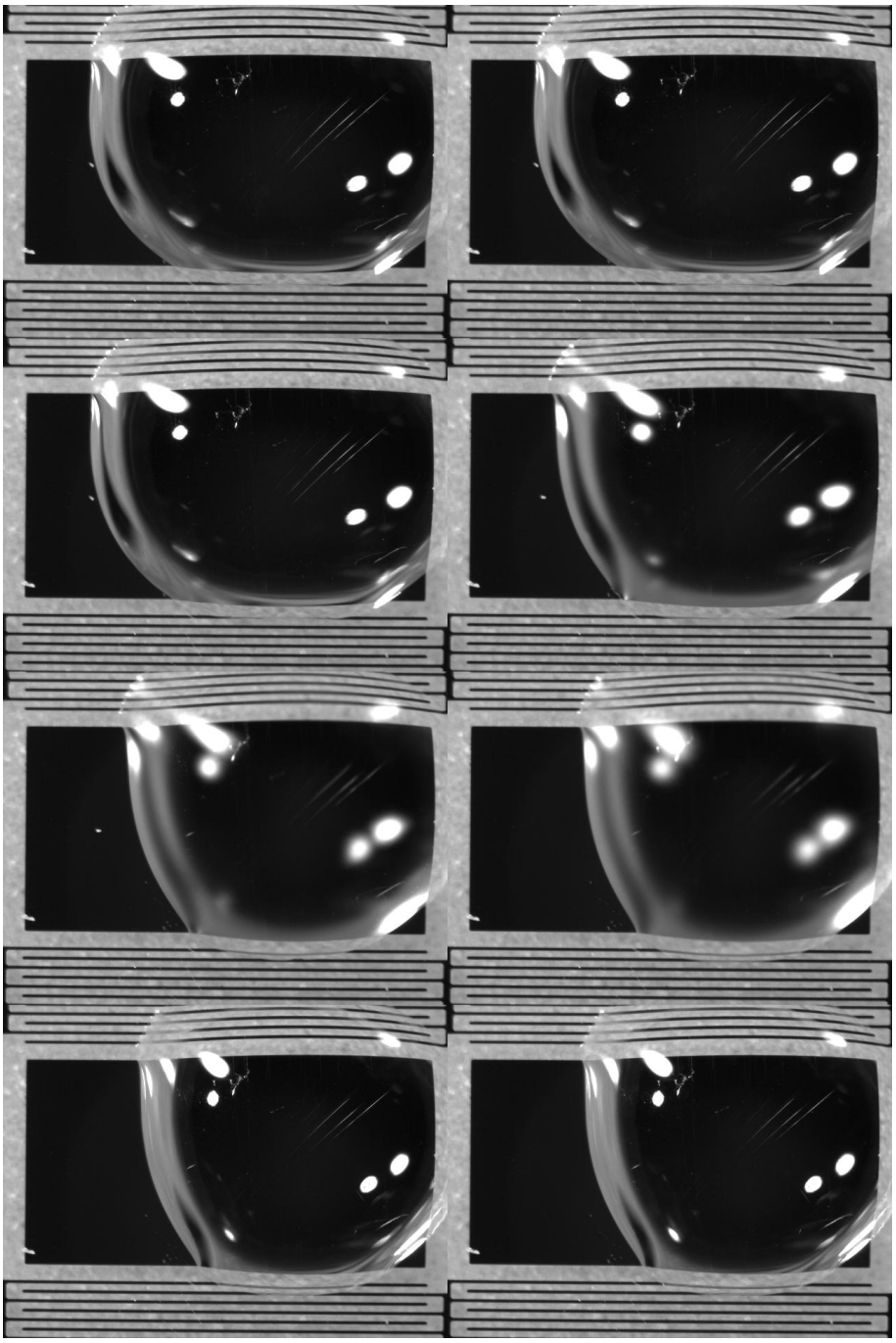

Figure 6.26 SAW delay line with surface prepared for immobilisation requires micro-fluidics integration

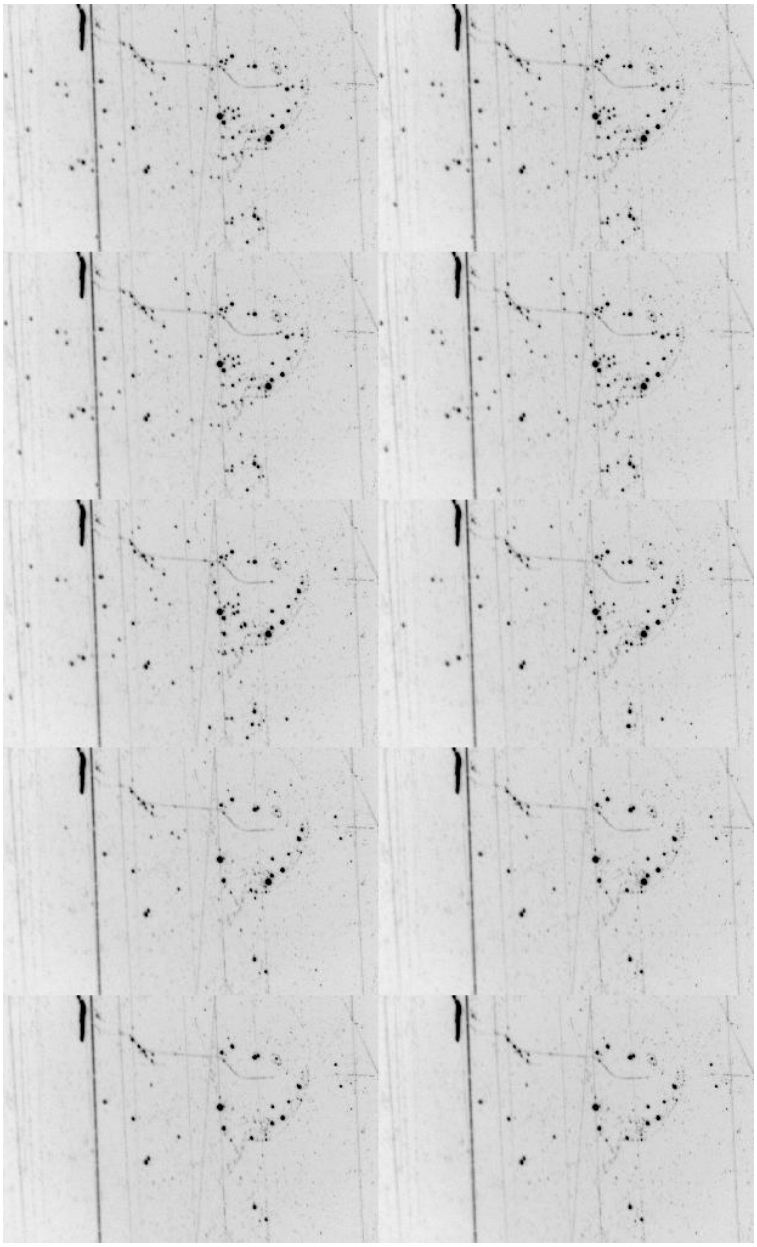

Figure 6.27 SAW surface during dry bond rupture scan

Specifically bound two micron phantom particles are used as described for QCM experiments and the same scan parameters as above. After the binding the SAW devices are rinsed and left floating on water surface to remove weakly bound particles. An image is captured before the bond rupture scan and a drop of water is added to the surface. Following the scan the drop is removed and another image captured.

The vigorous turbulence of the droplet during the scan and the fast moving particles suspended in the drop after rupture make it difficult to observe by the camera or naked eye. Once the scan activity has ceased Brownian motion of ruptured particles is seen where none existed before. The drop is removed to permit comparison with the initial image.

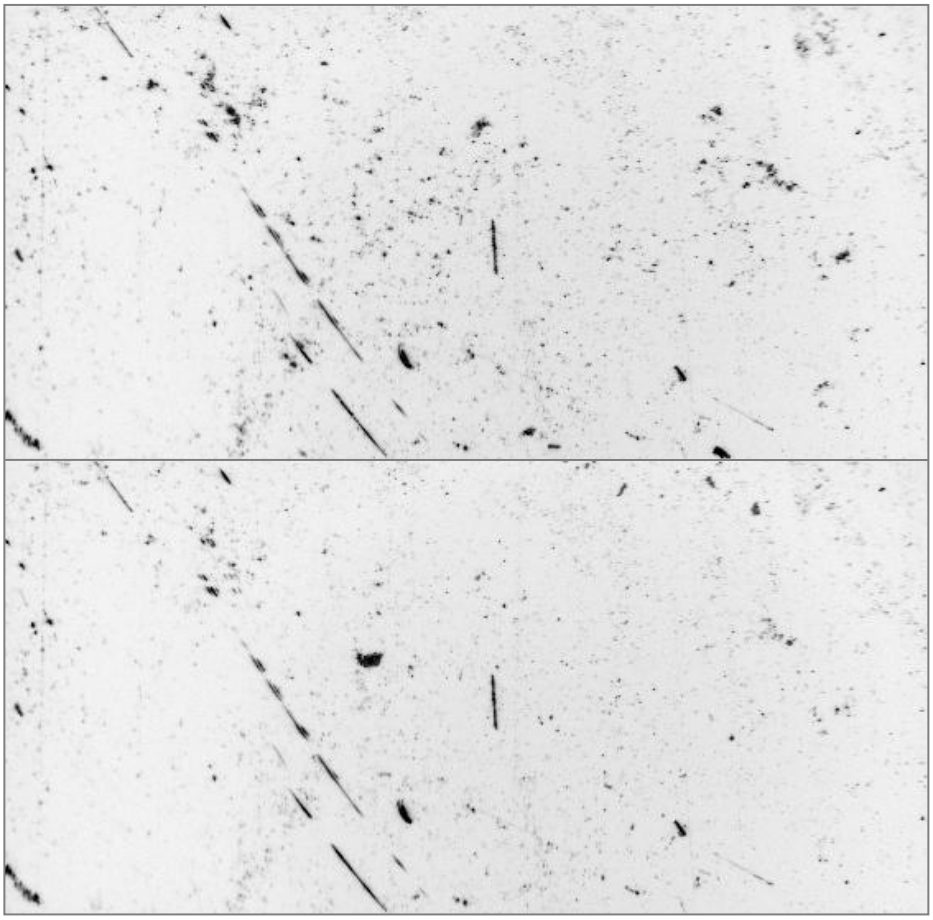

Figure 6.28 Entire sensor delay line showing before and after experiment. Several particles have grouped after rupture and drying.

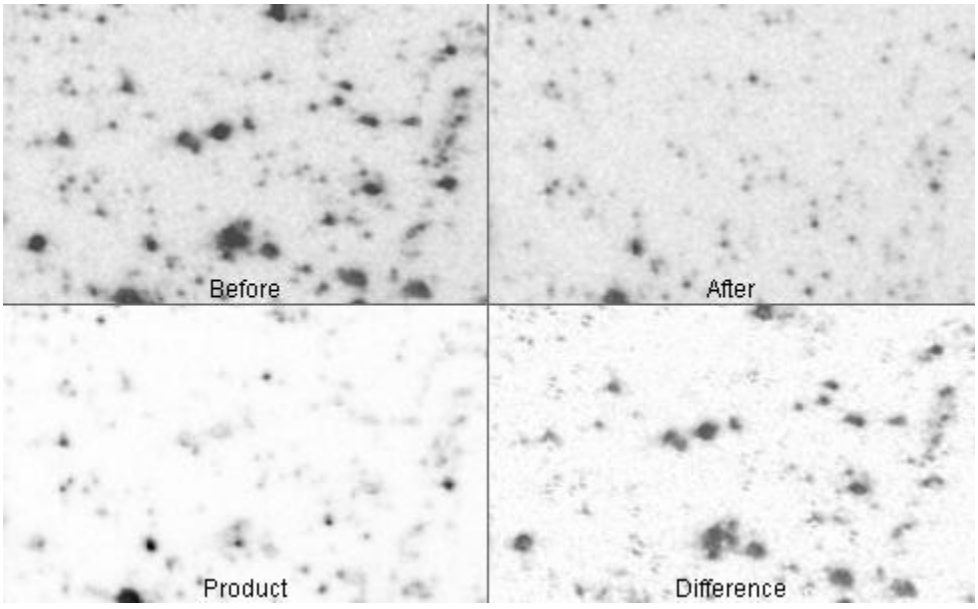

Figure 6.29 Detail view. The product image is indicative of the features and particles that do not move, and the difference image shows particles that have been ruptured during the experiment.

Figure 6.28 shows an overview of the SAW delay line before (top) and after the rupture scan (bottom). Many particles have been ruptured and a group of ruptured particles left

behind after the scan is evident. Figure 6.29 shows a close up view of Figure 6.28 as well as the difference and product images which highlight areas where particles and features have remained unchanged (product) and moved (difference)

6.8 Limitations

The SAW platform as presented here is limited by its simplicity. Simple devices were made because the fabrication of SAW devices is a new activity for this group. Several aspects of the device performance are limited by the constraints imposed by the QCM bond rupture hardware, these include the operating frequency and the amount of power that is available to drive the transducers. Dedicated electronics is required to operate SAW devices.

Bond rupture noise, the signal generated by detachment of particles, is not apparent in the prototype SAW but there is much room for manipulation of the transducers to achieve this goal. Further limitations arise in the microfabrication process which constrains the size of the transducer which, especially considering the low operating frequency of the device, forces the use of low quality IDT.

The impedance of the device could not be precisely matched to the driving hardware. The resulting impedance mismatch in the device is ignored on the basis that the wires in the system are much shorter than the electromagnetic wavelength and thus the result of back reflections will not be very detrimental. The power transferred to the device is affected.

The experiment methodology would be improved with integration of flow cells. Experiments are difficult to conduct in liquid environments and the SAW is smaller that the QCM making this still more difficult. The prepartation of the transducers takes place in solution and it is difficult to limit the influence of the added mass to the sensitive area. This is a limitation of the QCM also but the SAW device offeres better potential for encapsulation because of the confinement of energy to the surface and the single sided architecure.

In order to overcome inconsistencies in the material constants and fabricate a more predictable device a test structure may be made to determine these properties. Further SAW devices will embrace more complex structures to achieve better efficiency and signal processing. Additional finger pairs will improve the quality of the input IDT. Reduced bandwidth could also be achieved by increasing the characteristic frequency of the IDT allowing more finger pairs into the same transducer length.

Reflector gratings or unidirectional transducers will decrease insertion loss and more importantly increase the acoustic energy at the sensitive area improving sensor operation. The

edges at both ends may be cut at an angle or loaded with absorbing resin to suppress the reflections in the propagation direction of the primary wave.

Suitable guiding layers need to be evaluated. Whereas a suitable pit over the delay line may hold drops in place for the duration of the experiment, full integration into a microfluidic flow cell is preferred.

An improved SAW bond rupture device embracing the changes mentioned above requires access to direct-write lithography in order to overcome the size constraints. Revised driving electronics are also required.

6.9 Chapter Conclusion

This chapter has outlined the design and manufacture of a simple SAW sensor to evaluate the potential of the platform in the bond rupture application. Prototype SAW devices for bond rupture were fabricated and tested and the principle of SAW bond rupture is confirmed. It is concluded that the platform shows much promise for the advancement of bond rupture technology. The prototype device presented here was designed in a simplistic and uncomplicated manner and it is clear that further effort is required to enhance the capabilities of the electronics and fabrication in order to attain the best performance. A number of improvements are suggested and several avenues of new work have been identified.

7. CONCLUSION

This thesis investigated by experiment, the characteristics of QCM bond rupture. In the first instance this involved designing and building parts of the bond rupture hardware. After the bond rupture system was running the investigation into the mechanisms behind bond rupture of single particles began with the intent to evaluate and improve the bond rupture experiment process and transducers. The move toward Surface Acoustic Wave devices arose from this investigation and, along the way, many avenues for the advancement of bond rupture technology have been identified. All the previous wisdom gained while working with QCM was applied to the SAW device and the electronics hardware was developed and modified as required.

A summary of the results of this thesis and contributions to knowledge includes a comprehensive review of the literature regarding bond rupture, QCM, other transducers and sensing technologies (Chapter 2). This work is in part presented in a review article for general use. In addition, a broad spectra of QCM measurements and bond rupture experiments were undertaken and analysed (Chapter 3). This is a more comprehensive investigation of bond-rupture experiments than has been previously published. These experiments provide the basis for the modelling of single particle bond rupture (Chapter 4) and bond rupture devices (Chapter 5). The models are a valuable contribution toward furthering bond rupture techniques and expanding the penetration of bond rupture into related sensing fields. Finally, following from the work of the previous chapters a new prototype bond rupture device is designed, developed, tested and evaluated (Chapter 6). The insights of this chapter are vital for the development of SAW bond rupture devices.

There are many further avenues for research in the field of bond rupture on both the QCM and SAW platforms. There is potential for further development of the supporting electronics and software. It is expected that the rupture of a particle may briefly change the shape of the QCM voltage and that this could be analysed to detect bond rupture events.

The combination of an alternative transducer and a flexible model allows new ideas to be tested at decreased cost. The SAW platform in particular offers the ability to fabricate transducers that sense on a different axis to the driving transducer. Such a transducer would be insensitive to the driving signal and the frequency and bandwidth could be tailored to suit. Integration of such a device with a microfluidic flow cell is an interesting challenge. The move towards a single sided device is set to expose bond rupture to a range of established optical techniques. Integration with established devices is perhaps the greatest strength of the bond rupture methodology and the contribution of this thesis.

8. REFERENCES

ARNAU, A., SOGORB, T. & JIMENEZ, Y. (2002) Circuit for continuous motional series resonant frequency and motional resistance monitoring of quartz crystal resonators by parallel capacitance compensation. *Review of Scientific Instruments*, 73, 2737.

BALLATO, A. (1995) Piezoelectricity - Old Effect, New Thrusts. *IEEE Transactions on Ultrasonics Ferroelectrics and Frequency Control*, 42, 916-926.

BARIE, N. & RAPP, M. (2001) Covalent bound sensing layers on surface acoustic wave (SAW) biosensors. *Biosensors & Bioelectronics*, 16, 979-987.

BARIE, N., WESSA, T., BRUNS, M. & RAPP, M. (2004) Love waves in SiO2 layers on STW-resonators based on LiTaO3. *Talanta*, 62, 71-79.

BARNES, C., DSILVA, C., JONES, J. P. & LEWIS, T. J. (1992) The Theory of Operation of Piezoelectric Quartz Crystal Sensors for Biochemical Application. *Sensors and Actuators A-Physical*, 31, 159-163.

BEHME, G., BLOCKER, M., BIGLER, E., HESJEDAL, T. & FROHLICH, H. J. (1998) High resolution acoustic field imaging applied to surface acoustic wave devices. *Ultrasonics Symposium, 1998. Proceedings. IEEE 1998*

BENES, E. R., GROSCHL, R., SEIFERT, F. & POHL, A. (1998) Comparison between BAW and SAW sensor principles. *IEEE Transactions on Ultrasonics Ferroelectrics and Frequency Control*, 45, 1314-1330.

BERGGREN, C., BJARNASON, B. & JOHANSSON, G. (2001) Capacitive Biosensors. *Electroanalysis*, 13, 173-180.

BHATTACHARYYA, A. B., TULI, S. & MAJUMDAR, S. (1995) Spice Simulation of Surface-Acoustic-Wave Interdigital Transducers. *IEEE Transactions on Ultrasonics Ferroelectrics and Frequency Control*, 42, 784-786.

BOROVSKY, B., MASON, B. L. & KRIM, J. (2000) Scanning tunnelling microscope measurements of the amplitude of vibration of a quartz crystal oscillator. *Journal of Applied Physics*, 88, 4017-4021.

BRICE, J. C. (1985) Crystals for quartz resonators. *Reviews of Modern Physics*, 57, 105 LP - 146.

BUNKA, D. H. J. & STOCKLEY, P. G. (2006) Aptamers come of age - at last. *Nat Rev Micro*, 4, 588-596.

BUTT, H. J., CAPPELLA, B. & KAPPL, M. (2005) Force measurements with the atomic force microscope: Technique, interpretation and applications. *Surface Science Reports,* 59, 1-152.

BUTTRY, D. A. & WARD, M. D. (1992) Measurement of Interfacial Processes at Electrode Surfaces with the Electrochemical Quartz Crystal Microbalance. *Chemical Reviews*, 92, 1355-1379.

CALABRESE, G. S., WOHLTJEN, H. & ROY, M. K. (1987) Surface Acoustic-Wave Devices as Chemical Sensors in Liquids - Evidence Disputing the Importance of Rayleigh-Wave Propagation. *Analytical Chemistry*, 59, 833-837.

CHANG, K. S., JANG, H. D., LEE, C. F., LEE, Y. G., YUAN, C. J. & LEE, S. H. (2006) Series quartz crystal sensor for remote bacteria population monitoring in raw milk via the Internet. *Biosensors & Bioelectronics*, 21, 1581-90, 2006 Feb 15.

CHANG, S. M., MURAMATSU, H., NAKAMURA, C. & MIYAKE, J. (2000) The principle and applications of piezoelectric crystal sensors. *Materials Science & Engineering C-Biomimetic and Supramolecular Systems*, 12, 111-123.

COLLINGS, A. F. & CARUSO, F. (1997) Biosensors: recent advances. *Reports on Progress in Physics*, 60, 1397-1445.

COOPER, M. A. & SINGLETON, V. T. (2007) A survey of the 2001 to 2005 quartz crystal microbalance biosensor literature: applications of acoustic physics to the analysis of biomolecular interactions. *Journal of Molecular Recognition*, 20, 154-184.

COOPER, M. A. (2003) Biosensing using rupture event scanning (REVS)(TM). *Measurement Science & Technology*, 14, 1888-1893.

COOPER, M. A. (2003) Label-free screening of bio-molecular interactions. *Analytical and Bioanalytical Chemistry*, 377, 834-842.

COOPER, M. A., DULTSEV, F. N., MINSON, T., OSTANIN, V. P., ABELL, C. & KLENERMAN, D. (2001) Direct and sensitive detection of a human virus by rupture event scanning. *Nature Biotechnology*, 19, 833-7.

CULAR, S., BRANCH, D. W., BHETHANBOTLA, V. R., MEYER, G. D. & CRAIGHEAD, H. G. (2008) Removal of nonspecifically bound proteins on microarrays using surface acoustic waves. Ieee Sensors Journal, 8, 314-320.DE LIMA, M. M., SEIDEL, W., KOSTIAL, H. & SANTOS, P. V. (2004) Embedded interdigital transducers for high-frequency surface acoustic waves on GaAs. *Journal of Applied Physics*, 96, 3494-3500.

DEJOUS, C., SAVART, M., REBIERE, D. & PISTRE, J. (1995) A Shear-Horizontal Acoustic Plate Mode (SH-APM) Sensor for Biological Media. *Sensors and Actuators B-Chemical*, 27, 452-456.

DERJAGUIN, B. V., MULLER, V. M. & TOPOROV, Y. P. (1975) EFFECT OF CONTACT DEFORMATIONS ON ADHESION OF PARTICLES. *Journal of Colloid and Interface Science,* 53, 314-326.

D'ORAZIO, P. (2003) Biosensors in clinical chemistry. *Clinica Chimica Acta*, 334, 41-69.

DRAFTS, B. (2001) Acoustic wave technology sensors. *IEEE Transactions on Microwave Theory and Techniques*, 49, 795-802.

DU, J., HARDING, G. L., OGILVY, J. A., DENCHER, P. R. & LAKE, M. (1996) A study of love-wave acoustic sensors. *Sensors and Actuators A-Physical*, 56, 211-219.

DULTSEV, F. N., KLENERMAN, D. & OSTANIN, V. P. (2001). Measurement of Molecular Interactions. WO2000GB01587 20000425 11-01-2001

DULTSEV, F. N., OSTANIN, V. P. & KLENERMAN, D. (2000) "Hearing" bond breakage. Measurement of bond rupture forces using a quartz crystal microbalance. *Langmuir*, 16, 5036-5040.

DULTSEV, F. N., SPEIGHT, R. E., FLORINI, M. T., BLACKBURN, J. M., ABELL, C., OSTANIN, V. P. & KLENERMAN, D. (2001) Direct and quantitative detection of bacteriophage by "Hearing" surface detachment using a quartz crystal microbalance. *Analytical Chemistry*, 73, 3935-3939.

EDVARDSSON, M., RODAHL, M., KASEMO, B. & HOOK, F. (2005) A dual-frequency QCM-D setup operating at elevated oscillation amplitudes. *Analytical Chemistry*, 77, 4918-4926.

EVANS, E. & RITCHIE, K. (1997) Dynamic strength of molecular adhesion bonds. *Biophysical Journal,* 72, 1541-1555.

EVANS, E. & RITCHIE, K. (1999) Strength of a weak bond connecting flexible polymer chains. *Biophysical Journal,* 76, 2439-2447.

EVANS, E. (1998) Energy landscapes of biomolecular adhesion and receptor anchoring at interfaces explored with dynamic force spectroscopy. *Faraday Discussions*, 1-16.

EVANS, E. (2001) Probing the relation between force-lifetime-and chemistry in single molecular bonds. *Annual Review of Biophysics & Biomolecular Structure*, 30, 105-28.

EVANS, E., RITCHIE, K. & MERKEL, R. (1995) Sensitive Force Technique to Probe Molecular Adhesion and Structural Linkages at Biological Interfaces. *Biophysical Journal,* 68, 2580-2587.

FRANCIS, L. A., FRIEDT, J. M., ZHOU, C. & BERTRAND, P. (2006) In situ evaluation of density, viscosity, and thickness of adsorbed soft layers by combined surface acoustic wave and surface plasmon resonance. *Analytical Chemistry*, 78, 4200-4209.

GAGNEPAIN, J. J. (1981) Nonlinear Properties of Quartz Crystal and Quartz Resonators: A Review. *Frequency Control, 35th Annual Symposium on.* 1981.

GIZELI, E., BENDER, F., RASMUSSON, A., SAHA, K., JOSSE, F. & CERNOSEK, R. (2003) Sensitivity of the acoustic waveguide biosensor to protein binding as a function of the waveguide properties. *Biosensors & Bioelectronics*, 18, 1399-1406.

GODBER, B., THOMPSON, K. S. J., REHAK, M., ULUDAG, Y., KELLING, S., SLEPTSOV, A., FROGLEY, M., WIEHLER, K., WHALEN, C. & COOPER, M. A. (2005) Direct quantification of analyte concentration by resonant acoustic profiling. *Clinical Chemistry*, 51, 1962-1972.

GRANDBOIS, M., BEYER, M., RIEF, M., CLAUSEN-SCHAUMANN, H. & GAUB, H. E. (1999) How strong is a covalent bond? Science, 283, 1727-1730.

GRATE, J. W. & FRYE, G. C. (1996) *Acoustic Wave Sensors. Sensors Update*, 2, 37-83.

GRUBMULLER, H., HEYMANN, B. & TAVAN, P. (1996) Ligand Binding: Molecular Mechanics Calculation of the Streptavidin-Biotin Rupture Force. *Science,* 271, 997-999.

HAGLEITNER, C., HIERLEMANN, A., LANGE, D., KUMMER, A., KERNESS, N., BRAND, O. & BALTES, H. (2001) Smart single-chip gas sensor microsystem. *Nature*, 414, 293-296.

HANGGI, P., TALKNER, P. & BORKOVEC, M. (1990) Reaction-Rate Theory - 50 Years after Kramers. *Reviews of Modern Physics,* 62, 251-341.

HARTMANN, C. S. & ABBOTT, B. P. (1989) Overview of design challenges for single phase unidirectional SAW filters. *Ultrasonics Symposium, 1989. Proceedings. IEEE 1989*.

HASHIMOTO, K.-Y. (2000) Surface acoustic wave devices in telecommunications : modelling and simulation. Berlin ; New York :, Springer.

HAUPTMANN, P., LUCKLUM, R. & SCHRODER, J. (2003) Recent trends in bulk acoustic wave resonator sensors. *Ultrasonics, 2003 IEEE Symposium on*.

HEITMANN, V. & WEGENER, J. (2007) Monitoring Cell Adhesion by Piezoresonators: Impact of Increasing Oscillation Amplitudes. *Analytical Chemistry*, 79, 3392-3400.

HEYMANN, B. & GRUBMULLER, H. (2001) Molecular dynamics force probe simulations of antibody/antigen unbinding: Entropic control and nonadditivity of unbinding forces. *Biophysical Journal,* 81, 1295-1313.

HICKERNELL, F. S. (2000) The experimental SAW propagation characteristics of LiNbO3 and LiTaO3 with free and metallized surfaces.

HIRST, E. R., YUAN, Y. J., XU, W. L. & BRONLUND, J. E. (2008) Bond rupture immunosensors - A review. *Biosensors & Bioelectronics*, 23, 1759-1768.

HOA, X. D., KIRK, A. G. & TABRIZIAN, M. (2007) Towards integrated and sensitive surface plasmon resonance biosensors: A review of recent progress. *Biosensors and Bioelectronics*, 23, 151-160.

HOOK, F., RODAHL, M., KELLER, C., GLASMASTAR, K., FREDRIKSSON, C., DAHIQVIST, P. & KASEMO, B. (1999) The dissipative QCM-D technique: interfacial phenomena and sensor applications for proteins, biomembranes, living cells and polymers. *Frequency and Time*

Forum, 1999 and the IEEE International Frequency Control Symposium, 1999., Proceedings of the 1999 Joint Meeting of the European.

HUANG, J., CHEN, J., CHESLA, S. E., YAGO, T., MEHTA, P., MCEVER, R. P., ZHU, C. & LONG, M. (2004) Quantifying the effects of molecular orientation and length on two-dimensional receptor-ligand binding kinetics. *Journal of Biological Chemistry*, 279, 44915-44923.

HUANG, L. & COOPER, M. A. (2006) Real-time label-free acoustic technology for rapid detection of Escherichia coli O157 : H7. *Clinical Chemistry*, 52, 2148-2151.

HUIJSING, J. H. (1992) Integrated Smart Sensors. *Sensors and Actuators A-Physical*, 30, 167-174.

HUNSINGER, B. J. & HANMA, K. (1979). Surface acoustic wave device with reflection suppression. July

IEEE (2004) IEEE Standard for A Smart Transducer Interface for Sensors and Actuators - Mixed-Mode Communication Protocols and Transducer Electronic Data Sheet (TEDS) Formats. IEEE Std 1451.4-2004.

ISRAELACHVILI, J. N. (1985) Intermolecular and surface forces : with applications to colloidal and biological systems / Jacob N. Israelachvili, London ; Orlando, [Fla]. :, Academic Press.

JANSHOFF, A. & STEINEM, C. (2001) Energy landscapes of ligand-receptor couples probed by dynamic force spectroscopy. *Chemphyschem,* 2, 577-579.

JANSHOFF, A. & STEINEM, C. (2001) Quartz crystal microbalance for bioanalytical applications. *Sensors Update*, 9, 313-354.

JANSHOFF, A., GALLA, H. J. & STEINEM, C. (2000) Piezoelectric mass-sensing devices as biosensors - An alternative to optical biosensors? *Angewandte Chemie-International Edition*, 39, 4004-4032.

JIN-WOO, C., YING, D., AHN, C. H., HALSALL, H. B. & HEINEMAN, W. R. (1997) A microchip electrochemical immunosensor fabricated using micromachining techniques. *Proceedings - 19th International Conference - IEEE/EMBS Chicago, IL. USA*.

JOHNSON, K. L. & GREENWOOD, J. A. (1997) An adhesion map for the contact of elastic spheres. *Journal of Colloid and Interface Science,* 192, 326-333.

JOHNSON, K. L., KENDALL, K. & ROBERTS, A. D. (1971) SURFACE ENERGY AND CONTACT OF ELASTIC SOLIDS. *Proceedings of the Royal Society of London Series a-Mathematical and Physical Sciences,* 324, 301-&.

KANAZAWA, K. K. & GORDON, J. G. (1985) Frequency of a Quartz Microbalance in Contact with Liquid. *Analytical Chemistry*, 57, 1770-1771.

KARYAKIN, A. A., PRESNOVA, G. V., RUBTSOVA, M. Y. & EGOROV, A. M. (2000) Oriented immobilization of antibodies onto the gold surfaces via their native thiol groups *Analytical Chemistry*, 72, 3801-3811.

KIMURA, J. & KURIYAMA, T. (1990) Fet Biosensors. *Journal of Biotechnology*, 15, 239-254.

KODAMA, T., KAWABATA, H., YASUHARA, Y. & SATO, H. (1986) Design of Low-Loss SAW Filters Employing Distributed Acoustic Reflection Transducers. *Ultrasonics Symposium, 1986. Proceedings*. IEEE 1986

KUROSAWA, C., KUROSAWA, S., AIZAWA, H. & HORIBE, T. (2004) Computational simulation of vibration displacement on piezoelectric quartz crystal using finite element method. *Frequency Control Symposium and Exposition, 2004. Proceedings of the 2004 IEEE International.*

KUROSAWA, S., AIZAWA, H., TOZUKA, M., NAKAMURA, M. & PARK, J. W. (2003) Immunosensors using a quartz crystal microbalance. *Measurement Science & Technology*, 14, 1882-1887.

LANGE, K., BENDER, F., VOIGT, A., GAO, H. & RAPP, M. (2003) A surface acoustic wave biosensor concept with low flow cell volumes for label-free detection. *Analytical Chemistry*, 75, 5561-5566.

LANGE, K., BLAESS, G., VOIGT, A., GOTZEN, R. & RAPP, M. (2006) Integration of a surface acoustic wave biosensor in a microfluidic polymer chip. *Biosensors & Bioelectronics*, 22, 227-232.

LO, Y. S., ZHU, Y. J. & BEEBE, T. P. (2001) Loading-rate dependence of individual ligand-receptor bond rupture forces studied by atomic force microscopy. *Langmuir,* 17, 3741-3748.

LUPPA, P. B., SOKOLL, L. J. & CHAN, D. W. (2001) Immunosensors - principles and applications to clinical chemistry. *Clinica Chimica Acta*, 314, 1-26.

MARTIN, G., SCHMIDT, H. & WALL, B. (2004) New SPUDT cell structures. *IEEE Transactions on Ultrasonics Ferroelectrics and Frequency Control*, 51, 859-864.

MAUGIS, D. (1992) ADHESION OF SPHERES - THE JKR-DMT TRANSITION USING A DUGDALE MODEL. *Journal of Colloid and Interface Science,* 150, 243-269.

MCHALE, G., NEWTON, M. I. & MARTIN, F. (2002) Layer guided shear horizontally polarized acoustic plate modes. *Journal of Applied Physics*, 91, 5735-5744.

MCNAUGHT, A. D. & WILKINSON, A. (1997) IUPAC Compendium of Chemical Terminology, *Royal Society of Chemistry*, Cambridge, UK.

MECEA, V. M. (1994) Loaded vibrating quartz sensors. *Sensors and Actuators A-Physical*, 40, 1-27.

MECEA, V. M. (2005) From quartz crystal microbalance to fundamental principles of mass measurements. *Analytical Letters*, 38, 753-767.

MECEA, V. M., CARLSSON, J. O., ALM, O. & BOMAN, M. (2006) Out-of-plane vibrations of quartz resonators used in quartz crystal microbalance measurements in gas phase. *Sensors and Actuators A-Physical*, 125, 143-147.

MERKEL, R. (2001) Force spectroscopy on single passive biomolecules and single biomolecular bonds. *Physics Reports-Review Section of Physics Letters*, 346, 344-385.

MERKEL, R., NASSOY, P., LEUNG, A., RITCHIE, K. & EVANS, E. (1999) Energy landscapes of receptor-ligand bonds explored with dynamic force spectroscopy. *Nature*, 397, 50-53.

NAKAMURA, H. & KARUBE, I. (2003) Current research activity in biosensors. SO - *Analytical & Bioanalytical Chemistry*. 377(3). October 2003. 446-468.

NAKAMURA, H., YAMADA, T., ISHIZAKI, T. & NISHIMURA, K. (2001) A new design concept for low-loss SAW filters based on different-width split-finger SPUDT. *IEEE Transactions on Microwave Theory and Techniques*, 49, 761-768.

OGI, H., MOTOHISA, K., MATSUMOTO, T., MIZUGAKI, T. & HIRAO, M. (2006a) Wireless electrodeless piezomagnetic biosensor with an isolated nickel oscillator. *Biosensors & Bioelectronics,* 21, 2001-2005.

OGI, H., MOTOSHISA, K., MATSUMOTO, T., HATANAKA, K. & HIRAO, M. (2006b) Isolated Electrodeless High-Frequency Quartz Crystal Microbalance for Immunosensors. *Analytical Chemistry*, 78, 6903-6909.

OH, B. K., KIM, Y. K., PARK, K. W., LEE, W. H. & CHOI, J. W. (2004) Surface plasmon resonance immunosensor for the detection of Salmonella typhimurium. *Biosensors & Bioelectronics*, 19, 1497-1504.

PEKARCIKOVA, M., HOFMANN, M., MENZEL, S., SCHMIDT, H., GEMMING, T. & WETZIG, K. (2005) Investigation of high power effects on Ti/Al and Ta-Si-N/Cu/Ta-Si-N electrodes for SAW devices. *IEEE Transactions on Ultrasonics Ferroelectrics and Frequency Control*, 52, 911-917.

PERI, M. D. M. & CETINKAYA, C. (2005) Non-contact micro sphere-surface adhesion measurement via acoustic base excitations. *Journal of Colloid and Interface Science,* 288, 432-443.

PORTER, M. D., BRIGHT, T. B., ALLARA, D. L. & CHIDSEY, C. E. D. (1987) Spontaneously organized molecular assemblies. 4. Structural characterization of n-alkyl thiol monolayers on gold by optical ellipsometry, infrared spectroscopy, and electrochemistry. *Journal of the American Chemistry Society*, 109, 3559-3568.

RAIBLE, M., EVSTIGNEEV, M., REIMANN, P., BARTELS, F. W. & ROS, R. (2004) Theoretical analysis of dynamic force spectroscopy experiments on ligand-receptor complexes. *Journal of Biotechnology*, 112, 13-23.

RAYLEIGH, J. W. S., BARON (1945) The theory of sound, by John William Strutt, baron Rayleigh, with a historical introduction by Robert Bruce Lindsay, New York,, Dover publications,.

ROEDERER, J. E. & BASTIAANS, G. J. (1983) Microgravimetric Immunoassay with Piezoelectric-Crystals. *Analytical Chemistry*, 55, 2333-2336.

ROSHCHUPKIN, D. V., ROSHCHUPKINA, H. D. & IRZHAK, D. V. (2005) X-ray topography analysis of acoustic wave fields in the SAW-resonator structures. *IEEE Transactions on Ultrasonics Ferroelectrics and Frequency Control*, 52, 2081-2087.

SAUERBREY, G. (1959) Verwendung Von Schwingquarzen Zur Wagung Dunner Schichten Und Zur Mikrowagung. *Zeitschrift Fur Physik*, 155, 206-222.

SCHULTZ, J., MRKSICH, M., BHATIA, S. N., DAVID J, B., RICCO, A. J., WALT, D. R. & WILKINS, C. L. (2004) *WTEC Panel Report on International Research and Development in Biosensing*.

SCHWARZ, U. D. (2003) A generalized analytical model for the elastic deformation of an adhesive contact between a sphere and a flat surface. *Journal of Colloid and Interface Science,* 261, 99-106.

SCOUTEN, W. H., LUONG, J. H. T. & STEPHEN BROWN, R. (1995) Enzyme or protein immobilization techniques for applications in biosensor design. *Trends in Biotechnology*, 13, 178-185.

SHARMA, M.M., CHAMOUN, H., SITA RAMA SARMA, D.S.H., AND SCHECHTER , R.S. (1992) Factors controlling the hydrodynamic detachment of particles from surfaces. *Journal of Colloid and Interface Science*. 149 (1992), pp. 121–134

SHONS, A., NAJARIAN, J. & DORMAN, F. (1972) Immunospecific Microbalance. *Journal of Biomedical Materials Research*, 6, 565-&.

SLOBODNI.AJ & BUDREAU, A. J. (1972) Acoustic Surface-Wave Loss Mechanisms on Bi12geo20 at Microwave-Frequencies. *Journal of Applied Physics*, 43, 3278-&.

SMITH, W. R., REEDER, T. M., COLLINS, J. H., SHAW, H. J. & HANSEN, W. W. (1969) Dispersive Rayleigh Wave Delay Line Utilizing Gold on Lithium Niobate (Correspondence). *Microwave Theory and Techniques, IEEE Transactions on,* 17, 1043-1044.

SOKOLL, L. J. & CHAN, D. W. (1999) Clinical analyzers. Immunoassays. Analytical Chemistry, 71, 356R-362R.

STAYTON, P. S., FREITAG, S., KLUMB, L. A., CHILKOTI, A., CHU, V., PENZOTTI, J. E., TO, R., HYRE, D., LE TRONG, I., LYBRAND, T. P. & STENKAMP, R. E. (1999) Streptavidin-biotin binding energetics. *Biomolecular Engineering,* 16, 39-44.

STEGEMANN, B., BACKHAUS, H., KLOSS, H. & SANTNER, E. (2007) Spherical AFM Probes for Adhesion Force Measurements on Metal Single Crystals. IN MÉNDEZ-VILAS, A. & DÍAZ, J. (Eds.) *Modern Research and Educational Topics in Microscopy.*

STOKES, G. G. (1851) Trans. Cambridge Philos. Soc. , 9 8–106.

TABOR, D. (1977) Surface forces and surface interactions. *Journal Of Colloid And Interface Science,* 58.

THOMPSON, M., BALLANTYNE, S. M., CHERAN, L. E., STEVENSON, A. C. & LOWE, C. R. (2003) Electromagnetic excitation of high frequency acoustic waves and detection in the liquid phase. *Analyst*, 128, 1048-1055.

TOMBELLI, S., MINUNNI, M., LUZI, E. & MASCINI, M. (2005) Aptamer-based biosensors for the detection of HIV-1 Tat protein. *Bioelectrochemistry*, 67, 135-141.

TRESSLER, J. F., ALKOY, S. & NEWNHAM, R. E. (1998) Piezoelectric sensors and sensor materials. *Journal of Electroceramics*, 2, 257-272.

VAINSHTEIN, P. & SHAPIRO, M. (2009) Forces on a porous particle in an oscillating flow. *Journal of Colloid and Interface Science,* 330, 149-155.

van der Werff, M. (2009). Development of digital instrumentation for bond rupture detection, PhD Thesis, Massey University.VAN DER WERFF, M. J., YUAN, Y., HIRST, E. R., XU, W. L., CHEN, H. & BRONLUND, J. E. (2007) Quartz Crystal Microbalance Induced Bond Rupture Sensing for Medical Diagnostics. *Sensors Journal, IEEE*, 7, 762-769.

VO-DINH, T., CULLUM, B. M. & STOKES, D. L. (2001) Nanosensors and biochips: frontiers in biomolecular diagnostics. *Sensors and Actuators B-Chemical*, 74, 2-11.

VOINOVA, M. V., JONSON, M. & KASEMO, B. (1997) Dynamics of viscous amphiphilic films supported by elastic solid substrates. *Journal of Physics-Condensed Matter*, 9, 7799-7808.

VOINOVA, M. V., JONSON, M. & KASEMO, B. (2002) 'Missing mass' effect in biosensor's QCM applications. *Biosensors & Bioelectronics*, 17, 835-841.

WANG, H., WU, J., LI, J. S., DING, Y. J., SHEN, G. L. & YU, R. Q. (2005) Nanogold particle-enhanced oriented adsorption of antibody fragments for immunosensing platforms. *Biosensors & Bioelectronics*, 20, 2210-2217.

WATANABE, Y., IMAEDA, N., GOKA, S., SATO, T., SEKIMOTO, H. & ISHII, S. (2007) Absolute measurement of surface-vibration-patterns in piezoelectric devices using two lasers with different wavelengths. *Joint IEEE International Frequency Control Symposium/21st European Frequency and Time Forum*. Geneva, SWITZERLAND, IEEE, Electron Devices Soc & Reliability Group.

WATANABE, Y., SATO, T., GOKA, S. & SEKIMOTO, H. (2002) Non-scanning means for determining vibrational distribution in BAW and SAW devices. IN YUHAS, D. E. S. S. C. (Ed.) *IEEE International Ultrasonic Symposium. Munich, Germany, IEEE*.

WENZEL, S. W. & WHITE, R. M. (1990) Flexural Plate-Wave Gravimetric Chemical Sensor. *Sensors and Actuators A-Physical*, 22, 700-703.

WINK, T., ZUILEN, S. J. V., BULT, A. & BENNEKOM, W. P. V. (1997) Self-assembled Monolayers for Biosensors. *Analyst*, 122, 43-50.

WOHLTJEN, H. & DESSY, R. (1979a) Surface Acoustic-Wave Probe for Chemical-Analysis .1. Introduction and Instrument Description. *Analytical Chemistry*, 51, 1458-1464.

WOHLTJEN, H. & DESSY, R. (1979b) Surface Acoustic-Wave Probes for Chemical-Analysis .2. Gas-Chromatography Detector. *Analytical Chemistry*, 51, 1465-1470.

WOHLTJEN, H. & DESSY, R. (1979c) Surface Acoustic-Wave Probes for Chemical-Analysis .3. Thermomechanical Polymer Analyzer. *Analytical Chemistry*, 51, 1470-1475.

WRIGHT, P. V., THOMPSON, D. F. & CHANG, R. E. (1995) Single-phase unidirectional transducers employing uniform-width dithered electrodes*. Ultrasonics Symposium, 1995. Proceedings. IEEE 1995*

YU, S. D. (2004) Simulation of surface acoustic wave devices*. IEEE Transactions on Ultrasonics Ferroelectrics and Frequency Control*, 51, 616-623.

YUAN, C., CHEN, A., KOLB, P. & MOY, V. T. (2000) Energy Landscape of Streptavidin-Biotin Complexes Measured by Atomic Force Microscopy. *Biochemistry,* 39, 10219-10223.

YUAN, Y. J., VANDERWERFF, M. J., CHEN, H., HIRST, E. R., XU, W. L. & BRONLUND, J. E. (2007) Bond Rupture of Biomolecular Interactions by Resonant Quartz Crystal. *Analytical Chemistry*, 79, 9039-9044.

ZISKIND, G., FICHMAN, M. & GUTFINGER, C. (1997) Adhesion moment model for estimating particle detachment from a surface. *Journal of Aerosol Science,* 28, 623-634.

ZOLLER, M. J. & SMITH, M. (1983) Oligonucleotide-directed mutagenesis of DNA fragments cloned into M13 vectors. *Methods of Enzymology*, 100, 468-500.